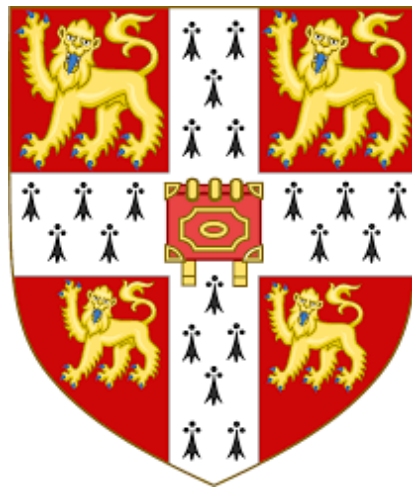


Aldehyde-driven transcriptional stress triggers an anorexic DNA damage response



Lee Mulderrig

University of Cambridge

Hughes Hall

MRC Laboratory of Molecular Biology

Cambridge, United Kingdom

This dissertation is submitted for the degree of Doctor of Philosophy

December 2021

Preface

This dissertation is my own work and contains nothing done in collaboration with others, except as specified in the text and Acknowledgements. This work has not been submitted either as a whole or in part for a degree or qualification at the University of Cambridge or any other institution of higher education. This dissertation does not exceed the length limit specified by the Degree Committee for the Faculty of Biology.

Lee Mulderrig

Acknowledgements

Firstly, I would like to acknowledge my supervisor, KJ Patel, for trusting me to work on such exciting scientific projects. I am particularly grateful for being given the freedom to explore my own research ideas and for his guidance throughout my PhD. With his help I have witnessed my experiments coalesce into impactful scientific discoveries.

I would like to thank Juan Garaycoechea with whom I worked very closely with during the early years of my PhD and prior to that. I thank Juan for his insight and guidance that served me well throughout my PhD.

I would also like to thank my second supervisor Gerry Crossan who has always been on hand to offer advice and support during my PhD.

Next, I would like to thank all the people who contributed to the work in this thesis. Juan Garaycoechea and Gerry Crossan initiated the work with the NER mice during their time in the lab. The single cell sequencing would not have been possible without collaboration with Menna Clatwothy's lab. John Ferdinand was crucial for preparing the samples for sequencing and Kelvin Tuong performed the analysis. I am grateful to John Tadross for performing the RNAscope on mouse tissues. I would also like to extend my thanks to Chris Millington for measuring formaldehyde adducts in *Adh5^{-/-} Csb^{m/m}* tissues. I would like to thank Felix Dinger for measuring GDF15 in *Adh5^{-/-} Csb^{m/m}* mice. I thank Steve O'Rahilly who was crucial in securing the GDF15 antibody and Mark Arends for his expertise in histopathology.

Working in the Patel lab has had its highs and lows, and these would not be the same without colleagues to celebrate with and receive support from. For this I thank members of the Patel lab past and present including, Fred Langevin, Michael Hodkinson, Juan Garaycoechea, Gerry Crossan, Lucas Pontel, Nina Oberbeck, Niek Wit, Guillermo Burgos Barragan, Ashley Kamimae-Lanning, Meng Wang, Laura Brandt, Felix Dingler and Ewa Gogola.

I would like to thank the LMB biomed team without whom the mouse work would not have been possible, I am grateful to Richard Berks, Angela Middleton, Claire Knox and Lesley Drynan for overseeing all the mouse strains. I would also like to thank Sara Wells, Heather Cater and Michelle Stewart for looking after our mouse strain at MRC Harwell.

Finally, I would like to thank my family and friends who continue to support me throughout the tough times and good.

Abstract

The genome is subjected to many forms of attack that can compromise its stability. Such forms of attack can emerge from endogenous or exogenous sources and must be counteracted by specialised repair pathways. Indeed, the absence of these pathways results in catastrophic human diseases. The biochemical steps and proteins involved with removal of damaged DNA from the genome are well characterised. However, the source of DNA damage for which these pathways have evolved to counteract remains unclear in many instances. Many of these pathways are also compensatory and have complex relationships with each other, therefore, attributing specific repair functions to them is not always straightforward.

This work genetically dissects the function the key DNA repair nuclease, XPF-ERCC1. This nuclease operates in the Fanconi Anaemia (FA) pathway and Nucleotide excision repair (NER). Unexpectedly, ablation of these two DNA repair pathways does not result in equivalent cellular or mouse phenotypes. However, these two pathways do appear to play independent roles in the cellular protection against the endogenous toxic metabolite, formaldehyde.

We find that endogenous formaldehyde impedes transcription, requiring repair via Cockayne Syndrome B (CSB). Mice deficient in formaldehyde clearance (*Adh5^{-/-}*) and CSB (*Csb^{m/m}*) develop cachexia, neurodegeneration and succumb to kidney failure, akin to human Cockayne Syndrome (CS). Furthermore, using scRNA-seq we reveal that formaldehyde-driven transcriptional stress stimulates the expression of the anorexiogenic peptide GDF15 by a subset of kidney proximal tubule (PT) cells. Blocking this response with a GDF15 antibody alleviates cachexia in *Adh5^{-/-}Csb^{m/m}* mice.

Therefore, CSB provides protection to the kidney and brain against DNA damage caused by endogenous formaldehyde, whilst also suppressing an anorexic endocrine signal. The activation of this signal might contribute to the cachexia observed in CS as well chemotherapy-induced anorectic weight loss. A plausible evolutionary purpose for such a response is to ensure aversion to genotoxins in food.

Abbreviations

FA	Fanconi anaemia
NER	Nucleotide excision repair
CS	Cockayne syndrome
PT	Proximal tubule
MMR	Mis-match repair
HNPCC	Hereditary non-polyposis colorectal cancer
HR	Homologous recombination
XP	Xeroderma pigmentosum
WS	Werner syndrome
TC-NER	Transcription coupled nucleotide excision repair
ROS	Reactive oxygen species
UV	Ultra-violet
XPCS	Xeroderma pigmentosum Cockayne syndrome
UDS	Unscheduled DNA synthesis
DNA Pol	DNA Polymerase
RNAPII	RNA Polymerase II
TTD	Trichothiodystrophy
VACTERL-H	Vertebral, Anal, Cardiac, Tracheo-esophageal fistula, Esophageal atresia, Renal, upper Limb and Hydrocephalus
PHENOS	Skin Pigmentation, small Head, small Eyes, Nervous System, Otology, Short stature
ICL	Interstrand crosslink
TLS	Translesion synthesis
HSC	Haematopoietic stem cell
AML	Acute myeloid leukaemia
LKS	Lineage negative c-kit positive sca-1 positive
DSB	Double strand break
OCT	Optical coherence tomography
EPO	Erythropoietin
PAS	Periodic acid schiff
H&E	Heamatoxalin and eosin
KPM	Kaplan-meier curve
N2-Me-dg	N2-Methyl-dG
I.P	Intraperitoneum
GSNO	S-nitrosoglutathione
HMG	S-hydroxymethylglutathione
iNOS	inducible nitric oxide synthase
scRNA-seq	Single cell RNA sequencing
UMAP	Uniform Manifold Approximation and Projection
GO	Gene ontology
MNP	Mononuclear phagocyte
TGF-B	Transforming growth factor B
LOH	Loop of henle
CD	Collecting duct
R.E.R	Respiratory exchange ratio
GWAS	Genome wide association study
CPD	Cyclobutane pyrimidine dimer
BER	Base excision repair
SASP	Senescence associated secretory phenotype

Table of Contents

Introduction	11
1.1 DNA Damage and Repair	11
1.2 XPF-ERCC1 – A central DNA repair protein	13
1.3 XPF-ERCC1 and Nucleotide Excision Repair	15
1.3.1 Xeroderma Pigmentosum	15
1.3.2 The molecular basis of XP	17
1.3.3 Mouse Models of XP.....	18
1.3.4 Cockayne Syndrome	18
1.3.5 The molecular basis of CS.....	19
1.3.6 Mouse Models of CS	23
1.3.7 XPCS.....	23
1.3.8 Trichothiodystrophy	25
1.4 XPF-ERCC1 and the Fanconi Anaemia Repair Pathway	25
1.4.1 Interstrand Crosslinks	25
1.4.2 Fanconi Anaemia.....	26
1.4.3 Maintenance of Genome stability by the FA pathway.....	26
1.4.4 The FA repair pathway.....	27
1.4.5 Mouse models of FA.....	28
1.4.6 NER as an alternative repair mechanism for ICLs.....	29
1.5 Sources of DNA damage	30
1.5.1 Aldehydes as sources of DNA damage.....	31
1.5.2 NER and aldehydes	34
1.6 Aims	36
Materials and Methods	37
2.1 Mouse Strains	37
2.1.1 Animal Husbandry.....	37
2.1.2 NER mice crossed with FANCA mice	37
2.1.3 Aldehyde deficient and <i>p53</i> ^{-/-} mice	38
2.1.4 NER mice crossed with aldehyde deficient mice	38
2.1.5 <i>Adh5</i> ^{sw/-} <i>Csb</i> ^{-/-} <i>Vav1-icre</i> mice	38
2.1.6 <i>Adh5</i> ^{-/-} <i>Ercc1</i> ^{c/-} <i>Nestin cre</i> mice.....	40
2.2 Animal Experiments at Harwell	40
2.2.1 Weights.....	40
2.2.2 X-ray	40
2.2.3 Grip strength.....	41
2.2.4 Echo MRI.....	41
2.2.5 Calorimetry.....	41
2.2.6 Open field	41
2.2.7 Intraperitoneal glucose tolerance test.....	41
2.2.8 Ophthalmoscope and optical coherence tomography	41
2.3 Animal Experiments at LMB	42
2.3.1 Methanol/ethanol exposure protocol.....	42
2.3.2 Cisplatin exposure protocol	42
2.3.3 GDF15 antibody treatment.....	42
2.3.4 Cerebellar ataxia scoring.....	42
2.4 Ex-vivo Studies	42

2.4.1 Colony-forming unit spleen (CFU-S ₁₂) assay	42
2.4.2 HSPC analysis by flow cytometry.....	43
2.4.3 Nuclei isolation and DNA content analysis.....	43
2.4.4 Serum biochemistry	44
2.4.5 Histology.....	44
2.4.6 Urine analysis.....	44
2.4.7 Blood counts	44
2.4.8 Immunofluorescence.....	44
2.4.7 RNA in situ hybridisation.....	45
2.5 Kidney single cell RNA sequencing.....	46
2.5.1 Kidney dissociation for scRNA-seq	46
2.5.2 scRNA-seq data analysis	46
2.6 Cell Culture.....	47
2.6.1 Cell lines.....	47
2.6.2 Generation of transformed mouse embryonic fibroblast (tMEF) lines.....	47
2.6.3 CRISPR/Cas9-mediated gene disruption of <i>ADH5</i> in HEK293 cells.....	48
2.6.4 CRISPR/Cas9-mediated gene disruptions in HAP1 cells.....	48
2.6.5 Western blotting	48
2.6.6 Antibodies	49
2.6.7 RNAPII RPB1 ubiquitylation.....	49
2.6.8 Colony survival assay.....	49
2.6.9 Cytotoxicity assays (MTS).....	50
2.7 Formaldehyde Adduct Detection.....	50
2.7.1 Synthesis of Nucleoside standards.....	50
2.7.2 Tissue sample preparation for determination of <i>N</i> ² -Me-dG in DNA.....	50
2.7.3 Snake Venom Phosphodiesterase preparation.....	51
2.7.4 LC-MS ² determination of <i>N</i> ² -Me-dG in DNA digests	51
2.8 Statistical analysis	52
<i>XPF-ERCC1 protects liver kidney and blood homeostasis outside the canonical excision pathways.....</i>	53
3.1 XPF-ERCC1 is required for normal tissue homeostasis in the liver, kidney and blood	53
3.2 Cells deficient in TC-NER are hypersensitive to crosslinking agents.....	59
3.3 NER and the FA pathway cooperate to repair formaldehyde lesions	62
3.4 TC-NER and the FA pathway preserve normal development.....	66
<i>Formaldehyde induced transcriptional stress drives Cockayne Syndrome</i>	79
4.1 Formaldehyde is toxic to cells lacking TC-NER.....	79
4.2 Formaldehyde triggers the ubiquitination and degradation of RNAPII	83
4.3 Generation of mice lacking NER and ADH5.....	87
4.4 <i>Adh5</i> ^{-/-} <i>Csb</i> ^{m/m} mice display characteristics of human CS.....	87
4.5 <i>Adh5</i> ^{-/-} <i>Xpa</i> ^{-/-} mice do not show evidence of a CS phenotype	101
4.6 Endogenous acetaldehyde does not reveal CS in mice.....	101
4.7 Discussion	104

<i>Formaldehyde drives the Adh5^{-/-}Csb^{m/m} phenotype.....</i>	108
5.1 Formaldehyde DNA adducts accumulate in ADH5 deficient brain and kidney	108
5.2 Methanol exacerbates the CS phenotype in Adh5 ^{-/-} Csb ^{m/m} mice.....	110
5.3 Methanol induces kidney failure in Adh5 ^{-/-} Xpa ^{-/-} mice.....	113
5.4 Ethanol does not reveal CS phenotypes in Adlh2 ^{-/-} Csb ^{m/m} mice	113
5.5 Discussion	116
<i>Single cell RNA-seq identifies cell types susceptible to formaldehyde-induced transcriptional stress.....</i>	118
6.1 Single cell RNA sequencing of murine kidneys.....	118
6.2 A subset of Adh5 ^{-/-} Csb ^{m/m} PT cells are damaged	125
6.3 Adh5 ^{-/-} Csb ^{m/m} PT cells display an inflammation signature.....	125
6.4 Adh5 ^{-/-} Csb ^{m/m} PT cells respond to damage by expressing GDF15	128
6.3 Discussion	132
<i>Formaldehyde transcriptional stress triggers an anorexic DNA damage response</i>	134
7.1 CSB suppresses formaldehyde induced GDF15 secretion.....	134
7.2 GDF15 expression is restricted to the kidney in Adh5 ^{-/-} Csb ^{m/m} mice.....	136
7.3 GDF15 triggers metabolic changes in Adh5 ^{-/-} Csb ^{m/m} mice	139
7.4 CSB suppresses a p53-dependent anorexic response	141
7.5 Blocking GDF15 alleviates cachexia in Adh5 ^{-/-} Csb ^{m/m} mice	143
7.6 Discussion	145
<i>Conclusions and future work.....</i>	147
8.1 Conclusions	147
8.1.1 NER and FA act independently to protect against formaldehyde genotoxicity.....	147
8.1.2 Formaldehyde drives the CS phenotype.....	148
8.1.3 An anorexic DNA damage response drives cachexia in CS	149
8.1.4 Formaldehyde causes transcription stress.....	151
8.2 Future directions	156
8.2.1 Formaldehyde and the brain	156
8.2.2 Blood formaldehyde and the CS phenotype.....	158
8.2.3 Formaldehyde and senescence.....	161
8.2.4 Dietary manipulation in CS.....	164
8.2.5 Concluding Remarks.....	167
<i>Bibliography.....</i>	168

Chapter 1

Introduction

1.1 DNA Damage and Repair

DNA is exposed to many different forms of insults that can compromise its integrity through base modifications, it is thought that 10^4 - 10^5 DNA lesions per day occur in each mammalian genome (Lindahl, 1993). These forms of attack can come from intrinsic and extrinsic sources and lead to mutagenic outcomes and cellular stress responses. To safeguard the genome, a range of specialised repair pathways exist that can mitigate against the different insults faced by DNA. Such is the fundamental requirement for protecting the genome that even the most primitive life forms have evolved DNA repair pathways. The biochemical steps involved in repairing DNA via specific repair pathways are well understood, however key questions remain in many instances such as what is the source of DNA damage? And how does DNA damage lead to the clinical features observed in DNA repair deficiency syndromes?

Mutations in genes that operate in DNA repair pathways often result in severe human disease. Interestingly, deficiency in different pathways manifest in different tissues with varied outcomes. For example, while it is common for inherited DNA repair defects to lead to cancer predisposition, loss of mismatch repair (MMR) leads predominantly to hereditary non-polyposis colorectal cancers (HNPCC) (Lynch & De la Chapelle, 1999); in contrast, mutations in the homologous recombination (HR) gene BRCA1 are responsible for almost a quarter of hereditary familial breast cancers (Antoniou et al., 2003). Perhaps these segmental clinical outcomes provide clues as to the nature of the insults that damage DNA in the first instance. This is certainly true in the case of Xeroderma Pigmentosum (XP) where patients deficient in nucleotide excision repair (NER) have a high predisposition to skin cancer and in this instance UV light is known to be the source of DNA damage (Fassihi et al., 2016; Cleaver, 1968).

Cancer as a clinical outcome of DNA repair deficiency is well understood. In fact, recent sequencing of tumours derived from patients with defective DNA repair have revealed mutational signatures in line with the repair defect. Sequencing of HNPCC's from MMR deficient individuals reveals a mutational signature associated with microsatellite instability, a process that occurs when MMR fails (Alexandrov et al., 2013). Likewise, BRCA1 deficiency results in a mutational signature associated with a high burden of indels with microhomology at the breakpoints, consistent with a failure to repair double strand breaks via HR (Nik-Zainal et al., 2016). While there are still mutational signatures with unknown aetiology, some signatures have been associated with environmental genotoxins such as UV, tobacco and alkylating agents. These observations highlight just how powerful this technique is in linking sources of damage to mutagenic outcomes (Alexandrov et al., 2013).

Cancer represents one clinical outcome of DNA damage and mutagenesis. On the other hand, premature ageing characterised by a rapid age-related decline in organ function is the other main clinical outcome of DNA repair deficiency. Werner syndrome (WS) and Cockayne syndrome (CS) are two human inherited DNA repair diseases that result in a premature ageing phenotype (Goto et al., 2013; Nance & Berry, 1992). Werner Syndrome occurs in patients with a mutation in a DNA helicase responsible for unwinding DNA to allow repair to take place (J.-L. Shen & Loeb, 2000). CS on the other hand occurs in patients with a mutation in the transcription coupled NER (TC-NER) factors CSA and CSB. The average lifespan for patients with both these diseases is dramatically reduced; the median lifespan of an individual with CS is 11.5 while for Werner syndrome it is 48 (Goto et al., 2013; B. T. Wilson et al., 2016). In addition to reduced lifespan these patients also display growth failure and functional decline in organs such as the brain and liver (Goto et al., 2013; Nance & Berry, 1992). Reactive oxygen species (ROS) have been postulated to be the driving source of DNA damage behind both of these diseases (Weissman et al., 2007) however causative evidence for this is lacking, as is a mechanism by which DNA damage leads to age related functional decline.

These rare human DNA repair diseases outline the importance of responding appropriately to DNA damage and reveal the consequences of failing to do so. In some instances, these human diseases point towards an evolutionary requirement to protect the genome from specific forms of DNA damage, XP and UV for example. For others the extreme severity of the condition makes it less clear as to what form of damage the repair pathway is protecting against. Humans deficient in the nuclease XPF-ERCC1 develop XFE progeroid syndrome, characterised by neurological deficits, hepatobiliary, musculoskeletal and haematopoietic

symptoms (Niedernhofer et al., 2006). Therefore, this repair protein must protect against fundamental sources of DNA damage that can accumulate and cause physiological harm in humans, it remains unclear however what these forms of damage are.

1.2 XPF-ERCC1 – A central DNA repair protein

ERCC1 operates in association with XPF as a structure specific nuclease; both proteins are required in order to function. The XPF-ERCC1 complex operates in many DNA repair pathways including the Fanconi Anaemia (FA) repair pathway, global genome (GG) NER and TC NER (Figure 1.01). In all these pathways the function of XPF-ERCC1 remains as a nuclease that excises damaged DNA. Perhaps then the severe human phenotypes associated with XFE progeroid syndrome are a result of joint inactivation of all these repair pathways. Patient mutations in ERCC1 and XPF reflect the multi-functionality of this nuclease with a myriad of phenotypes depending on which pathway is deficient (Bogliolo et al., 2013; Fassihi et al., 2016; Kashiwama et al., 2013; Natale & Raquer, 2017). *Ercc1*^{-/-} mice develop neurological deficits, cachexia, renal dysfunction as well as haematological problems, ultimately though they succumb to liver failure (Niedernhofer, et al., 2006; McWhir, et al 1993). Therefore, in support of the mouse as a useful tool in studying DNA repair, *Ercc1*^{-/-} mice phenocopy the human equivalents. This mouse model offers an opportunity to study the physiological consequences of DNA damage, however the question remains as to why these humans and mice are so severely affected. Is this due to combined deficiency of the DNA repair pathways XPF-ERCC1 operates in?

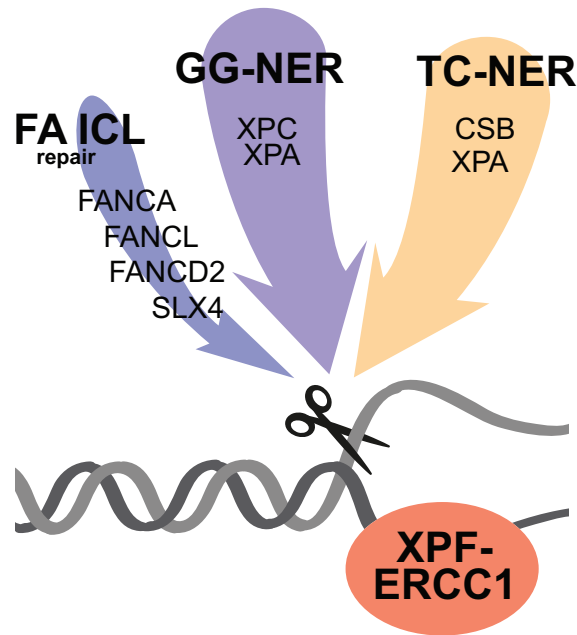


Figure 1.01 – DNA repair pathways that use the XPF-ERCC1 nuclease

Model illustrating how several DNA repair pathways descend on the XPF-ERCC1 nuclease in order to complete the repair process. The FANCA, FANCL, FANCD2 and SLX4 proteins operate in FA ICL repair to facilitate cutting of the DNA by XPF-ERCC1. XPF-ERCC1 also operates in GG-NER and TC-NER, which have some of the same downstream factors such as XPA but detect damage differently through the functions of XPC and CSB respectively.

1.3 XPF-ERCC1 and Nucleotide Excision Repair

XPF-ERCC1 is essential for NER to take place. NER consists of two sub-pathways known as GG-NER and TC-NER that descend into the same downstream factors (including XPF-ERCC1) but differ in the way they sense DNA damage (Figure 1.02). GG-NER is triggered through an active sensing mechanism of helix distorting DNA lesions whereas the stalling of RNAPII at the site of DNA damage triggers TC-NER (Marteijn et al., 2014). Patient mutations in XPF or ERCC1 that leave the FA pathway intact result in the human clinical conditions Xeroderma Pigmentosum, Cockayne Syndrome or in extreme situations a combination of both (XPCS) (Fassihi et al., 2016; Kashiyaama et al., 2013; Natale & Raquer, 2017).

1.3.1 Xeroderma Pigmentosum

Dermatologist Moriz Kaposi originally described Xeroderma Pigmentosum (XP) in 1874 when he observed multiple skin tumours in young patients. Further studies have revealed that XP patients have a remarkable 10,000-fold risk of developing non-melanoma skin cancer and a 200-fold increase in melanoma (Bradford et al., 2011). Genetically, 8 complementation groups have been assigned to XP; XPA, B, C, D, E, F, G and V and these groups can be divided into 2 subgroups. Complementation groups XPC, XPE and XPV have been shown to have increased skin cancer predisposition however they have normal sunburn reaction and do not suffer neurological problems. Groups XPA, XPB, XPD, XPF and XPG sunburn very easily, have slightly lower skin cancer predisposition but develop progressive neurological degeneration (Fassihi et al., 2016). More recently it has been observed that XPC patients also have an increased predisposition towards leukaemia and sequencing from these cancers indicated an increased mutational burden compared to control tumours (Yurchenko et al., 2020).

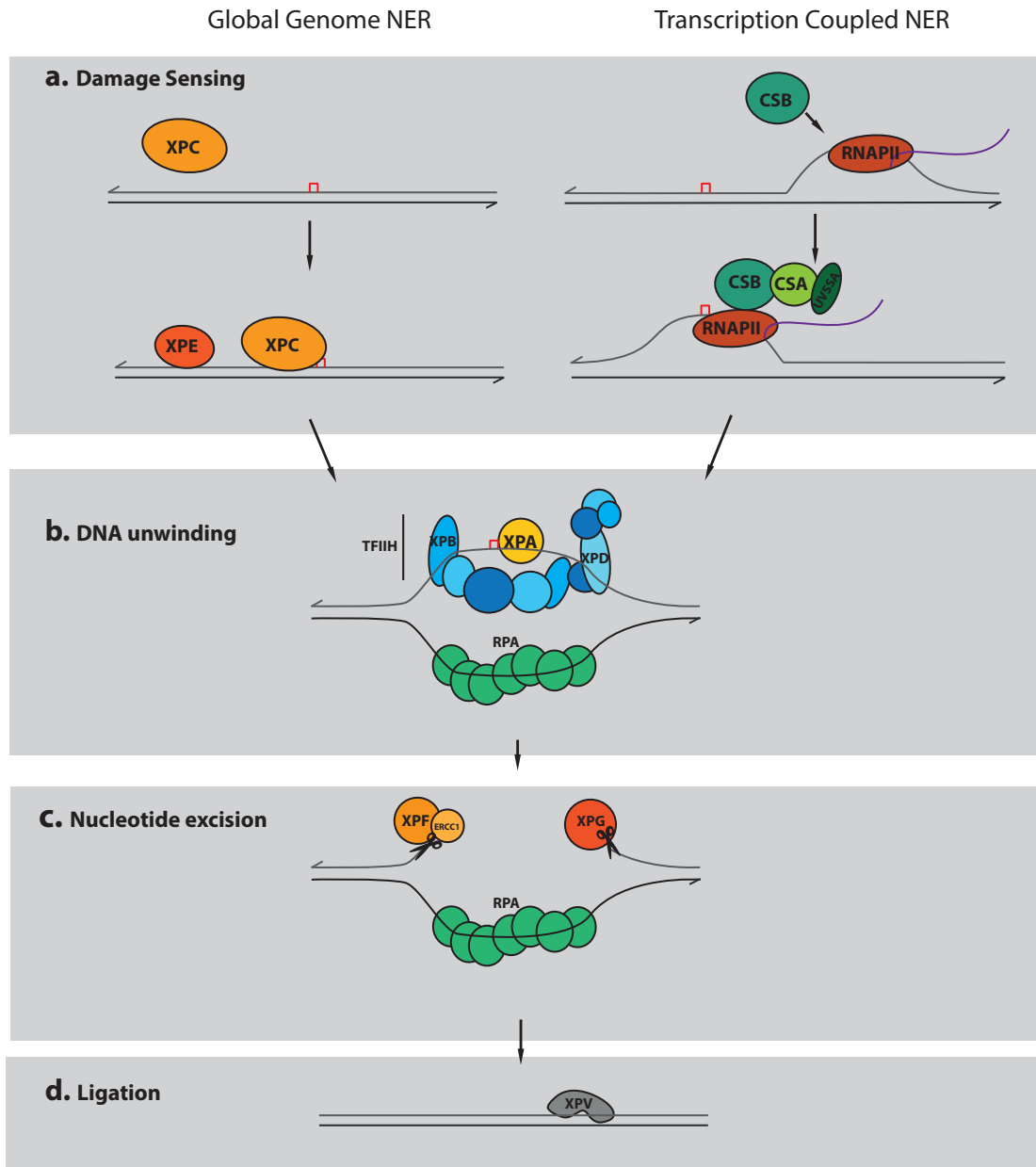


Figure 1.02 – Nucleotide Excision Repair Pathway

a) NER can be divided into 2 branches (TC and GG), which differ in how they sense damage, either by stalling of RNAPII or XPC sensing helix distortions. **b)** After lesion sensing, the damage is verified by XPA and then TFIIH unwinds the DNA through XPB and XPD subunits. **c)** The unwound DNA can now be cut by the nucleases XPF-ERCC1 and XPG either side of the lesion. **d)** The remaining gap is then filled in by replicative polymerases, XPV acts a back-up translesional polymerase to bypass lesions not excised by NER

1.3.2 The molecular basis of XP

In 1968 the relationship between UV and XP became clear when it was observed that XP cells fail to repair DNA after UV irradiation (Cleaver, 1968). In this experiment, the levels of unscheduled DNA synthesis (UDS) were measured after UV exposure, fibroblasts from XP patients did not perform UDS whereas control fibroblasts showed evidence of repair by UDS (Cleaver, 1968). Once the cellular defect in XP cells had been identified, efforts were then made to clone and complement the defect. This was successfully done for many XP genes by using rodent CHO cells that had been classified into complementation groups and then screening random human DNA fragments for successful cross complementation (Thompson et al., 1994; Weber et al., 1988; Weeda et al., 1990; Westerveld et al., 1984).

The identification of the genes involved in XP along with the source of DNA damage that these factors repair led to the hypothesis of a DNA repair pathway acting in concert to repair UV DNA lesions. This pathway is known as NER, furthermore 2 distinct sub-pathways have been identified, GG-NER and TC-NER. DNA damage is detected in GG-NER by the XPC protein which can bind to helix distorting lesions (Sugasawa et al., 1998). XPE also has lesion binding ability but this appears to be restricted to a subset of DNA lesions (Scrima et al., 2008). XPC binding to helix-distorting lesions provides a substrate for the association of the TFIIH complex, a complex of 10 proteins that includes the helicases XPB and XPD which can unwind the DNA around the lesion (Tapias et al., 2004). After unwinding the DNA the bubble structure is recognised by the nucleases XPF-ERCC1 and XPG which excise the lesion at short distances 5' and 3' respectively (Fagbemi et al., 2011). A central regulator of excision in NER is XPA which is required to recruit XPF-ERCC1 (Orelli et al., 2010).

Finally, with the DNA containing the lesion being excised, the ~30 nucleotide gap requires filling in and ligating. This can be done by either DNA Pol δ , ϵ or κ and DNA ligase 1 or XRCC1-DNA ligase 3. The particular polymerase and DNA ligase used depends upon the replicative rate of the cell type. Rapidly dividing cells show a preference for DNA Pol ϵ and DNA ligase 1 whereas non-dividing cells appear to utilise DNA Pol δ or DNA Pol κ in combination with XRCC1-DNA ligase 3. (Moser et al., 2007; Ogi et al., 2010). Additionally, a back-up pathway for lesions that are not excised by canonical NER exists that involves bypass of the lesion by polymerase η (XPV) (Masutani et al., 1999).

1.3.3 Mouse Models of XP

Mice deficient in *Xpc* and *Xpa* were originally described in 1995 however, these mice developed no overt phenotype. Cells from these mice lines did show defects in UDS and sensitivity to UV, and when the mice were exposed to UV light they displayed a high incidence of skin cancers (de Vries et al., 1995; Nakane et al., 1995; Sands et al., 1995). Subsequently, *Xpe* mice have also been generated and this line too displayed a similar phenotype to the *Xpc* and *Xpa* lines (Itoh et al., 2004). *Xpv* codes for the translesion synthesis polymerase η which is required for error-free repair of UV lesions not excised by canonical GG-NER (Masutani et al., 1999). Therefore, mice and cells deficient in the XPV gene are also very sensitive to UV toxicity and the mice have a high predisposition to skin cancer when exposed to UV (Ohkumo et al., 2006). Mouse models for other XP genes exist however these factors operate in other pathways leading to complex, severe phenotypes that are unlikely to stem from just loss of GG-NER.

1.3.4 Cockayne Syndrome

Mutations in the genes *CSA* and *CSB* result in the human disease Cockayne Syndrome (CS). CS is a rare, autosomal-recessive disorder that was first described by the English physician Edward Cockayne in 1946 where he described two children with dwarfism, retinal atrophy and deafness (Cockayne, 1946). More recent examinations of cohorts of CS patients have revealed the heterogeneous nature of the disease and have resulted in a comprehensive overview of the various clinical manifestations (Kubota et al., 2015; Laugel, 2013; B. T. Wilson et al., 2016). The cardinal feature of CS is growth failure, although weight at birth is often within the normal range the growth failure in CS patients generally begin within the first year of life and is profound, with few CS patients ever reaching 20kg (Baer et al., 2021; Nance & Berry, 1992). This growth failure is exacerbated by postnatal feeding difficulties, gastroesophageal reflux and vomiting, with many CS patients having to be fed via a nasogastric tube or percutaneous gastrostomy (Laugel, 2013; B. T. Wilson et al., 2016). The growth failure and feeding difficulties lead to distinct facial features; CS patients lack subcutaneous orbital fat leading to sunken eyes and a prominent nose (Kubota et al., 2015; Laugel, 2013; B. T. Wilson et al., 2016). Despite being well defined in CS, the basis of the growth failure remains a mystery.

Another cardinal feature of CS is progressive neurological decline and microcephaly. While early cognitive development appears normal intellectual disability is soon apparent with 20% of CS patients never progressing beyond single words of speech and many having reduced fine and gross motor skills (Nance & Berry, 1992). Cerebellar ataxia, tremors, incoordination

and in some cases, seizures are also present in CS which stem from pathological changes within the brain. MRI imaging of the brains of CS individuals have revealed a range of defects including calcification of the basal ganglia, cerebellar atrophy and myelination defects (Nance & Berry, 1992; B. T. Wilson et al., 2016). Along with neurological decline, a prominent feature of CS is a decline in vision and hearing, cataracts have been noted within the first 3 years of life and retinal degeneration as early as 44 months old. Though hearing loss may not manifest until teenage years, its prominence in CS has been reported and is similar to retinal degeneration, with a recent study observing hearing loss present in 43% of patients and retinal degeneration on 44% (B. T. Wilson et al., 2016). Pathological observations have documented loss of neurons in the spiral ganglia and loss of ganglion cells in the retina coupled with demyelination (Nance & Berry, 1992; B. T. Wilson et al., 2016). These observations suggest that there is a common basis for the neurological, hearing and vision deterioration in CS.

The median life span of CS is 18 years, many different causes of death have been reported including pneumonia, hypertensive crisis and cachexia (Laugel, 2013; Nance & Berry, 1992). Recently, renal failure has been associated with many causes of death in CS, with one study observing 69.2% of deceased patients having suffered renal failure (Kubota et al., 2015). The pathological changes in the kidney of CS patients include glomerulosclerosis, a thickened basement membrane and tubular atrophy. Prior to renal failure, patients have been observed to dramatically reduce food intake resulting in extreme cachexia (Kubota et al., 2015; Stern-Delfils et al., 2020).

1.3.5 The molecular basis of CS

CS cells, like XP cells, are very sensitive to the effects of UV irradiation. However, a defect in excision repair by UDS that is present in XP cells is absent in CS cells (Andrews et al., 1978). However, in 1982 when Mayne and Lehman measured the recovery of RNA synthesis (RRS) in CS cells, they revealed that levels of RNA synthesis failed to recover after UV exposure (Mayne & Lehmann, 1982). This led to speculation that the CS proteins operate in a special form of excision repair, one that was coupled to transcription.

TC-NER is unlike other DNA repair pathways in that it is not triggered by the DNA lesion itself but rather by the stalling of RNA polymerase II (RNAPII), which serves as a damage signal and recruits the Cockayne Syndrome B (CSB) protein (Anindya et al., 2010). RNAPII bound CSB then recruits CSA through a CSA-interaction motif which then in turn recruits UVSSA (van der Weegen et al., 2020). Once assembled this complex can promote forward

translocation of RNAPII over small transcription obstacles through CSB's ATPase activity. However, if the obstacle cannot be bypassed by RNAPII forward translocation then CSA ubiquitinates RNAPII at K1268 leading to the recruitment of the TFIIH complex (Kokic et al., 2021). The TFIIH complex may then facilitate backtracking of the stalled RNAPII (Kokic et al., 2019), making DNA accessible for repair by the XPA, XPF-ERCC1 and XPG proteins that excise the damaged nucleotides. Once the damaged strand is restored, RNAPII can resume transcription (Gregersen & Svejstrup, 2018; Lans et al., 2019).

During transcription, RNAPII moves along a gene in a processive manner polymerising mRNA. However, damage to the DNA template strand poses a challenge to the transcriptional machinery, stalling the progression of RNAPII (Brueckner et al., 2007; J. Xu et al., 2017). The transcription machinery responds to such obstacles by initiating TC-NER but also triggers global shutdown of transcription and degradation of the RNAPII (M. D. Wilson et al., 2013). Although CSB has a role in TC-NER, CSB depletion also leads the global shutdown of transcription and RNAPII degradation which has led many to question what aspect of CSB's role in the response to transcriptional DNA damage leads to CS.

Lehmann and Mayne initially proposed that the reduction in RNA synthesis in CS cells was due to the DNA lesions blocking the RNAPII and therefore reducing transcriptional output (Mayne & Lehmann, 1982). If this were true, however, then the reduction in transcription would be limited to the elongation process, but CS cells also display a defect in transcription initiation (Rockx et al., 2000). Furthermore, a UV treated plasmid is enough to trigger a reduction in gene expression once transfected into wild type cells (M. J. Muñoz et al., 2017). These studies suggest that a signaling process must take place that prevents initiation of new transcripts; most likely through the RNAPII that encounters the lesion. This is likely to be beneficial in the presence of stalled RNAPII's to avoid RNAPII molecules accumulating at DNA lesions. Intriguingly, after UV damage promoter proximal RNAPII molecules are driven into transcription elongation, possibly as lesion sensors to trigger TC-NER (Lavigne et al., 2017).

RNAPII is modified upon DNA damage (Nakazawa et al., 2020; Rockx et al., 2000; Tufegdžić Vidaković et al., 2020). At the steady state level, the actively transcribing RNAPII is hyperphosphorylated (RNAPII Ilo) while the non-transcribing RNAPII is not phosphorylated (RNAPII Ila). When the RNAPII Ilo encounters a lesion during transcription it becomes poly-ubiquitinated and degraded. This degradation then leads to more of the RNAPII Ila to begin transcribing and thus becoming hyperphosphorylated (M. D. Wilson et al., 2013). Recently,

using a mutant of RNAPII that cannot be ubiquitinated at K1268, it has been suggested that ubiquitination of RNAPII acts as an initiator of TC-NER (Kokic et al., 2021; Nakazawa et al., 2020) and is required for the degradation of RNAPII. Excessive RNAPII degradation could therefore be the reason why global transcription is shut down in response to DNA damage. In the CSB-deficient background, RNAPII levels do not recover after DNA damage providing a molecular mechanism to the global shutdown of transcription observed in CS cells (Tufegdžić Vidaković et al., 2020).

Both XP and CS involve deficiency in DNA repair and there is some clinical overlap in the manifestation of skin photosensitivity. However, while XP is characterised by an extremely high skin cancer predisposition, CS patients only show a predisposition to burn in response to UV exposure (Laugel, 2013). In fact, CS is notable for the complete absence of any form of cancer in contrast to the 10,000-fold risk of developing non-melanoma skin cancer in XP (Bradford et al., 2011). Although the age at death is much younger in CS, which may preclude any tumours from arising, it is more likely that while the absence of GG-NER results in mutagenesis after UV exposure whereas the absence of TC-NER does not (Reid-Bayliss et al., 2016). Instead, DNA damage in TC-NER deficient cells has been shown to lead to cellular senescence and apoptosis (Crochemore et al., 2019; S. Wang et al., 2020), perhaps explaining why organs decline in CS rather than become cancerous.

The molecular basis of CS remains hotly debated. What aspect or aspects of the transcriptional response to DNA damage absent in CS cells contributes to the clinical phenotype of CS? It is important to note that while informative, many of the cellular studies that have been used to unravel the role of the CS proteins in global transcription shutdown and RNAPII degradation have been performed by exposure to high doses of UV that are unlikely to be physiological (Nakazawa et al., 2020; Tufegdžić Vidaković et al., 2020). This creates an extreme situation that is unlikely to be played out *in vivo*, raising the possibility that the DNA damage burden is not high enough to trigger these responses. In contrast, patients with mutations in XPF and ERCC1 have been described that have classical CS, suggesting that excising the damaged DNA through TC-NER is critical in suppressing the CS phenotype (Kashiyama et al., 2013).

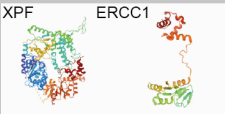
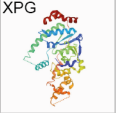
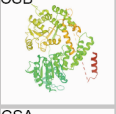
	Function	Disease		Function	Disease
	Damage Verification	XP		5' Nuclease	XP, XPCS, FA, XFE
	3' -5' Helicase	XP, XPCS, TTD		3' Nuclease	XP, XPCS,
	Damage sensor	XP		Polymerase	XP
	5' -3' Helicase	XP, XPCS, TTD		Senses stalled RNAPII	CS
	Damage sensor	XP		CSB binding partner	CS

Figure 1.03 – Functions of the NER proteins along with the associated human disease

The 8 Xeroderma Pigmentosum complementation groups along with the function of each protein and associated human diseases (XP – Xeroderma Pigmentosum, CS – Cockayne Syndrome, XPCS Combined Xeroderma Pigmentosum and Cockayne Syndrome, FA – Fanconi's Anaemia and TTD – Trichothiodystrophy, XFE – XFE progeroid syndrome).

1.3.6 Mouse Models of CS

A mouse model of CS was first described in 1997 when a mouse harbouring a patient mutation of *CSB* was generated (G. T. van der Horst et al., 1997). *Csb*^{-/-} and *Csa*^{-/-} mice develop normally, showing no signs of neurological deficits and are indistinguishable from wild type mice. In response to UV and chemically induced mutagenesis, *Csb*^{-/-} mice show an increased predisposition towards cancer, although this occurred in fewer animals and progressed slower than *Xpa*^{-/-} deficient mice. However, cells from *Csa*^{-/-} and *Csb*^{-/-} mice display the classical RRS defect after UV exposure, highlighting a deficiency in TC-NER (G. T. van der Horst et al., 1997; G. T. J. Van Der Horst et al., 2002). The presence of the cellular defect alongside a subtle phenotype in mouse models of CS suggests that perhaps the burden of damage is not high enough to trigger the severe phenotype observed in human CS patients. In support of this idea *Csa*^{-/-} and *Csb*^{-/-} mice treated with cisplatin, which causes transcription blocking lesions, are predisposed to hearing loss (Rainey et al., 2016) outlining how increased transcriptional stress can reveal aspects of the CS phenotype in *Csa*^{-/-} and *Csb*^{-/-} mice.

The CS phenotype in humans is progressive, similarly, mice lacking CSB display some progressive features of CS when aged. 20-month-old *Csb*^{-/-} mice display a mild loss of spiral ganglion, reduced subcutaneous fat and increased metabolism. Furthermore, these defects have been suggested to be due to defective mitochondria (Scheibye-Knudsen et al., 2012). Mechanistically, it has been suggested that mitochondrial dysfunction occurs in the absence of CSB due to dysregulated PARylation. Persistent PARylation depletes cellular NAD leading to mitochondrial damage. Interestingly, the mild phenotype of *Csb*^{-/-} mice have been rescued by supplementation of nicotinamide riboside (Scheibye-knudsen et al., 2015). However, given the mild phenotype of *Csb*^{-/-} mice, it is unclear whether supplementation of nicotinamide riboside would alleviate the more severe human disease.

1.3.7 XPCS

In addition to XP and CS, mutations in the helicases XPB and XPD and the nucleases XPF, ERCC1 and XPG, can result in another clinically distinct human disease, XPCS. XPCS is a very severe human disease that combines the clinical characteristics of CS and XP, which is the CS phenotype in combination with the skin cancer predisposition of XP. XPCS is very rare, with only 42 patients reported so far (Natale & Raquer, 2017).

In mice, complete deletion of XPB and XPD are embryonic lethal. Mouse lines with viable mutations in XPD lead to a mild form of XPCS, developing cachexia and progressive loss of

germ cells. As with other XP mouse lines, no skin cancers are observed unless treated with UV in which case squamous cell carcinomas develop (J.-O. Andressoo et al., 2009; J. O. Andressoo et al., 2006). Mice lacking the NER nuclease XPG are very compromised, however on a C57BL/6 x FVB F1 background can survive until 18 weeks. These mice display a combined XPCS phenotype with cachexia and neurological deficits prominent (Barnhoorn et al., 2014b).

Ercc1^{-/-} mice are well studied and when bred in a C57BL/6 x FVB F1 background survive for just 3 weeks in contrast to 18 weeks for *Xpg*^{-/-} mice. *Ercc1*^{-/-} mice suffer from neurological decline, are sterile, have reduced haematopoietic stem cells, kidney dysfunction, growth failure and ultimately succumb to liver failure at weaning age (McWhir et al., 1993; Niedernhofer et al., 2006; Weeda et al., 1997). Mice deficient in XPF display a similar phenotype to the *Ercc1*^{-/-} mice (Ming Tian et al., 2004). Correcting the liver defect in *Ercc1*^{-/-} mice by using an *Ercc1* transgene driven by an albumin promoter, prolongs the lifespan of these mice by a few weeks only for them to succumb to renal failure (Selfridge et al., 2001). Increased DNA damage has been observed in the brains of *Ercc1*^{-/-} mice, measured by γH2AX, a marker of DNA double strand breaks, linking deficiency of this DNA repair factor with increased DNA damage and tissue decline (Jaarsma et al., 2011; Vermeij et al., 2016). Tissue specific deletion of *Ercc1* in the skin results in a hypersensitivity to UV induced cancer, highlighting the need for *Ercc1* in protection against DNA damaging agents (Doig et al., 2006). However, the endogenous source of DNA damage that leads to the multisystem organ dysfunction in *Ercc1*^{-/-} mice remains unclear and is unlikely to be UV given the phenotype affects the brain, liver and kidney.

Surprisingly, when mice lacking CSB are crossed with mice that lack XPA the result is a severe XPCS phenotype (van der Pluijm et al., 2007). This has led to the proposal that there is an interaction between NER and other functions of CSB, whereby failure to repair lesions through GG-NER leads to an increased number of lesions that form a block for transcription. This interaction would explain some of the severe XPCS phenotypes observed in mice deficient in XPG, XPD and XPB. However, the *Ercc1*^{-/-} mice display additional complications such as blood defects, which may indicate that other repair deficiencies interact to contribute to the phenotype of these mice. Indeed this is reflected in human patients with XPF-ERCC1 deficiency that have additional distinct phenotypes to XPCS patients, referred to as XPE progeroid syndrome (Niedernhofer, et al., 2006).

1.3.8 Trichothiodystrophy

The NER helicases XPD and XPB form part of the TFIIH complex which forms a critical part of the NER process but also has an important role in promoter opening during transcription initiation (Coin et al., 1999). Due to this function in transcription initiation, mutations in XPB, XPD and another TFIIH subunit, TTDA, can result in the human disease trichothiodystrophy (TTD). TTD patients display ichthyosis, brittle hair and nails, intellectual impairment, decreased fertility and short stature with patients that have mutations in XPB and XPD displaying additional photosensitivity (Bergmann & Egly, 2001). Surprisingly, XPD and XPB mouse lines do not display the classical TTD phenotypes (Jan De Boer et al., 1998). However, TTD is a result of defective transcription and not due to a failure to repair DNA damage.

NER genes therefore are implicated in several human diseases (Figure 3.01) making it difficult to attribute specific DNA repair functions to clinical phenotypes. Even within each genetic disease (CS, XP, XPCS and TTD) there exists different severities and subgroups (Bergmann & Egly, 2001; Fassihi et al., 2016; Laugel, 2013). It is important therefore to genetically dissect specific functions to be able to implicate them in phenotypes.

1.4 XPF-ERCC1 and the Fanconi Anaemia Repair Pathway

In addition to NER, XPF-ERCC1 operates in the Fanconi Anaemia (FA) repair pathway through its structure specific nuclease activity. The substrate that XPF-ERCC1 acts on is similar in structure to the unwound bubble structure that forms during NER. However the preceding steps in the FA DNA repair pathway differ greatly to NER (Ceccaldi et al., 2016), as does the clinical outcome in patients that have mutations in XPF-ERCC1 affecting its activity in FA repair. In contrast to mutations that affect XPF-ERCC1's function in NER leading to XP, CS and XPCS, mutations that affect its function in the FA repair pathway lead to classical FA (Bogliolo et al., 2013; Fassihi et al., 2016; Kashiyama et al., 2013; Natale & Raquer, 2017).

1.4.1 Interstrand Crosslinks

On 2 December 1943 the SS *John Harvey* was docked at the port of Bari on the Adriatic coast in southern Italy. Unknown to the inhabitants of Bari and to the approaching German bombers, deep in the hull of the SS *John Harvey* lay 2000 M47A1 mustard gas bombs. The German bombers released their payload, sinking the SS *John Harvey* and releasing the

mustard gas into the atmosphere and the oily water of the harbour where it came into contact with military personal (Pechura et al., 1993) .

Mustard gas exerts its toxicity through its ability to form DNA interstrand crosslinks (ICLs), one of the most toxic DNA lesions a cell can encounter. ICLs are covalent bonds that form between opposing DNA strands, blocking essential cellular processes such as replication and transcription (Guainazzi et al., 2010; Rink et al 1993). Unfortunately for the casualties of the Bari Air Raid the consequences of exposure to ICLs were later discovered to be aplastic anaemia and acute myeloid leukaemia highlighting the exquisite sensitivity of the haematopoietic system to ICLs (Pechura et al., 1993).

1.4.2 Fanconi Anaemia

The Bari Air Raid is an example of human exposure to exogenous ICLs; however, it has been well established that ICLs also occur endogenously and much of the evidence for this has come from studying a rare genetic disease known as Fanconi's Anaemia (FA). FA was originally described in 1927 by the Swiss paediatrician, Guido Fanconi, where he described 3 brothers with short stature, physical abnormalities and anaemia (Fanconi, 1927). FA is a rare recessive autosomal or X-linked genetic disorder with complex heterogeneous clinical features (Alter et al., 2003; Kutler et al., 2003). Recent examinations of cohorts of FA individuals have expanded on the original clinical observations made by Guido Fanconi and include congenital abnormalities that fall in either the VACTERL-H (Vertebral, Anal, Cardiac, Tracheo-esophageal fistula, Esophageal atresia, Renal, upper Limb and Hydrocephalus) or PHENOS (skin Pigmentation, small Head, small Eyes, Nervous System, Otology, Short stature) categories (Fiesco-Roa et al., 2019). While the congenital abnormalities in FA are extremely heterogeneous most FA patients show haematological manifestations including aplastic anaemia, myelodysplastic syndrome and leukemia, the current cumulative incidence for FA patients either succumbing to bone marrow failure or receiving a haematopoietic cell transplant by age 50 is 70% (Alter et al., 2003; Kutler et al., 2003). Another notable feature of FA is the development of head and neck and anogenital squamous cell carcinomas at rates that are hundreds-fold greater than those observed in the general population (Kutler et al., 2003).

1.4.3 Maintenance of Genome stability by the FA pathway

The connection between the haematological features of FA and the victims of the Air Raid on Bari is DNA damage. Indeed, the molecular basis of FA was unravelled in 1972 when Sasaki & Tonomura exposed cells isolated from FA patients to nitrogen mustard, along with other

ICL-causing compounds, and observed a huge increase in the number of chromosome aberrations (Sasaki & Tonomura, 1973). In fact, the hallmark of FA deficient cells is their extreme sensitivity to crosslinking agents and as such these agents have become the gold standard for the clinical diagnosis of FA (Auerbach, 2009). Additionally, cells deficient in the FA pathway display cell cycle irregularities; they spontaneously have a prolonged G2 phase that can be exacerbated by treatment with crosslinking agents (Sala-Trepat et al., 2000). In line with its function in FA repair, cells deficient in ERCC1 also display chromosomal aberrations, G2 accumulation and hypersensitivity when exposed to ICL's (Niedernhofer et al., 2004; Niedernhofer et al., 2006)

Identifying the proteins involved in the FA pathway has been key to its understanding, in 1992 Strathdee *et al* cloned the *FANCC* gene and complemented a patient cell line to rescue the ICL sensitivity of the patients cells, identifying the first component of the FA repair pathway (Strathdee et al., 1992). After the identification of the FANCC complementation group, 21 more followed, cellular deficiency of which results in the classical FA sensitivity to ICLs. It is now understood that all the products of the FA genes operate in a common repair pathway that facilitates the repair of an ICL. ICL repair can be divided into 5 main steps: FA core complex assembly, the ubiquitination of the FANCD2/FANCI dimer, and excision of the ICL, lesion bypass and homologous recombination.

1.4.4 The FA repair pathway

Recent biochemical reconstitution studies along with structural work have revealed a detailed step-by-step process of the repair of an ICL by the FA repair pathway. ICL's form a replication impediment that stimulates the ubiquitination of FANCD2 and FANCI (Knipscheer et al., 2009). Ubiquitination of the FANCD2-FANCI dimer first requires assembly of the FA core complex which consists of eight subunits; FANCA, FANCB, FANCC, FANCE, FANCF, FANCG, FANCL and FAAP100 (Rajendra et al., 2014). The structure of the core complex revealed that it is formed of two central dimers of FANCB and FAAP100 flanked by two copies of FANCL, these two heterodimers act as a scaffold to assemble the remaining 5 subunits (Shakeel et al., 2019).

Once the core complex has assembled it functions as an E3 ubiquitin ligase to mono-ubiquitinate the FANCD2-FANCI dimer (Alpi et al., 2008). Using *Xenopus* egg extracts, Knipscheer *et al* demonstrated that FANCD2 was essential for the repair of a cisplatin ICL. Extract that was complemented with FANCD2 harbouring a mutated ubiquitin site could also no longer repair a cisplatin ICL, identifying the monoubiquitination of FANCD2 as an

essential step in ICL repair (Knipscheer et al., 2009). Recent structural work has highlighted the importance of the ubiquitination step, revealing that only in the presence of ubiquitinated FANCD2 can the FANCI-FANCD2 dimer form a clamp around DNA to recruit the nuclease incision complex (Alcón et al., 2020)

In order to excise the ICL from DNA, nucleases must next be recruited to cut the ICL, this is facilitated by the scaffold FANCP (SLX4), which interacts with 3 known nucleases, MUS81-EME1, SLX1 and XPF-ERCC1 (Andersen et al., 2009; Fekairi et al., 2009; I. M. Muñoz et al., 2009; Svendsen et al., 2009). Although all three nucleases have been implicated in ICL repair, XPF-ERCC1 has been shown to be essential for the “unhooking” of the ICL by biochemical assays (Hodskinson et al., 2014). Indeed deficiency in XPF-ERCC1 in the *Xenopus* system specifically inhibited the incision step of ICL repair (Klein Douwel et al., 2014). Interestingly, while XPF-ERCC1 is recruited by XPA to incise bubble structures during NER, SLX4 greatly enhanced the activity of XPF-ERCC1 towards processing fork like structures and had no effect on bubble like structures (Hodskinson et al., 2014). This indicates that while XPF-ERCC1 operates as a nuclease in both NER and FA, other proteins in those pathways determine substrate specificity.

Once dual excisions of the crosslink have taken place, one chromatid contains the unhooked crosslink while the other contains a double strand break. The chromatid containing the crosslink is then bypassed by translesion synthesis and can serve as a template to repair the sister chromatid by homologous recombination (Long et al., 2011).

1.4.5 Mouse models of FA

In order to study the physiological consequences of an inability to repair ICLs, numerous mouse models of FA have been generated. The first mouse model of FA was described in 1996 and contained a targeted disruption in exon 9 of the *Fancc* gene. In contrast to the severe human phenotype this mouse line has a much milder phenotype, however, the mice did show reduced fertility and a reduction in bone marrow progenitor cells (Whitney et al., 1996). Subsequent mouse lines from targeted deletions in the *Fanca*, *Fancd2*, *Fancm*, *Fanci* and *Fanccp* genes have been described that confirm that FA mice have an FA-like phenotype though much milder than the human form of the disease (Crossan et al., 2011; Dubois et al., 2019; Houghtaling et al., 2003; Wong et al., 2003). However, despite the mild phenotype of the mice, cells from FA deficient mice still have the cellular defect of hypersensitivity to ICL agents and abnormal chromosomes after ICL exposure (Crossan et al., 2011; Dubois et al., 2019; Houghtaling et al., 2003; Whitney et al., 1996; Wong et al., 2003).

Although FA mice do not succumb to bone marrow failure, studies on FA mice have been able to shed some light on the blood defects that result due to FA DNA repair deficiency. The numbers of haematopoietic stem cells are reduced in the embryonic foetal liver of FA mice (Kamimae-Lanning et al., 2013a). Bone marrow cells from various adult FA mouse lines have also have a reduced ability to reconstitute irradiated recipients after transplantation (Barroca et al., 2012; Crossan et al., 2011; Zhang et al., 2010) and in the case of *Fancd2*^{-/-} mice, HSCs appear to show increased cell cycle entry (Zhang et al., 2010). Finally, it has also been shown that *Fancd2*^{-/-} mice HSC defects can be rescued in the absence of p53 (Ceccaldi et al., 2012).

Studying FA defects outside the haematopoietic system in mouse models has also led to insights into the disease. FA deficient mice display hypogonadism and diminished fertility due to reduced primordial germ cells (Wong et al., 2003). Furthermore, the study of primordial germ cells in FA mice has narrowed down the temporal window within which the germ cell defects arise, during this window the primordial germ cells also displayed elevation of the apoptotic markers, p53 and cleaved caspase 3 (R. J. Hill & Crossan, 2019). In summary, knockout mice reveal specific cell types are vulnerable to loss of the FA pathway; these cell types are highly proliferative and in the absence of the FA pathway undergo p53-dependant apoptosis.

In contrast to the mild defects observed in FA deficient mice, *Ercc1*^{-/-} mice display a very severe phenotype leading to multisystem degenerative features, severe growth defects and a drastically shortened lifespan, similar to *Xpg*^{-/-} mice and consistent with a role in NER. However, consistent with a defect in ICL repair, *Ercc1*^{-/-} mice also display a reduced number of haematopoietic stem cells (Prasher et al., 2005) and are sterile with a similar reduction in primordial germ cells as FA deficient mice (R. Hill & Crossan, 2019). This suggests that the phenotype of *Ercc1*^{-/-} mice may be due to joint inactivation of FA repair and NER.

1.4.6 NER as an alternative repair mechanism for ICLs

XPF-ERCC1 deficiency results in a catastrophic phenotype in humans and mice, this nuclease plays a central role in the FA repair pathway, TC-NER and GG-NER. Could this phenotype be due to combined inactivation of these 3 pathways? If so, could there be a substrate common to several of these pathways that triggers the severe phenotype?

In *E. coli*, NER is essential for ICL repair: the endonuclease UvrA₂BC makes incisions at either side of the crosslink on the same DNA strand, leaving a gap and a large monoadduct on the opposite strand (Sladek et al., 1989; van Houten et al., 1986). The gap serves as a substrate for HR or can be bypassed by TLS in a *recA*⁻ mutant. This pathway is essentially conserved in yeast, where NER factors are absolutely required to unhook the crosslink, allowing subsequent HR or TLS (McHugh et al., 2000, Sarkar et al., 2006).

Perhaps mammals have needed to evolve new pathways as they encounter new exogenous or endogenous genotoxins. Alternatively, both NER branches have been implicated in replication-independent ICL repair, with GG-NER being required for ICL removal during G1 phase of the cell cycle and TC-NER factors being required for transcription-coupled ICL repair (Enoiu et al., 2012a; Muniandy et al., 2009b). Therefore, NER might provide an alternative ICL repair pathway, especially in tissues with low proliferative rates, and cannot therefore rely on replication-coupled repair of crosslinks. If this were the case, then it may be expected that the severe *Ercc1* phenotype may be explained by the inactivation of TC-NER, GG-NER and FA repair.

1.5 Sources of DNA damage

By studying whether joint inactivation of NER and FA can lead to the severe phenotype observed in XPF-ERCC1 deficiency it may be possible to identify lesions that drive the phenotype. However, the source of DNA damage that can lead to these lesions remains yet to be discovered.

DNA repair pathways protect organisms in extreme situations such as the Bari air raid, or chemotherapy for cancer, but these pathways have evolved to protect against DNA damage that occurs naturally. In the absence of these pathways severe human diseases can occur such as XP, FA and CS. For XP a source of DNA damage has been identified – UV. This has advanced the treatment of XP individuals enormously (DiGiovanna & Kraemer, 2012) and led to further insight into how this exogenous DNA damaging agent leads to skin cancer in the general population (Brash et al., 1991). For CS, the source of damage is unlikely to be UV given the nature of the phenotype and so identifying a source of DNA damage that can lead to CS is of great importance and may explain the physiological purpose of TC-NER.

ROS has been proposed as the source of damage and in support of this CS deficient cells are sensitive to oxidative DNA damaging agents such as paraquat and potassium bromate

(Ranes et al., 2016). Oxidative DNA base modifications such as 8-oxo-7, 8-dihydro-guanine (8-oxoG) serve as a useful biomarker of oxidative damage and elevated levels have been observed in *Ercc1*^{-/-} mice (Selfridge et al., 2001). Additionally, 8-oxoG can be repaired via 8-oxoG DNA glycosylase 1 (OGG1), and mice deficient in both CSB and OGG1 show a 3.4-fold higher accumulation of 8-oxoG than *ogg1*^{-/-} mice (Osterod et al., 2002). However, unlike more bulky lesions such as cisplatin crosslinks and cyclobutane dimers, 8-oxoG lesions do not lead to stalling of the RNAPII (Charlet-Berguerand et al., 2006). In agreement with this, oxidative DNA damage failed to induce a strong RNA synthesis block like UV (De Waard et al., 2003). Finally, although tissues from *Csb*^{m/m} *Ogg1*^{-/-} mice had elevated 8-oxoG lesions no CS phenotype was reported, questioning the role of this lesion in the CS phenotype (Osterod et al., 2002).

More recently, simple aldehydes have been identified as endogenous sources of DNA damage in Fanconi Anaemia and have been shown to greatly precipitate the FA phenotype in mice (Garaycoechea et al., 2012; Langevin et al., 2011; Pontel et al., 2015). However, whether these simple aldehydes can drive DNA repair phenotypes other than FA has not yet been investigated.

1.5.1 Aldehydes as sources of DNA damage

Aldehydes are simple ubiquitous compounds that are common constituents of food sources and produced as by-products of cellular metabolism. Chemically, simple aldehydes such as formaldehyde and acetaldehyde can react with DNA and lead to many different modifications *in vitro* and *in vivo* (Cheng et al., 2003a; Moeller et al., 2011; Yu et al., 2015). Additionally, *Schizosaccharomyces pombe* that lack a range of DNA repair pathways have been shown to have cellular sensitivity to formaldehyde and acetaldehyde (Anandarajan et al., 2020). Mammalian cells that lack FA repair have also been shown to be sensitive to formaldehyde and acetaldehyde (Langevin et al., 2011; Rosado et al., 2011). Given that these 2 aldehydes can form interstrand crosslinks, substrates for the FA repair pathway to repair, it was then important to test whether enough endogenous aldehydes could accumulate to lead to the FA phenotype *in vivo*.

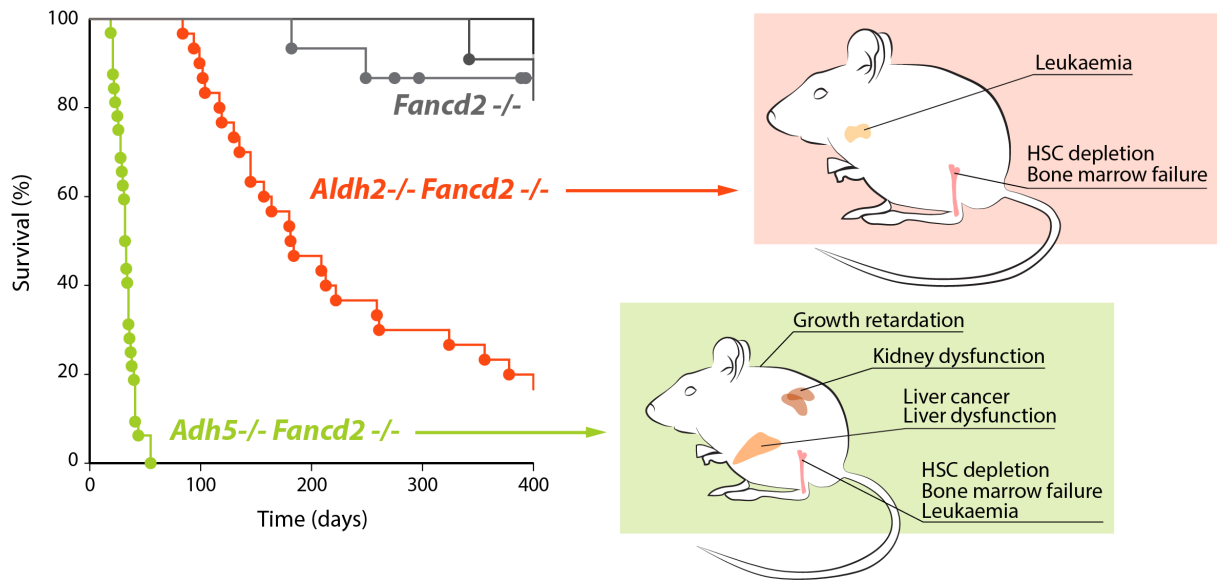


Figure 1.04 – Overview of mice lacking aldehyde detoxification genes and the FA pathway

Left, Kaplan-meier survival curve of *Aldh2*^{-/-} *Fancd2*^{-/-} and *Adh5*^{-/-} *Fancd2*^{-/-} mice compared to *Fancd2*^{-/-} mice. **Right**, Overview of the phenotypes of *Aldh2*^{-/-} *Fancd2*^{-/-} and *Adh5*^{-/-} *Fancd2*^{-/-} mice.

In order to test this, mice lacking the enzymes that detoxify formaldehyde and acetaldehyde (ADH5 and ALDH2) were crossed with mice deficient in the FA pathway. The result was a striking revelation of the Fanconi phenotype in double knock out (*Adh5^{-/-} Fancd2^{-/-}* and *Aldh2^{-/-} Fancd2^{-/-}*) mice (Langevin et al., 2011; Pontel et al., 2015). Both these mouse lines are born at very low mendelian ratios, display developmental abnormalities and succumb to bone marrow failure (Figure 1.04). Additionally they have extremely low HSC numbers and have a high predisposition to lymphoid leukaemia's (Garaycochea et al., 2012; Langevin et al., 2011; Pontel et al., 2015). Furthermore, when both mouse lines were exposed to exogenous sources of formaldehyde and acetaldehyde (methanol and ethanol) the phenotype was precipitated (Garaycochea et al., 2012; Langevin et al., 2011; Pontel et al., 2015).

In humans, polymorphisms in *ALDH2* are common within the East Asian population, which lead to over a 100-fold decrease in enzymatic activity and results in the Asian flushing syndrome (P. J. Brooks et al., 2009). This polymorphism is so prevalent that it was possible to assess whether combined loss-of-function of *ALDH2* and mutations in FA genes led to a genetic interaction in humans. Strikingly, humans that lack the FA repair pathway and carry the *ALDH2* polymorphism display an extreme form of FA, often surviving just a few years compared with FA patients who commonly survive into adulthood (Hira et al., 2013) Taken together these data support the idea that acetaldehyde and formaldehyde are endogenous factors that may contribute to the FA phenotype in mice and humans.

To further probe into the basis of HSC loss of *Aldh2^{-/-}Fancd2^{-/-}* mice, HSCs were isolated and transplanted into wild type mice to be clonally expanded and then sequenced. This sequencing revealed that HSCs from *Aldh2^{-/-}Fancd2^{-/-}* mice contained many more deletions and chromosomal rearrangements than controls. The mutational landscape of the HSCs suggests that in the absence of the FA pathway a double strand break is formed that is repaired via HR and non-homologous end joining with the latter leading to mutagenic outcomes (Garaycochea et al., 2018). The endogenous lesion therefore must lead to the formation of a double strand break in the absence of FA, possibly an ICL, although curiously there was no evidence of any TLS which agrees with a lack of any genetic interaction between *Aldh2* and *Rev1* (Oberbeck et al., 2014). Interestingly, p53 deficiency in these mice rescued the numerical HSC defect but did not lead to an increase in mutation burden (Garaycochea et al., 2018) raising the question why does p53 trigger apoptosis in these cells if not to protect from mutations?

Despite the severe HSC defect in both *Adh5*^{-/-} *Fancd2*^{-/-} and *Aldh2*^{-/-} *Fancd2*^{-/-} lines, mice lacking *Adh5* rather than *Aldh2* gave rise to a much more severe phenotype. *Adh5*^{-/-} *Fancd2*^{-/-} mice succumb to bone marrow failure after just 4 weeks and in addition to HSC defects also displayed liver and kidney dysfunction along with severe growth failure. Surprisingly, bone marrow transplantation not only rescued the bone marrow failure but also the kidney defects in these mice, suggesting that kidney defects may be exacerbated by systemic formaldehyde (Pontel et al., 2015).

The liver and kidneys from *Adh5*^{-/-} *Fancd2*^{-/-} mice have an increased burden of DNA damage measured by gH2AX foci. Therefore it is likely that these organs are declining in function due to DNA damage (Pontel et al., 2015). This is intriguing as liver and kidney degeneration are not features of human FA, they are however features of mice that lack ERCC1 as is the severe growth failure (Niedernhofer et al., 2006). Therefore, ADH5 deficiency may result in the accumulation of sufficient endogenous formaldehyde to necessitate additional repair pathways that utilise the XPF-ERCC1 nuclease complex, possibly NER.

1.5.2 NER and aldehydes

The evidence that aldehydes can act as drivers of the FA phenotype in mice and humans suggests they are a physiological relevant source of DNA damage. However, aldehydes can lead to many DNA lesions (Cheng et al., 2003a; Moeller et al., 2011; Yu et al., 2015). It is therefore possible that other DNA repair pathways are required for protection against aldehydes. An important source of DNA damage for XP is UV light. However, patients from the XP complementation groups A, B, D, F and G present with neurological problems in addition to the severe skin cancer predisposition (Fassihi et al., 2016). Additionally, there is recent evidence that XPC patients have an increased predisposition towards AML (Yurchenko et al., 2020) and that bone marrow failure can arise in *Xpc*^{-/-} mice that lack Rev1 (Martín-Pardillos et al., 2017) suggesting that NER may protect against additional sources of DNA damage.

While an important source of DNA damage has been identified for XP, the same cannot be said for CS. Although CS patients sunburn easily, the multisystem complications that occur suggest that there must be other important drivers of DNA damage in CS. In addition to UV, CSA and CSB deficient cells are also sensitive to chemotherapeutic agents such as cisplatin and oxaliplatin (Enoiu et al., 2012b; Slyskova et al., 2018). Although these agents do not point towards an endogenous driver of the disease, they do suggest that agents that can crosslink DNA by forming intrastrand crosslinks can block the progression of RNAPII,

triggering repair via TC-NER. These crosslinking agents also block RNAPII and trigger the global shutdown of transcription and degradation of RNAPII (Slyskova et al., 2018; Tufegdžić Vidaković et al., 2020).

It has been demonstrated *in vitro* that both acetaldehyde and formaldehyde can lead to intrastrand crosslinks (Lu et al., 2010; Moeller et al., 2011; Sonohara et al., 2019), suggesting that they may also lead to the stalling of RNAPII and trigger TC-NER, global transcription shutdown and RNAPII degradation. This raises the possibility that naturally occurring aldehydes could be a physiological source of DNA damage that drives the CS phenotype.

1.6 Aims

XPF-ERCC1 deficiency leads to an extremely severe phenotype afflicting many organs; how much of this phenotype is due to joint inactivation of the FA pathway and NER is unclear. On the other hand, aldehydes have been shown to be a physiological driver of the FA phenotype in humans and mice, therefore part of the XPF-ERCC1 phenotype may be driven by these genotoxins. XPF-ERCC1 also operates in NER, therefore I want to ask if DNA damage by aldehydes requires repair via NER? Finally, DNA damage can lead to many clinical features. Some such as cancer predisposition are well defined; others such as the age-related decline in organ function are poorly understood. So, if aldehydes contribute to the phenotype of NER deficiencies I want to understand what drives this.

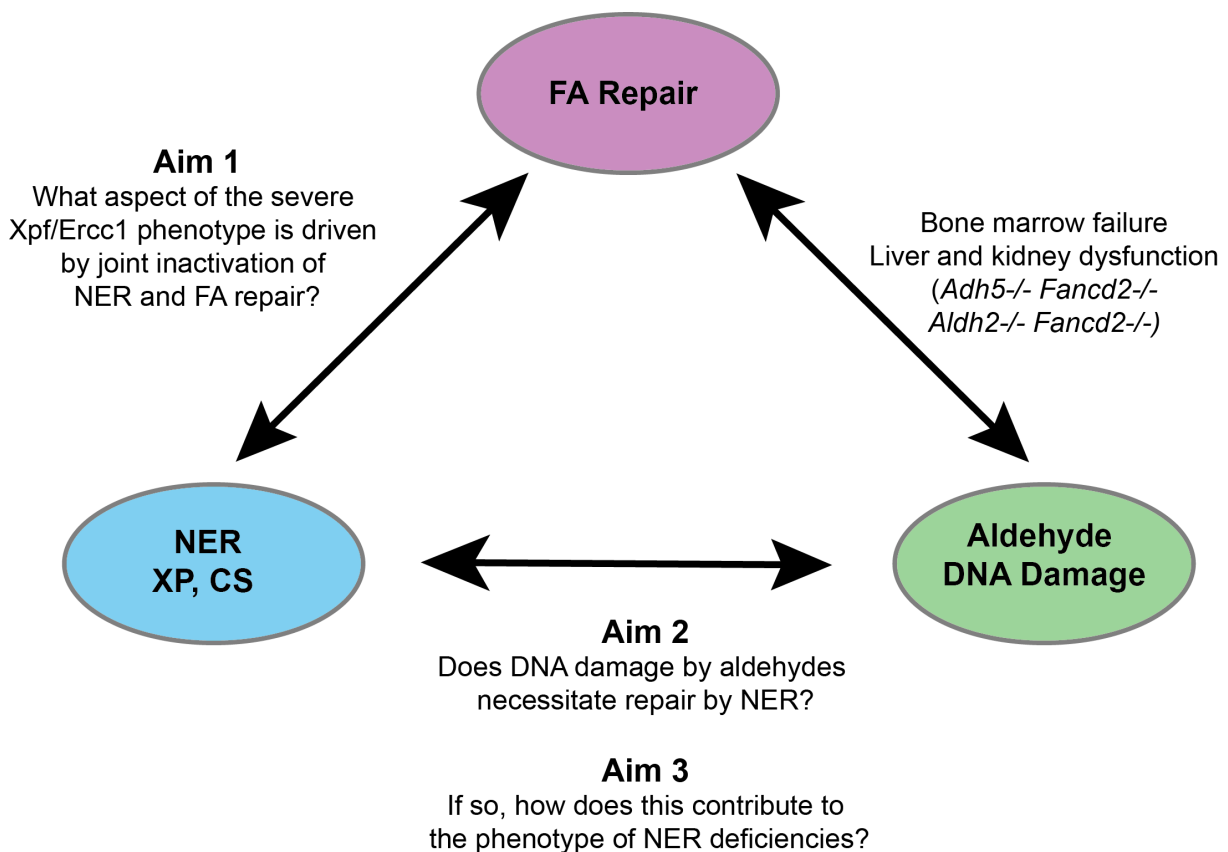


Figure 1.05 – Aims of this Thesis

Figure outlining the relationship between NER, the FA pathway and DNA damaged derived from aldehydes. This thesis will investigate how these repair pathways and sources of DNA damage all intersect.

Chapter 2

Materials and Methods

2.1 Mouse Strains

2.1.1 Animal Husbandry

All animal experiments undertaken in this study were with approval of the MRC Laboratory of Molecular Biology animal welfare and ethical review body and the UK Home Office under the Animal (Scientific Procedures) Act 1986 license PFC07716E. All mice were maintained under specific pathogen-free conditions in individually ventilated cages (Techniplast GM500, Techniplast) on Ligno-cel FS14 spruce bedding (IPS, LTD) with environmental enrichment (fun tunnel, chew stick, and Enviro-Dri nesting material (LBS)) at 19-23 °C with light from 7:00 am to 7:00 pm and fed Dietex CRM pellets (Special Diet Services) *ad libitum*.

2.1.2 NER mice crossed with FANCA mice

The *Fanca*^{tm1a(EUCOMM)Wtsi} (MGI 4434431, C57BL/6N) and *Ercc1*^{tm1a(KOMP)Wtsi} (MGI 4362172, C57BL/6) alleles have been described previously (Garaycochea et al., 2012; R. Hill & Crossan, 2019). *Xpa*^{tm1Hvs} (MGI 1857939, C57BL/6), *Ercc6*^{tm1Gvh} (*Csb*^m, MGI 1932102, C57BL/6) and *Xpc*^{tm1Ecf} (MGI 1859840, C57BL/6) mice were described previously and a kind gift from G.T. van der Horst, Errol Friedberg and Jan Hoeijmakers (Cheo et al., 1997; de Vries et al., 1995; G. T. van der Horst et al., 1997). To generate *Xpa*^{-/-}*Fanca*^{-/-}, *Xpc*^{-/-}*Fanca*^{-/-} and *Csb*^{m/m}*Fanca*^{-/-} mice on a pure C57BL/6 background, *Fanca*^{+/-} mice were crossed with *Xpa*^{+/-}, *Xpc*^{+/-} and *Csb*^{+/m}, respectively. From the resulting progeny we intercrossed NER^{+/-} *Fanca*^{+/-} to generate all possible genotypes. To further bias the breeding for the generation of double mutants, we intercrossed mice that were both NER^{-/-}*Fanca*^{+/-}. To generate mice in a C57BL/6 x 129S6/Sv F₁ background, the various C57BL/6 alleles were first backcrossed onto the 129S6/Sv background: *Fanca*^{+/-} and *Csb*^{+/m} 10 generations, *Xpa*^{+/-} 6 generations and *Ercc1*^{+/-} 7 generations. For *Fanca*^{-/-} and *Ercc1*^{-/-} F₁ mice, C57BL/6 heterozygous mice were

crossed with 129S6/Sv heterozygous mice. For $Xpa^{-/-}Fanca^{-/-}$ and $Csb^{m/m}Fanca^{-/-}$ F₁ mice, $Fanca^{+/-}$ 129S6/Sv were crossed with $Xpa^{+/-}$ or $Csb^{+/-}$ to generate double heterozygous mice, these mice were then intercrossed to generate $Xpa^{-/-}Fanca^{+/-}$ and $Csb^{m/m}Fanca^{+/-}$ 129S6/Sv which were crossed with $Xpa^{-/-}Fanca^{+/-}$ and $Csb^{m/m}Fanca^{+/-}$ C57BL/6, respectively. For the phenotyping of C57BL/6 x 129S6/Sv F₁ mice, mice were used between 8 – 12 weeks. Embryos were generated in a C57BL/6 background and analysed at day E13.5 of development. Females used in timed matings were used between 8 and 18 weeks old.

2.1.3 Aldehyde deficient and $p53^{-/-}$ mice

$Adh5^{tm1Stam}$ (also known as $Gsnor^{-/-}$) (MGI 3033711, C57BL/6) mice were previously described (L. Liu et al., 2004) and obtained from Dr. L. Liu at UCSF. The $Aldh2$ mice ($Aldh2^{tm1a(EUCOMM)Wtsi}$, MGI ID: 4431566, C57BL/6) were reported previously (Langevin et al., 2011) and the $Trp53$ allele that has been reported previously (Donehower et al., 1992) was used in a C57BL/6 x 129S4S6/Sv hybrid background.

2.1.4 NER mice crossed with aldehyde deficient mice

To generate $Adh5^{-/-}Xpa^{-/-}$, $Adh5^{-/-}Csb^{m/m}$ and $Adh5^{-/-}Xpc^{-/-}$ mice, $Adh5^{+/-}$ mice were crossed with $Xpa^{+/-}$, $Csb^{+/-}$ and $Xpc^{+/-}$ respectively. From the resulting progeny we inter-crossed $Adh5^{+/-}$ NER^{+/−} mice to generate all possible genotypes. To further bias the breeding for double homozygous mice we inter-crossed mice that were $Adh5^{-/-}$ NER^{+/−} or $Adh5^{+/-}$ NER^{+/−}. Likewise, to generate $Aldh2^{-/-}Csb^{m/m}$ mice we crossed $Csb^{+/-}$ mice with $Aldh2^{+/-}$ and then from resulting progeny we inter-crossed $Aldh2^{+/-}Csb^{+/-}$ mice to generate all possible genotypes. To further bias the breeding for double homozygous mice we inter-crossed mice that were $Aldh2^{+/-}Csb^{m/m}$ or $Aldh2^{-/-}Csb^{+/-}$.

2.1.5 $Adh5^{sw/-}$ $Csb^{-/-}$ $Vav1-icre$ mice

$Adh5^{sw/+}$ mice were generated by firstly targeting C57BL/6N embryonic stem (ES) cells with a vector containing an inverted exon 3 flanked by loxP sites, a neomycin resistance cassette flanked by FRT sites and homology arms. Targeting was confirmed by growing clones in the presence of neomycin and subsequent PCR (Figure 2.01a-b). Validated clones were then injected into blastocysts to generate chimeric mice. After confirmation of germ line transmission by PCR mice were crossed with FLP deleter mice (Henrich et al., 2000) to remove the neomycin cassette. Next, $Adh5^{sw/+}$ mice were crossed with $Adh5^{+/-}Csb^{m/m}$ to generate $Adh5^{sw/+}Csb^{m/m}$ which were then further cross with $Adh5^{+/-}Csb^{m/m} Vav1-icre$ to generate experimental mice.

Adh5 Switch Allele

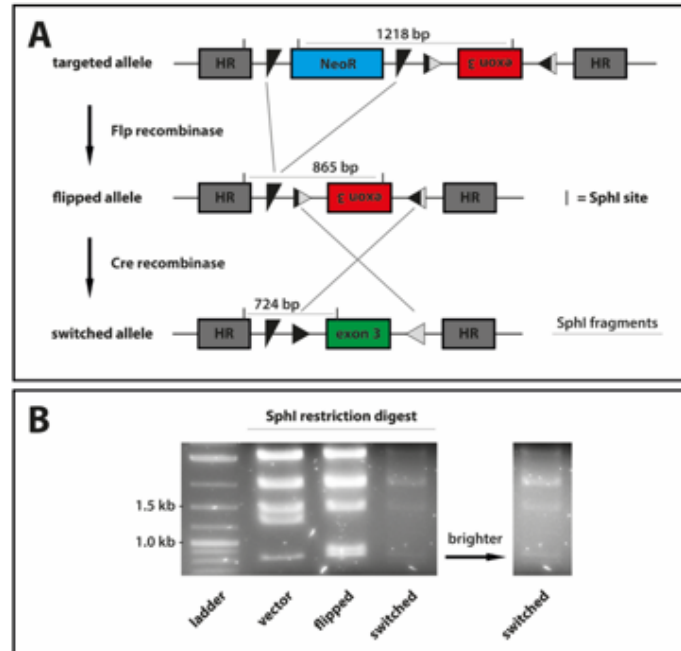


Figure 2.01 – *Adh5* switch allele

a) Outline of the allele that was targeted in ES cells, once targeted clones were validated mice were generated by blastocyst injections. The neomycin resistance cassette was then removed by crossing germline confirmed carriers of the targeted allele with mice carrying the Flp recombinase allele. Finally, in order to switch on expression of *Adh5* the allele was crossed with Cre recombinase carrying mice. **b)** PCR of DNA from confirmed ES cell clones after Sph1 restriction digest, the 1.2kb band in the targeted vector is reduced to 0.8kb after Flp recombinase and reduced further in size to 0.7kb after Cre recombinase.

2.1.6 *Adh5*^{-/-} *Ercc1*^{c/-} *Nestin cre* mice

For central nervous specific loss of ERCC1 the *Ercc1*^{tm1a(KOMP)Wtsi} (MGI 4362172, C57BL/6) allele was first crossed with the FLP deleter mice to make the *Ercc1* conditional allele *Ercc1*^{tm1c(KOMP)Wtsi}. *Ercc1*^{c/+} were then crossed with *Adh5*^{-/-} mice until *Ercc1*^{c/c} *Adh5*^{-/-} were born which were then crossed with *Ercc1*^{+/-} *Adh5*^{+/-} *Nestin Cre*^{+/-}. Nestin cre limits the expression of Cre to the central nervous system resulting (Tronche et al., 1999) in the *Ercc1*-null allele or *Ercc1*^{tm1d(KOMP)Wtsi}.

2.2 Animal Experiments at Harwell

The *in vivo* phenotyping tests below were carried out at MRC Harwell and more detailed descriptions of these protocols are available on the IMPRESS website (www.mousephenotype.org/impress). All procedures conducted are done so in accordance with the Animals (Scientific Procedures) Act 1986 Amendment Regulations 2012 (SI 4 2012/3039). Mice were housed in Tecniplast IVC cages (1284L and 1285L) with Aspen bedding (Datesand) which is autoclaved (134oC for 3 minutes) in the cage base and cage bases are changed weekly. It is an important requirement to ensure that the mice have access to an enriched environment without comprising the scientific data collected. We comply with our MLC Policy on the Use of Environmental Enrichment. Tunnels and bedding are provided for each cage. Food and water are provided *ad libitum*. RM3 (E) Diet (Special Diet Services) is irradiated to 2.5 Mrads. Mains water is supplied through a reverse osmosis (RO) filter and then chlorinated to 9-13 ppm. Water bottles are changed weekly with autoclaved bottle and cap. The lighting regime is 12 hours light, 12 hours dark with 30-minute dusk to dawn, dawn to dusk period. Health checks are conducted daily and a maximum number of 5 animals are housed per cage.

2.2.1 Weights

The mice were weighed using a dynamic weighing balance (Ohaus) and were always weighed in the morning to limit the effect of the circadian rhythm on body weight.

2.2.2 X-ray

X-ray images of the mice were collected whilst the mice were anaesthetised (isoflurane). The X-rays were captured using the Faxitron Ultrafocus X-Ray machine (US).

2.2.3 Grip strength

Grip strength was measured using a grip strength meter (Bioseb, France), recording the maximum force generated by a mouse using all four limbs. Grip strength measures were carried out in triplicate for each mouse.

2.2.4 Echo MRI

Body composition of the mice was assessed using an EchoMRI whole body composition analyser (Echo Medical System, Houston, USA). The analysis output quantified fat mass, lean mass and water content of the mice.

2.2.5 Calorimetry

The metabolic rate of the mice was assessed using indirect calorimetry. Mice were individually housed overnight for a period of 21 hours in Phenomaster cages (TSE Systems, Germany) with standard bedding and igloos. The air content in each cage was sampled for 1 minute, in turn and a reference cage with no mice in it was also sampled for comparison. The oxygen consumption and carbon dioxide production for each mouse was then determined as the difference between the reference amount of gas and the level in the mouse cage.

2.2.6 Open field

Animals were transported to the testing room 30 minutes before the test. Lighting conditions were set between 150-200 lux. Animals were placed in a chamber for 20 minutes and activity levels were determined using a beam break system.

2.2.7 Intraperitoneal glucose tolerance test

Mice were fasted overnight for 16 hours then injected with 10ml/kg of 20% glucose. Blood glucose measurements were then taken at 15, 30, 60 and 120 minutes post injection.

2.2.8 Ophthalmoscope and optical coherence tomography

Mice were first examined using the ophthalmoscope and any abnormalities were noted. Mice were then anaesthetized and eyes were imaged using the OCT camera to capture images of the retina and fundus.

2.3 Animal Experiments at LMB

All animal experiments undertaken in this study were with approval of the MRC Laboratory of Molecular Biology animal welfare and ethical review body and the UK Home Office under the Animal (Scientific Procedures) Act 1986 license PFC07716E.

2.3.1 Methanol/ethanol exposure protocol

For methanol treatment, mice received 1.5 g/kg via intra-peritoneal injection once a week until the conclusion of the experiment. Daily weights were taken, as were monthly 50 µl blood samples via tail bleed for serum biochemistry.

For ethanol exposure, the drinking supply was replaced with a solution of 10:20:80 blackcurrant Ribena:ethanol:water. Daily weights were taken, as were monthly 50 µl blood samples via tail bleed for serum biochemistry.

2.3.2 Cisplatin exposure protocol

For low dose cisplatin exposure 50µl blood samples were taken prior to 0.5 mg/kg weekly cisplatin intra-peritoneal injections. Mice were weighed daily throughout before terminal blood sampling after 4 weeks. For high dose exposure, 4 mg/kg cisplatin was used for 6 weeks.

2.3.3 GDF15 antibody treatment

For GDF15 mAB treatment experiments *Adh5^{-/-}Csb^{m/m}* mice were treated with 10mg/kg mAB or IgG control by sub cutaneous injection once a week for 4 weeks. The GDF15 mAB and IgG control were provided by Pfizer.

2.3.4 Cerebellar ataxia scoring

Cerebellar ataxia scoring was performed as previously described (Guyenet et al., 2010)(Guyenet et al., 2010) at monthly intervals once the mice were 3 months old.

2.4 Ex-vivo Studies

2.4.1 Colony-forming unit spleen (CFU-S₁₂) assay

Mice were sacrificed between 8 and 12 weeks and 1 or 2x10⁵ nucleated bone marrow cells were injected intravenously into recipient mice that had been irradiated with 8 Gy split between two equal 4 Gy doses 4 hours apart. 12 days after transplantation the mice were

sacrificed, the spleens were fixed in Bouin's solution (Sigma) for at least 24 hours and the gross colonies were enumerated and expressed relative to the number of nucleated bone marrow cells injected.

2.4.2 HSPC analysis by flow cytometry

Bone marrow cells were isolated from the femora of mutant mice and aged-matched controls by flushing cells and passing them through a 70- μ m filter. The following antibodies were used to stain for HSCs: FITC- conjugated lineage cocktail with antibodies anti-CD3e (clone 145-2C11, eBioscience), CD4 (clone H129.19, BD Pharmingen), CD8a (clone 53-6.7, BD Pharmingen), CD11b/Mac-1 (clone M1/70, BD Pharmingen), CD11c (clone N418, eBioscience), Ly-6G/Gr-1 (clone RB6- 8C5, eBioscience), B220 (clone RA3-6B2, BD Pharmingen), Fc ϵ R1 α (clone MAR-1, eBioscience), TER-119 (clone Ter119, BD Pharmingen), CD41 (clone MWReg30, BD Pharmingen); anti-c-Kit (PerCP-Cy5.5, clone 2B8, eBioscience), anti-Sca-1 (PE-Cy7, clone D7, eBioscience), anti-CD48 (biotin, clone HM48-1, BioLegend) and anti-CD150 (PE, clone TC15- 12F12.2, BioLegend). After staining for 15 minutes in PBS + 2% FCS, the cells were washed and incubated with streptavidin conjugated to Brilliant Violet 421 (BioLegend) for another 15 minutes.

Foetal livers from E13.5 embryos were dissected and placed in 1 ml of PBS + 2% FCS. The foetal livers were triturated gently using a P1000 pipette until a homogenous suspension was formed. The cells were then passed through a 40 μ m cell strainer (Falcon) and nucleated cells were counted with 3% acetic acid on a Vi-Cell XR cell viability counter (Beckman Coulter). 10×10^6 foetal liver cells were spun down for 5 minutes at 1200 rpm and stained as above.

2.4.3 Nuclei isolation and DNA content analysis

Liver and kidneys were dissected and passed through a 40- μ m filter. Cells were washed twice in LA buffer (250 mM sucrose, 5 mM MgCl₂ and 10 mM Tris-HCl, pH 7.4). After washing, the cell pellet was resuspended in 1 ml of buffer LB (2 M sucrose, 1 mM MgCl₂ and 10 mM Tris-HCl, pH 7.4) and centrifuged at 16000g for 30 minutes. The white nuclei-containing pellet was resuspended in LA buffer and kept on ice for analysis. For DNA content analysis, nuclei were fixed dropwise in cold 96% ethanol. Nuclei were pelleted and resuspended in 400 μ l of PBS. Propidium iodide solution (Sigma) was added at a final concentration of 40 μ g/ml together with Ribonuclease A (Sigma) at a final concentration of 100 μ g/ml. The samples were incubated on ice for one hour and then analysed on LSRII flow cytometer (BD Pharmingen). The data was analysed with FlowJo 10.0.6 (Tree Star).

2.4.4 Serum biochemistry

Serum was collected from 200 μl of whole blood into Microvette 200 conical tubes (MCV200-SER) after centrifugation. Levels of urea, creatinine, aspartate aminotransferase, albumin, and alkaline phosphatase of serum samples were measured using a Siemens Dimension RxL analyser by Cambridge Biochemical Assay Laboratory. GDF15 was measured using a commercial ELISA (R&D Systems) according to the manufacturer's instructions with two modifications. We used an extended standard curve extending from 2000 pg ml^{-1} to 7.8 pg ml^{-1} and added 10 μl sample to 50 μl RD1W at the binding step (instead of 50 μl). Additional samples for GDF15 were measured by the Cambridge Biochemical Assay Laboratory, University of Cambridge using a Mouse GDF15 DuoSet ELISA (R&D Systems) which had been modified to run as an electrochemiluminescence assay on the Meso Scale Discovery assay platform.

2.4.5 Histology

Histological analysis was performed on tissues that had been fixed in neutral buffered formalin for 24h. The samples were paraffin embedded and 4 μm sections were cut before staining with haematoxylin and eosin.

2.4.6 Urine analysis

Multistix SG10 from Siemens was used for semi-quantitative readout of protein in the urine by addition of 5 μl to the strip.

2.4.7 Blood counts

Total blood was collected in K₃EDTA MiniCollect tubes (Greiner bio-one) and analysed on a scil VetABC Plus+ blood counter (Horiba)

2.4.8 Immunofluorescence

Mice were anaesthetised with pentobarbital and perfused transcardially with 4% paraformaldehyde. The brain was carefully dissected out and post-fixed overnight in 4% paraformaldehyde. Brain tissue was then sectioned at 40 μm with a vibrating microtome and sections were processed, free floating. Sections were washed in PBST (PBS 0.1% Triton X) for 10 minutes before blocking for 1 hour in 5% normal goat serum. Next, sections were incubated with MAC2 (Cedarlane, clone M3/38) antibody at 1/2000 overnight at 4°C before

being washed once in PBST for 10 minutes and stained with Alexaflour 488 anti-rat secondary (Invitrogen) for 1 hour in the dark at room temperature. Sections were then transferred to slides and mounted using one drop of Vectashield containing DAPI (Vectorlabs) before cover slipping and adding nail varnish. Images were taken on a Zeiss LSM 780 confocal microscope (Zeiss). For kidney KIM-1 immunofluorescence, kidneys were snap frozen and 10 µm sections were cut using a freezing microtome and placed on slides, which were then stored at -80. For staining slides were air dried at room temperature for 5 minutes then fixed in 2% PFA for 5-10 minutes. For staining, slides were washed in PBS for 10 minutes before blocking in 10% fetal calf serum (GIBCO) at room temperature for 30 minutes in a humid chamber. KIM-1 primary antibody (R&D Systems, AF1817) was then added at 1/500 overnight at 4°C in a humid chamber. The next day slides were washed in PBS for 10 minutes before secondary anti-goat alexa-flour 488 (Invitrogen) was added at 1/1000 for 30 minutes. Slides were then washed with PBS for 10 minutes before being mounted using one drop of Vectashield containing DAPI (Vectorlabs) before cover slipping and adding nail varnish. Images were taken on a Zeiss LSM 780 confocal microscope (Zeiss).

2.4.7 RNA in situ hybridisation

Tissues for *in situ* hybridization were dissected and placed into 10% formalin/PBS for 24 h at room temperature, transferred to 70% ethanol and processed into paraffin. Five-micrometre sections were cut and mounted onto Superfrost Plus (Thermo Fisher Scientific). Detection of mouse *Gdf15* was performed on formalin-fixed paraffin-embedded sections using Advanced Cell Diagnostics (ACD) RNAscope 2.5 LS Reagent Kit-RED (no. 322150) and RNAscope LS 2.5 Probe Mm-Gdf15-O1 (no. 442948) (ACD). In brief, sections were baked for 1 h at 60 °C before loading onto a Bond RX instrument (Leica Biosystems). Slides were deparaffinized and rehydrated on board before pre-treatments using Epitope Retrieval Solution 2 (no. AR9640, Leica Biosystems) at 95 °C for 15 min, and ACD Enzyme from the LS Reagent kit at 40 °C for 15 min. Probe hybridization and signal amplification was performed according to the manufacturer's instructions. Fast red detection of mouse *Gdf15* was performed on the Bond RX using the Bond Polymer Refine Red Detection Kit (Leica Biosystems, no. DS9390) according to the ACD protocol. Slides were then counterstained with haematoxylin, removed from the Bond RX and were heated at 60 °C for 1 h, dipped in xylene and mounted using EcoMount Mounting Medium (Biocare Medical, no. EM897L). Slides were imaged on an automated slide-scanning microscope (Axioscan Z1 and Hamamatsu orca flash 4.0 V3 camera) using a 20× objective with a numerical aperture of 0.8.

2.5 Kidney single cell RNA sequencing

2.5.1 Kidney dissociation for scRNA-seq

Kidneys were placed into a small tube containing 1 ml Digest mix (RPMI, 25 µg/ml Liberase TM, 50 µg/ml DNase) and minced to less than 2mm³. Volume was increased to 5ml with digest mix and samples were incubated at 37°C for 30 min in a shaking incubator. Samples were passed through a 100 µm cell strainer using a 1ml syringe plunger and washed by centrifugation with PBS. Samples were resuspended in PBS, cell number determined and loaded on to a 10x genomics platform.

2.5.2 scRNA-seq data analysis

Following sequencing, BCL files were demultiplexed to Fastq files using CASAVA. Subsequently splitting to single cells and mapping of genes was carried out using Cellranger. The single-cell data (10x *cellranger* output) was corrected for ambient RNA expression using *SoupX* (v1.2.1)(Young & Behjati, 2018). After *SoupX*, doublet detection was performed using *scrublet* (v0.2.1)(Wolock et al., 2019) with adaptations outlined in Popescu *et al.*(Popescu et al., 2019). Briefly, after *scrublet* was performed, the data was iteratively sub-clustered using standard *Seurat*-inspired *scanpy* (v.1.4.5.post2) workflow (Stuart et al., 2019; Wolf et al., 2018) and a median *scrublet* score for each subcluster was computed. Median absolute deviation was computed from the cluster *scrublet* scores and a one tailed t-test was performed with Benjamini-Hochberg (BH) correction (Benjamini & Hochberg, 1995) applied where cells with significantly outlying cluster *scrublet* scores (BH pval < 0.1) were flagged as potential doublets. The data was then processed using *scanpy* with standard quality control steps; cells were filtered if number of genes > 2500 or < 200. Similar to Park *et al.* (J. Park et al., 2018), percentage mitochondrial content cut-off was set at <50%. Genes were retained if expressed by at least 3 cells. Gene counts for each cell were normalised to contain a total count equal to 10000 per cell. Highly variable genes were selected based on the following parameters: minimum and maximum mean expression are ≥ 0.0125 and ≤ 3 respectively; minimum dispersion of genes = 0.5. The effects of total counts per cell, percentage of mitochondrial content and cell cycle states were regressed out prior to scaling of variable genes. Neighbourhood graph graphs were constructed with 20 neighbours using 80 PCs (all cells) or 30 PCs (proximal tubules only). Clustering was performed using Leiden algorithm(Traag et al., 2019) with resolution set at 0.5. Uniform Manifold Approximation and Projection (UMAP; v3.10.0)(McInnes et al., 2018) was used for dimensional reduction and

visualization; Partition-based graph abstraction (PAGA)-initialization was used to compute the UMAP embedding for all cells while default (spectral) was used for PT; the minimum distance was set at 0.3; all other parameters were used as per default settings in *scanpy*.

Differential gene testing was performed using the Wilcoxon test rank sum implemented in *scanpy's rank_genes_groups* module. BH post-hoc correction was applied to the p-values calculated after DEG analysis. Genes that attained corrected *P* value of < 0.05 were considered statistically significant.

2.6 Cell Culture

2.6.1 Cell lines

HAP1 cells (Haplogen) were purchased from Horizon Discovery and cultured in IMDM medium (Gibco) supplemented with 10% dialysed foetal calf serum and penicillin/streptomycin. Cells were grown at 37 °C and 5% CO₂. All cell lines used in the study were tested to be mycoplasma-free. Transformed mouse embryonic fibroblasts (tMEFS) were cultured in standard Dulbecco's modified Eagle's medium (DMEM)(GIBCO) supplemented with 10% fetal calf serum (GIBCO) and penicillin/streptomycin. Flp-In T-REx HEK293 (Thermo Fisher Scientific) cell lines were cultured in standard Dulbecco's modified Eagle's medium (DMEM) supplemented with 10% fetal calf serum and penicillin/streptomycin. CSB KO HEK293 cells were published previously(Tufegdžić Vidaković et al., 2020) and a kind gift from Jesper Svejstrup.

2.6.2 Generation of transformed mouse embryonic fibroblast (tMEF) lines

Adh5^{+/-}Xpc^{+/-}, *Adh5^{+/-}Xpa^{+/-}* and *Adh5^{+/-}Csb^{+/-m}* animals were time mated and humanely killed at embryonic day 13.5. Primary MEF cultures were obtained as described previously(Crossan et al., 2011) and transformed using pBABE-SV40-Puro virus as described previously(Crossan et al., 2011). For the complementation of tMEF lines, WT and K991R CSB cDNA constructs were amplified with a N-terminal 2xFLAG tag from mouse cDNA. They were then sequenced and cloned into pExpress and subsequently into pLoxBsr. The plasmids were transfected into tMEF using Lipofectamine LTX (Invitrogen) following the manufacturer's instructions. Positive clones were selected using 10µg/ml blasticidin and screened for expression by anti-FLAG western blot. Selection was maintained on positive clones.

2.6.3 CRISPR/Cas9-mediated gene disruption of *ADH5* in HEK293 cells

Wild type and CSB KO HEK293 cells were targeted using the top oligo sequence CACCGATCACTGGAAAACAACCCTC and bottom oligo sequence AAACGAGGGTTGTTTTCCAGTGATC cloned into pX458. Cells were transfected with Turbofectin 8.0 (Origene). Two days post-transfection, GFP-positive cells were single-cell sorted into 96-well plates containing medium supplemented with 20% fetal calf serum, using a MoFlo cell sorter (Beckman-Coulter). After 14 days of incubation at 37 °C, individual clones were analysed for expression of ADH5 protein by western blotting.

2.6.4 CRISPR/Cas9-mediated gene disruptions in HAP1 cells

Guide sequences for each gene disruption can be found in **Supplementary Table 1**. Plasmids containing each pair of guide sequences were obtained from the Wellcome Trust Sanger Institute. HAP1 cells were transfected with the vector containing guides along with the Cas9 containing PX461 vector using Turbofectin (Origene). Two days post-transfection, GFP+ cells were single-cell sorted into 96-well plates containing medium supplemented with 20% foetal calf serum, using a MoFlo cell sorter (Beckman-Coulter). After 14 days of incubation at 37 °C, individual clones were analysed for expression of the relevant protein by western blotting. Targeted loci were subjected to Sanger sequencing (GATC). **Supplementary Table 2** contains the primers used to amplify the relevant loci by PCR and **Supplementary Table 3** contains the primers used for Sanger Sequencing. For FANCL targeting, LR-PCR was used to screen clones with correct integration of the targeting construct, the primers can be found in **Supplementary Table 2**.

2.6.5 Western blotting

Cells were lysed for 30 min on ice in RIPA buffer (Thermo Fisher Scientific), including protease inhibitor cocktail (Roche) and phosphatase inhibitor cocktail (Roche). For the detection of FANCD2 in HAP1 cells, cells were treated with MMC 500 ng/ml overnight and protein samples were run on a 3–8% Tris-Acetate gel (Thermo Fisher Scientific). Samples were blotted to a 0.45 µm nitrocellulose membrane. Protein samples were run on a 4–12% Bis-Tris gel (Thermo Fisher Scientific) to detect XPC, XPA, XPF and CSB in HAP1 cells. Antibodies used were anti-XPC (D1M5Y, Cell Signaling, 1:1000), XPF (D3G8C, Cell Signalling, 1:1000), XPA (D9U5U, Cell Signalling, 1:1000), CSB (ab96089, abcam, 1:1000) and FANCD2 polyclonal antisera (1:3000) (Pace et al., 2002). For ADH5 and FLAG-tag blots, cells were lysed for 30 min on ice in RIPA buffer (Thermo Fisher Scientific), including protease and phosphatase inhibitor cocktail (Roche) and phosphatase inhibitor cocktail

(Roche). Protein samples were run on a 4-12% Bis-Tris gel (Thermo Fisher Scientific) and blotted to a 0.45 µm nitrocellulose membrane. For RNAPII RPB1 ubiquitylation and degradation, blots were performed as previously described (Tufegdžić Vidaković et al., 2019). A list of primary antibodies can be found below.

2.6.6 Antibodies

For screening HEK293 cells an in-house rabbit anti-ADH5 antibody was used which has been previously described (Pontel et al., 2015). For screening complemented tMEF clones anti-FLAG (Sigma, clone M2) was used at 1/1000. For the degradation of RPB1 blots, RPB1 (Cell Signalling, D8L4Y) was used at 1/1000 and for ubiquitylation of RPB1, RPB1 (abcam, 4H8) was used at 1/10,000. In both RPB1 blots, mouse anti-vinculin (Sigma, Cat V9131) was used as a loading control at 1/10,000.

2.6.7 RNAPII RPB1 ubiquitylation

Detection of ubiquitylated RPB1 was performed as previously described in detail (Tufegdžić Vidaković et al., 2019). Briefly, Dsk2 beads were prepared by transfecting One Shot BL21 competent cells with pGEX3-Dsk2, inducing, harvesting protein and added to glutathione Sepharose beads. Human cell lysates were also prepared as previously described (Tufegdžić Vidaković et al., 2019), 30 minutes after exposure to UV or indicated concentration of formaldehyde. Cell lysates and Dsk2 beads were then incubated together overnight before analysis by Western Blot.

2.6.8 Colony survival assay

Haploid HAP1 cells were allowed to diploidise spontaneously and enriched for diploid cells based on DNA content by flow cytometry. All colony survival assays were carried out with diploid HAP1 cells, which were trypsinised and resuspended at a concentration of 2×10^5 cells/ml. Drugs (mitomycin C, cisplatin, acetaldehyde or formaldehyde) were added at a 2X concentration in a total volume of 2 ml and incubated for 2 hours at 37°C. After 2 hours, two 1/10 serial dilutions were made and 100 µl cells were plated onto a 6 well plate-containing 5 ml IMDM supplemented with 10% dialysed foetal calf serum and penicillin/streptomycin. For UV and X-ray irradiation, cells were diluted to 1×10^5 cells/ml in 1 ml PBS, irradiated in a 6 well plate, and then immediately after irradiation, cells were spun down and resuspended in 1 ml IMDM and two 1/10 serial dilution were made and 100 µl cells were plated onto 6 well plates. Cells were grown at 37°C for 7 days. For visualization, colonies were washed with PBS and then stained with 6% v/v glutaraldehyde containing 0.5% crystal violet for 1 hour before washing again with PBS.

2.6.9 Cytotoxicity assays (MTS)

1×10^3 cells (tMEFS or HEK293) were plated in a 96-well plate in triplicate for each condition. The cells were exposed to the indicated doses of formaldehyde (Thermo Fisher Scientific) or UV 24 h after plating. Cell viability was measured using MTS reagent (Promega), 4 days after plating. Absorbance at 492 nm was measured with a Pherastar spectrophotometer.

2.7 Formaldehyde Adduct Detection

2.7.1 Synthesis of Nucleoside standards

Chemistry and the standards used were the same as reported in *Dingler et. al*(Dingler et al., 2020a).

2.7.2 Tissue sample preparation for determination of N^2 -Me-dG in DNA

Organs were snap frozen and stored at $-80\text{ }^\circ\text{C}$ until analysis. 10-20 mg of tissue was cut and lysed in a 2 ml Eppendorf, using 730 μl of Puregene cell lysis solution (Qiagen), 4 μl of proteinase K (Fisher BioReagents™) and a 7 mm stainless steel metal ball (Qiagen). Samples were homogenized in a tissue lyser (Qiagen/Retsch) for 4 min at 30 Hz, then incubated at $37\text{ }^\circ\text{C}$ for 30 min, 600 rpm (using a ThermoMixer). Then 4 μl of RNase A solution (Qiagen) was added, vortexed and incubated at $37\text{ }^\circ\text{C}$ for 1 h at 600 rpm.

The supernatant was transferred to a new tube (1.7 ml) and cooled on ice for 1 min. Then 266 μl protein precipitation solution was added (Qiagen, Puregene) and vortexed briefly, cooled on ice for 5 min, spun $21,300 \times g$, 3 min. The supernatant was transferred into a fresh tube containing 600 μl isopropanol, mixed by inversion $10\times$ and left at RT for 5 min for the DNA to precipitate. DNA was pelleted by spinning at $21,300 \times g$ for 2 min. The supernatant was discarded, and the DNA pellet washed with 600 μl of 70 % ethanol, spun at $21,300 \times g$, 2 min. Again, the supernatant was discarded, and the pellet left to air-dry for 5 mins before dissolving the pellet by addition of 500 μl of 50 mM NaCNBD₃ in 200 mM NaOAc (pH=5.2, diluted from 3M stock (Sigma)), and dissolved and reacted for 48 h at RT at (1000 RPM for the first 1 h, then 600 rpm) in an Eppendorf ThermoMixer.

DNA was precipitated out of the NaCNBD₃ solution by addition of 900 µl isopropanol, spun at 21,300 × g, 5 min and the supernatant discarded. This step was repeated with 70% EtOH and the pellet left to air dry. The DNA was dissolved overnight at RT in 100 µl of ultra-pure water (Romil) and quantified by nanodrop.

DNA was digested in a total volume of 100 µl in reactions containing 5000 ng DNA, 2 U shrimp alkaline phosphatase, 2 µl (New England Biolabs), 3.8 U snake venom phosphodiesterase I, 2 µl (Sigma, P3243) and 10 U DNase I, 1 µl (Roche) in 1× DNase I digestion buffer.

Also added to all digests were the internal standards ¹⁵N-*N*²-Me-dG and ¹⁵N-dA. For standard curve generation, a non-reduced sample of DNA isolated from WT murine 32D cells was used (5000 ng) and the standards 2'-deoxyadenosine (dA) and *N*²-Me-dG added at various concentrations. The range of the standard curves was as follows: 0.24 to 100 fmol for *N*²-Me-dG, 8.5 to 272 nmol for dA. The curves contained 6 points plus a zero control (H₂O used instead of standards). The response ratio (non-labelled to labelled spike) was plotted vs the amount of non-labelled spike injected onto to the column.

After an overnight digest (>16 h) samples were filtered with a 2000 MWCO Vivacon[®] 500 (Sartorius), 40 min, 16000 × g (at the midpoint (20 min) the tubes were rotated 180° in the centrifuge to yield more flow through). Samples were then transferred to a MS vial (Waters, 186000385c) and analyzed.

2.7.3 Snake Venom Phosphodiesterase preparation

A vial of snake venom phosphodiesterase I, (Sigma, P3243) was dissolved in 20 µl of 10x DNase I digestion buffer (Roche) and 180 µl 50% glycerol, the enzyme was stored at -20 °c until use.

2.7.4 LC-MS² determination of *N*²-Me-dG in DNA digests

Samples were analyzed on TSQ Altis Triple Quadrupole Mass Spectrometer in selected reaction monitoring mode (SRM) interfaced to an UltiMate 3000 uHPLC and. The uHPLC was fitted with a nanoEase M/Z Symmetry C18 Trap Column, 100Å, 5 µm, 180 µm × 20 mm (Waters) at RT and a reversed phase EASY-Spray™ HPLC analytical column (2 µm particle size, 75 µm × 50 cm, Thermo Fisher Scientific) connected to an EASY-Spray™ source at 35 °C.

10 μ l of sample (500 ng of digested DNA on column) was injected per run using a 10 μ l sample loop and the full loop inject mode. Buffers used were from Romil and of Ultra LC standard. Buffer A: H₂O (0.1 % acetic acid), buffer B MeCN (0.1 % acetic acid). The gradient was 0-2.5 min – 1 % B, 22 min – 45 % B, 23.5 min – 99 % B. This was followed by 2 wash pulses (1-99 % B) and equilibration to 1% B (45 min total run time). The trap column was held at a constant 1 % B and switching from the trap to the main column occurred at 1 min 24 sec and back at 40 min.

Mass spectrometry conditions were as follows: source voltage of 2300V in positive ionisation mode; ion transfer tube temperature 250 °C, CID gas pressure 1.5 mTorr, scan widths for Q1 and Q3 at 0.7 m/z , a chromatographic file was used with a peak width of 6 sec. Dwell times: 50 ms for *N*²-Me-dG and 20 ms for the rest. Collision energy voltage and RF voltage were optimized with authentic standards using the vendor-provided tune software for each fragment in the SRM, however the dA parameters were reduced to 10 % of the optimal value due to their high abundance and consequently high ion current.

Data was analysed using the FreeStyle 1.6 software and the Genesis peak detection algorithm with its default settings. The amount of *N*²-Me-dG per genome was based on a calculation using the number of nucleosides in the mouse genome ($n=1$)

2.8 Statistical analysis

Sample number (n) indicates the number of independent biological samples in each experiment. Sample numbers and experimental repeats are indicated in figure legends or Methods. Unless otherwise stated in the figure legend, data are shown as the mean \pm s.e.m. and the two-sided nonparametric Mann–Whitney test was used to assess statistical significance. Analysis was performed using GraphPad Prism.

Chapter 3

XPF-ERCC1 protects liver kidney and blood homeostasis outside the canonical excision pathways

Patient mutations in XPF-ERCC1 can give rise to XP, CS, XPCS or FA depending on how the mutation affects the function of this key DNA repair nuclease (Bogliolo et al., 2013; Fassihi et al., 2016; Kashiyama et al., 2013; Natale & Raquer, 2017). Functionally, the XPF-ERCC1 nuclease makes excisions to remove DNA damage during NER and FA repair (Figure 1.01). Mice deficient in ERCC1 display a severe phenotype, whereas mice deficient in the essential NER protein XPA, and mice deficient the essential FA repair protein FANCA, display very mild phenotypes (de Vries et al., 1995; Niedernhofer, Garinis, Raams, Lalai, Robinson, Appeldoorn, Odijk, Oostendorp, Ahmad, van Leeuwen, et al., 2006; Wong et al., 2003). Therefore, to investigate the contribution of XPF-ERCC1 in its role in excision repair to the overall phenotype we exploited mutations in repair pathways that segregate the role of this nuclease.

3.1 XPF-ERCC1 is required for normal tissue homeostasis in the liver, kidney and blood

Using isogenic mouse lines, we sought to investigate whether joint inactivation of NER and FA repair leads to the severe XPF-ERCC1 phenotype. To begin to address this, we first wanted to establish and compare the phenotype of mice lacking NER, the FA pathway or the nuclease XPF-ERCC1. To this end, we used mice lacking FANCA, a component of the FA core complex required for the ubiquitination of FANCD2 and therefore essential for the recruitment of XPF-ERCC1 during FA repair. Mice lacking XPA, a critical component of both the GG and TC branches of NER and essential for the recruitment of XPF-ERCC1 during NER and finally mice lacking ERCC1, required for excision in both branches of NER and FA repair.

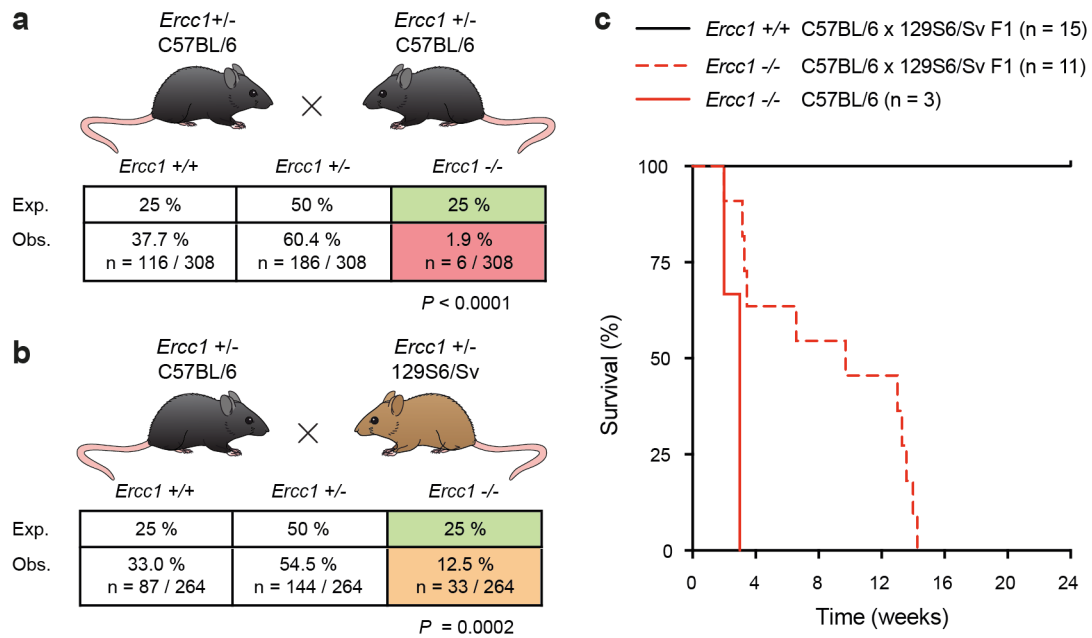


Figure 3.01. Generating *Ercc1*^{-/-} mice.

a) *Ercc1*^{+/-} crosses in a C57BL/6 background showing that *Ercc1*^{-/-} mice are genotyped at sub-mendelian ratios 2-3 weeks after birth (1.9% instead of the expected 25%, Fishers exact test: $P < 0.0001$). **b)** *Ercc1*^{+/-} crosses to generate *Ercc1*^{-/-} mice in a C57BL/6 x 129S6/Sv F1 background (12.5% instead of the expected 25%, Fisher's exact test: $P = 0.0002$). **c)** Survival of *Ercc1*^{-/-} and control mice in C57BL/6 and C57BL/6 x 129S6/Sv F1 genetic backgrounds.

Disruption of *Ercc1* in an inbred C57BL/6 background yields very few *Ercc1*^{-/-} mice, just 1.9% from heterozygous crosses. (Figure 3.01a and 3.01c) (R. Hill & Crossan, 2019). However, the severity of the phenotype can be attenuated in a C57BL/6 x 129S6/Sv F1 hybrid genetic background, yielding homozygous mice at 12.5%. The longevity of *Ercc1*^{-/-} mice on each background also varies with the inbred strain surviving no longer than 4 weeks compared to 12-13 weeks for the C57BL/6 x 129S6/Sv F1 hybrids (Figure 3.01b and 3.01c) (Weeda et al., 1997). The genetic modification is the same in these two backgrounds though the F1 hybrids benefit from hybrid vigour that likely leads to the loss of recessive modifier loci. Nonetheless, with *Ercc1*^{-/-} mice surviving to 12-13 weeks in an F1 hybrid background a side-by-side comparison of liver, kidney and haematopoietic function between *Ercc1*^{-/-}, *Fanca*^{-/-}, and *Xpa*^{-/-} mice was possible.

Ercc1^{-/-} mice succumb to liver failure, therefore we started our comparison by assessing liver function through biochemical analysis of blood serum and found, in agreement with previous work (McWhir et al., 1993), that *Ercc1*^{-/-} mice have raised levels of alanine transaminase (ALT), a marker of liver damage that suggests a degree of hepatocyte cell death. In contrast, both *Xpa*^{-/-} and *Fanca*^{-/-} mice had normal levels (Figure 3.02a). Histologically, only *Ercc1*^{-/-} mice displayed karyomegaly in the liver, which is thought to be a consequence of excessive DNA damage (Figure 3.02a). Liver failure can be rescued in the *Ercc1*^{-/-} mice by liver specific expression of a transgene containing *Ercc1*, however the mice then succumb to renal failure (Selfridge et al., 2001). We confirmed that renal function was affected in *Ercc1*^{-/-} mice by increased serum creatinine levels and signs of sclerotic glomeruli. Neither *Xpa*^{-/-} or *Fanca*^{-/-} mice displayed any signs renal dysfunction (Figure 3.02b). Taken together these data indicate that the liver and kidney of *Ercc1*^{-/-} mice are severely compromised in contrast to *Xpa*^{-/-} and *Fanca*^{-/-} mice whose liver and kidney function appear normal.

Although both *Xpa*^{-/-} and *Fanca*^{-/-} mice have very mild phenotypes, it is well documented that FA pathway-deficient mice have a reduced frequency of haematopoietic stem cells (HSCs) (Garaycochea et al., 2012; Parmar et al., 2010). Whilst young *Xpa*^{-/-} mice do not have an overt HSC defect, it has been reported that the haematopoietic progenitor pool is reduced in 1-year old *Xpa*^{-/-} mice (Prasher et al., 2005). *Ercc1*^{-/-} mice have been shown to have a severe HSC defect, though this is thought to be due to loss of the FA pathway (Prasher et al., 2005). We therefore set out to directly compare haematopoiesis between *Xpa*^{-/-}, *Fanca*^{-/-} and *Ercc1*^{-/-} mice. To do this we quantified the frequency of haematopoietic stem and progenitor cells (HSPCs) defined as lineage (CD3, CD4, CD8, B220, Mac-1, Gr-1, TER-119) negative c-kit positive and Sca-1 positive (LKS), in addition to the frequency of HSCs (LKS CD48 negative CD150 positive).

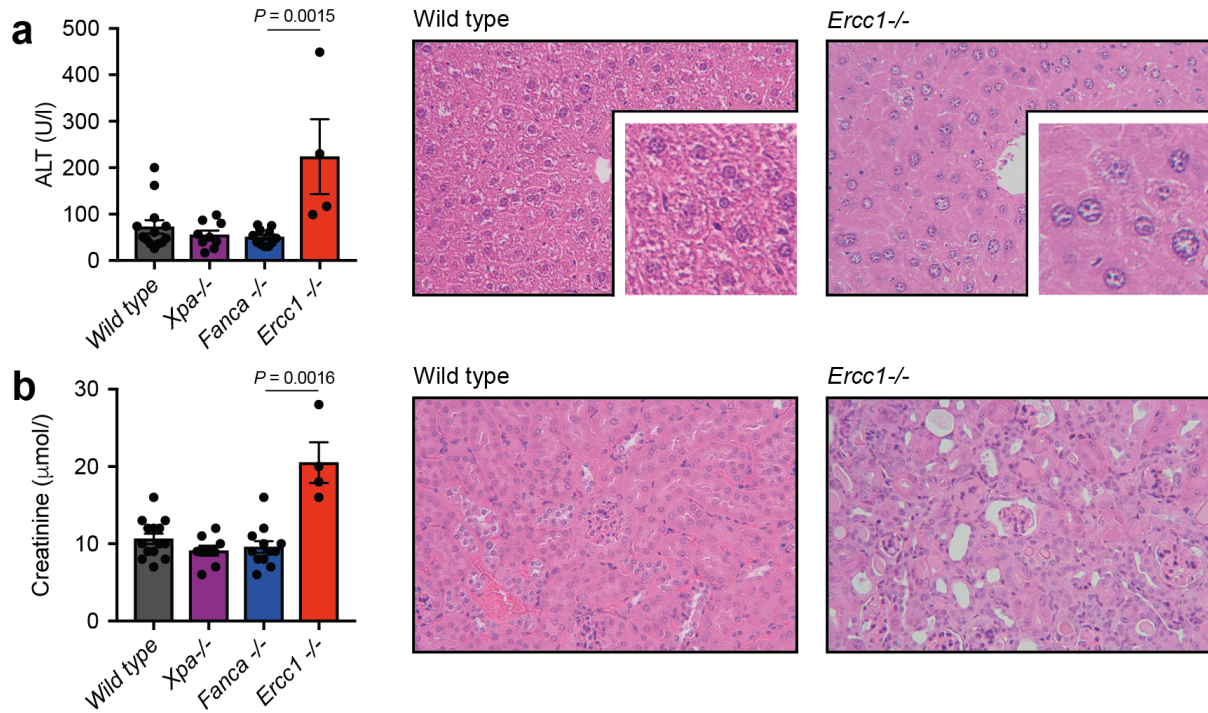


Figure 3.02. The nuclease XPF-ERCC1 protects the liver and kidney

a) Left: serum levels of alanine transaminase (ALT). Right: haematoxylin and eosin (H&E) staining of liver sections (X200, inset X400). **b**) Left: serum levels of creatinine. Right: H&E staining of kidney sections (X200). Mice were 8-12 weeks of age C57BL/6 x 129S6/Sv F1 background n= 13, 9, 11 and 4, error bars represent s.e.m., two-tailed Mann Whitney test.

We found that young *Xpa*^{-/-} mice had comparable frequencies of LKS cells (Figure 3.03a) and HSCs (Figure 3.03b) when compared to wild type littermates. In contrast, *Ercc1*^{-/-} and *Fanca*^{-/-} mice had a significant reduction both in the frequency of LKS cells and HSCs when compared to wild type or *Xpa*^{-/-} controls (Figure 3.03a-b). Surprisingly, the magnitude of the HSC defect observed in *Ercc1*^{-/-} mice was significantly greater than that observed in *Fanca*^{-/-} mice (Figure 3.03b, 11.8-fold compared to 1.8-fold).

To exclude the possibility that liver and kidney failure were compounding the more severe HSC defect in *Ercc1*^{-/-} mice, we next quantified HSCs in embryos. During development HSCs expand in the fetal liver between E12-E16 before populating the bone marrow at E17.5 (Christensen et al., 2004). The haematopoietic defect in FA-deficient mice begins *in utero* around day E12.5-E14.5 and should precede liver and kidney dysfunction in *Ercc1*^{-/-} mice (Domenech et al., 2018; Kamimae-Lanning et al., 2013b). Therefore, we set up timed mating's to generate embryos at E13.5 and quantified the frequency of LKS cells and HSCs in the foetal liver by flow cytometry (Figure 3.03c). Here we also see that HSC loss is significantly reduced in the *Ercc1*^{-/-} mice when compared to *Fanca*^{-/-} mice (Figure 3.03c-e).

Therefore, lack of ERCC1 not only affects organs that are unperturbed in *Fanca*^{-/-} mice and *Xpa*^{-/-} mice, but also leads to a more severe contraction in the HSC pool, thought to be due to deficiency in ICL repair. One explanation for these observations is that ERCC1 deficiency removes not only the dominant FA ICL-repair pathway, but also an additional pathway of HSC protection. Alternatively, this could be due to a more crucial role of XPF-ERCC1 acting in the same pathway as FANCA to protect HSCs.

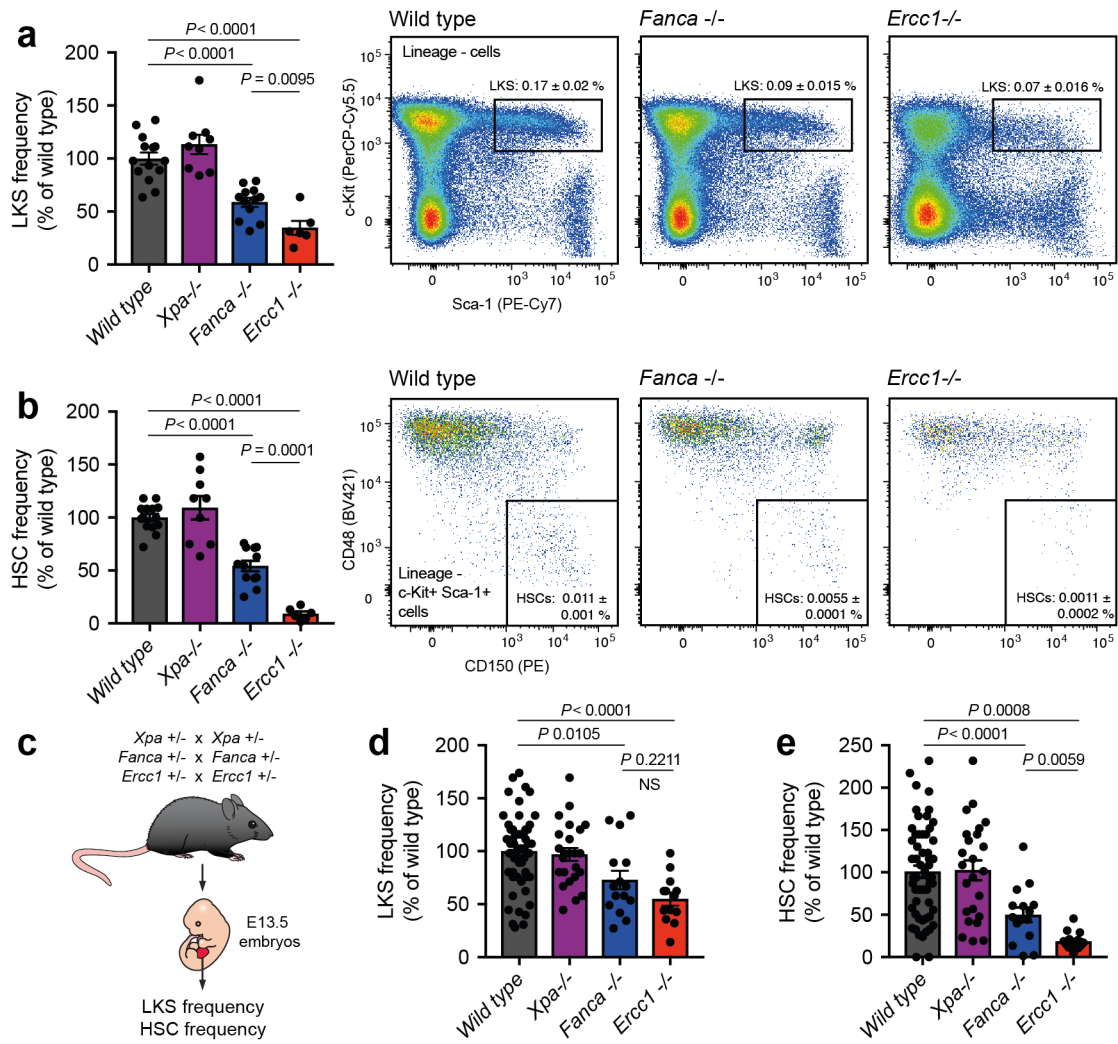


Figure 3.03 XPF-ERCC1 protects blood homeostasis in adult mice and embryos

a) Left: quantification of stem and progenitor cells (lineage- c-kit⁺ Sca-1⁺, LKS) assessed by flow cytometry. Right: representative flow cytometry profiles of 150.000 lineage- cells. **b)** Left: quantification of haematopoietic stem cells (lineage- c-kit⁺ Sca-1⁺ CD48-CD150⁺, HSC) assessed by flow cytometry. Right: flow cytometry profiles of LKS cells from a). Mice were 8-12 weeks of age C57BL/6 x 129S6/Sv F1 background n= 13, 9, 11 and 4, error bars represent s.e.m., two-tailed Mann Whitney test. **c)** Scheme for the generation of E13.5 embryos for the quantification of HSCs in the foetal liver. **d)** Quantification of LKS cells by flow cytometry in E13.5 foetal liver. **e)** Quantification of HSCs by flow cytometry in E13.5 foetal liver. In d-e, pups were 13.5 in a C57BL/6 background, n=56, 24, 12 and 13, error bars represent s.e.m., P: two tailed Mann-Whitney test.

3.2 Cells deficient in TC-NER are hypersensitive to crosslinking agents

The more severe phenotype observed in *Ercc1*^{-/-} mice could be due to simultaneous inactivation of two pathways that cooperate to protect against ICL's. To test whether this was the case we next took a genetic *in vitro* approach to assess how cellular deficiency in these pathways affected the sensitivity to crosslinking agents. For this approach we used the human somatic haploid cell line, HAP1. Using CRISPR/Cas9 gene targeting we generated a panel of isogenic cell lines deficient in different components of the NER pathway: XPC, that senses helix distortions and initiates GG-NER; CSB, that detects the stalling of the RNA polymerase and triggers TC-NER; XPA, a scaffold protein required by both branches of NER; and XPF, the endonuclease that forms a complex with ERCC1 to cleave DNA on the 5' side of the lesion.

The cell lines were validated for genomic alterations by Sanger sequencing (Figure 3.04a), protein loss by western blot (Figure 3.04b) and functionally validated by hypersensitivity to UV (Figure 3.05a). We found that haploid *XPF*⁻ cells diploidised spontaneously, so all survival experiments were carried out with diploid lines. HAP1 cells have been previously reported to become diploid over time in a p53 dependent manner (Olbrich et al., 2017). Perhaps therefore XPF deficiency results in activation of p53 and subsequent diploidisation.

To assess how our cell lines respond to ICL inducing agents we exposed them to cisplatin and MMC. In agreement with its documented role in crosslink repair, *XPF*^{-/-} cells were extremely sensitive to both agents (Figure 3.05b and 3.05c). In contrast, *XPC*^{-/-} cells were indistinguishable from the parental wild type cells. *XPA*^{-/-} and *CSB*^{-/-} cells were sensitive to ICL inducing agents but this was much milder than the *XPF*^{-/-} cells. As XPA and CSB both operate in the TC branch of NER, this suggests a role for TC-NER, but not GG-NER, in maintaining cellular resistance to crosslinking agents.

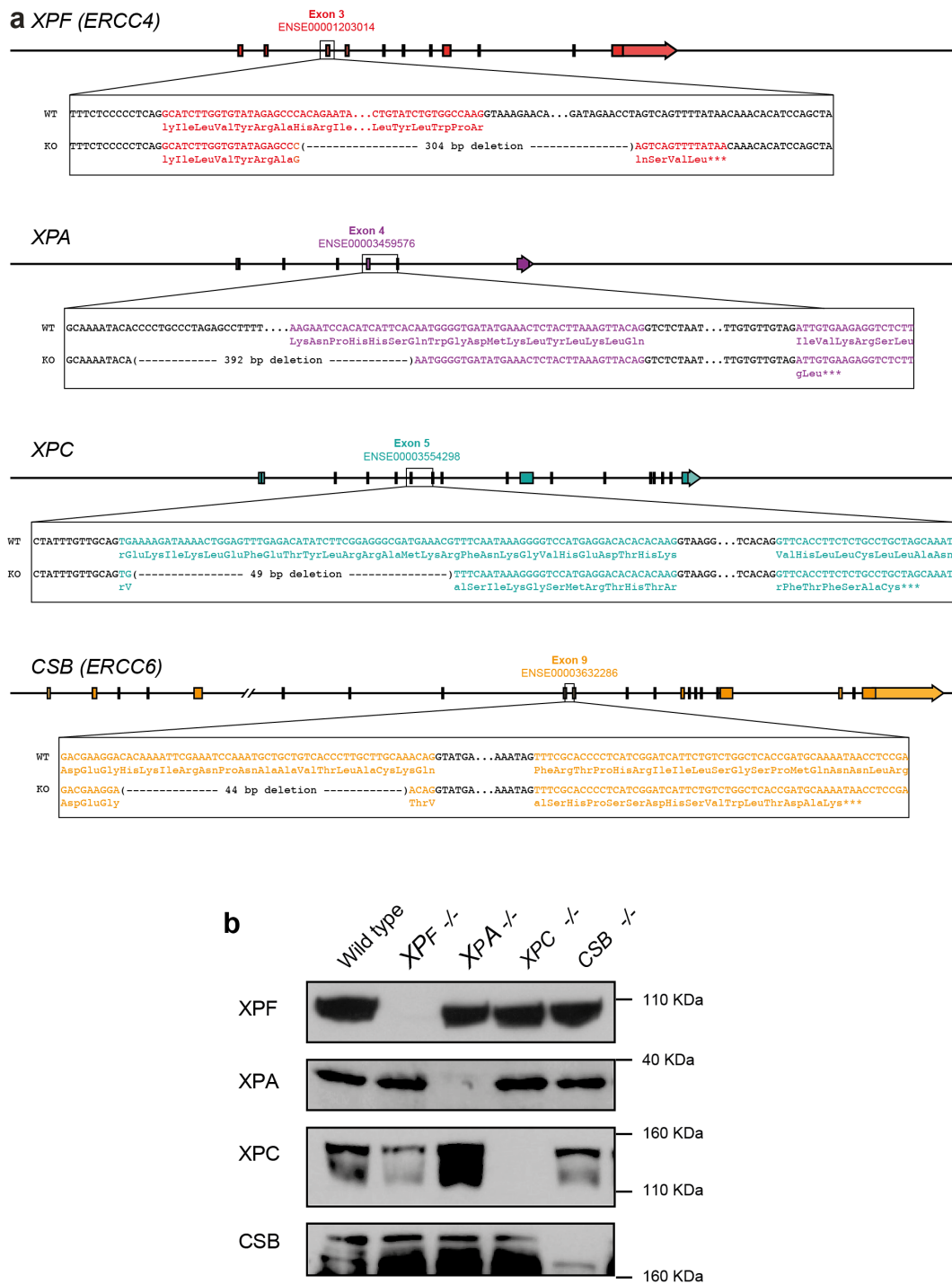


Figure 3.04 – Generation of HAP1 knock out lines

a) Maps of human NER genes. The inset shows the nucleotide and predicted amino acid sequence of wild type and knock out HAP1 lines generated by introducing deletions with CRISPR/Cas9. **b)** Western blots showing lack of NER proteins in HAP1 knock out lines.

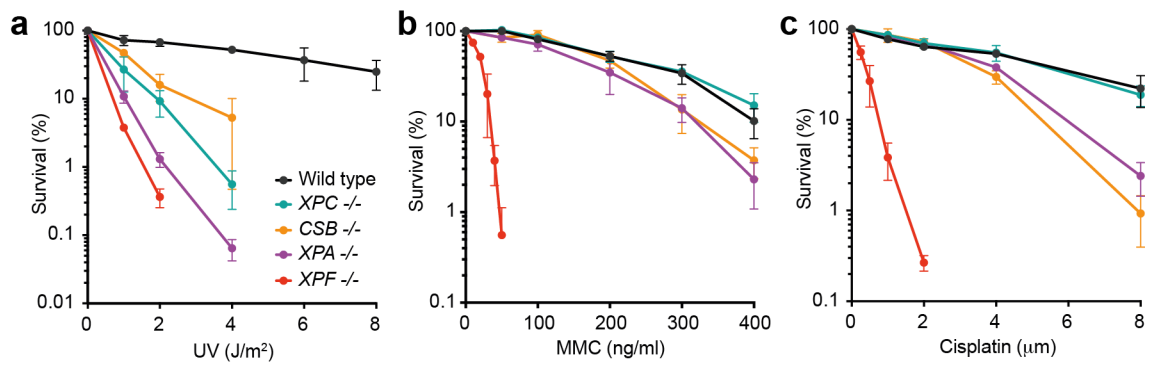


Figure 3.05 – TC-NER confers protection against ICL-inducing agents.

a) Survival of HAP1 cells in response to UV. **b)** Survival of HAP1 cells in response to mitomycin C (mmc). **c)** Survival of HAP1 cells in response to cisplatin. In a-c each data point represents the mean of at least two independent experiments, each carried out in duplicate, error bars represent s.e.m.

3.3 NER and the FA pathway cooperate to repair formaldehyde lesions

Cells deficient in TC-NER are sensitive to crosslinking agents, but not as hypersensitive as cells deficient in the NER nuclease XPF. This is most likely due to XPF's function in the FA repair pathway, known to repair ICL's. To assess whether XPF hypersensitivity to ICL's was due to its combined function in NER and FA repair we inactivated FA repair in wild type and *XPA*^{-/-} cells, using a targeting construct to introduce isogenic disruptions in the *FANCL* locus (Figure 3.06a and 3.06c). By introducing an identical construct into the wild type and *XPA*^{-/-} cells we were able to generate comparable cell lines. FANCL is the E3 ubiquitin ligase responsible for FANCD2 monoubiquitination, an essential step in ICL repair (Knipscheer et al., 2009; Meetei et al., 2003). We validated the disruption of the *FANCL* locus by long-range PCR (Figure 3.06d) and detected loss of FANCD2 ubiquitination by western blot (Figure 3.06b). We then quantified the survival of these cells in response to crosslinking agents.

FANCL^{-/-} and *XPF*^{-/-} lines, both deficient in FA DNA repair, were hypersensitive to the ICL-inducing agents MMC and cisplatin (Figure 3.07a and 3.07b). However, *XPF*^{-/-} cells were far more sensitive than FA-deficient cells. We found that *XPA*^{-/-}*FANCL*^{-/-} cells were no more sensitive than *FANCL*^{-/-} cells to MMC, but loss of XPA resulted in additive sensitivity to cisplatin (Figure 3.07a and 3.07b). This increased sensitivity could be explained by the fact that cisplatin readily generates intrastrand crosslinks (i.e. crosslinking of adjacent bases on the same DNA strand), lesions commonly removed by NER (J. C. Huang et al., 1994). However, in neither case, joint inactivation of NER and FA repair was sufficient to account for the hypersensitivity of *XPF*^{-/-} cells. We found that *XPF*^{-/-} and *XPA*^{-/-}*FANCL*^{-/-} cells were equally sensitive to other sources of DNA damage, like UV light and ionizing radiation, suggesting that the extreme sensitivity of *XPF*^{-/-} was specific to ICL-causing agents (Figure 3.07c and 3.07d).

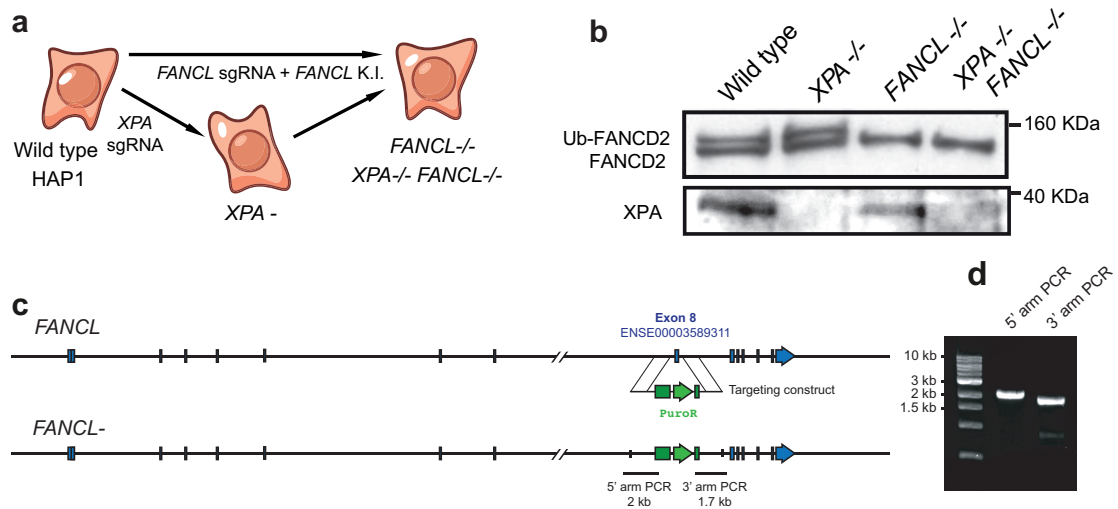


Figure 3.06 – Generating cells deficient in NER and the Fanconi Pathway

a) Scheme for the isogenic disruption of the *FANCL* locus in wild type or *Xpa* deficient HAP1 cells. **b)** Western blot showing the lack of *FANCD2* mono-ubiquitination and absence of *XPA* protein in HAP1 knock out lines. **c)** Map of the human *FANCL* gene and targeting of exon 8 to generate isogenic disruptions in *FANCL*. **d)** Agarose gel showing disruption of the *FANCL* locus by long range PCR. Primers hybridise outside the homology arms and within the targeting construct.

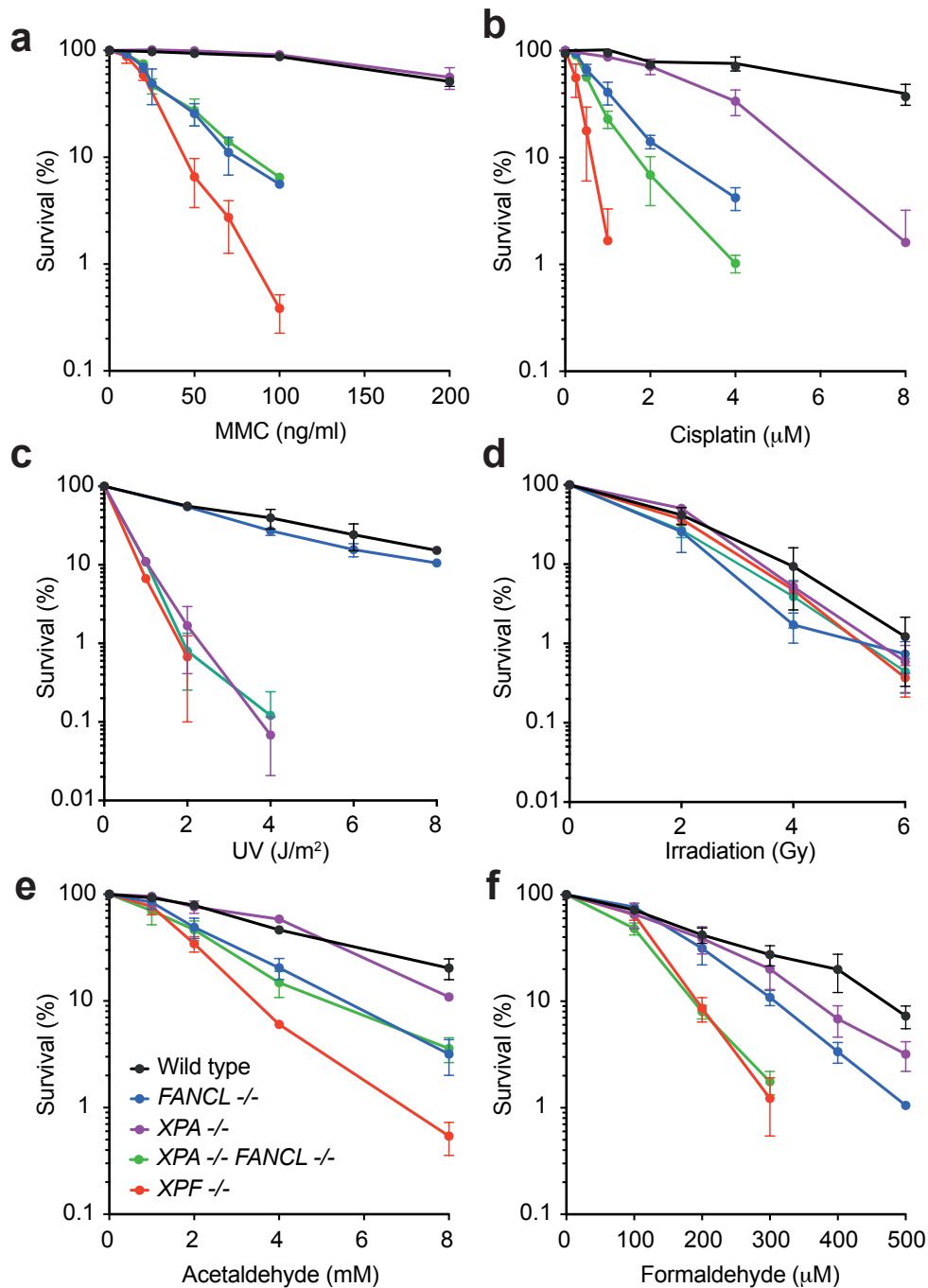


Figure 3.07 – NER and the FA pathway cooperate to protect cells from formaldehyde

a-f) Survival of HAP1 cells in response to mitomycin C (MMC), cisplatin, UV, irradiation, acetaldehyde and formaldehyde. Each data point represents the mean of at least two independent experiments, each carried out in duplicate, error bars represent s.e.m.

These results highlight that the XPF-ERCC1 nuclease plays a critical role in ICL repair, but is also perhaps involved in alternative repair routes, which are not NER. Whilst cisplatin or MMC are of significant clinical relevance, we have recently found that reactive aldehydes, by-products of cellular metabolism, could be an important source of endogenous DNA crosslinks (Langevin et al., 2011; Pontel et al., 2015). We therefore exposed $XPA^{-/-}FANCL^{-/-}$ and control cell lines to the simple aldehydes: acetaldehyde and formaldehyde (Figure 3.07e and 3.07f). Loss of NER did not further sensitise $FANCL^{-/-}$ cells to acetaldehyde. In contrast, $XPA^{-/-}FANCL^{-/-}$ cells were more sensitive to formaldehyde than either single mutant, with comparable sensitivity to $XPF^{-/-}$ cells. Although closely related, the reactivity and types of lesions caused by these aldehydes differ (Cheng et al., 2003b). The increased sensitivity to formaldehyde may be due to this compound causing a different spectra of DNA lesions, which might include base adducts, DNA inter- and intrastrand crosslinks as well as DNA-protein crosslinks (Kuykendall & Bogdanffy, 1992). However, NER and FA repair are both required to maintain cellular resistance to the same endogenous genotoxin - formaldehyde. Although we have exposed cells to exogenous formaldehyde *in vitro*, it is also clear that cells within organisms are exposed to reactive aldehydes without exogenous exposure. Therefore, NER and FA repair constitute alternative pathways to repair lesions caused by this endogenous compound and both rely upon the activity of XPF-ERCC1.

3.4 TC-NER and the FA pathway preserve normal development

To test the physiological importance of the observation that NER and FA act as alternative pathways to maintain resistance to some ICL agents we turned to mouse models. We set out to generate mice deficient in both NER and the FA DNA repair pathway. To this end, we first crossed $Xpa^{+/-}$ and $Fanca^{+/-}$ mice on a pure C57BL/6 background. To generate double mutant mice, we exploited the fact that NER-deficient mice are fertile and set up $Xpa^{-/-}$ $Fanca^{+/-}$ x $Xpa^{-/-}$ $Fanca^{+/-}$ crosses, which would generate the highest frequency of double mutants while minimizing the amount of breeding required. We then compared the number of $Fanca^{-/-}$ pups genotyped at 2-3 weeks between the NER proficient and deficient crosses (Figure 3.08a and 3.08b). We found $Xpa^{-/-}$ $Fanca^{-/-}$ pups to be underrepresented compared to $Fanca^{-/-}$ pups (1.5% instead of 13.3%, $P < 0.0001$) and born as rarely as $Ercc1^{-/-}$ pups in a C57BL/6 background (Figure 3.01a, 1.5% vs 1.9%, $P = 0.67$). This indicated a genetic interaction between NER and ICL repair to preserve mouse development. To investigate the significant reduction in the frequency of double mutants, we performed timed matings between $Fanca^{+/-}$ or $Xpa^{-/-}$ $Fanca^{+/-}$ crosses and sacrificed pregnant females at day E13.5. $Xpa^{-/-}$ $Fanca^{-/-}$ pups were found at a frequency of 11.4% (from n= 35, vs 29% $Fanca^{-/-}$ pups n=72, $P = 0.04$) and were grossly underdeveloped compared to controls (Figure 3.08e).

Therefore, NER and ICL repair genetically interact to preserve mouse development in a C57BL/6 background. To further dissect this observation, we crossed $Fanca^{+/-}$ mice with mice only lacking GG-NER ($Xpc^{-/-}$) or TC-NER ($Csb^{m/m}$). $Xpc^{-/-}$ mice are sensitive to UV light exposure but have otherwise near-normal lifespans and no overt phenotypes (Cheo et al., 1997). $Csb^{m/m}$ mice are also sensitive to UV light and show retinal degeneration, as well as mild growth retardation and neurodegenerative changes, an extremely mild version of human CS (G. T. van der Horst et al., 1997). We found that $Xpc^{-/-}$ $Fanca^{-/-}$ pups were born at the same frequency as $Fanca^{-/-}$ pups (11.5% vs 13.3%, $P = 0.5616$) (Figure 3.08c). In contrast, $Csb^{m/m}$ $Fanca^{-/-}$ pups were underrepresented compared to $Fanca^{-/-}$ pups (5.5% vs 13.3%, $P = 0.0020$) (Figure 3.08d). When put together, these results show that the FA pathway genetically interacts with components of TC-NER pathway, but not GG-NER, to preserve development. These results agree with the observation that both the FA pathway and TC-NER are required to protect cells from crosslinking agents *in vitro* (Figure 3.05b and 3.05c). In sum, TC-NER and FA repair are jointly required to preserve normal mouse development in a C57BL/6 background.

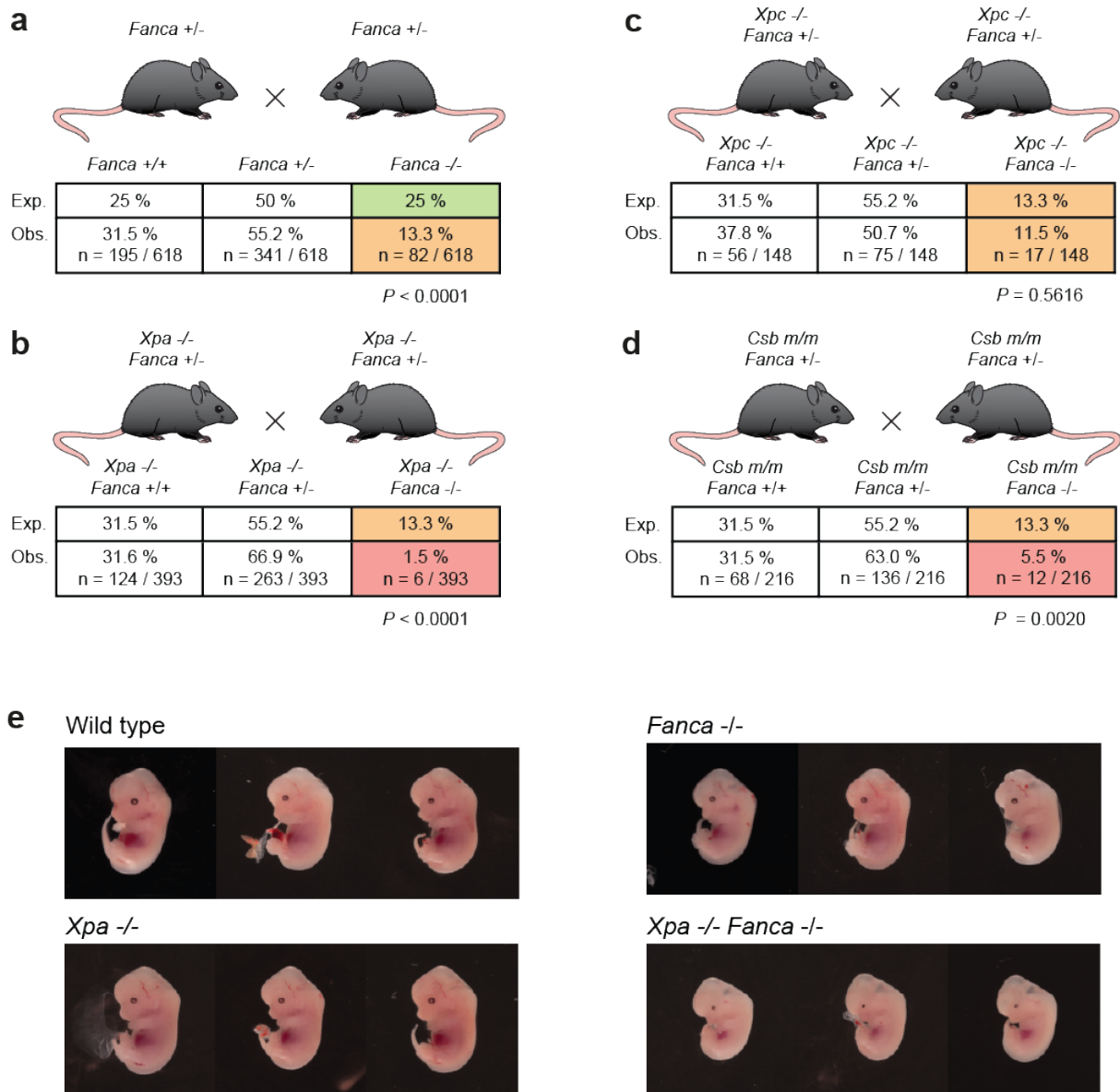


Figure 3.08 – TC-NER and the FA pathway cooperate to ensure normal mouse development.

a) *Fanca*^{+/-} crosses in a C57BL/6 background showing that *Fanca*^{-/-} mice are genotyped at sub-mendelian ratios 2-3 weeks after birth (13.3% instead of the expected 25%, *P*: Fisher's exact test compared to expected numbers). **b)** *Xpa*^{-/-} *Fanca*^{+/-} crosses for the generation of double mutant mice in a C57BL/6 background. **c)** *Xpc*^{-/-} *Fanca*^{+/-} crosses for the generation of double mutant mice in a C57BL/6 background. **d)** *Csb*^{m/m} *Fanca*^{+/-} crosses for the generation of double mutant mice in a C57BL/6 background. **e)** Examination of E13.5 embryos generated from *Fanca*^{+/-} or *Xpa*^{-/-} *Fanca*^{+/-} crosses in a C57BL/6 background.

3.5 Simultaneous inactivation of NER and ICL repair does not recapitulate XPF-ERCC1 deficiency

The strong genetic interaction between TC-NER and FA repair *in utero* prompted us to ask if joint inactivation of these repair pathways might explain some aspects of the *Ercc1*^{-/-} phenotype. *Ercc1*^{-/-} mice on a C57BL/6 background are born at an extremely low ratio but a C57BL/6 x 129S6/Sv F1 hybrid background circumvents this lethality and allows the study of the role of XPF-ERCC1 in postnatal life (Figure 3.01b) (Weeda et al., 1997). In complete contrast to the very mild phenotypes of *Csb*^{m/m}, *Xpa*^{-/-} and *Fanca*^{-/-} mice, *Ercc1*^{-/-} mice suffer from multisystem degenerative features, severe growth deficits and short lifespan. In order to investigate if some aspects of this phenotype are due to joint inactivation of NER and FA repair, we sought to generate *Xpa*^{-/-} *Fanca*^{-/-} mice on an C57BL/6 x 129S6/Sv F1 hybrid background and compare this to the phenotype of *Ercc1*^{-/-} C57BL/6 x 129S6/Sv F1 mice. Indeed, the embryonic lethality of double mutants in the C57BL/6 background (Figure 3.08b) was completely rescued on the F1 genetic background (Figure 3.09a). The C57BL/6 congenic background is known to potentiate the phenotype of DNA repair-deficient mice (Barnhoorn et al., 2014b; Bellelli et al., 2018; Ghezraoui et al., 2018). Postnatal growth is severely retarded in *Ercc1*^{-/-} mice. However, the weight of both *Xpa*^{-/-} *Fanca*^{-/-} and *Csb*^{m/m} *Fanca*^{-/-} was indistinguishable from *Fanca*^{-/-} mice at 8 weeks of age (Figure 3.09b).

We then set out to assess liver and kidney function in these double mutants, as these two tissues lose homeostasis accompanied by morphological changes in *Ercc1*^{-/-} mice (Figure 3.02a-b). The hepatocytes of these mice display polyploidy and this is associated with compromised liver function. We observed no gross histological abnormalities in the liver of *Xpa*^{-/-} *Fanca*^{-/-} or *Csb*^{m/m} *Fanca*^{-/-} mutants. Whilst we could detect polyploid nuclei in the liver of *Ercc1*^{-/-} mice, we detected normal DNA content in *Xpa*^{-/-} *Fanca*^{-/-} and *Csb*^{m/m} *Fanca*^{-/-} livers (Figure 3.10a-c). Liver function was also normal as judged by the concentration of albumin and liver enzymes in blood serum (Figure 3.10d-e). We then focused our attention on the kidney phenotype, as *Ercc1*^{-/-} mice show abnormal renal histopathology (glomerulosclerosis and protein casts) and renal dysfunction (significantly elevated serum creatinine and urea) (Selfridge et al., 2001). However, we did not detect any of these changes in mice lacking both NER and the FA pathway (Figure 3.11a-c).

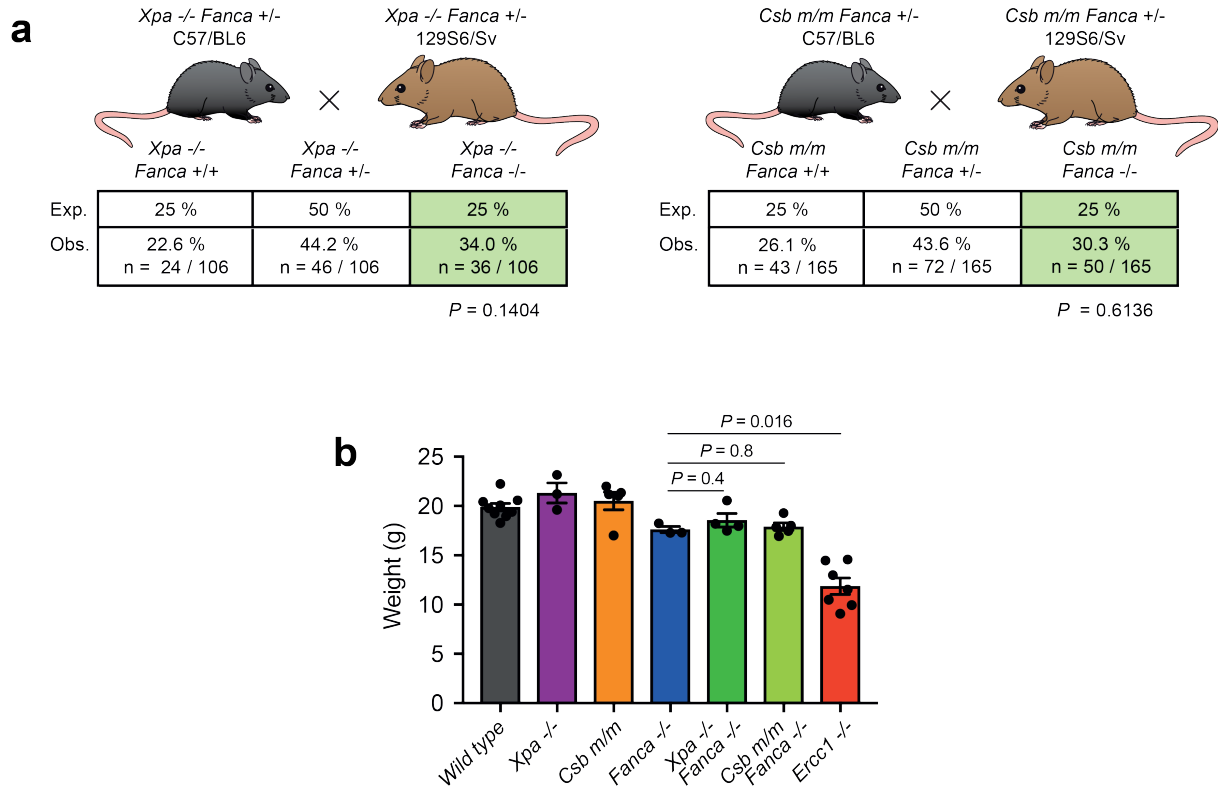


Figure 3.09 – A hybrid C57BL/6 129S6/Sv cross gives rise to pups lacking TC-NER and the FA pathway, at Mendelian ratios

a) Crosses for the generation of double mutant mice in a C57BL/6 x 129S6/Sv F1 background, pups were genotyped 2-3 weeks after birth (P : Fisher's exact test, compared to expected numbers). **b)** Weights of 8-week-old females in a C57BL/6 x 129S6/Sv F1 background (P : two-tailed Mann-Whitney test, $n=9, 3, 5, 3, 4, 5$ and 7).

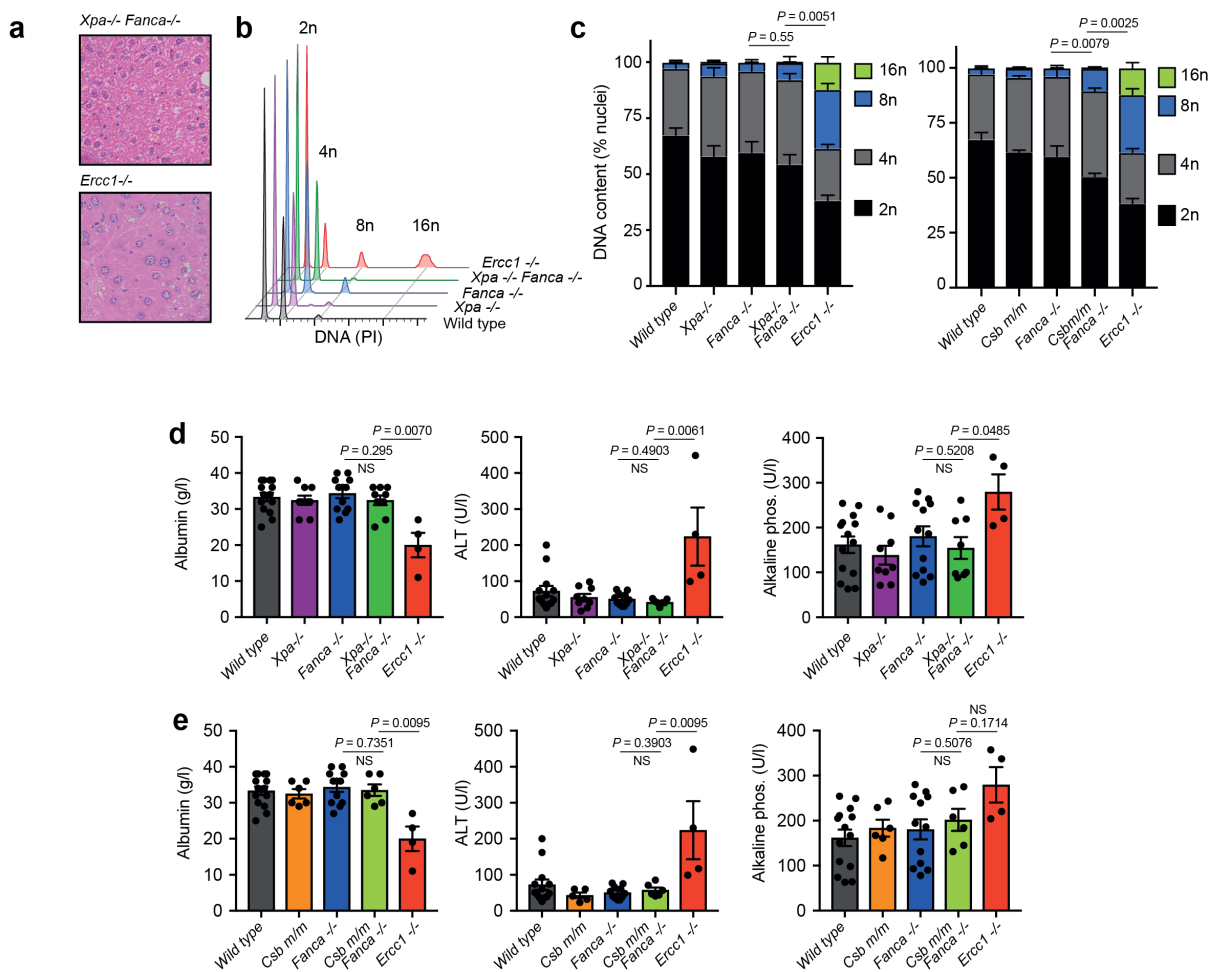


Figure 3.10 – Liver function is preserved in the absence of NER and the Fanconi Pathway

a) H&E staining of liver sections (X400). **b)** Representative histograms for the flow cytometric analysis of DNA content in the nuclei of liver cells. **c)** Quantification of DNA content in the nuclei of liver cells (P: two tailed Mann-Whitney test for the frequency of 8n nuclei) **d-e)** Serum levels of albumin, alanine transaminase (ALT) and alkaline phosphatase. In **a-e)** mice were 8-12 weeks old, C57BL/6 x 129S6/Sv F1 background, error bars represent s.e.m., P: two tailed Mann Whitney test. In **c)** n= 6,5,5,5,7, in **d-e)** n= 14,9,12,9 and 4.

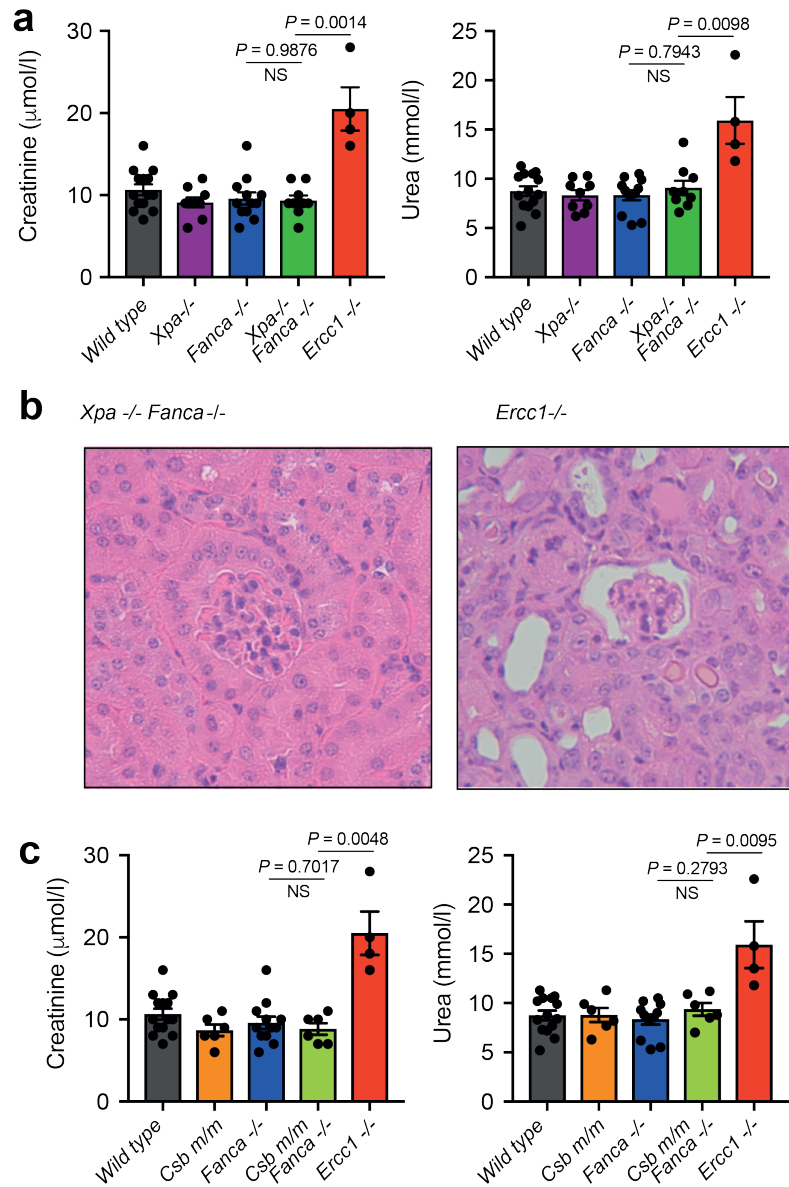


Figure 3.11 – Kidney function is preserved in mice lacking NER and the Fanconi pathway

a) Serum levels of urea and creatinine. **b)** H&E staining of kidney sections (x200). **c)** Serum levels of urea and creatinine. In **a** and **c)** mice were 8-12 weeks old, C57BL/6 x 129S6/Sv F1 background, error bars represent s.e.m., P: two tailed Mann Whitney test. In **a** and **c)** n=14,9,12,9 and 4.

Finally, we asked if loss of NER could exacerbate the haematopoietic phenotype of *Fanca*^{-/-} mice. We used flow cytometry to quantify LKS cells and HSCs and observed no difference between *Xpa*^{-/-}*Fanca*^{-/-} and *Fanca*^{-/-} controls (Figure 3.12a and 3.12b). Next, we performed the spleen colony-forming unit assay, which relies on transplantation and is a functional measure of the frequency of stem and progenitor cells; again, we did not detect any difference between the number of *Fanca*^{-/-} and *Xpa*^{-/-}*Fanca*^{-/-} progenitors (Figure 3.12c). In all these analyses, *Ercc1*^{-/-} bone marrow was more compromised compared to *Fanca*^{-/-}, *Xpa*^{-/-}*Fanca*^{-/-} and *Csb*^{m/m}*Fanca*^{-/-} mice. Although liver and kidney failure could confound this more severe haematopoietic defect, we showed that the HSC compartment is already contracted *in utero*, prior to severe liver and kidney dysfunction (Figure 3.03c-e). In summary, the phenotype of mice with joint inactivation of NER and FA repair in the C57BL/6 x 129S6/Sv F1 background seems indistinguishable from that of *Fanca*^{-/-} controls. This is in complete contrast to the severe phenotype of *Ercc1*^{-/-} mice, which therefore cannot be explained by simultaneous inactivation of NER and ICL repair.

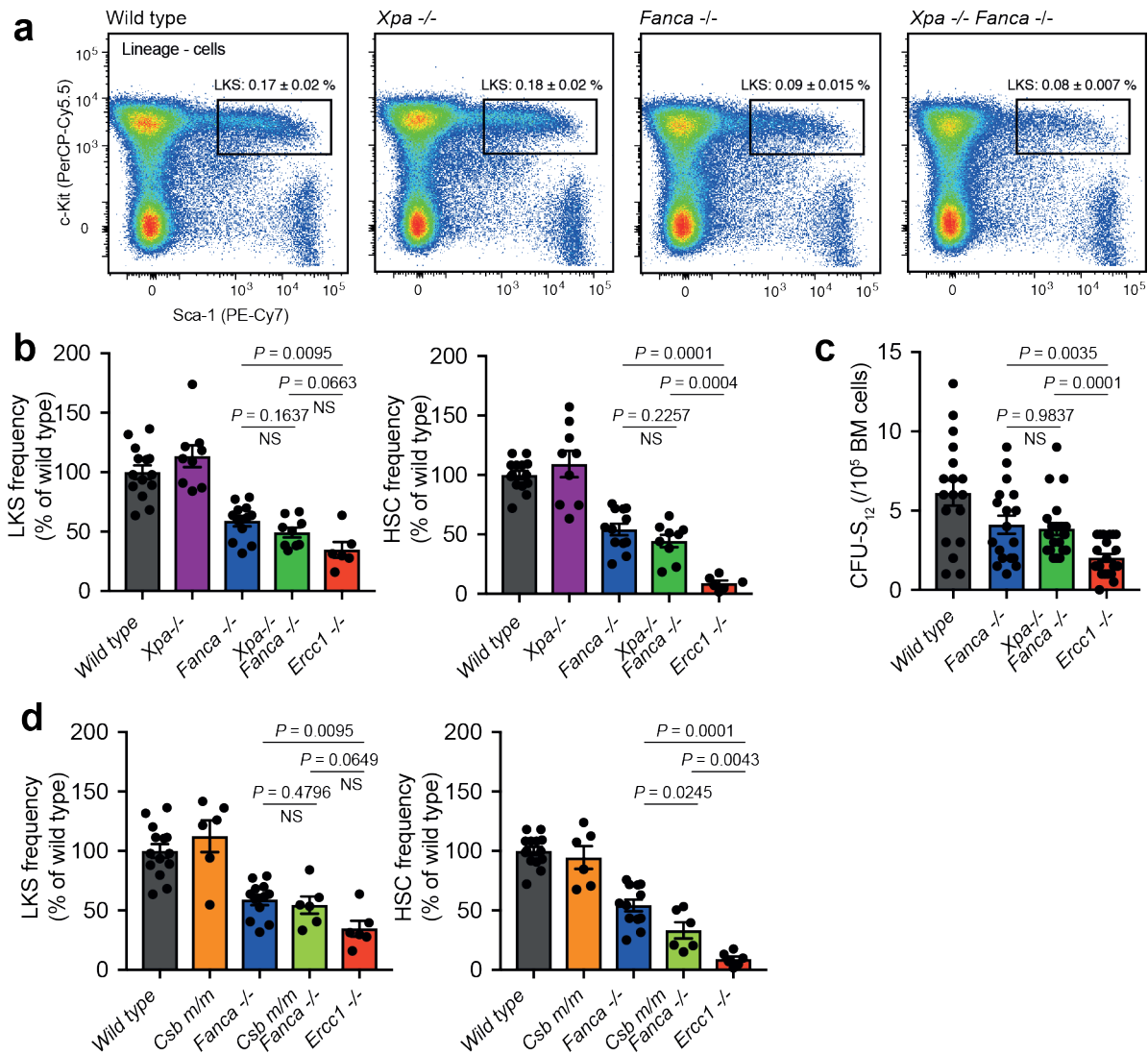


Figure 3.12 – Loss of NER does not potentiate hematopoietic defects in Fanconi mice

a) Representative flow cytometry profiles of 150,000 lineage- cells for the quantification of stem and progenitor cells (lineage- c-kit⁺ Sca-1⁺, LKS) **b)** Quantification of LKS and haematopoietic stem cells and progenitor cells (lineage- c-kit⁺ Sca-1⁺, LKS) **c)** Quantification of colony forming units – spleen (CFU-S) by transplantation of bone marrow into irradiated recipients. **d)** Quantification of LKS and haematopoietic stem cells and progenitor cells (lineage- c-kit⁺ Sca-1⁺, LKS). In **b-d)** mice were 8-12 weeks old, C57BL/6 x 129S6/Sv F1 background, error bars represent s.e.m., P: two tailed Mann Whitney test. In **b-d)** n=14,9,12,9 and 6.

3.6 Discussion

The nuclease XPF-ERCC1 is a central DNA repair protein that operates in multiple pathways, deficiency of which leads to severe phenotypes in mice and humans. We sought to understand what aspects of this phenotype are driven by joint inactivation of NER and FA repair. In this chapter, by genetically segregating the functions of XPF-ERCC1 in different repair pathways we yield insights into which functions are required to protect cells from ICLs and preserve liver, kidney and bone marrow function. The results presented here show that joint inactivation of NER and the FA pathway do not phenocopy XPF-ERCC1 deficiency, both at the cellular level and in adult mice. These findings shed light on the mechanisms of ICL repair and suggest functions of XPF-ERCC1 outside of the canonical excision pathways (Figure 3.14).

ICLs are toxic lesions that covalently bind the two strands of DNA together, blocking both transcription and replication. NER removes these adducts in bacteria and yeast. Mammals, however, have evolved the FA pathway, which orchestrates replication coupled ICL excision. Several cellular and biochemical studies suggest that NER pathway might also remove ICLs in mammals, outside of replication or during blocked transcription, and that this pathway may act preferentially in certain tissues (Enoiu et al., 2012a; Muniandy et al., 2009a). Here, we first test this hypothesis with an isogenic cellular system, and show that TC-NER provides resistance against classical crosslinking agents (Figure 3.05), in agreement with previous reports using patient-derived lines (Furuta et al., 2002). However, the FA ICL repair pathway provides the major route of protection against these agents. Although loss of FANCL completely disables FA repair, we find, surprisingly, that loss of the nuclease XPF-ERCC1 results in much greater hypersensitivity, with *XPF*^{-/-} cells being far more sensitive to cisplatin and MMC than *FANCL*^{-/-} cells. We show that this increased sensitivity cannot be fully explained by the generation of intrastrand crosslinks or XPF-ERCC1's function in NER, because *XPA*^{-/-}*FANCL*^{-/-} cells that lack NER are still not as sensitive as *XPF*^{-/-} cells (Figure 3.07). These data suggest that the XPF-ERCC1 nuclease has an alternative function in ICL repair. One possibility is that XPF-ERCC1 has a second function in FA-dependant ICL repair, potentially in the resolution of 'normal' HR intermediates following unhooking of the crosslink, or dealing with 'toxic' DSBs when FA unhooking fails (Ahmad et al., 2008; Al-Minawi et al., 2008; Bennardo et al., 2008; Motycka et al., 2004) (Figure 3.14). A second possibility is that XPF-ERCC1 functions in an alternative ICL-repair pathway, for example those involving the FAN1 or SNM1A nucleases. In support of this, while SNM1A is non-epistatic with FANCC, it

has an epistatic relationship with XPF-ERCC1, suggesting that these two nucleases function in a common pathway distinct from FA ICL repair (Ishiai et al., 2004; A. T. Wang et al., 2011).

We also found that NER and the FA pathway genetically interact to protect cells from formaldehyde, an endogenous source of crosslinks. Interestingly, we did not find that a genetic interaction between NER and the FA pathway in response to acetaldehyde, suggesting that these two closely related aldehydes cause a different spectra of DNA lesions. However, this prompted us to investigate if the genetic interaction between NER and the FA pathway extended to mice, to ask if these two pathways cooperate to protect tissues from endogenous DNA damage. Indeed, we find that TC-NER and the FA pathway are jointly required to preserve mouse development in a C57BL/6 isogenic background. It is worth pointing out that *Xpa*^{-/-} *Fanca*^{-/-} pups were born at a reduced ratio when compared *Csb*^{m/m} *Fanca*^{-/-}, suggesting that while TC-NER is the major NER pathway required for mouse development in the absence of the FA pathway, there may be additional redundancy between GG-NER and TC-NER (Figure 3.08). However, generation of *Xpa*^{-/-} *Fanca*^{-/-} and *Csb*^{m/m} *Fanca*^{-/-} on a C57BL/6 x 129S6/Sv F1 background rescued the embryonic lethality and revealed phenotypes indistinguishable from single mutant controls (Figure 3.10, 3.11 and 3.12). This indicates that NER and FA ICL repair genetically interact, particularly during development, but that this interaction is subtle in adult mice, and heavily affected by modifier loci, adding to the list of DNA repair deficient mice whose phenotype is exacerbated in the C57BL/6 background (Barnhoorn et al., 2014b; Bellelli et al., 2018; Ghezraoui et al., 2018).

Nevertheless, the C57BL/6 x 129S6/Sv F1 background allowed us to compare the phenotype of adult mice lacking the XPF-ERCC1 nuclease and those deficient in NER and/or ICL repair. At the organismal level, HSCs are one of the cell populations which are most affected by loss of the FA ICL repair pathway and this observation is true of FA deficient mice across all genetic backgrounds. Previous studies have suggested a more severe haematopoietic phenotype in ERCC1 hypomorphic mice compared to the haematopoietic phenotype of FA null mice (Cho et al., 2013; Prasher et al., 2005; Verhagen-Oldenampsen et al., 2012). Here, for the first time, we provide a side-by-side comparison of *Fanca*^{-/-} and *Ercc1*^{-/-} HSC compartments in embryos and adult mice. Importantly, we show that the more severe HSC defect in *Ercc1*^{-/-} mice is not solely due to joint inactivation of NER and FA ICL repair, because the haematopoietic defect of *Xpa*^{-/-} *Fanca*^{-/-} mice is indistinguishable from *Fanca*^{-/-} mice. This mirrors the greater sensitivity of *XPF*^{-/-} HAP1 cells compared to *XPA*^{-/-} *FANCL*^{-/-} cells in response to crosslinking agents and points to an additional function of XPF-ERCC1 in the protection of HSCs.

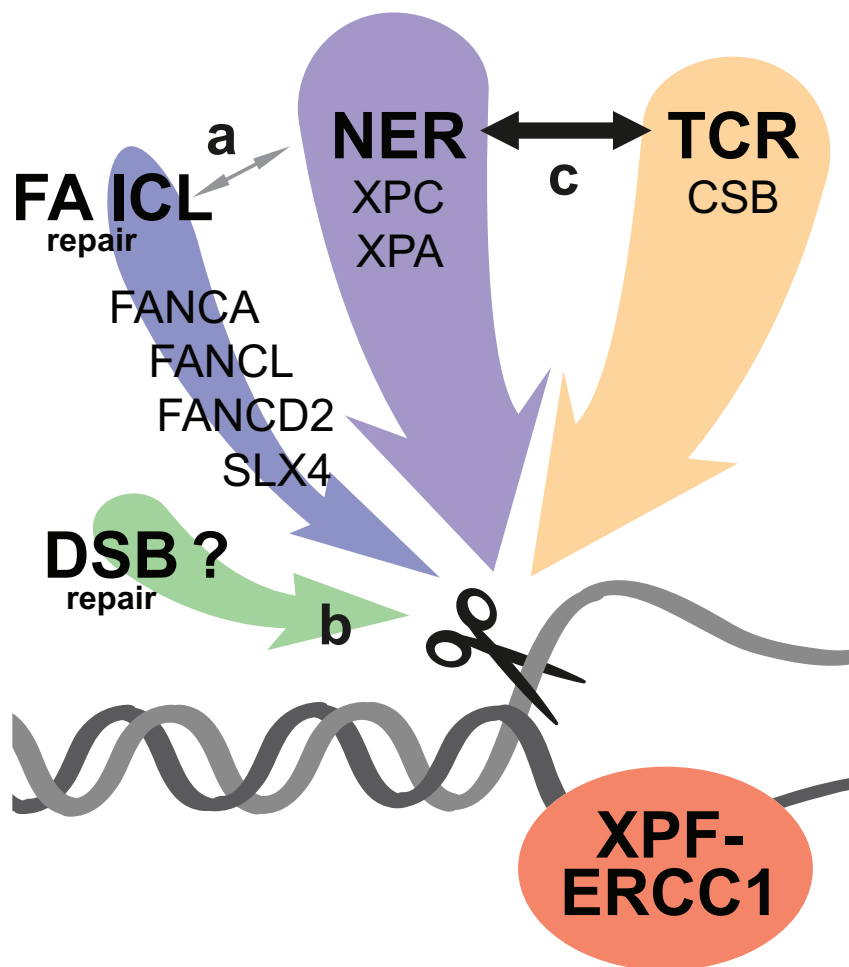


Figure 3.14 – Model of the interactions between DNA repair pathways that converge on the nuclease XPF-ERCC1

a) NER and FA ICL repair interact to protect against certain crosslinkers in vitro and to ensure normal development in a C57BL/6 background. **b)** XPF-ERCC1 has a role in ICL repair outside NER and ICL unhooking, potentially the repair of DNA double strand breaks (DSBs). **c)** The XPF-ERCC1 phenotype is likely due to deficiency in NER and TCR rather than NER and FA ICL repair. How exactly XPF-ERCC1 operates in TCR, and the nature of this damage, remains to be established.

Perhaps the most striking observation from our study is the mild phenotype of *Xpa*^{-/-}*Fanca*^{-/-} mice, which phenocopying FANCA deficiency completely contrasts with the severe, complex and short-lived phenotype of *Ercc1*^{-/-} animals. This observation challenges the prevailing model that joint inactivation of NER and ICL repair pathways greatly contributes to the severe multi-organ failure of XPF-ERCC1 deficiency and, when put together with previous work, draws our attention to the function of this multifunctional nuclease outside the canonical NER and ICL excision pathways. Recent reports have indicated that XPF-ERCC1 has additional roles in transcription, specifically fine-tuning levels of key target genes through its recruitment of the CCCTC-binding factor (CTCF) chromatin organizer (Chatzinikolaou et al., 2017; Kamileri et al., 2012; Le May et al., 2010, 2012). Although, the endonuclease activities of both XPF-ERCC1 and XPG are required to recruit CTCF to chromatin in cell lines (Le May et al., 2012), XPG-catalytic-dead mice (*Xpg*^{E791A} and *Xpg*^{D811A}) develop normally and have normal life-spans (Shiomi et al., 2004; M. Tian et al., 2004). Therefore, the physiological relevance of XPF-ERCC1-mediated recruitment of CTCF remains unclear.

Mutations in XPD, XPB, XPG, XPF, ERCC1 and CSB cause CS, characterized by hypersensitivity to sun light, cachexic dwarfism, neurodegeneration and features of premature ageing. This complex phenotype cannot be explained by the sole loss of TC-NER, mostly because patients with mutations in *XPA* do not develop CS (DiGiovanna & Kraemer, 2012). Additionally, while *Xpa*^{-/-} and *Csb*^{m/m} mice fail to recapitulate CS, *Csb*^{m/m}*Xpa*^{-/-} and *Csb*^{m/m}*Xpc*^{-/-} double mutants show short life span, progressive neurodegeneration and cachectic dwarfism. The fact that loss of CSB can potentiate the phenotype of *Xpa*^{-/-} mice, already deficient for TC-NER, shows that CSB has redundant functions to NER. It is not known if the nuclease XPF-ERCC1 also operates with CSB in these additional functions. However, given the phenotypic overlap between *Csb*^{m/m}*Xpa*^{-/-} and *Ercc1*^{-/-} mice, and the lack of synergistic phenotype of *Xpa*^{-/-}*Fanca*^{-/-} mice shown in this study, we propose that a major component of the phenotype of XPF-ERCC1 deficiency results from joint inactivation of NER and CSB functions outside of NER, referred to here as transcription coupled repair (TCR) rather than NER and ICL repair (Figure 3.14).

The clinical heterogeneity of patients with NER deficiency has challenged the DNA repair field for decades. Only by careful genetic dissection can the contribution of the many factors involved begin to be understood. Here, we used clinically relevant mouse models to dissect two of the most comprehensively studied functions of XPF-ERCC1, its roles in NER and ICL repair, and show that deficiency in both these pathways does not result in liver, kidney and more severe haematopoietic defects. Further genetic dissection of the functions of XPF-ERCC1 will be required to address exactly how this key nuclease protects homeostasis in

multiple tissues. Additionally, identifying the nature of the DNA damage that necessitates XPF-ERCC1 *in vivo* remains an important question. This chapter identifies that the exquisite sensitivity of XPF-ERCC1 cells to formaldehyde can't be explained by FA deficiency alone. However, joint inactivation of NER and FA repair explains the additional sensitivity of FA cells to formaldehyde (Figure 3.07f). Formaldehyde has been shown to drive the phenotype of FA *in vivo* (Pontel et al., 2015) therefore, the next chapter will ask if the same is true for NER.

Chapter 4

Formaldehyde induced transcriptional stress drives Cockayne Syndrome

Cells that lack XPF-ERCC1 are exquisitely sensitive to formaldehyde. Part of this sensitivity can be explained by deficiency in FA repair, which has been shown to protect against formaldehyde *in vitro* and *in vivo* (Pontel et al., 2015; Rosado et al., 2011). The additional sensitivity of XPF-ERCC1 cells to formaldehyde can be explained by its role in NER *in vitro* (Figure 3.07f). This chapter will probe further into which branch of NER is required for the cellular protection against formaldehyde and address whether endogenous formaldehyde accumulates *in vivo* to drive NER phenotypes.

4.1 Formaldehyde is toxic to cells lacking TC-NER

Human $XPA^{-/-}$ HAP1 cells are sensitive to formaldehyde, additionally, $XPA^{-/-} FANCL^{-/-}$ cells show an increased sensitivity compared to either $XPA^{-/-}$ or $FANCL^{-/-}$ cells (Figure 3.07f). This suggests that NER is required for cellular protection against formaldehyde in a manner that is independent of FA repair. Interestingly, the closely related aldehyde acetaldehyde only shows toxicity in cells lacking FA repair and not cells deficient in NER (Figure 3.07e). We therefore set out to test whether TC-NER, GG-NER or both are required for cellular protection against formaldehyde.

In order to do this, transformed mouse embryonic fibroblast (tMEF) lines that lack GG-NER ($Xpc^{-/-}$), TC-NER ($Csb^{m/m}$), or both ($Xpa^{-/-}$), alone or in combination with the formaldehyde-detoxifying enzyme ADH5 were derived from mice. We performed timed matings of mice that were $NER^{+/-} Adh5^{+/-}$ and harvested embryos at day E13.5 to derive primary MEF cultures. Cells with the desired genotypes were transformed with the SV40 large T antigen by retroviral transduction (Crossan et al., 2011).

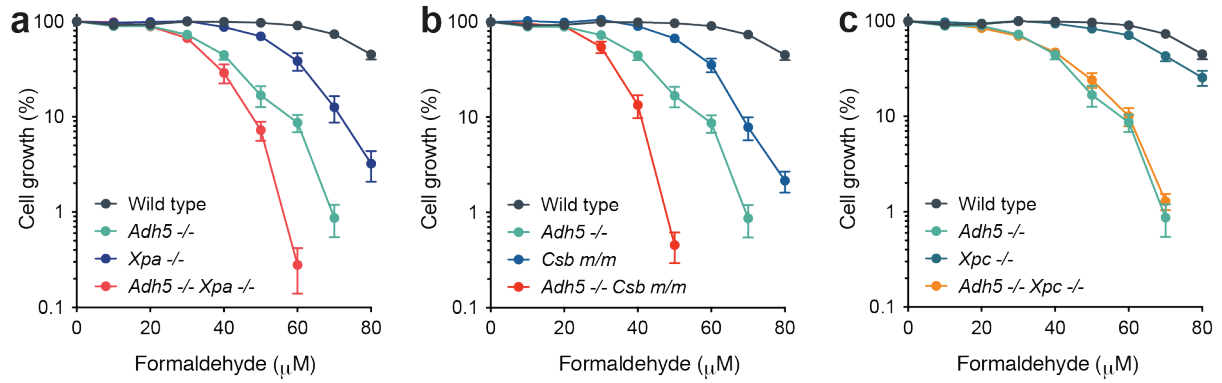


Figure 4.01 – TC-NER deficient tMEF are hypersensitive to formaldehyde

a-c) Cytotoxicity of formaldehyde in tMEF cell lines deficient in NER and formaldehyde detoxification (triplicate experiments, data shown as mean and s.e.m)

To test tMEFs for cellular sensitivity they were assessed for growth inhibition by culturing cells in media supplemented with increasing concentrations of formaldehyde for 4 days before adding the MTS reagent. Once added the MTS reagent detects live cells via colorimetric changes which can be captured by measuring absorbance at 492nm on a spectrophotometer.

We found that *Xpa*^{-/-} and *Csb*^{m/m} cells were hypersensitive to formaldehyde (Figure 4.01a-b); in contrast *Xpc*^{-/-} cells were comparable to wild type controls (Figure 4.01c). Furthermore, combined ablation of *Adh5* conferred additional formaldehyde sensitivity when either *Xpa* or *Csb* were inactivated (Figure 4.01a-b) but not *Xpc* (Figure 4.01c). This indicated that both formaldehyde detoxification and TC-NER (but not GG-NER) are required to protect cells against formaldehyde toxicity.

CSB is also involved in the repair of oxidative damage independently of its role in TC-NER (Ranes et al., 2016). Ubiquitylation of CSB at lysine 991 is required for the repair of oxidative damage, we therefore set out to test if this ubiquitylation site was required for protection against formaldehyde toxicity. We complemented *Csb* deficient cells with either wild type *Csb* or a separation of function point-mutant, which has intact TC-NER but is defective in oxidative damage repair (K991R). For this, 2x FLAG tag cDNA constructs of WT and K991R CSB were cloned into plox-BSR and transfected into *Csb*^{m/m} and *Adh5*^{-/-} *Csb*^{m/m} tMEF cell lines. Positive clones were selected by using blasticidin and screened by Western blotting probing for the FLAG epitope tag. Similar to what was previously reported for UV exposure (Ranes et al., 2016), we found that the CSB K991R mutant was able to rescue the hypersensitivity to formaldehyde (Figure 4.02a-c).

These data, in addition to the requirement for XPA, which operates downstream of CSB in TC-NER, indicate that it is likely to be the role of CSB in TC-NER leads to cellular protection against formaldehyde.

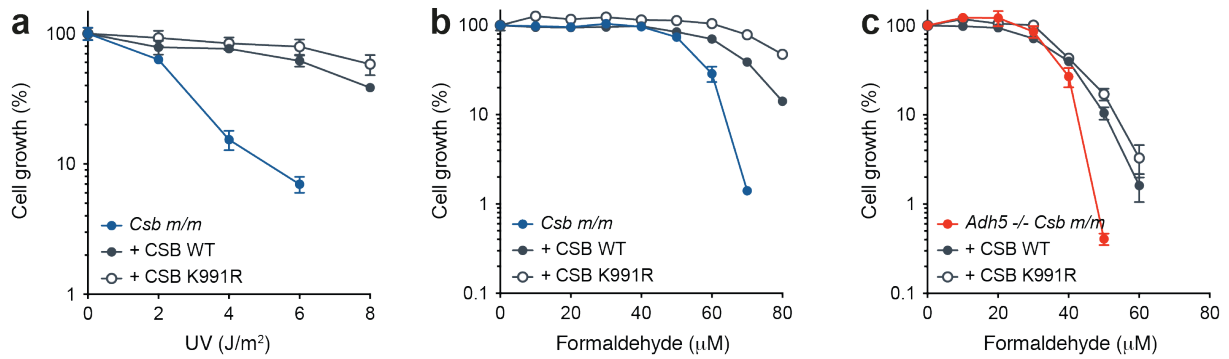


Figure 4.02 – Formaldehyde toxicity is rescued in CSB K991R mutant cells
a-c) Cytotoxicity of UV (a) and formaldehyde (b) in *Csb^{m/m}* (a,b) or *Adh5^{-/-} Csb^{m/m}* (c) tMEF cell lines complemented with either WT or K991R CSB. Data plotted as mean and s.e.m; experiments performed in triplicate.

4.2 Formaldehyde triggers the ubiquitination and degradation of RNAPII

Actively transcribing RNAPII (Ilo) stalls when it encounters transcription-blocking lesions in the DNA template strand leading to a global shutdown of transcription. The largest RNAPII subunit, RPB1, is rapidly poly-ubiquitylated and degraded. Following Ilo degradation, the non-transcribing RNAPII (Ila) then begins transcribing, becoming Ilo and depleting the pools of Ila (Figure 4.04a) (Tufegdžić Vidaković et al., 2020; M. D. Wilson et al., 2013). This has been demonstrated in human HEK293 cells in response to transcription-blocking damage caused by UV irradiation (Tufegdžić Vidaković et al., 2020).

To determine if formaldehyde elicits the same transcription-blocking response, we first sought to confirm our observation that ADH5 and CSB maintain resistance to formaldehyde in HEK293 cells. This was achieved using CRISPR/Cas9 mediated gene editing with previously established small guide RNAs cloned into pX458. Two days post transfection, GFP positive cells were FACS cell sorted into 96-well plates and cultured for 12 days, before screening for protein loss by western blot (Figure 4.03a). Using MTS cytotoxicity assays, cellular sensitivity to UV and formaldehyde were confirmed (Figure 4.03b-c). This revealed that ADH5 CSB DKO HEK293 cells also show a genetic interaction in response to formaldehyde.

Next, to determine if formaldehyde triggers poly-ubiquitylation of RNAPII, we exposed wild type HEK293 cells to UV or formaldehyde. Ubiquitylated proteins from these cell extracts were then enriched using GST-Dsk2 affinity resin followed by Western blotting to detect ubiquitylated RNAPII. GST-Dsk2 affinity resin was prepared by isolating Dsk2 protein from overexpression in *E. coli* and combining with glutathione-coated beads. Dsk2 is a yeast protein that has a high affinity for ubiquitin, allowing for the enrichment of ubiquitylated proteins (Tufegdžić Vidaković et al., 2019). We found that formaldehyde exposure stimulates the poly-ubiquitylation (Figure 4.04b) and degradation (Figure 4.04c) of RNAPII in a dose-dependent manner. After recovery (24 hours) its expression was restored in a similar way to UV exposure (Figure 4.04c).

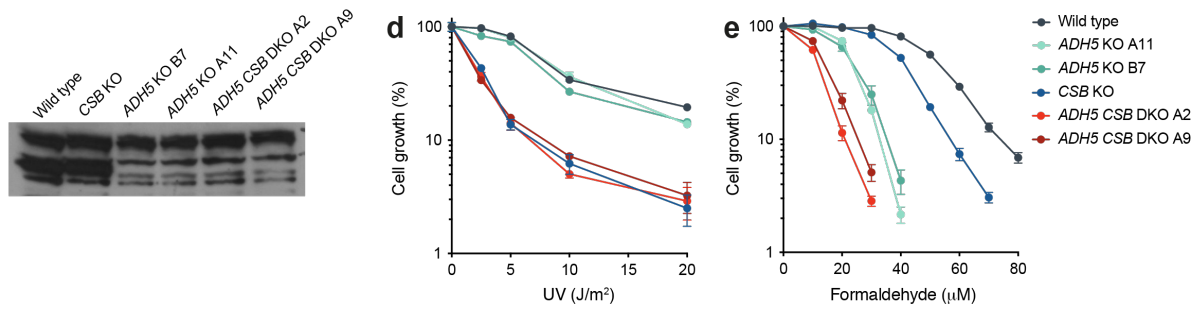


Figure 4.03 – TC-NER deficient HEK293 cells are hypersensitive to formaldehyde

a) ADH5 Western Blot from HEK293 cell lines. **b-c)** Cytotoxicity of formaldehyde and UV in generated HEK293 lines (triplicate experiments, data shown as mean and s.e.m)

Finally, we tested if the stability of RNAPII was reduced after exposure to low concentrations of formaldehyde in *ADH5^{-/-}CSB^{-/-}* cells (Figure 4.04d). We found that in the absence of CSB and ADH5, RNAPII was much more sensitive to degradation in response to formaldehyde. In summary, both detoxification and CSB protect cells against formaldehyde toxicity, and increased formaldehyde exposure can lead to transcription-blocking DNA damage, triggering RNAPII poly-ubiquitylation and degradation.

4.3 Generation of mice lacking NER and ADH5

CS is a catastrophic illness in humans, characterised by profound cachexia, progressive neurological impairment and kidney failure (Kubota et al., 2015; Laugel, 2013; Nance & Berry, 1992; B. T. Wilson et al., 2016). Perplexingly, CSA or CSB deficient mice have very subtle phenotypes and normal longevity (G. T. van der Horst et al., 1997; G. T. J. van der Horst et al., 2002). To test if sufficient formaldehyde is generated endogenously to necessitate repair by NER, we inter-crossed mice that lacked ADH5 with those lacking NER components (*Xpa*, *Xpc* or *Csb*).

In agreement with previous data, *NER*^{+/-} inter-crosses yielded *NER*^{-/-} mice at expected Mendelian ratios (Figure 4.05a). However, in the absence of ADH5, we observed that both *Adh5*^{-/-}*Xpa*^{-/-} and *Adh5*^{-/-}*Csb*^{m/m} mice were significantly underrepresented (7.5% and 5.4%, respectively, instead of 25%) whereas *Adh5*^{-/-}*Xpc*^{-/-} mice were born at the expected ratio (Figure 4.05b). This, in addition to the cellular hypersensitivity of *Adh5*^{-/-}*Csb*^{m/m} and *Adh5*^{-/-}*Xpa*^{-/-} cells to formaldehyde, shows that *Adh5* genetically interacts with genes required for TC-NER but not GG-NER. Additionally, we noted that if the mothers were formaldehyde-detoxification proficient (*Adh5*^{+/-}), then the frequency of *Adh5*^{-/-}*Csb*^{m/m} mice born was partially rescued (Figure 4.05c). This indicates that maternal formaldehyde detoxification is sufficient to preserve the development of *Adh5*^{-/-}*Csb*^{m/m} embryos.

4.4 *Adh5*^{-/-}*Csb*^{m/m} mice display characteristics of human CS

Failure to thrive is a prominent yet mysterious aspect of CS and is characterized by reduced weight gain after birth and a reduction in subcutaneous fat (Nance & Berry, 1992). In order to monitor the growth of *Adh5*^{-/-}*Csb*^{m/m} mice, males and females were weighed weekly and also subjected to echo-MRI at 3 and 12 months of age to monitor fat content. This revealed that *Adh5*^{-/-}*Csb*^{m/m} mice were smaller with a marked, age-dependent reduction in body fat. Intriguingly, both the size difference and leanness were much more pronounced in males than females (Figure 4.06a,b,d). This reduction in mass was not observed in *Adh5*^{-/-}*Xpc*^{-/-} mice and subtle in *Adh5*^{-/-}*Xpa*^{-/-} males; indeed, these two lines were phenotypically normal (Figure 4.06c). Therefore, *Adh5*^{-/-}*Csb*^{m/m} mice display a failure to thrive phenotype reminiscent of human CS.

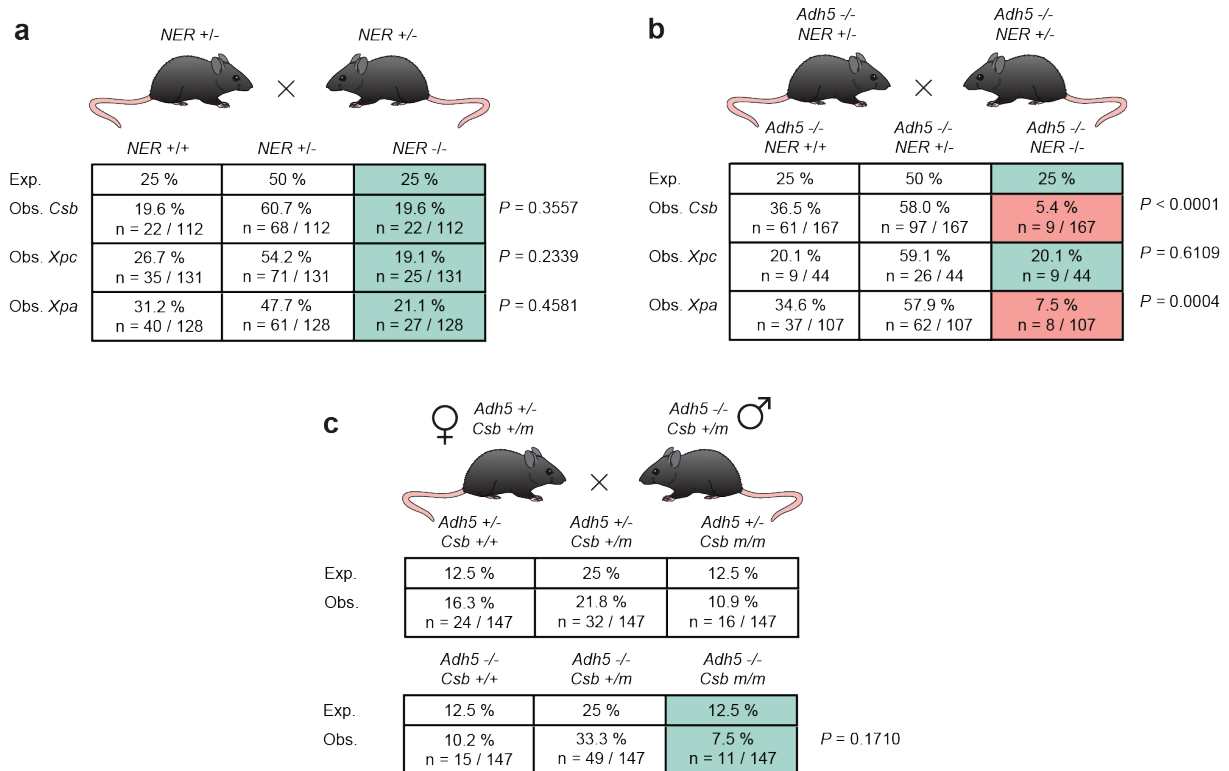


Figure 4.05 – *Adh5*^{-/-} *Csb*^{m/m} mice are born at sub-Mendelian ratios

a) Ratios of pups from *Csb*^{+/-}, *Xpc*^{+/-} and *Xpa*^{+/-} crosses showing that homozygous mice are born at Mendelian ratios (P calculated by Chi-squared test) **b)** Ratios of pups born from *Adh5*^{-/-}*Csb*^{+/-}, *Adh5*^{-/-}*Xpc*^{+/-} and *Adh5*^{-/-}*Xpa*^{+/-} crosses showing that both *Adh5*^{-/-}*Csb*^{m/m} and *Adh5*^{-/-}*Xpa*^{-/-} pups are born at sub-Mendelian ratios (P calculated by Chi-squared test). **c)** Ratios of pups born from *Adh5*^{+/-}*Csb*^{+/-} and *Adh5*^{-/-}*Csb*^{+/-} crosses showing the ratio of *Adh5*^{-/-}*Csb*^{m/m} pups is partially rescued when the mother is aldehyde-detoxification proficient (*Adh5*^{+/-} instead of *Adh5*^{-/-} in b, P calculated by Chi-squared test). For a, b, and c, mice were genotyped between 2-3 weeks of age.

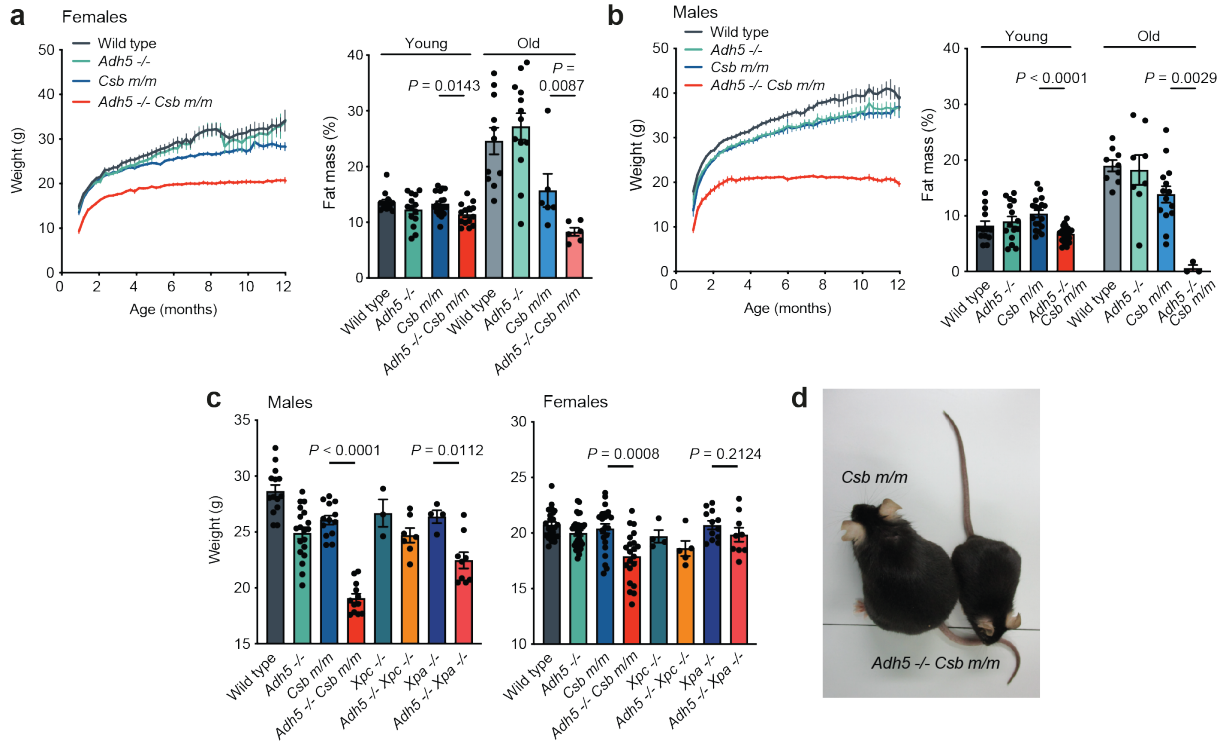


Figure 4.06 – *Adh5*^{-/-} *Csb*^{m/m} mice show a failure to thrive

a-b) Growth curves of male and female mice based on weekly weights. Data shown as mean and s.e.m. *n* = 18, 15, 18 and 20 for males and *n* = 14, 14, 18 and 14 for females. Along with fat mass from EchoMRI performed at 11 weeks (young) and 53 weeks (old). *P* calculated by two-sided Mann-Whitney test; data shown as mean and s.e.m.; *n* = 13, 15, 18, 19, 9, 8, 14 and 3 for males and *n* = 13, 14, 18, 14, 11, 13, 6 and 6 from females left to right. **c)** Weights of adult male and female mice at 8 weeks of age (Data shown as mean and s.e.m.; *P* calculated by two-sided Mann-Whitney test; *n* = 14, 19, 13, 12, 4, 9, 3, 7 for males left to right and 24, 30, 22, 21, 12, 9, 4, 5 for females left to right). **d)** Image of *Csb*^{m/m} and *Adh5*^{-/-} *Csb*^{m/m} littermates at 12 months of age.

CS patients display progressive neurological deficits that manifest within the first few years of life and lead to cerebellar ataxia, tremors, intellectual disability and in some cases seizures (Nance & Berry, 1992; B. T. Wilson et al., 2016). We sought to determine whether or not *Adh5^{-/-}Csb^{m/m}* mice develop any neurological defects that are present in CS. To do this we performed cerebellar ataxia scoring at regular intervals as the mice aged, a method that has been successfully employed to characterise the neurological deficits in *Ercc1^{-/-}* mice (Fuhrmann-Stroissnigg et al., 2017). This revealed that *Adh5^{-/-}Csb^{m/m}* mice developed ataxia, hind limb claspings and kyphosis after approximately 6 months (Figure 4.07a-c). X-ray scans of *Adh5^{-/-}Csb^{m/m}* mice and controls confirm the extent of the kyphosis (Figure 4.07d). Finally, *Adh5^{-/-}Csb^{m/m}* mice showed age-related decline in grip strength performance (Figure 4.07e). Taken together these data indicate that *Adh5^{-/-}Csb^{m/m}* mice develop progressive neurological deficits similar to those described in *Ercc1^{-/-}* mice and human CS patients.

CS patients develop retinal degeneration (Nance & Berry, 1992). To characterise the retinas of *Adh5^{-/-}Csb^{m/m}* mice we performed ophthalmoscope analysis and optical coherence tomography (OCT). These experiments did indeed reveal the presence of abnormal retinas, particularly in *Adh5^{-/-}Csb^{m/m}* male mice that had a mottled, aged appearance. In addition, the retinal layers in *Adh5^{-/-}Csb^{m/m}* mice appeared much thinner when observed by OCT, indicating a degree of degeneration (Figure 4.08 a-c).

To investigate the basis of the neurological phenotypes observed during the *in vivo* testing, the brains of aged *Adh5^{-/-}Csb^{m/m}* mice were characterised. The gross appearance of the brains at necropsy was similar although *Adh5^{-/-}Csb^{m/m}* brains appeared to have a smaller cerebellum (Figure 4.09a). This was supported by histological sections of the cerebellum that revealed a reduction in overall size (Figure 4.09b). The mass of *Adh5^{-/-}Csb^{m/m}* brains were also significantly reduced compared to littermate controls, furthermore, we observed an age-dependence in the decline in brain mass (Figure 4.09c). In response to brain injury microglial cells become activated, indeed human CS brain pathology shows an increase in these tissue-resident macrophages (Nance & Berry, 1992). After perfusion of *Adh5^{-/-}Csb^{m/m}* mice and controls, brains were sectioned and stained for the presence of activated microglia using fluorescent antibodies against the activated microglial marker MAC2. *Adh5^{-/-}Csb^{m/m}* brains showed increased numbers of MAC2+ cells (Figure 4.09d-e), particularly in older mice, indicative of a neuroinflammatory response. Taken together these data suggest that there is ongoing damage within the brain of *Adh5^{-/-}Csb^{m/m}* mice that triggers cerebellar atrophy and inflammation, this is consistent with the behavioral deficits observed in these mice and also with brain pathologies in human CS.

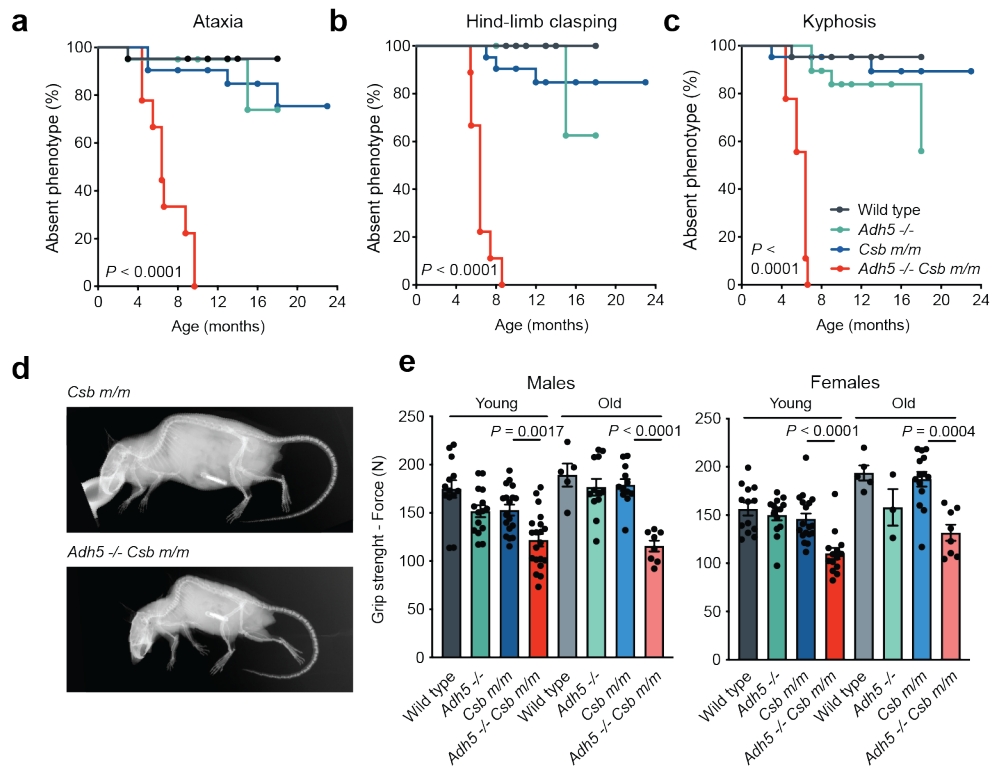


Figure 4.07 – *Adh5^{-/-}Csb^{m/m}* mice display behavioral deficits

a-c) Age of onset plots for ataxia, hind limb clasp and kyphosis. P calculated by Mantel-Cox logrank test, n = 21, 19, 22 and 9. **d)** Representative x-rays of *Csb^{m/m}* and *Adh5^{-/-}Csb^{m/m}* mice at 1 year of age showing kyphosis in the *Adh5^{-/-}Csb^{m/m}* mouse. **e)** Bar graph of grip strength for young (3 months) and old (1 year) mice, determined by placing all four limbs on a grid attached to a force gauge. P calculated by two-sided Mann-Whitney test, data shown as mean and s.e.m.; n = 13, 15, 18, 20, 5, 12, 12 and 8 for males left to right and 13, 14, 18, 14, 5, 3, 14 and 8 for females left to right.

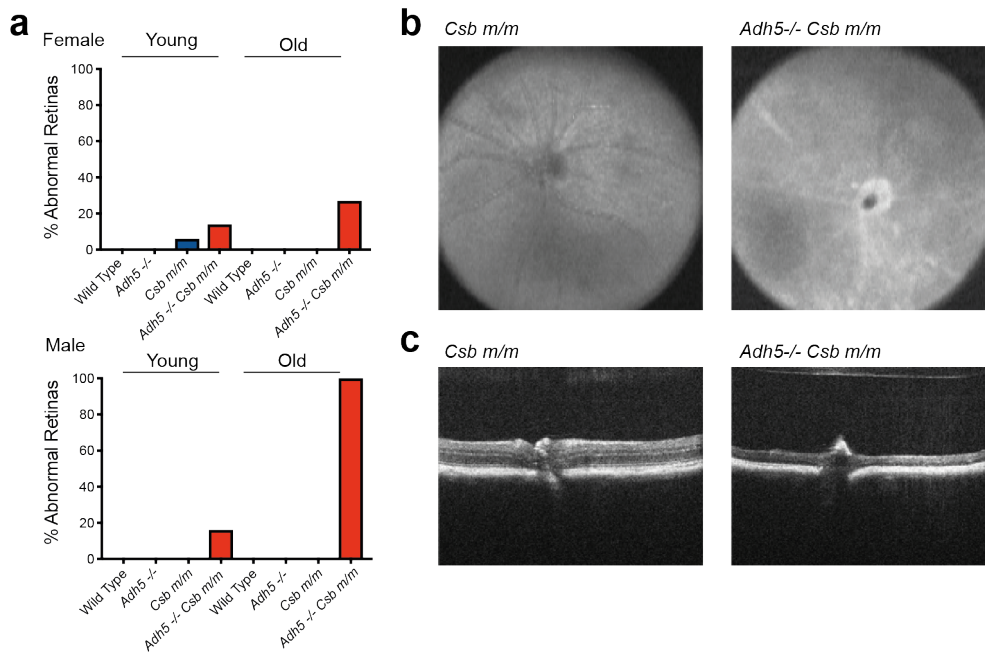


Figure 4.08 – *Adh5^{-/-} Csb^{m/m}* mice have abnormal retinas

a) Bar chart indicating the percentage of mice with abnormal retinas when assessed with an ophthalmoscope ($n=12, 17, 13, 13, 10, 14, 12, 8$ for females and $15, 17, 14, 17, 10, 16, 11, 4$ for males). **b-c)** Images taken of the retina and the retina layers during optical coherence tomography ($n=3$).

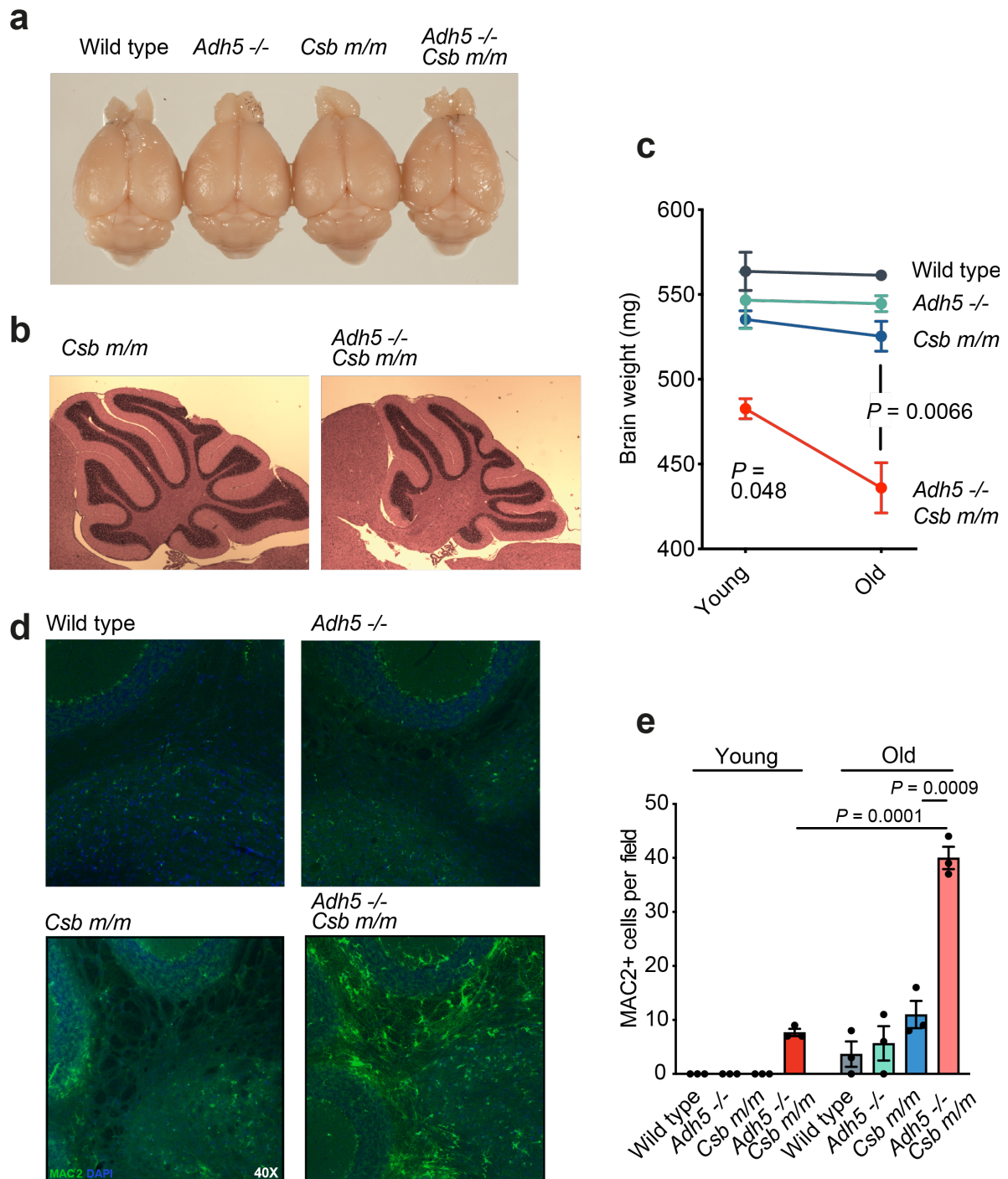


Figure 4.09 – *Adh5*^{-/-} *Csb*^{m/m} mice display brain abnormalities

a) Representative photographs of *Adh5*^{-/-}*Csb*^{m/m} brains alongside controls. **b)** Representative H&E stained sections of *Csb*^{m/m} and *Adh5*^{-/-}*Csb*^{m/m} cerebellum revealing smaller cerebellum in *Adh5*^{-/-}*Csb*^{m/m}. **c)** Brain weights of mice taken at 3 months (young) and 18 months (old). P calculated by two-tailed Student's t-test; data shown as mean and s.e.m., *n*=3 mice. **d)** Representative immunofluorescence images of the cerebellum of *Csb*^{m/m} and *Adh5*^{-/-}*Csb*^{m/m} mice stained with MAC2 and DAPI at 40x magnification. **e)** Quantification of the number of MAC2+ cells per field in young (3 month) and old (18 month) mice. P calculated by two-tailed Student's t-test; data shown as mean and s.e.m., *n* = 3 mice.

CS is a premature aging syndrome that leads to premature death, to see if our model reflects this, we aged *Adh5^{-/-}Csb^{m/m}* and control mice. We observed that *Adh5^{-/-}Csb^{m/m}* mice have a shortened lifespan compared to wild type and *Csb^{m/m}* mice. Whilst the reduction in lifespan is comparable to *Adh5^{-/-}* mice, there is striking difference in the cause of death in *Adh5^{-/-}Csb^{m/m}* (Figure 4.10a). The majority of *Adh5^{-/-}* mice succumb to liver and lymphoid malignancies in agreement with previous reports (Wei et al., 2010), in contrast *Adh5^{-/-}Csb^{m/m}* mice display a progressive decline in their overall body condition and ultimately succumb to renal failure (Figure 4.10b-d). To arrive at the diagnosis of renal failure we first noted that most *Adh5^{-/-}Csb^{m/m}* mice showed small nodular kidneys at necropsy (Figure 4.11a-b), and found elevated serum urea and creatinine, biochemical markers of the kidney dysfunction (Figure 4.11c).

Kidney failure has been reported as a cause of death in CS patients and has been the subject of recent studies, however, the reason the kidney fails in CS is not clear (Kubota et al., 2015; Stern-Delfils et al., 2020). To validate our conclusion of renal failure as a cause of death in *Adh5^{-/-}Csb^{m/m}* mice we sought the advice of an expert histopathologist. The conclusion, derived from H&E sections of terminal kidney samples supported the notion that the changes present were consistent with overlapping features of ongoing kidney damage due to toxic injury to the proximal tubules and end-stage renal failure (Figure 4.11d). However, end-stage kidney failure results in numerous secondary pathological changes within the kidney. In order to understand the primary cellular target of formaldehyde toxicity we expanded our histological analysis to several time points, young, middle aged and terminal. This revealed that young (3 months) *Adh5^{-/-}Csb^{m/m}* kidneys had only scattered, focal, very mild chronic inflammation in the cortical interstitium, consistent with focal tubule loss. Middle-aged (1 year old) kidneys showed a mild degree of renal damage in the form of patchy mild chronic interstitial fibrosis associated with tubular atrophy and mild chronic inflammatory infiltration (Figure 4.12a-c). The absence of any glomerular changes prior to end stage kidney failure is consistent with the lack of protein in the urine (Figure 4.12d) and suggests the glomerular changes observed in the end stage kidneys are secondary to the tubular pathology.

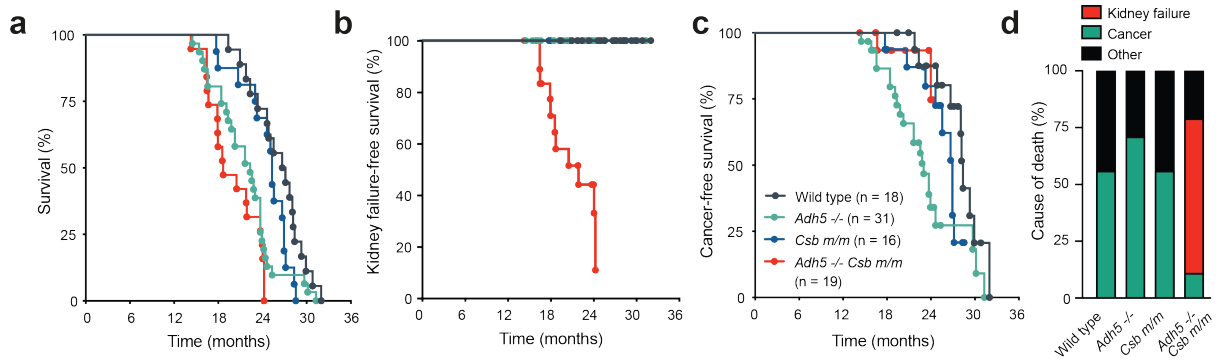


Figure 4.10 – *Adh5*^{-/-} *Csb*^{m/m} cause of death

a) Kaplan Meier curve of *Adh5*^{-/-} *Csb*^{m/m} and control mice **b)** Kidney failure-free survival of wild type, *Adh5*^{-/-}, *Csb*^{m/m} and *Adh5*^{-/-} *Csb*^{m/m} mice (n = 18, 31, 26 and 19) **c)** Cancer-free survival of wild type, *Adh5*^{-/-}, *Csb*^{m/m} and *Adh5*^{-/-} *Csb*^{m/m} mice (n = 18, 31, 26 and 19) **d)** Bar chart indicating the cause of death for wild type, *Adh5*^{-/-}, *Csb*^{m/m} and *Adh5*^{-/-} *Csb*^{m/m} mice (n = 18, 31, 16 and 19).

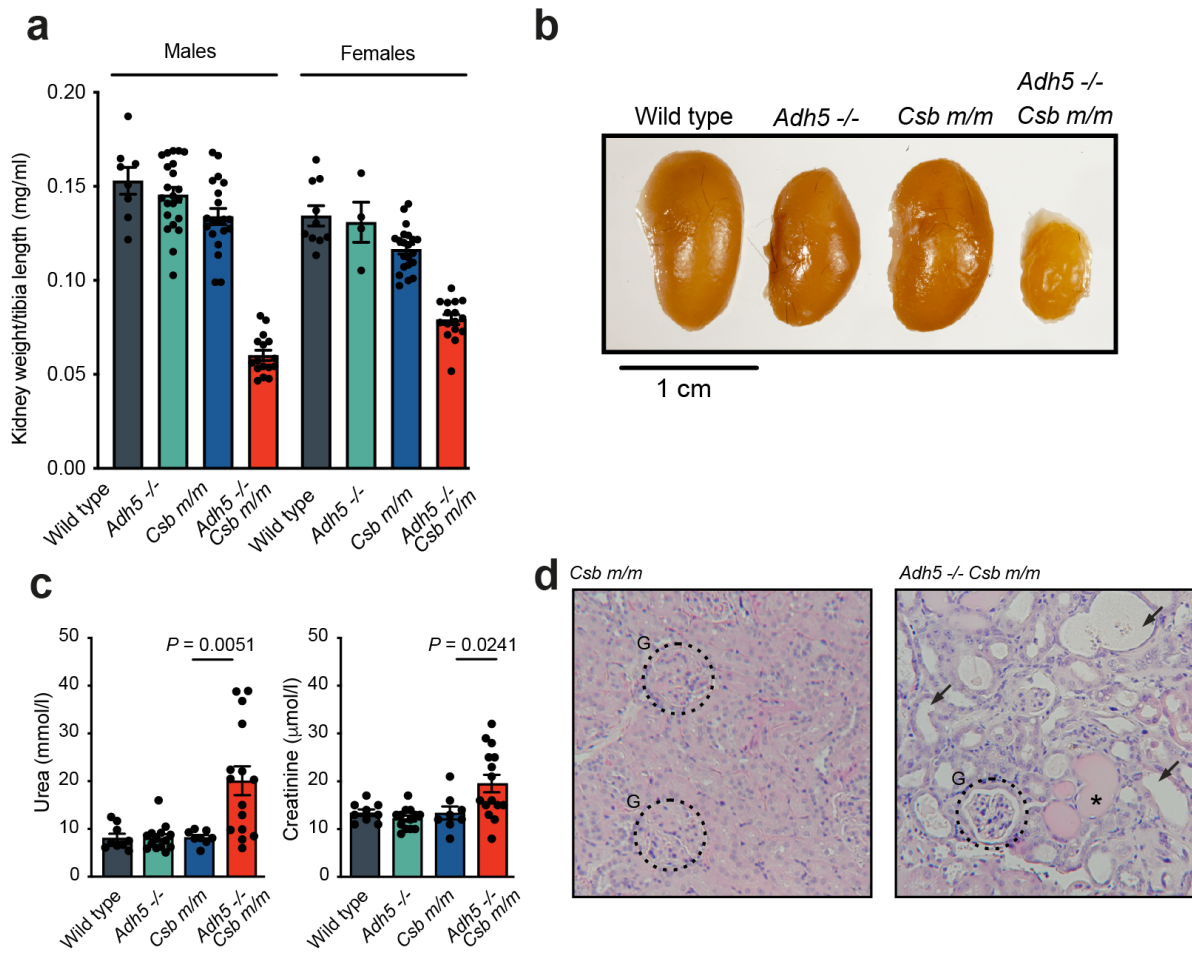


Figure 4.11 – *Adh5*^{-/-}*Csb*^{m/m} mice succumb to kidney failure

a) Kidney weights made relative to tibia length for male and female mice (n=9, 20, 18, 13, 9, 4, 18, 12 from left to right) **b)** Representative image of kidneys from terminal mice taken after 24 hours of fixation. **c)** Terminal serum urea and creatinine levels (P calculated by two-sided Mann-Whitney test; data shown as mean and s.e.m.; n = 9, 14, 8 and 15 mice) **d)** Representative H&E stained sections of kidney from *Csb*^{m/m} and *Adh5*^{-/-}*Csb*^{m/m} mice, G indicates glomeruli and arrows indicate atrophic tubules, with tubular thyroidisation evidence (*).

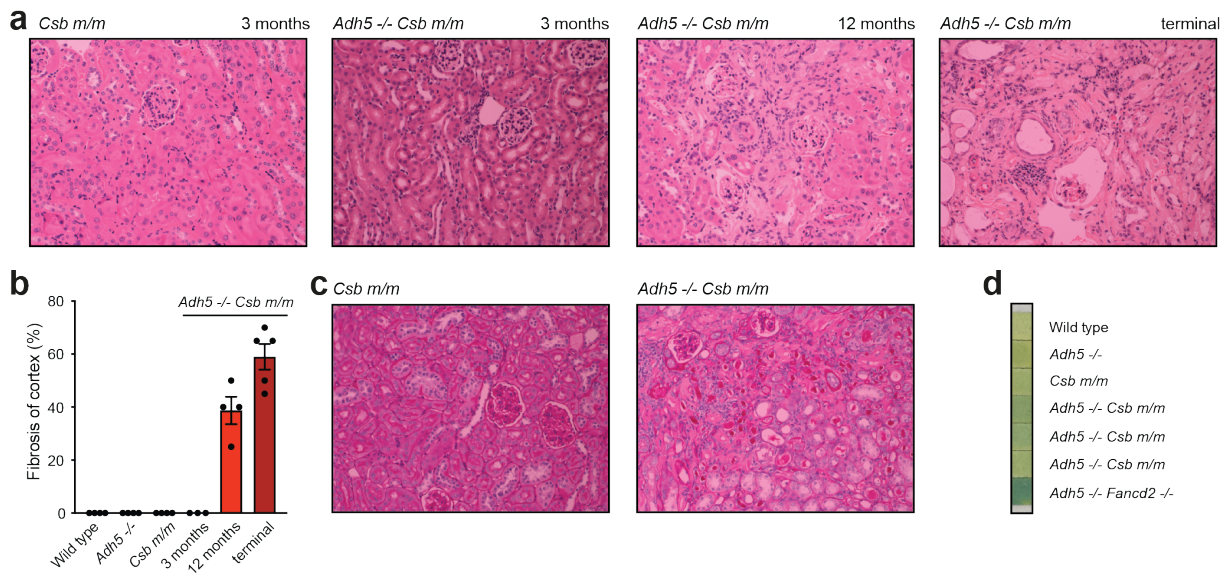


Figure 4.12 – Progressive kidney dysfunction in *Adh5^{-/-} Csb^{m/m}* mice

a) Representative H&E stained sections of kidney from *Csb^{m/m}* and *Adh5^{-/-} Csb^{m/m}* mice at sequential timepoints. **b)** Bar chart of the percentage of fibrosis in the cortex of H&E stained kidney sections at sequential time points in *Adh5^{-/-} Csb^{m/m}* and terminal controls. **c)** Representative PAS stained sections of kidney showing intratubular casts from *Csb^{m/m}* and *Adh5^{-/-} Csb^{m/m}* terminal mice. **d)** Urine obtained from indicated mice were tested for the presence of proteinuria by multistix 10SG.

The kidneys are an important source of erythropoietin (EPO), a hormone that acts to stimulate red blood cell production in the bone marrow. In the presence of excessive kidney dysfunction, insufficient EPO is released to maintain erythropoiesis, resulting in anemia. More specifically, the circulating red blood cells in EPO deficiency remain the same size (normocytic) and have a normal red colour (normochromic). Blood samples from aged *Adh5*^{-/-} *Csb*^{m/m} mice that have kidney failure indicate that these mice also present with normocytic normochromic anaemia (Figure 4.13a).

Human CS patients display liver dysfunction with transaminases typically being mildly elevated (B. T. Wilson et al., 2016). As discussed in chapter 3, while *Csb*^{m/m} mice have normal liver function, some of the more severe XPCS mouse models display signs of liver dysfunction with *Ercc1*^{-/-} mice succumbing to liver failure (Figure 3.02a). Detailed analysis of *Adh5*^{-/-} *Csb*^{m/m} mice at necropsy did not reveal evidence of malignancies in their livers as is typical of *Adh5*^{-/-} mice. However, analysis of serum biochemistry markers of liver dysfunction revealed elevation of alkaline phosphatase and alanine transaminase along with a reduction in albumin in *Adh5*^{-/-} *Csb*^{m/m} serum, suggesting a degree of liver injury (Figure 4.14a). In support of this we also observed an age-related increase in polyploid liver cells in *Adh5*^{-/-} *Csb*^{m/m} mice which was confirmed by liver H&E staining (Figure 4.14b-c). These data suggest that while the kidney fails in these mice, the liver is also affected.

Taken together, these data indicate that *Adh5*^{-/-} *Csb*^{m/m} mice display the hallmark features of human CS, a failure to thrive, neurological deficits and organ dysfunction. Ultimately these mice succumb to kidney failure, which is associated with anaemia, and show a reduced predisposition towards malignancies compared with *Adh5*^{-/-} mice.

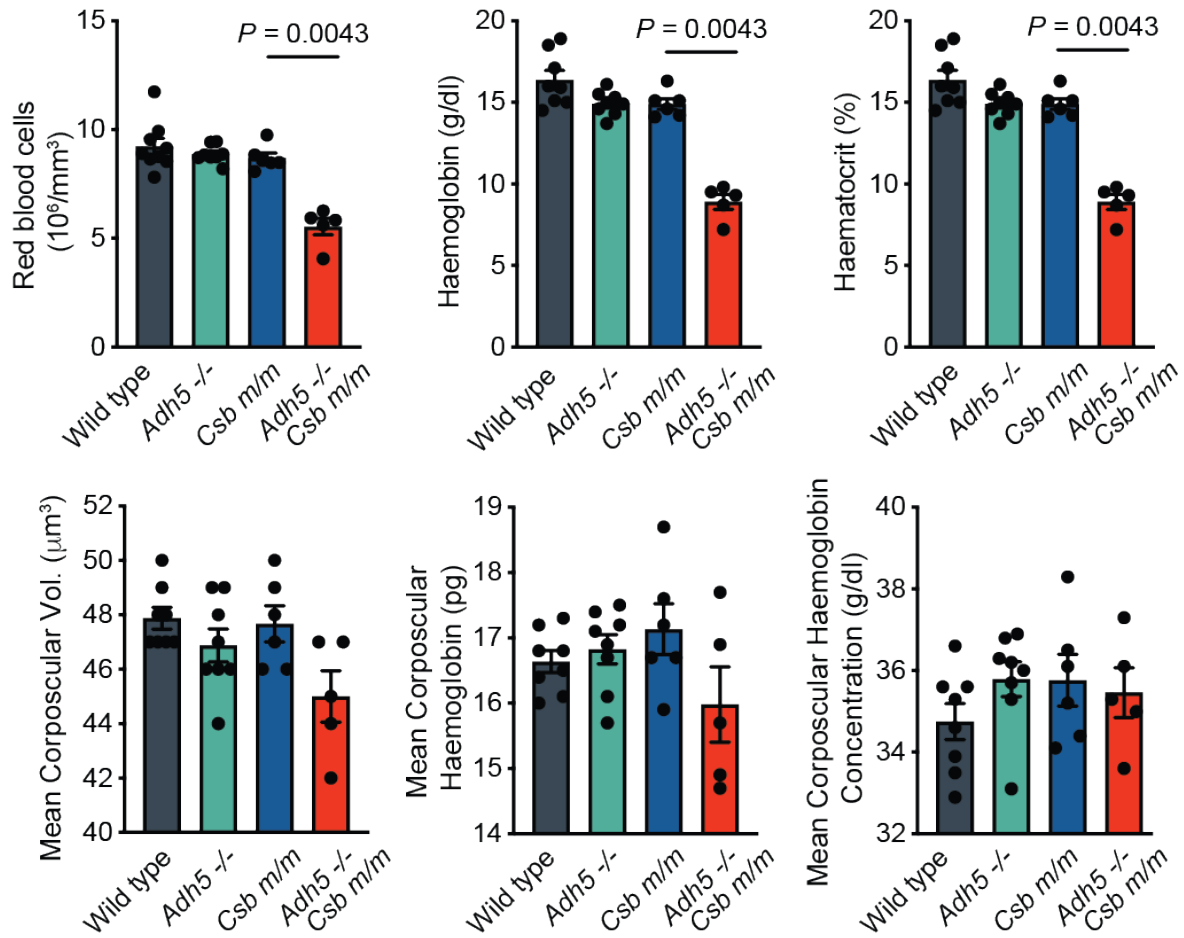


Figure 4.13 – *Adh5*^{-/-} *Csb*^{m/m} mice display normocytic normochromic anaemia

Peripheral blood counts from aged *Adh5*^{-/-} *Csb*^{m/m} mice with controls data shown as mean and s.e.m *P* calculated by two-sided Mann-Whitney test (n=8, 8, 6, 6).

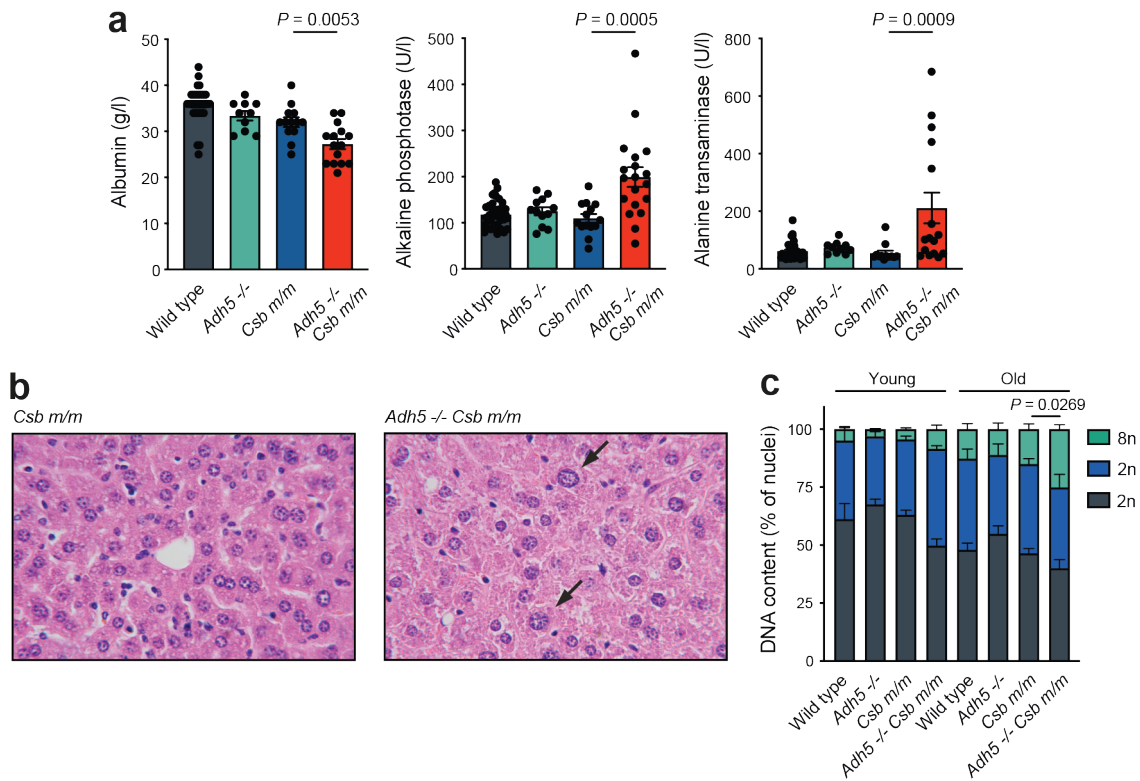


Figure 4.14 – *Adh5*^{-/-} *Csb*^{m/m} mice display liver dysfunction

a) Terminal serum measurements of albumin, alkaline phosphatase and alanine transaminase. *P* calculated by two-sided Mann-Whitney test; data show as mean and s.e.m.; *n* = 33, 10, 13 and 16. **b)** Representative H&E-stained sections of liver from age-matched *Csb*^{m/m} and *Adh5*^{-/-} *Csb*^{m/m} mice, arrows indicate cells with enlarged nuclei. **c)** Quantification of hepatocyte nuclear DNA content in young (3 month) and old (18 month) mice. *P* calculated by two-sided Student's *t*-test for the content of 8n nuclei; data shown as mean and s.e.m.; *n* = 3 mice.

4.5 *Adh5*^{-/-}*Xpa*^{-/-} mice do not show evidence of a CS phenotype

Patients with *XPA* mutations do not develop CS, there is however a degree of phenotypic overlap with the development of progressive neurological impairment in *XPA* patients. *XPA* is required for TC-NER and for cellular protection against formaldehyde (Figure 4.01a). Additionally, we observe a requirement for *XPA* in normal development in an *Adh5* deficient background (Figure 4.05b). However, the growth failure was subtle in *Adh5*^{-/-}*Xpa*^{-/-} mice indicating that CSB and *XPA* are not equivalent. This suggests that loss of *Adh5* could not precipitate a CS phenotype in the absence of *XPA*. However, the CS phenotype is progressive. Therefore, a cohort of *Adh5*^{-/-}*Xpa*^{-/-} mice were aged to monitor the appearance of age-related phenotypes like neurodegeneration or kidney dysfunction in order to determine if they developed signs of CS, (Figure 4.15a). Unlike *Adh5*^{-/-}*Csb*^{m/m} mice (Figure 4.07), we did not observe ataxia, hind limb claspings and kyphosis in *Adh5*^{-/-}*Xpa*^{-/-} mice. These mice ultimately succumbed to cancers in a similar fashion to *Adh5*^{-/-} mice (Figure 4.15b). Additionally, there was no biochemical evidence of kidney dysfunction in terminal blood samples from these mice (Figure 4.15c-d).

4.6 Endogenous acetaldehyde does not reveal CS in mice

Previously we did not observe hypersensitivity of NER deficient HAP1 cells to acetaldehyde (Figure 3.07e), however this is somewhat unexpected given the similarity to formaldehyde. Given the widespread consumption of alcohol, a precursor to acetaldehyde, and the prevalence of inactivating *ALDH2* polymorphism in the human population, we decided to test whether accumulation of acetaldehyde could drive the CS phenotype *in vivo* by generating mice deficient in acetaldehyde detoxification (*Aldh2*) and CSB. However, in agreement with the HAP1 cytotoxicity data, *Aldh2*^{-/-}*Csb*^{m/m} mice grew to normal size (Figure 4.16a) did not display a reduced lifespan (Figure 4.16b) or show any signs of kidney dysfunction (Figure 4.16c). These data suggest that CSB is not required to protect against endogenous acetaldehyde and that in contrast to formaldehyde, the closely related aldehyde acetaldehyde does not drive the CS phenotype *in vivo*.

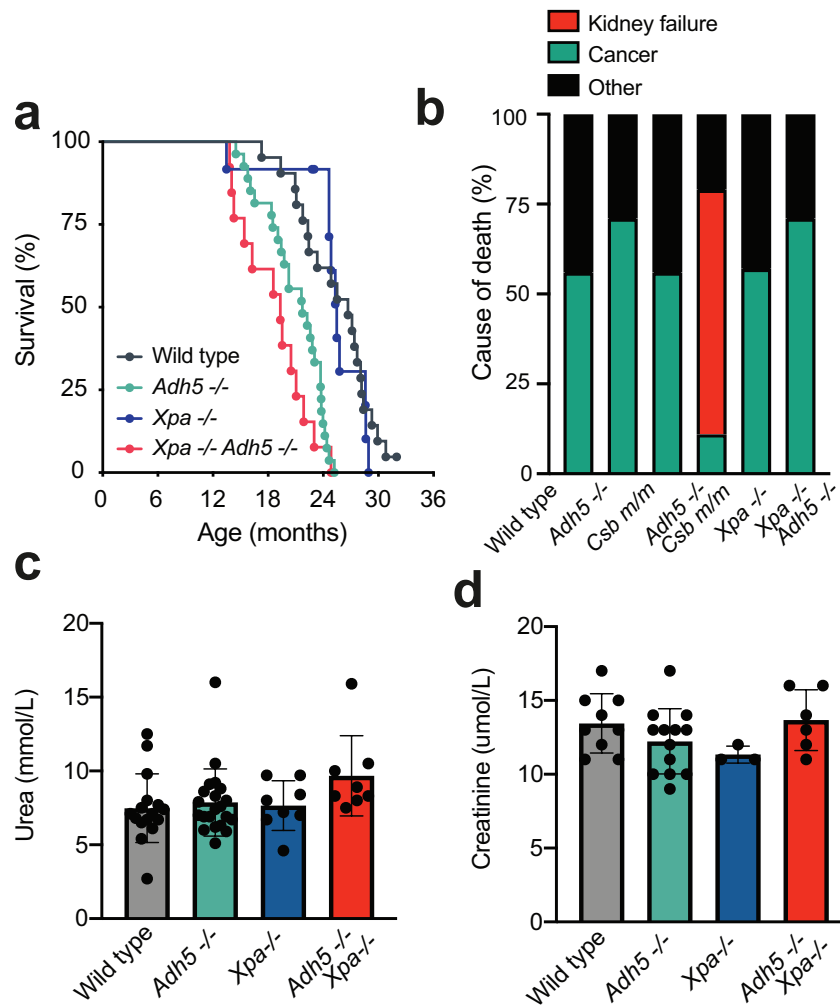


Figure 4.15 – *Adh5*^{-/-} *Xpa*^{-/-} do not develop kidney failure

a) Kaplan Meier survival curve of *Adh5*^{-/-} *Xpa*^{-/-} mice along with control mice ($n = 18, 31, 10$ and 13). **b)** Bar chart indicating the cause of death for various mouse strains, contrasting *Adh5*^{-/-} *Csb*^{m/m} and *Adh5*^{-/-} *Xpa*^{-/-} lines. **c-d)** Terminal serum urea and creatinine levels in *Adh5*^{-/-} *Xpa*^{-/-} mice along with control mice.

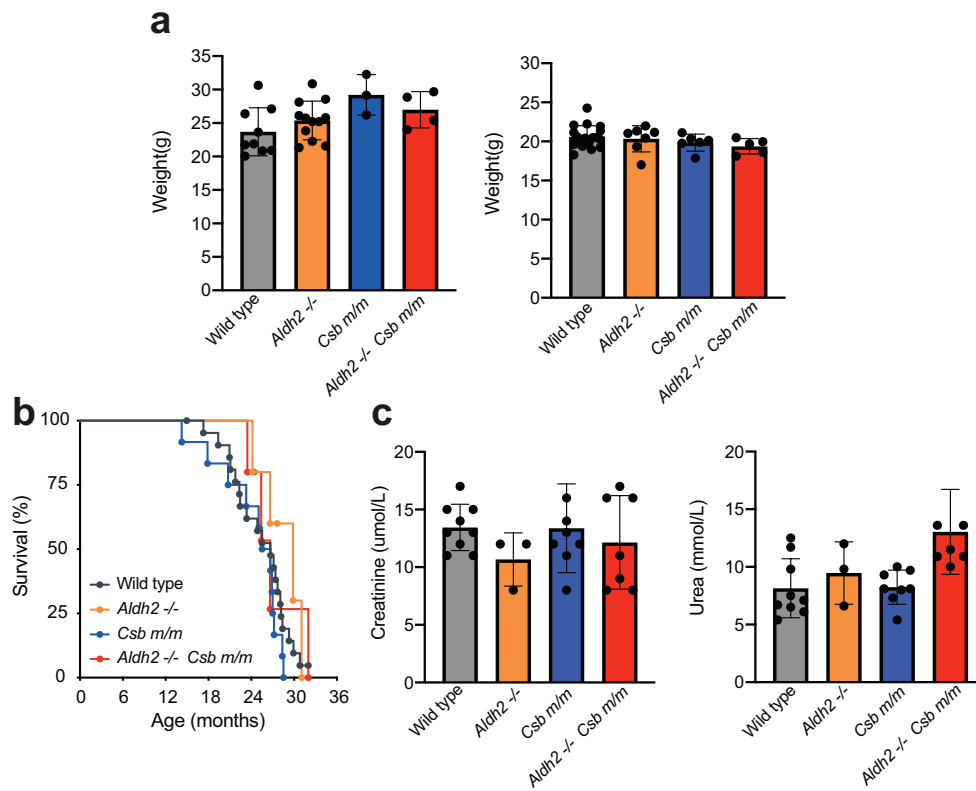


Figure 4.16 – *Aldh2*^{-/-}*Csb*^{m/m} mice do not develop CS phenotype

a) Weights of adult male and female mice at 8 weeks of age (data shown as mean and s.e.m.; *P* calculated by two-sided Mann-Whitney test; *n* = 14, 19, 13, 12, 4, 9, 3, 7 for males left to right and 24, 30, 22, 21, 12, 9, 4, 5 for females left to right). **b)** Kaplan Meier survival curve of *Aldh2*^{-/-}*Csb*^{m/m} mice along with control mice (*n* = 18, 31, 10 and 13). **c)** Terminal serum urea and creatinine levels in *Aldh2*^{-/-} *Csb*^{m/m} mice along with control mice.

4.7 Discussion

Here we show, most strikingly of all, that in *Csb^{m/m}* mice the absence of ADH5 reveals the hallmarks of the human CS phenotype. Human CS is a complex disease that affects many organ systems. Prominent among the CS human phenotype is the failure to thrive which manifests as low body weight and progressive loss of subcutaneous fat (Laugel, 2013; Nance & Berry, 1992; B. T. Wilson et al., 2016). Alongside this, neurological deficits become present at an early age and progress rapidly; these are likely due to the cerebellar atrophy and demyelination that are present in CS (Laugel, 2013; B. T. Wilson et al., 2016). Ultimately, progressive cachexia and feeding difficulties alongside renal failure contribute to the cause of death in these individuals (Kubota et al., 2015; Nance & Berry, 1992). *Csb^{m/m}* mice, despite carrying a patient mutation, do not show the human features of CS (G. T. van der Horst et al., 1997). However, by crossing *Csb^{m/m}* mice with mice deficient in ADH5 we have revealed that *Adh5^{-/-}Csb^{m/m}* mice model this human disease. This mouse model displays a failure to thrive as evidenced by the low body weight and progressive loss of fat, neurological deficits in the form of ataxia, hind limb claspings and reduced grip strength performance. On close examination, the tissues from *Adh5^{-/-}Csb^{m/m}* mice display abnormalities in the brain, eyes, liver and ultimately these mice succumb to kidney failure. The *Adh5^{-/-}Csb^{m/m}* mice therefore closely model the human CS phenotype.

Despite the findings in the *Adh5^{-/-}Csb^{m/m}* model, questions remain about the role of formaldehyde in CS. Why do *Csb^{m/m}* mice not develop CS in the presence of ADH5? And why do humans develop CS in the presence of ADH5? Perhaps the difference between the human and mouse models of CS can be explained by fundamental differences in physiology, experimental mice have shorter life spans and exist in sterile conditions and perhaps different levels of formaldehyde exposure. Indeed, a rat model of CS has recently been generated that appears to display a more pronounced CS phenotype than the mouse model (Y. Xu et al., 2019). Perhaps this suggests that higher organisms or organisms of a large size have a greater endogenous formaldehyde burden. In line with this idea, formaldehyde DNA adducts can be detected in rats and primates that are ADH5 proficient (Moeller et al., 2011; Yu et al., 2015). These studies indicate that formaldehyde can adduct DNA even in the presence of ADH5 and that primates have higher levels of endogenous formaldehyde exposure than rodents. This agrees with the hypothesis that CS reveals itself in humans deficient in CSB and not in mice due to the higher burden of formaldehyde.

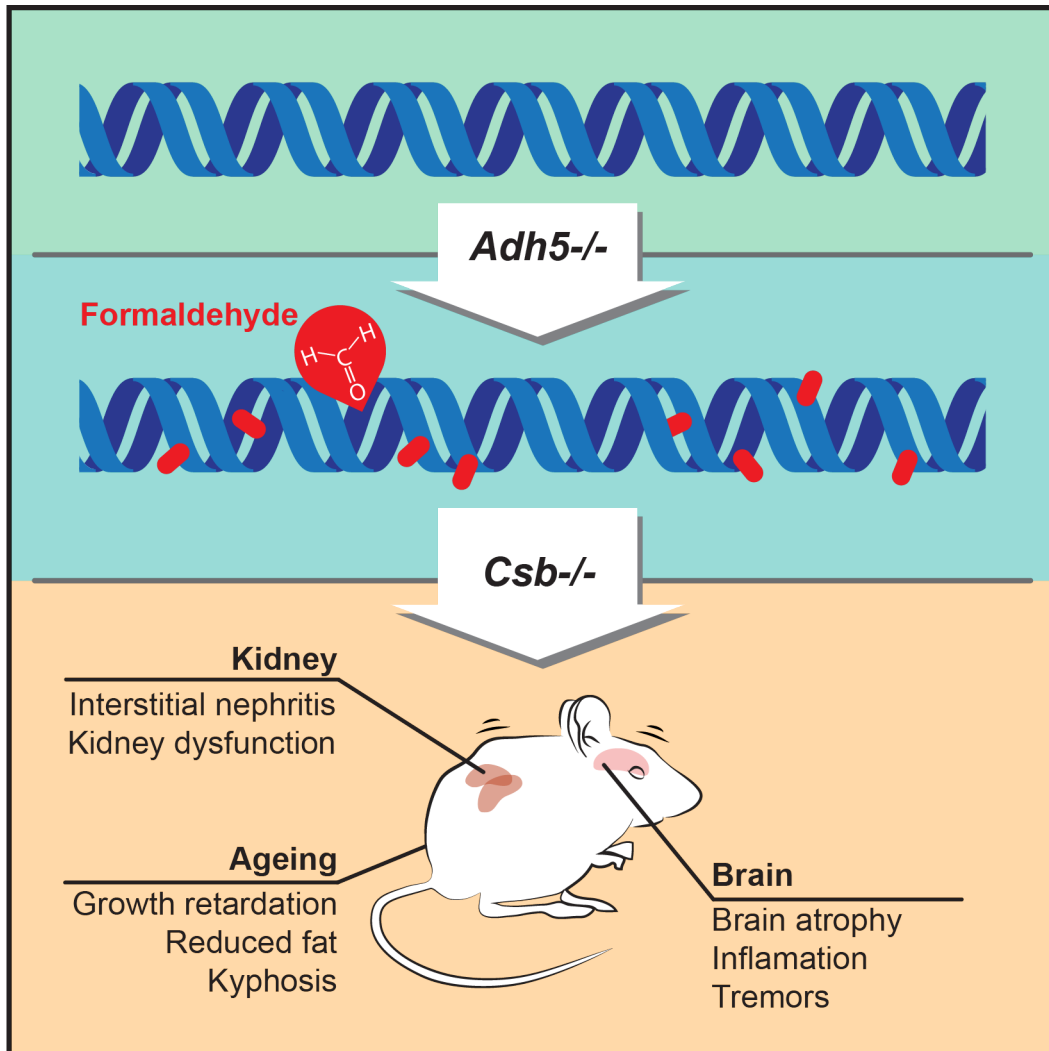


Figure 4.17 – Two Tier Protection model in the context of the CS phenotype

In the absence of *Adh5*, formaldehyde adducted DNA results in the need for DNA repair, CSB operates in TC-NER and when absent in the context of *Adh5* deficiency the CS phenotype is revealed in mice.

In this chapter we have shown a requirement for TC-NER in the cellular protection against formaldehyde both in human and mouse. These data support previous finding that *XPA*^{-/-} HAP1 cells are hypersensitive to formaldehyde (Figure 3.07f) and agrees with a recent genetic screen that maps the DNA damage response to formaldehyde. This work highlighted the need for both the FA pathway and NER in protecting cells from formaldehyde toxicity (Olivieri et al., 2020).

The stalling of RNAPII at sites of DNA damage triggers TC-NER (Anindya et al., 2010), this is regulated by modifications to the RNAPII which are important signals to respond appropriately to transcription blocking lesions (M. D. Wilson et al., 2013). UV lesions are well-known to block transcription, indeed this DNA damaging agent has been utilized to create a detailed biochemical picture of how cells respond to transcription blocking lesions (Gregersen & Svejstrup, 2018). However, UV is unlikely to represent an endogenous source of transcription-blocking DNA damage driving CS. While it remains a useful tool and has shaped our understanding on the response to transcription blocks, it remains crucial to identify the endogenous DNA damaging agents that elicit such responses. Here we place formaldehyde as an endogenous genotoxin that can trigger the response to transcription blocking lesions, suggesting it can cause DNA damage that the RNAPII cannot transcribe past, triggering TC-NER, RNAPII ubiquitination and degradation.

We find that both XPA and CSB are required for cellular resistance to formaldehyde, suggesting a requirement for the canonical TC-NER machinery in the repair of formaldehyde lesions. However, *in vivo* we also observe a milder phenotype in *Adh5*^{-/-}*Xpa*^{-/-} mice when compared to *Adh5*^{-/-}*Csb*^{m/m} mice, analogous to the phenotype of human patients with mutations in *XPA* and *CSB* (Fassihi et al., 2016; Kubota et al., 2015; Laugel, 2013; B. T. Wilson et al., 2016). The discordance in phenotype between *Adh5*^{-/-}*Xpa*^{-/-} and *Adh5*^{-/-}*Csb*^{m/m} mice highlights again that CSB deficiency leads to additional phenotypes than that of TC-NER deficiency and might be because CSB protects RNAPII from degradation in response to formaldehyde. This function is proposed to explain the severity of the phenotype in human patients with CS (Tufegdžić Vidaković et al., 2020). Alternatively, formaldehyde lesions such as crosslink precursors or monoadducts may require CSB for lesion bypass but not XPA or downstream factors. This would be similar to the ability of yeast homolog of CSB (Rad26) to employ RNAPII forward-translocating activity to facilitate lesion bypass without triggering TC-NER (J. Xu et al., 2017). However, the precise role of CSB outside of TC-NER in protecting against the CS phenotype remains unclear.

The revelation of CS in *Adh5^{-/-}Csb^{m/m}* mice is striking and represents another model in which *Adh5* deficiency reveals the associated human phenotype. Much like *Csb^{m/m}* mice, mice deficient in the FA ICL repair pathway (e.g., *Fancd2^{-/-}*) have very subtle phenotypes that do not recapitulate Fanconi Anemia. As we have shown here for *Csb^{m/m}* mice, loss of *Adh5* also greatly potentiates the phenotype of *Fancd2^{-/-}* mice (Pontel et al., 2015). However, the contrast between the two models is stark. *Adh5^{-/-}Fancd2^{-/-}* rapidly succumb to bone marrow failure in a matter of weeks whereas *Adh5^{-/-}Csb^{m/m}* mice suffer a slow decline in several organs, predominantly the kidney and brain. FANCD2 is required for the FA repair pathway which is coupled to replication and therefore cells that are highly proliferative such as the haematopoietic system rely heavily on this pathway to remove formaldehyde mediated DNA damage. CSB, however, is required for transcription-coupled repair and so highly replicative tissues can rely upon FA repair to remove formaldehyde DNA damage but those long-lived post-mitotic cells that are very transcriptionally active such as neurons and nephrons appear dependent upon CSB to mediate repair of formaldehyde DNA lesions.

Adh5^{-/-}Csb^{m/m} and *Adh5^{-/-}Fancd2^{-/-}* mice are therefore examples of the physiological consequences of formaldehyde in the absence of specific DNA repair pathways. These mouse lines demonstrate the potent genotoxicity of formaldehyde and outline the necessary DNA repair pathways for maintaining physiological homeostasis in the presence of formaldehyde. However, when endogenous levels of formaldehyde are increased by genetically disrupting another formaldehyde detoxifying enzyme (ALDH2) the consequences are striking. *Adh5^{-/-}Aldh2^{-/-}* mice that have both FA repair and NER intact display a phenotype that is consistent with overlapping features of FA and CS (Dingler et al., 2020b). Additionally, humans lacking ADH5 and ALDH2 in combination have been reported that also have phenotypic overlap between CS and FA (Dingler et al., 2020b; Oka et al., 2020). Taken together these studies suggest that even in the presence of CSB and FANCD2, humans and mice can suffer from features of CS and FA in the presence of overwhelming formaldehyde.

Chapter 5

Formaldehyde drives the *Adh5*^{-/-}*Csb*^{m/m} phenotype

Previously we have shown that formaldehyde is toxic to cells lacking CSB, resulting in the stalling and degradation of RNAPII. In addition, mice lacking the formaldehyde-detoxifying enzyme ADH5 and CSB have a phenotype that closely resembles human patients with CS. However, in addition to detoxifying formaldehyde, ADH5 can also detoxify nitric oxide, the failure to do so can lead to pathophysiological nitrosative stress (L. Liu et al., 2004). Therefore, we set out to ask if formaldehyde toxicity was responsible for the degenerative changes observed in the *Adh5*^{-/-} *Csb*^{m/m} mouse model outlined in Chapter 4.

5.1 Formaldehyde DNA adducts accumulate in ADH5 deficient brain and kidney

If formaldehyde is driving the phenotype of *Adh5*^{-/-}*Csb*^{m/m} mice, the loss of *Adh5* ought to result in higher levels of formaldehyde. It has recently been shown that *Adh5*^{-/-} have elevated levels of formaldehyde in the serum (Dingler et al., 2020b). We set out to ask if those elevated levels of serum formaldehyde resulted in damage to the genome. We first quantified the formaldehyde DNA adducts *N*²-hydroxymethyl-dG (*N*²-HO-dG), this can be reduced to *N*²-methyl-dG (*N*²-Me-dG) and quantified by LC-MS (Figure 5.01a) (Dingler et al., 2020b; Pontel et al., 2015). This adduct results from the spontaneous reaction of formaldehyde with guanine however it is unlikely to be the DNA lesion which CSB is counteracting because it is unlikely to lead to RNAPII stalling. It is, however, a useful biomarker of formaldehyde exposure to DNA.

We took kidney and brain samples from mice at 10-12 months old, extracted and digested DNA that and then spiked in heavy labeled internal controls (¹⁵N *N*²-Me-dG and ¹⁵N dA). LC-MS was then performed on the samples to determine the relative amount of *N*²-methyl-dG in each sample. The amount of *N*²-methyl-dG per genome was calculated based on the number of nucleosides per mouse genome.

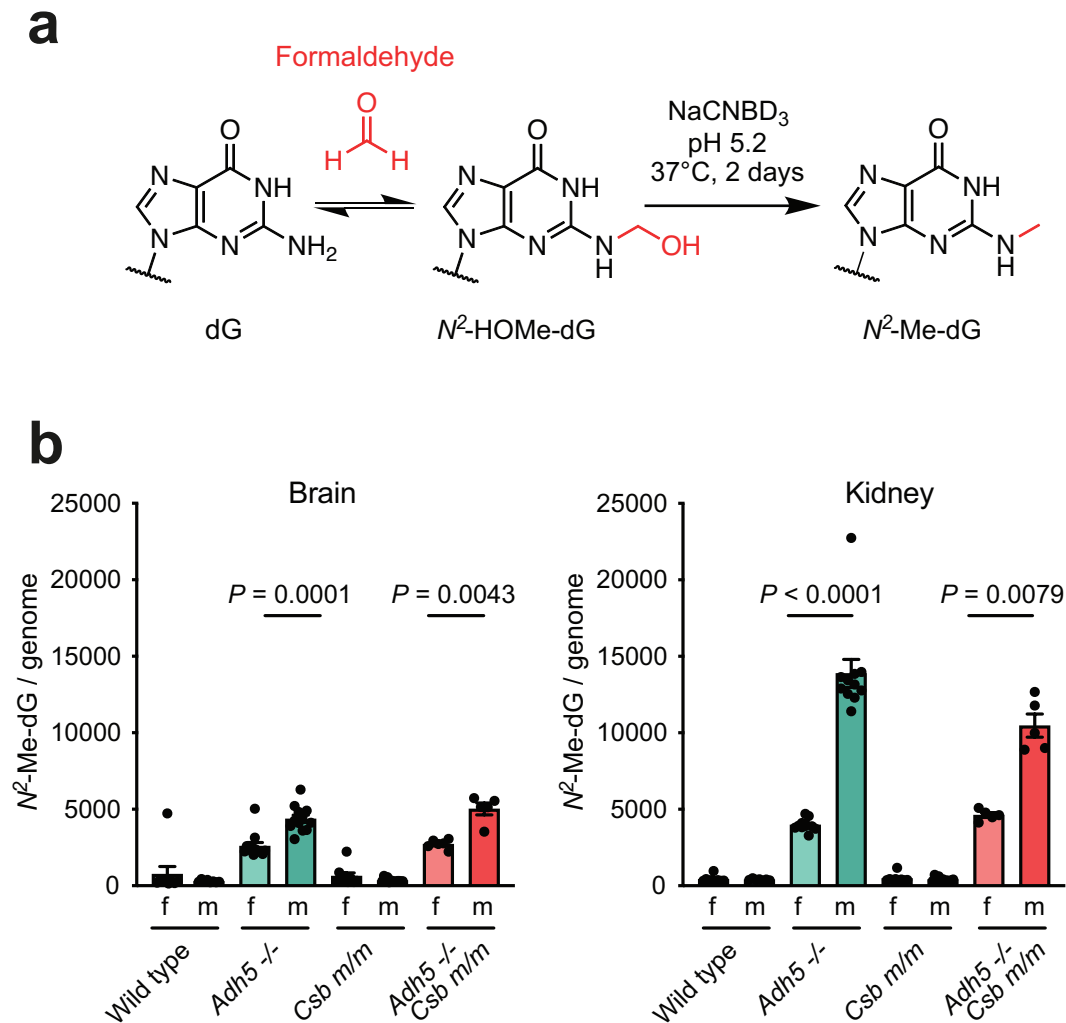


Figure 5.01 – Formaldehyde DNA adducts accumulate in *Adh5*^{-/-} brain and kidney

a) Scheme outlining how formaldehyde reacts with guanine to form the *N*²-HOMe-dG adduct, which can then be detected and quantified by mass spectrometry after reduction to *N*²-Me-dG. **b)** Bar chart representing the frequency of *N*²-Me-dG per genome in DNA isolated from brain and kidney of *Adh5*^{-/-} *Csb*^{m/m} female (f) and male (m) mice and controls. *P* calculated by two-sided Mann-Whitney test, data shown as mean and s.e.m; n = 9, 8, 12, 12, 9, 13, 6 and 5 from left to right.

Levels of *N*²-Me-dG were significantly elevated in the brain and kidney of both *Adh5*^{-/-} and *Adh5*^{-/-}*Csb*^{m/m} mice (Figure 5.01b). Interestingly, higher *N*²-Me-dG levels were observed in male *Adh5*^{-/-} mice compared to females, in line with the more severe CS phenotype observed in male *Adh5*^{-/-}*Csb*^{m/m} mice (Figure 4.06 and 4.08). The importance of this data therefore is that it reveals that ADH5 deficiency leads to increased formaldehyde DNA adducts and that there is a correlation between the organs and the sex most affected and higher levels of adducts.

5.2 Methanol exacerbates the CS phenotype in *Adh5*^{-/-}*Csb*^{m/m} mice

If endogenous formaldehyde drives the degenerative CS phenotype in *Adh5*^{-/-}*Csb*^{m/m} mice then we reasoned that an additional exogenous source of formaldehyde would exacerbate this phenotype. Methanol, which is oxidised to formaldehyde, has been previously used for this purpose. Indeed, exposing *Adh5*^{-/-} mice to 15% methanol in the drinking water, leads to a significant increase in the frequency of *N*²-Me-dG adducts in liver, kidney and bone marrow (Pontel et al., 2015). We challenged *Adh5*^{-/-} mice by intraperitoneal injection of 1.5g/kg methanol. Surprisingly, male *Adh5*^{-/-} mice rapidly succumb to kidney failure, but the female mice could tolerate this dose (Figure 5.02). This suggested that while this dose would not be appropriate for male *Adh5*^{-/-}*Csb*^{m/m} mice, females could be challenged with it. This data is also in line with the adduct data (Figure 5.01b) and indicates that the basal levels of formaldehyde in addition to the 1.5g/kg of methanol results in lethality in male mice deficient in ADH5 but not females.

Having established that *Adh5*^{-/-} females tolerated a 1.5g/kg methanol challenge, we next challenged a cohort of *Adh5*^{-/-}*Csb*^{m/m} females along with controls. Throughout the challenge, we sampled blood once a month to monitor kidney function and on termination we harvested brain and kidney for signs of the CS phenotype (Figure 5.03a). The consequence of this treatment was striking, monthly blood samples revealed a rapid decline in kidney function in *Adh5*^{-/-}*Csb*^{m/m} mice, who then succumbed to kidney failure by 3-6 months after treatment (Figure 5.03b-d) compared to 15-18 months in the case of untreated controls. At necropsy, *Adh5*^{-/-}*Csb*^{m/m} mice treated with methanol showed small nodular kidneys and histology confirmed chronic end-stage kidney failure with pathology that was like the aged untreated *Adh5*^{-/-}*Csb*^{m/m} mice (Figure 5.03e-f).

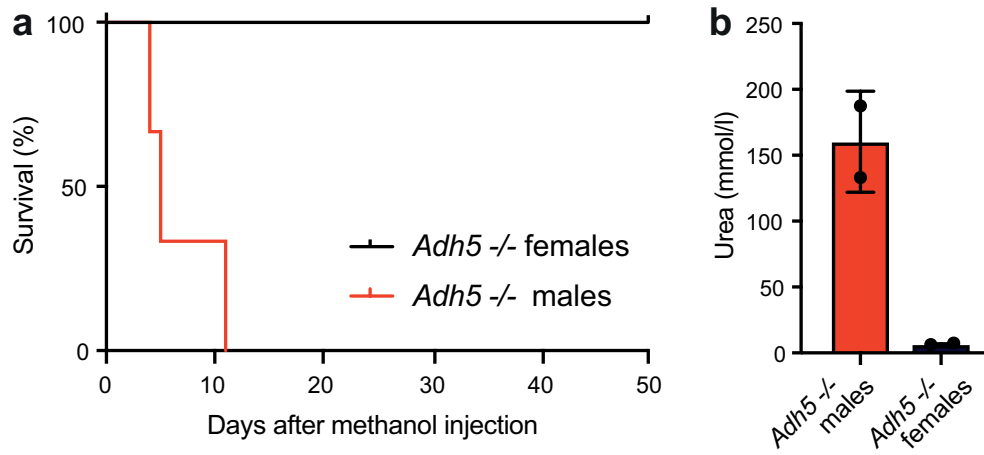


Figure 5.02 – 1.5g/kg methanol challenge of *Adh5*^{-/-} mice

a) Kaplan-Meier Curve indicating the length of survival after 1.5g/kg methanol I.P for male and female *Adh5*^{-/-}, n=3. **b)** Urea measurements after methanol I. Ps for male and female *Adh5*^{-/-}, n=2 data shown as mean and s.e.m.

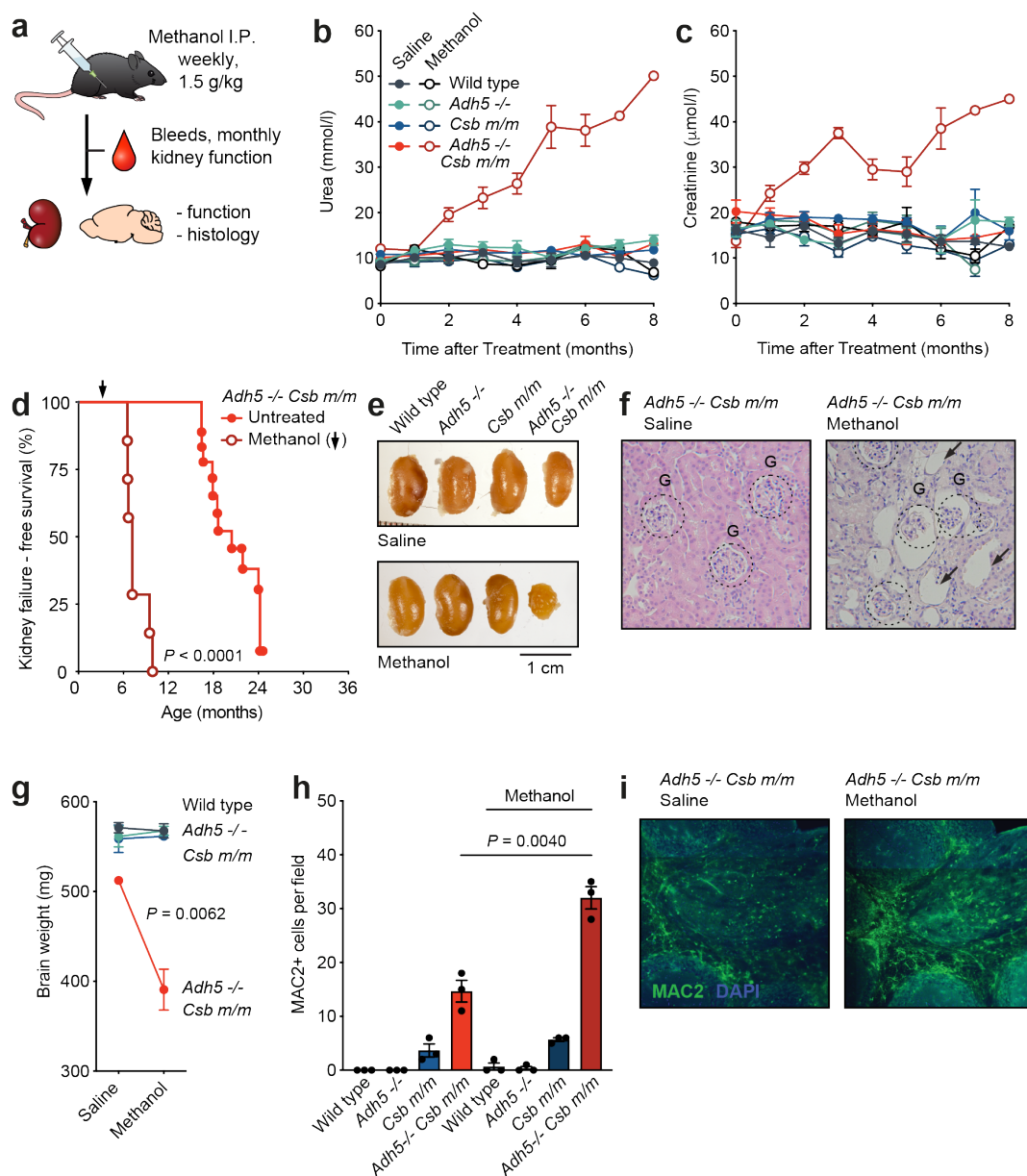


Figure 5.03 - Methanol exposure exacerbates the Cockayne Syndrome phenotype in *Adh5*^{-/-}*Csb*^{m/m} mice

a) Scheme outlining weekly intra-peritoneal (I.P.) injection of 1.5g/kg methanol and analysis of treated mice. **b-c**) Monthly serum levels of urea (**b**) and creatinine (**c**) from mice exposed to methanol and saline controls, data plotted as mean and s.e.m.; $n = 4$. **d**) Kidney failure-free survival curve of *Adh5*^{-/-}*Csb*^{m/m} mice with and without methanol exposure (P calculated by Mantel-Cox logrank test; $n = 7$ and 19). **e**) Representative image of kidneys from age-matched mice exposed to methanol or saline, taken after 24 hours of fixation. **f**) Representative H&E-stained sections of kidney from *Adh5*^{-/-}*Csb*^{m/m} exposed mice, G indicates glomeruli and arrows indicate atrophic tubules. **g**) Brain weights of age matched exposed mice, P calculated by two tailed Student's t -test; data shown as mean and s.e.m., $n = 3$ mice. **h**) Quantification of the number of MAC2+ cells per field in exposed mice P calculated by two tailed Student's t -test; data shown as mean and s.e.m., $n = 3$ mice. **i**) Representative immunofluorescence images of the cerebellum of *Adh5*^{-/-}*Csb*^{m/m} exposed mice stained with MAC2 and DAPI at 40x.

Finally, we analysed the brains as before and found that brains of methanol treated mice showed a decrease in mass accompanied by the increased presence of MAC2+ microglial cells (Figure 5.04a-c). Together these data reveal that by increasing the basal levels of formaldehyde through exogenous exposure the CS phenotype in *Adh5^{-/-}Csb^{m/m}* mice can be precipitated, highlighting the role of formaldehyde in this phenotype.

5.3 Methanol induces kidney failure in *Adh5^{-/-} Xpa^{-/-}* mice

Aged *Adh5^{-/-}Xpa^{-/-}* mice do not phenocopy *Adh5^{-/-}Csb^{m/m}* mice as they do not develop features of CS, however XPA is required for cellular protection against formaldehyde and is an essential factor for TC-NER. To examine whether these mice reveal features of CS when challenged with a higher burden of formaldehyde, we next decided to challenge a cohort of these mice with the same methanol challenge outlined above (Figure 5.03a). All *Adh5^{-/-}Csb^{m/m}* mice succumb to renal failure by approximately 10 months when exposed to weekly methanol I. Ps (Figure 5.03d). *Adh5^{-/-}Xpa^{-/-}* mice, however, only begin to show signs of kidney dysfunction after 6 months of methanol I. Ps, succumbing to kidney failure by 18 months of age. Necropsy and histology reveal that *Adh5^{-/-}Xpa^{-/-}* kidneys develop the same appearance and pathological changes that are present in *Adh5^{-/-}Csb^{m/m}* kidneys in aged and methanol treated mice. Together these data suggest that while *Adh5^{-/-}Xpa^{-/-}* mice do not develop CS spontaneously, a higher burden of formaldehyde DNA damage can lead to aspects of the CS phenotype in *Adh5^{-/-}Xpa^{-/-}* mice pointing to an *in vivo* role for XPA in protection against formaldehyde toxicity.

5.4 Ethanol does not reveal CS phenotypes in *Adlh2^{-/-} Csb^{m/m}* mice

Finally, we tested if the closely related aldehyde acetaldehyde could drive the CS phenotype in *Aldh2^{-/-}Csb^{m/m}* mice when exposed to a large dose of exogenous acetaldehyde. In an analogous way to methanol, ethanol is oxidized to acetaldehyde. We exposed mice continuously to 20% ethanol as the only source of drinking water. This approach has been used previously to induce genotoxicity in *Aldh2^{-/-}* and *Aldh2^{-/-}Fand2^{-/-}* mice (Garaycochea et al., 2012; Langevin et al., 2011). However, in contrast to *Aldh2^{-/-}Fand2^{-/-}* mice exposed to ethanol and *Adh5^{-/-}Csb^{m/m}* exposed to methanol, *Aldh2^{-/-}Csb^{m/m}* did not display any reduction in lifespan compared to challenged *Aldh2^{-/-}* mice (Figure 5.05a), nor did they display any kidney impairment (Figure 5.05b). These data suggest that there is no role for CSB in the protection against acetaldehyde toxicity.

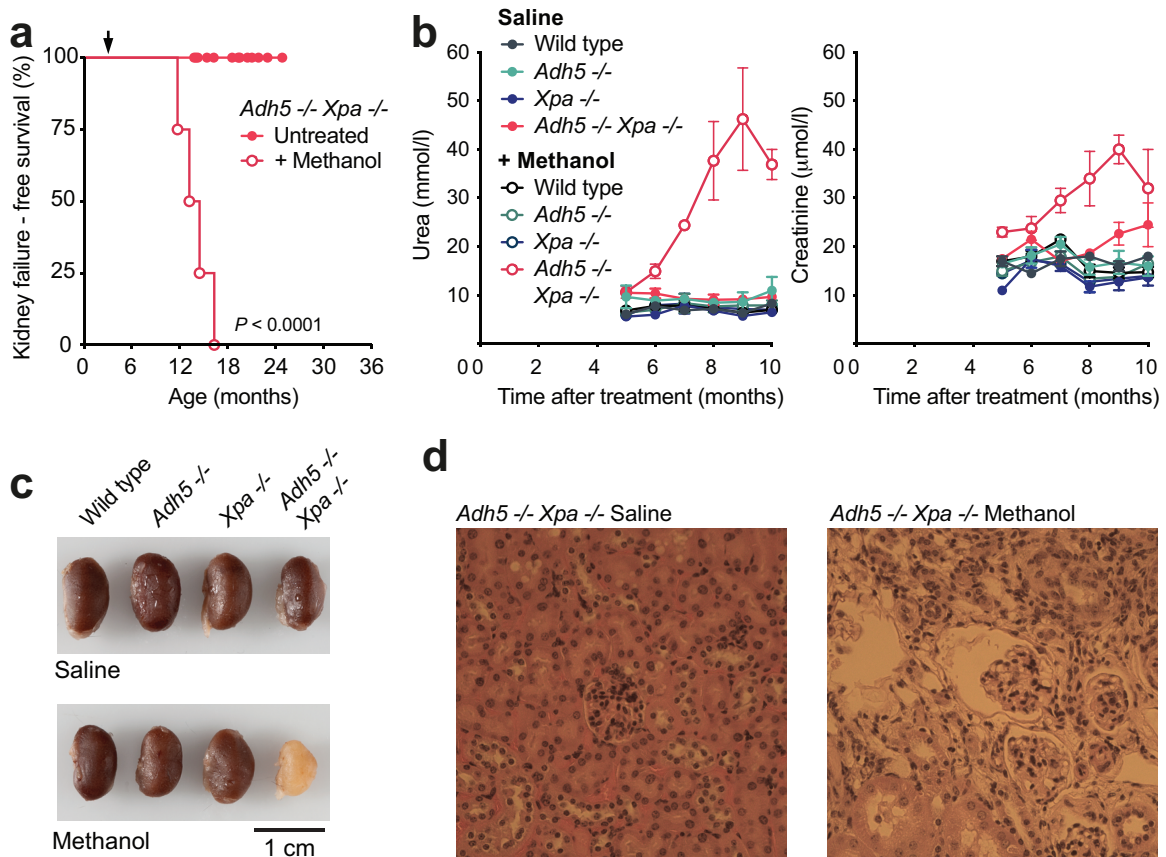


Figure 5.04 – Methanol exposure leads to kidney failure in *Adh5*^{-/-} *Xpa*^{-/-} mice

a) Kidney failure-free survival curve of *Adh5*^{-/-}*Xpa*^{-/-} mice with and without methanol exposure (P calculated by Mantel-Cox logrank test; $n = 4$ and 13). **b**) Monthly serum levels of urea and creatinine from mice exposed to methanol or saline, data plotted as mean and s.e.m.; $n = 4$. **c**) Representative photos of kidneys from exposed *Adh5*^{-/-} *Xpa*^{-/-} mice with controls. **d**) Representative H&E-stained sections of methanol exposed *Adh5*^{-/-} *Xpa*^{-/-} kidneys with saline control

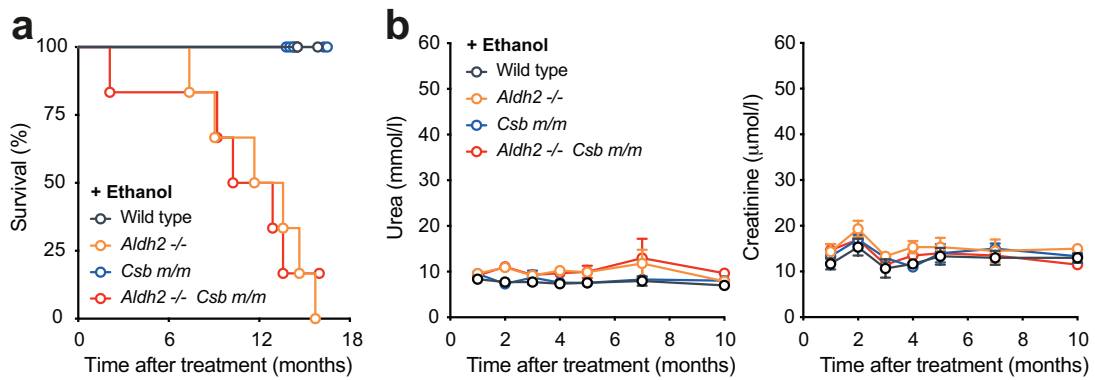


Figure 5.05 – *Aldh2*^{-/-} *Csb*^{m/m} mice tolerate an ethanol challenge

a, Kaplan-Meier survival curve of wild type, *Aldh2*^{-/-}, *Csb*^{m/m} and *Aldh2*^{-/-}*Csb*^{m/m} mice treated with 20% ethanol continuously in the drinking water ($n = 6$). **b**, Monthly serum levels of urea and creatinine from mice exposed to 20% ethanol continuously in the drinking water, data plotted as mean and s.e.m.; $n = 6$.

5.5 Discussion

The *Adh5^{-/-}Csb^{m/m}* mouse phenotype suggests that a toxic substrate of ADH5 leads to the degenerative features of CS in the absence of CSB. The ADH family of enzymes has a broad specificity of substrates with many enzymes having overlapping substrates. As with most ADH enzymes, ADH5 has a degree of affinity for several substrates, the primary substrates of ADH5 however are formaldehyde and S-nitrosoglutathione (GSNO) (Barnett & Buuxton, 2016). Formaldehyde reacts with glutathione to form S-hydroxymethylglutathione (HMG) this is then oxidized by ADH5 to form S-formylglutathione, which is then further metabolized by S-formylglutathione hydrolase to give formate. ADH5 also converts GSNO into GSNHOH, an unstable intermediate, which reacts with glutathione to form glutathione disulfide that is then reduced into two molecules of glutathione, this reaction is catalyzed by the enzyme glutathione reductase (Hedberg et al., 2003; Sanghani et al., 2002).

It is possible therefore that the CS phenotype in *Adh5^{-/-}Csb^{m/m}* mice is due to an abundance of nitric oxide (NO). This same caveat in the formaldehyde DNA damage hypothesis exists for the *Adh5^{-/-}Fancd2^{-/-}* model; here however there is evidence that nitric oxide does not have a prominent role. Firstly, mice deficient in inducible nitric oxide synthase (iNOS) the main enzyme responsible for producing NO *in vivo* were not able to rescue the embryonic lethality of *Adh5^{-/-}Fancd2^{-/-}* and secondly *iNOS^{-/-}Fancd2^{-/-}* showed no improvement over *Fancd2^{-/-}* in terms of the numerical HSC defect (Pontel et al., 2015). These data suggest that a reduction in NO does not confer any resistance against the *Adh5^{-/-}Fancd2^{-/-}* phenotype, raising doubts about its physiological relevance in the absence of DNA repair.

In this chapter we have shown evidence to support the hypothesis that formaldehyde drives the *Adh5^{-/-}Csb^{m/m}* phenotype. We find that the worst affected tissues also contain high levels of the formaldehyde adduct, *N*²-Me-dG. This adduct occurs as a result of formaldehyde reacting spontaneously with DNA, therefore, in the tissues that fail in *Adh5^{-/-}Csb^{m/m}* mice, there is evidence of formaldehyde modifying DNA. Given the involvement of CSB in transcription-coupled responses, it seems highly likely that the presence of formaldehyde adducted DNA creates a difficult terrain to transcribe, necessitating CSB. However, the formaldehyde modification that we are detecting does not accumulate in the *Adh5^{-/-}Csb^{m/m}* mice, suggesting that this adduct does not block transcription, it is likely however that other formaldehyde lesions exist that do. Formaldehyde can lead to the formation of DNA-DNA crosslinks, DNA-protein crosslinks (Yu et al., 2015) and DNA-RNA hybrids that would create an impediment to the transcribing RNAPII (Schwab et al., 2015).

To support the notion that endogenous formaldehyde drives the *Adh5*^{-/-}*Csb*^{m/m} phenotype we challenged the mice with methanol, a source of exogenous formaldehyde that increases tissue levels of the *N*²-Me-dG adduct (Pontel et al., 2015). This challenge greatly accelerated the functional decline of the kidney and brain in *Adh5*^{-/-}*Csb*^{m/m} mice, demonstrating the importance of the two-tiered protection that ADH5 and CSB confer against exogenous formaldehyde *in vivo*. Indeed, the kidney and the brain are both severely affected in *Adh5*^{-/-}*Csb*^{m/m} mice endogenously and when challenged, highlighting how these organs heavily rely on CSB for protection against formaldehyde.

Interestingly, the methanol challenge revealed kidney failure in *Adh5*^{-/-}*Xpa*^{-/-} mice, though these mice took much longer to develop kidney problems when compared to *Adh5*^{-/-}*Csb*^{m/m} mice. This is evidence that the canonical TC-NER machinery does protect against formaldehyde toxicity *in vivo*, albeit to a lesser degree than CSB and agrees with our earlier *in vitro* cytotoxicity assays (Figure 4.01a-c). Perhaps then, the CS phenotype manifests itself in the presence of overwhelming transcription blocking lesions and CSB alone can trigger a type of repair or lesion bypass of a subset of these lesions, enough to prevent the CS phenotype in *Xpa*^{-/-}*Adh5*^{-/-} mice endogenously but not when challenged with methanol. Taken together this suggests that canonical TC-NER is required for protection against formaldehyde *in vitro* and *in vivo* however there is also a role for CSB outside of TC-NER which is required for protection against endogenous formaldehyde.

The *Adh5*^{-/-}*Csb*^{m/m} mouse model recapitulates human CS; we have provided evidence that this model is driven by formaldehyde and are now able to modulate these effects with exogenous formaldehyde in the form of a methanol challenge. However, the reason why organs fail in the context of human CS and indeed our *Adh5*^{-/-}*Csb*^{m/m} mice remain unclear and will be the focus of the following chapter.

Chapter 6

Single cell RNA-seq identifies cell types susceptible to formaldehyde-induced transcriptional stress

Kidney failure is a cause of morbidity and mortality in CS patients. Pathological findings have suggested changes in tubules, glomeruli basement membranes and proteinuria (Kubota et al., 2015; Stern-Delfils et al., 2020); however, the pathogenesis of kidney failure in CS remains poorly understood. Each nephron, the functional unit of the kidney, consists of multiple specialised cell types that are spatially configured to enable the filtration and reabsorption of key nutrients and excretion of waste and toxins. Recent advances in single cell RNA sequencing (scRNA-seq) have allowed identification of cell types susceptible to particular disease states (Young et al., 2018). The kidney is the organ that fails in *Adh5*^{-/-} *Csb*^{m/m} mice; therefore, in the following chapter we will explore the changes that take place in the kidney that leads to the degeneration of this organ.

6.1 Single cell RNA sequencing of murine kidneys

In order to generate a detailed expression map of the *Adh5*^{-/-} *Csb*^{m/m} kidneys, we used scRNA-seq to profile nephron cellular responses to formaldehyde-induced transcriptional stress. To do this we analysed kidneys from three *Adh5*^{-/-} *Csb*^{m/m} aged male mice and controls. These mice were between 10 and 12 months old, well before the terminal state of kidney failure that would have led to many secondary changes complicating the interpretation of the data. Kidneys from *Adh5*^{-/-} *Csb*^{m/m} and control mice were dissociated to generate single cell suspensions and sequenced using the 10x Genomics platform (Figure 6.01a). In total, high-quality data was captured from 106,531 cells.

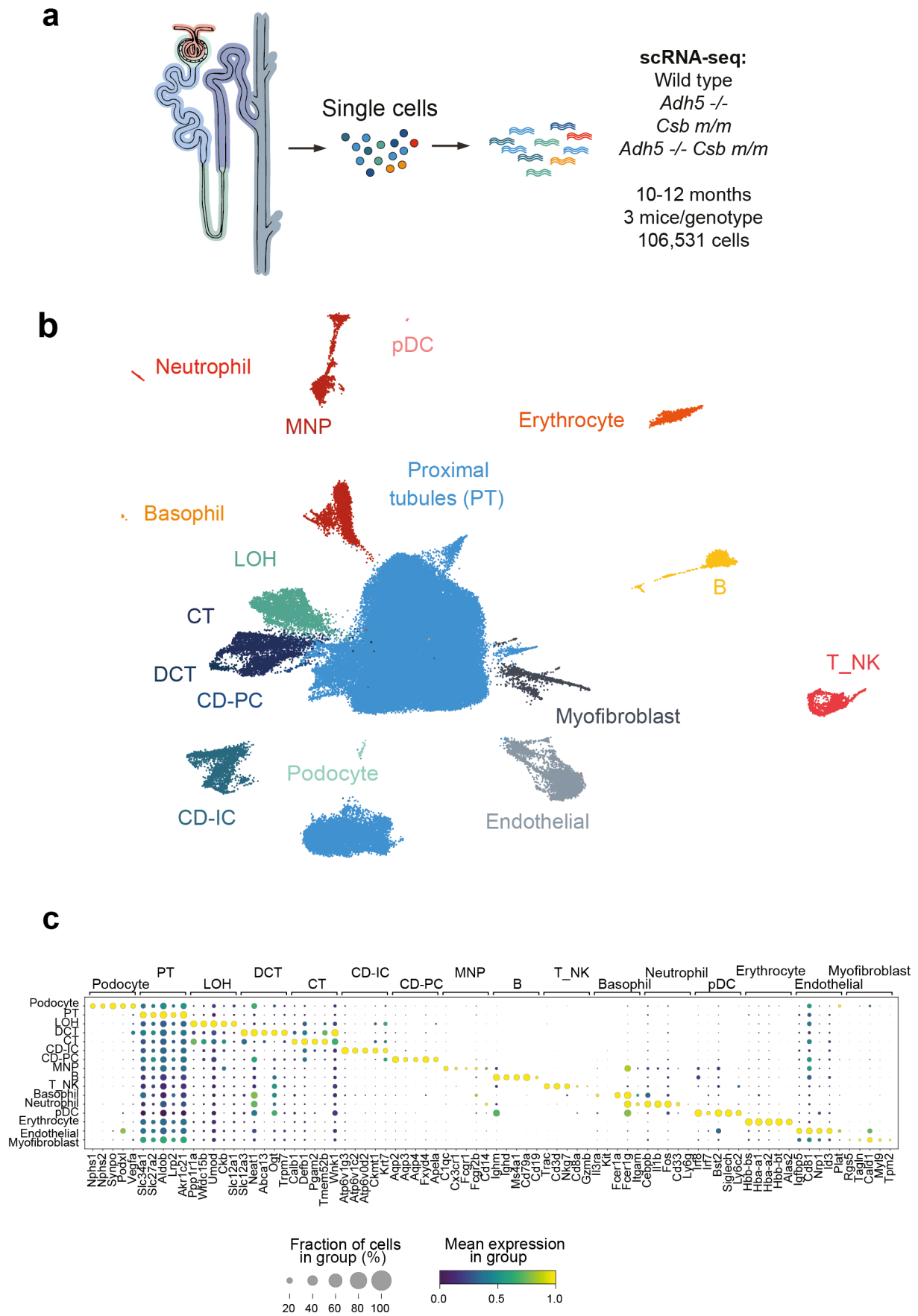


Figure 6.01 – scRNA-seq of murine kidneys

a) Scheme outlining the single cell RNA sequencing performed on *Adh5*^{-/-}*Csb*^{m/m} and control kidneys. Mice aged 10-12 months; *n* = 3 mice per genotype. **b)** UMAP plot of 106,531 murine kidney cells from *Adh5*^{-/-}*Csb*^{m/m} and control mice, (pDC, plasmacytoid dendritic cell; MNP, mononuclear phagocyte; LOH, loop of henle; CT, connecting tubule; DCT, distal convoluted tubules; CD-PC, collecting duct – principle cell; CD-IC, collecting duct – intercalated cell; T_NK, T cells/NK cells; B, B cells) **c)** dot plots indicating marker genes for each cell type, with the fraction of cells expressing each marker and the mean expression levels.

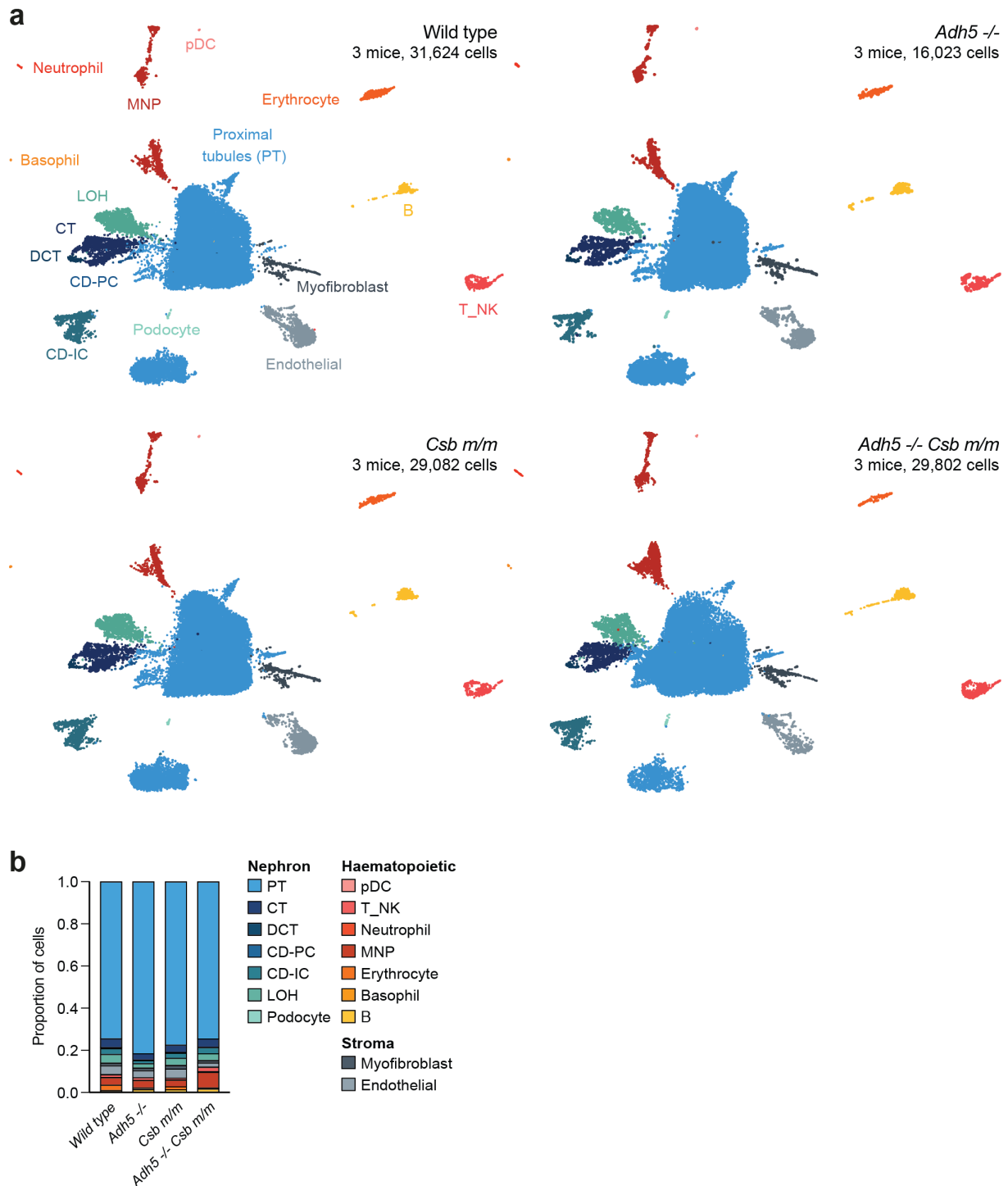


Figure 6.02 – scRNA-seq data for Wild type, *Adh5*^{-/-}, *Csb*^{-/-} and *Adh5*^{-/-}*Csb*^{m/m} kidneys

a) UMAP plots of murine kidney scRNA-seq data for wild type, *Adh5*^{-/-}, *Csb*^{m/m} and *Adh5*^{-/-}*Csb*^{m/m} mice, $n = 3$ and $n = 31,624$, $16,023$, $29,082$, $29,802$ cells (pDC, plasmacytoid dendritic cell; MNP, mononuclear phagocyte; LOH, loop of henle; CT, connecting tubule; DCT, distal convoluted tubules; CD-PC, collecting duct – principle cell; CD-IC, collecting duct – intercalated cell; T_NK, T cells/NK cells; B, B cells). **b)** Bar chart showing the composition of cell types in the scRNA-seq data

After validation, the Uniform Manifold Approximation and Projection (UMAP) of the data demonstrated distinct nephron epithelial cell clusters, as well as several immune cell clusters, that were annotated based on canonical marker expression (Figure 6.01b-c). UMAPs were generated for each individual genotype with the number of cells for each data set as follows, 31,624 wild type cells, 16,023 *Adh5*^{-/-} cells, 29,082 *Csb*^{m/m} cells and 29,802 *Adh5*^{-/-} *Csb*^{m/m} cells (Figure 6.02a). The UMAPs, along with a bar chart indicating the cellular composition of each genotype (figure 6.02b), indicated the successful sequencing of each genotype and that we had acquired an extensive dataset for interrogating the expression differences between the failing *Adh5*^{-/-}*Csb*^{m/m} kidneys and allelic controls.

As in previous scRNA-seq kidney datasets (J. Park et al., 2018), the proximal tubule (PT) cells were the most highly represented cell type in our experiment. Glomerular filtrate flows directly into the PT, which plays a vital role in amino acid and glucose reabsorption and in acid-base homeostasis. When considering all kidney cell types, PT cells showed the greatest number of differentially expressed genes (DEGs) in *Adh5*^{-/-}*Csb*^{m/m} kidneys compared to wild type counterparts (Figure 6.03b).

Additionally, when all genotypes were plotted on the same UMAP and coloured differently there was also an indication of a different gene expression pattern in PT cells of *Adh5*^{-/-}*Csb*^{m/m} kidneys that partitioned to a specific region of the PT cluster (Figure 6.03b) indicated by the arrow. To explore this further, we interrogated the 81,343 PT cells in isolation (Figure 6.04a). Based on gene expression the PT cells were further subdivided into 8 sub-clusters (PT-0 to PT-7) that enabled us to identify expression markers for each PT sub-cluster (Figure 6.04d). Separating the 8 PT sub-clusters by genotype revealed that the *Adh5*^{-/-}*Csb*^{m/m} PT cells displayed a strikingly different profile of PT sub-clusters than other genotypes (Figure 6.04b-c). Notably, the PT-4 sub-cluster was markedly expanded in *Adh5*^{-/-}*Csb*^{m/m} kidneys compared with controls. In summary, scRNA-seq analysis identified PT cells as those with the most altered transcriptional profile in *Adh5*^{-/-}*Csb*^{m/m} kidneys when compared to allelic controls, particularly with an expansion of those cells in the PT-4 sub-cluster.

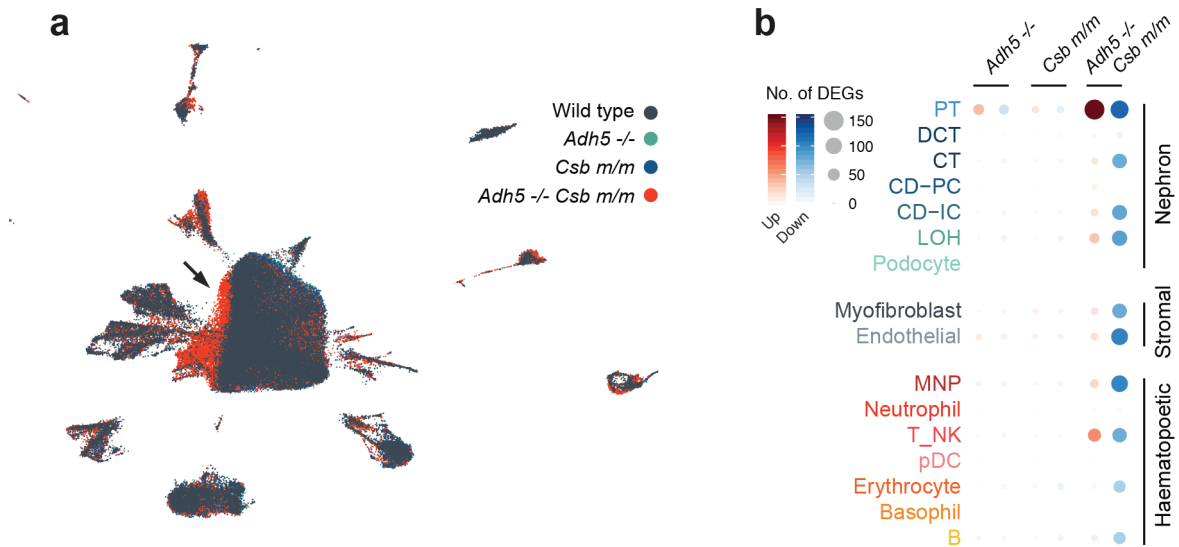


Figure 6.03 – scRNA-seq data reveal PT cells have a different expression pattern in *Adh5*^{-/-}*Csb*^{m/m} kidneys

a) UMAP plot of all scRNA-seq data with each genotype labelled a different colour, arrow indicates PT cells that are distinct to *Adh5*^{-/-}*Csb*^{m/m} kidneys. **b)** Number of differentially expressed genes (DEGs) that are up-regulated (red) or down-regulated (blue) between *Adh5*^{-/-}, *Csb*^{m/m} and *Adh5*^{-/-}*Csb*^{m/m} versus wild type across clusters in the kidney.

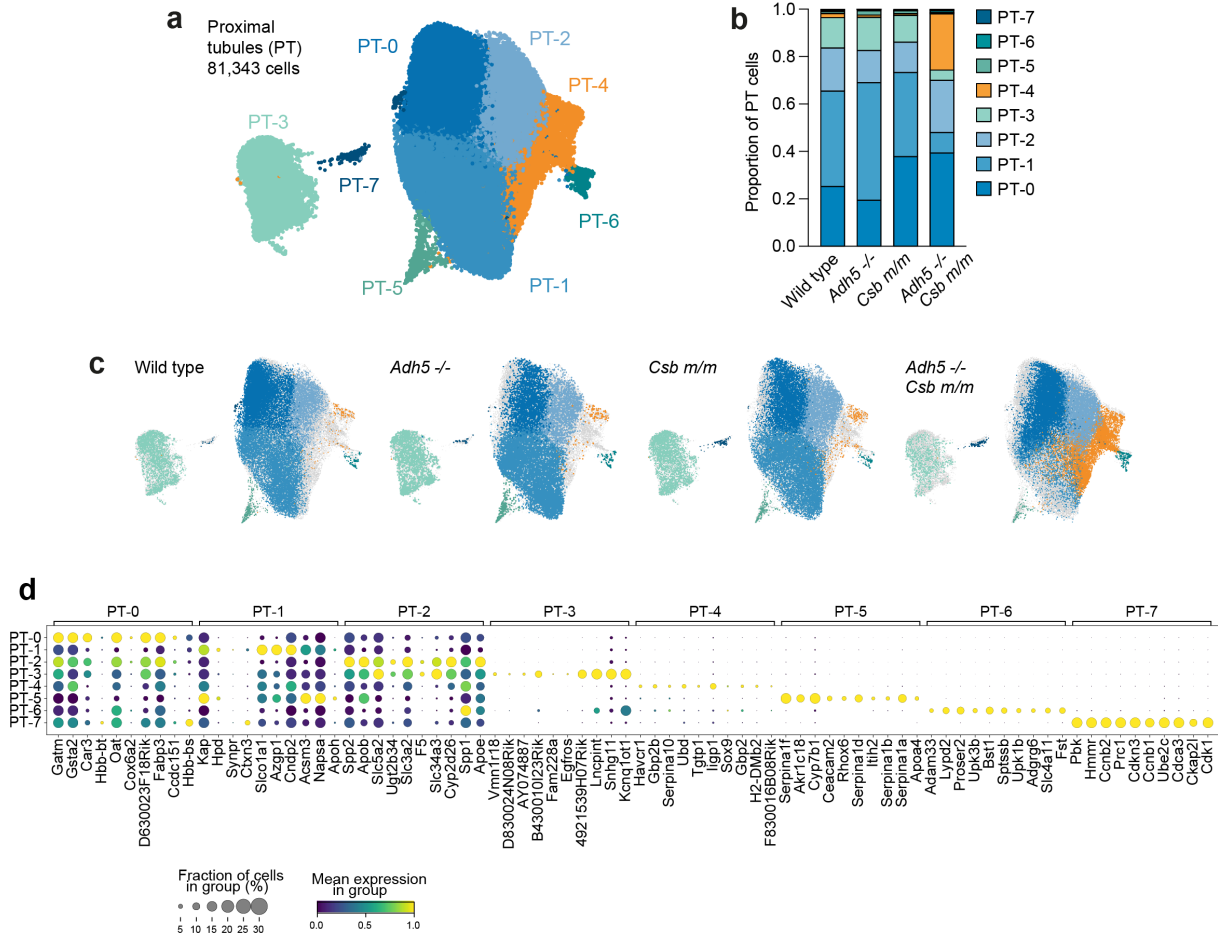


Figure 6.04 – scRNA-seq data reveal PT cells in *Adh5*^{-/-}*Csb*^{m/m} kidneys segregate into a distinct cluster of cells

a) UMAP plot of 81,343 proximal tubule (PT) cells from *Adh5*^{-/-}*Csb*^{m/m} and control mice, $n = 3$ per genotype. **b)** Bar chart indicating the proportion of cells in each PT sub-cluster across all genotypes. **c)** UMAP plot of PT sub-clusters split by genotype. **d)** Dot plots indicating marker genes for each PT subcluster, with the fraction of cells expressing each marker and the mean expression levels.

6.2 A subset of *Adh5*^{-/-}*Csb*^{m/m} PT cells are damaged

To address how the differences in gene expression in *Adh5*^{-/-}*Csb*^{m/m} PT cells relate to their altered state and function, we first ranked the top 100 marker genes for each PT sub-cluster (**Supplementary Table 4**). Given that the PT-4 sub cluster contained a unique profile that was predominantly *Adh5*^{-/-}*Csb*^{m/m} cells we paid close attention to the genes in this list. Within the marker genes for PT-4 we identified several that were indicative of kidney injury (*Kim-1*, *Spp1*, *Cyr61* and *B2m*) (Dieterle et al., 2010; Feng et al., 2019; J. Huang et al., 2013; Vaidya et al., 2006), with *Kim-1* being the top marker gene for this cluster and expression being restricted to those cells from *Adh5*^{-/-}*Csb*^{m/m} PTs (Figure 6.04d and Figure 6.05a-c). Kidney injury molecule 1 (KIM-1) is a membrane protein induced in PT cells in response to chemotherapeutic agents such as cisplatin, and is an established clinical biomarker of PT damage (C. R. Brooks et al., 2015; Vaidya et al., 2006). *Cyr61* codes for a matricellular protein induced in multiple mouse models of kidney injury, along with *Spp1*, which is implicated in several kidney pathologies (Feng et al., 2019). This expression profile is consistent with the conclusion that the PT-4 sub-cluster represents a population of damaged PT cells. To confirm that these transcriptional changes resulted in altered protein expression, we carried out immunostaining of KIM-1 in kidney sections and found that only *Adh5*^{-/-}*Csb*^{m/m} tubular cells stained positive, supporting the scRNA-seq data (Figure 6.05b).

6.3 *Adh5*^{-/-}*Csb*^{m/m} PT cells display inflammation

In order to obtain insight into the molecular processes that might be altered in these cells, we applied STRING analysis to the top 100 marker genes of PT-4. This identified five major nodes that enriched for distinct gene ontology (GO) terms (Figure 6.06a). One of the enriched pathways was alcohol metabolic processes, suggesting that these cells may be adapting to loss of ADH5. Additionally, there was an enrichment of genes that regulate apoptosis, a process triggered to promote clearance of damaged or dysfunctional cells. One mechanism by which apoptotic cells are cleared from the PT is through phagocytosis; intriguingly a recent study indicated that KIM-1-dependant phagocytosis can trigger MHCII antigen presentation (C. R. Brooks et al., 2015). Consistent with this we observed increased expression of many genes involved in antigen presentation, particularly MHCII (Figure 6.06a). Tubular injury is also known to result in an inflammatory response, which is at least in part mediated by type I interferons (IFN). Indeed type I IFN receptor-deficient mice protected from tubular necrosis in response to ischemia/reperfusion injury (Freitas et al., 2011). Notably, PT-4 cells showed a marked induction of interferon β response genes.

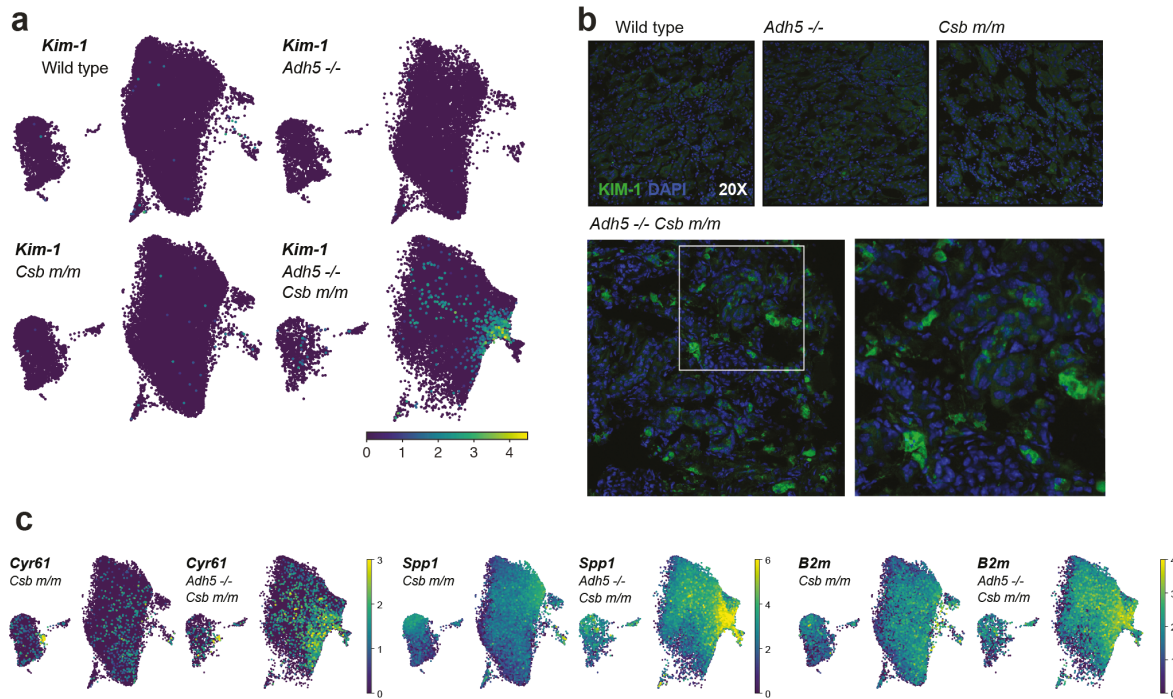


Figure 6.05 –Proximal tubule damage in *Adh5*^{-/-}*Csb*^{m/m} kidneys

a) Feature plots of *Kim-1* expression from PT sub-clusters of *Adh5*^{-/-}*Csb*^{m/m} cells and controls. **b)** Immunofluorescence images of *Adh5*^{-/-}*Csb*^{m/m} and control kidney sections stained with Kim-1 and DAPI at 20x and 40x taken from mice aged 12 months. **c)** Feature plots of *Cyr61*, *Spp1* and *B2m* expression from PT sub-clusters of *Csb*^{m/m} and *Adh5*^{-/-}*Csb*^{m/m} cells.

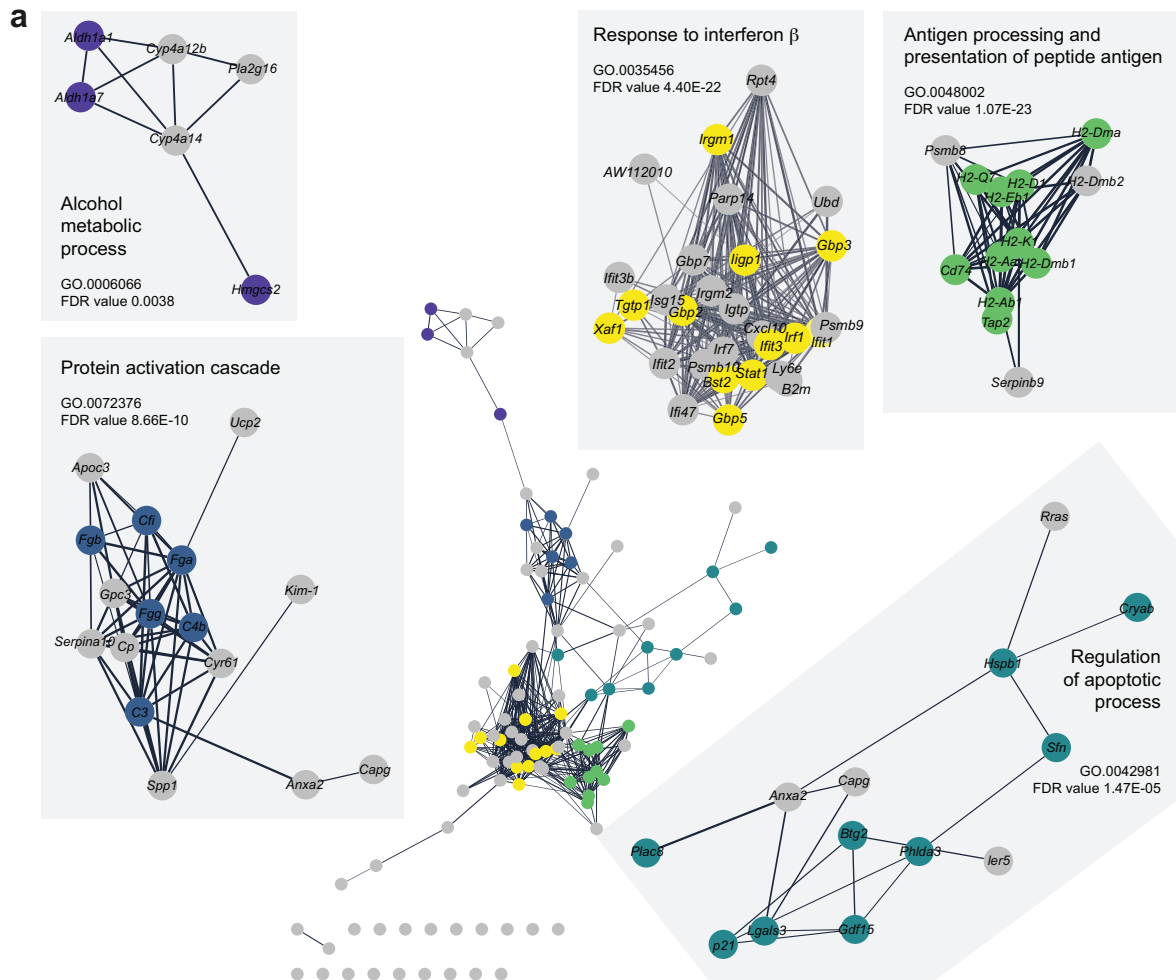


Figure 6.06 – Top 100 DEGs expressed in PT4 subcluster

Network of top 100 marker genes from PT sub-cluster PT-4 (marker genes were calculated by comparing expression of genes in PT-4 to all other PT cells). Data visualised in cytoscape v3.7.1 using the STRING app. Nodes are coloured based on top GO term enrichment pathway.

Finally, there was an enrichment of protein activation cascade genes in PT-4 cells, which included markers of kidney injury (*Kim-1*, *Cyr61*, *Spp1*) but also fibrinogen genes, which are known to be elevated in kidney injury and may play a role in remodeling damaged tissue (J. Liu et al., 2017). Taken together this suggests that the PT-4 sub-cluster cells are triggering the inflammation that we can observe in the kidneys of *Adh5^{-/-}Csb^{m/m}* mice (Figure 4.12).

To confirm the presence of inflammation, we focused on the immune cells present in the scRNA-seq data. Firstly, by assessing the composition of immune cells in each genotype, it was clear that there was an increase in the number of immune cells in the *Adh5^{-/-}Csb^{m/m}* kidneys, particularly mononuclear phagocyte (MNP) cells (Figure 6.07a). When considering the differential gene expression between the immune cell clusters, the most transcriptionally altered in *Adh5^{-/-}Csb^{m/m}* kidneys were the MNP and T_NK cell types. MNP UMAPs revealed that there was a large increase in tissue resident macrophages (Figure 6.07c-d). This data suggests that there is indeed inflammation in the *Adh5^{-/-}Csb^{m/m}* kidneys most likely triggered by the PT-4 cells in agreement with the notion that macrophages are recruited to clear dead cells.

6.4 *Adh5^{-/-}Csb^{m/m}* PT cells express GDF15

When considering differential gene expression in cells within the PT-4 cluster, cells obtained from *Adh5^{-/-}Csb^{m/m}* kidneys showed increased expression of several genes compared with wild type and allelic controls, including *p21* and *Gdf15* (Figure 6.06a). Expression of both these genes were elevated in the PT-4 cluster of *Adh5^{-/-}Csb^{m/m}* cells compared to control PT cells (Figure 6.08a-b and Figure 6.09a). *p21* is a cell cycle inhibitor and DNA damage checkpoint protein (Campisi & D'Adda Di Fagagna, 2007; Espinosa et al., 2003). *Gdf15* encodes a protein of the transforming growth factor- β (TGF- β) superfamily that is a well-known appetite suppressor (Mullican et al., 2017). Both *p21* and GDF15 are induced when cells undergo senescence, a well-established outcome of p53 activation (Basisty et al., 2020; Campisi & D'Adda Di Fagagna, 2007; H. Park et al., 2016). p53 activation can trigger many cellular processes including cell cycle arrest and apoptosis, indeed we identified additional p53 target genes which were induced in *Adh5^{-/-}Csb^{m/m}* PT cells (Figure 6.09a-b). This indicates that expression of *Gdf15* and *p21* are likely to be a consequence of a generalised p53 transcriptional response in these cells, possibly triggered by DNA damage. Finally, we confirmed expression of *Gdf15* mRNA in the PT cells of *Adh5^{-/-}Csb^{m/m}* by RNA *in situ* hybridisation (Figure 6.08c).

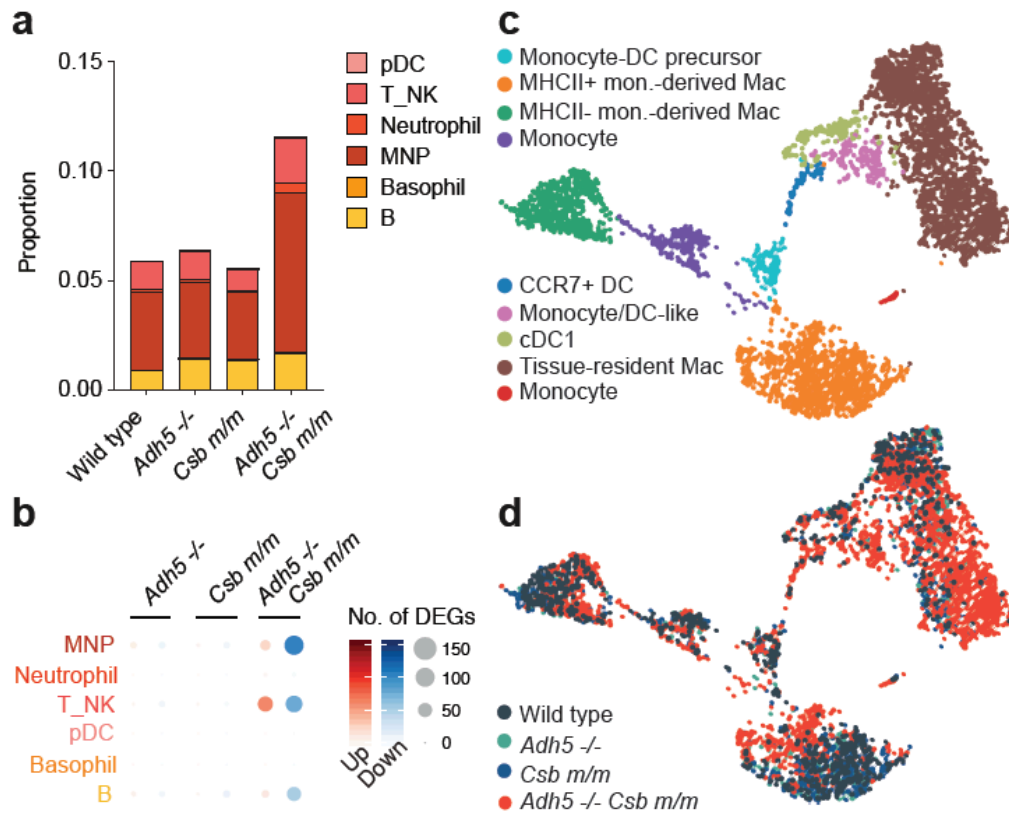


Figure 6.07 – Evidence of inflammation in *Adh5*^{-/-} *Csb*^{m/m} kidneys

a) Bar chart indicating the proportion of immune cells in single cell data sets for each genotype. **b)** Dot plot indicating the number of differentially expressed genes in each immune cell type in *Adh5*^{-/-}, *Csb*^{m/m} and *Adh5*^{-/-} *Csb*^{m/m} mice relative to wild type. **c)** Feature plot of the different cell types that comprise the MNP cluster. **d)** Feature plot of the MNP cluster with genotypes organised by colour.

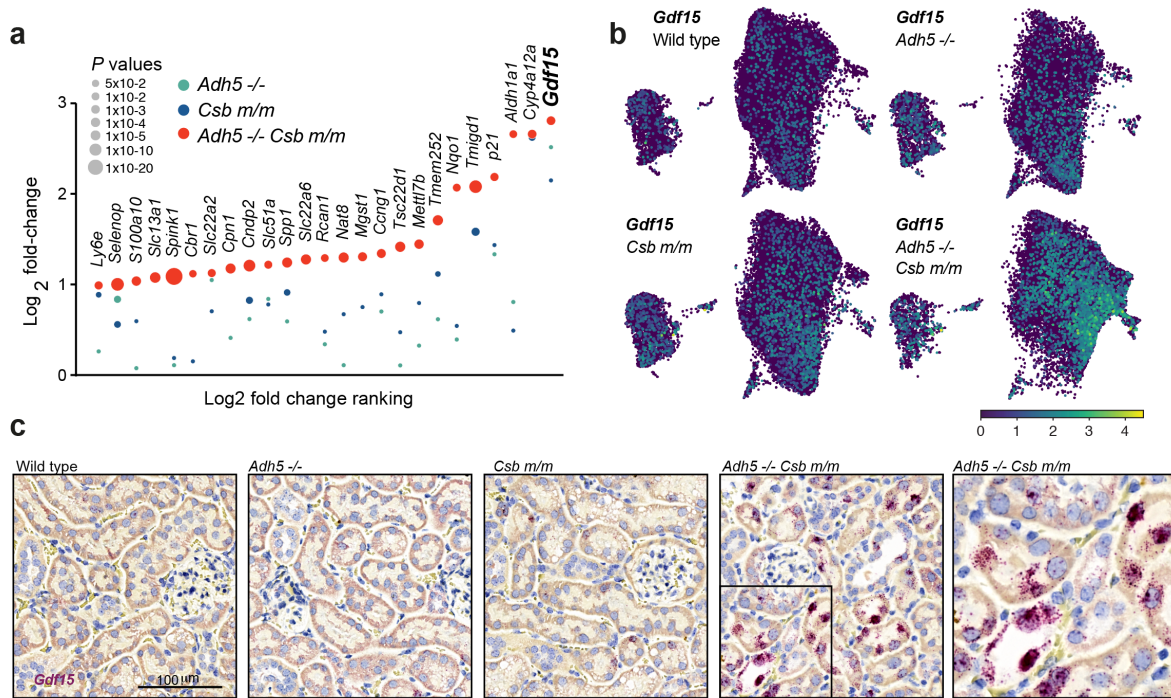


Figure 6.08 – Evidence of GDF15 expression in *Adh5*^{-/-}*Csb*^{m/m} PT cells

a) Log₂ fold change plot of DEGs from PT-4 made relative to wild type PT-4 cells. **b)** Feature plots of *Gdf15* expression from PT sub-clusters of *Adh5*^{-/-}*Csb*^{m/m} cells and controls. **c)** Representative images of *in situ* hybridisation for *Gdf15* mRNA (red spots) performed on *Adh5*^{-/-}*Csb*^{m/m} and control kidney sections, n=3.

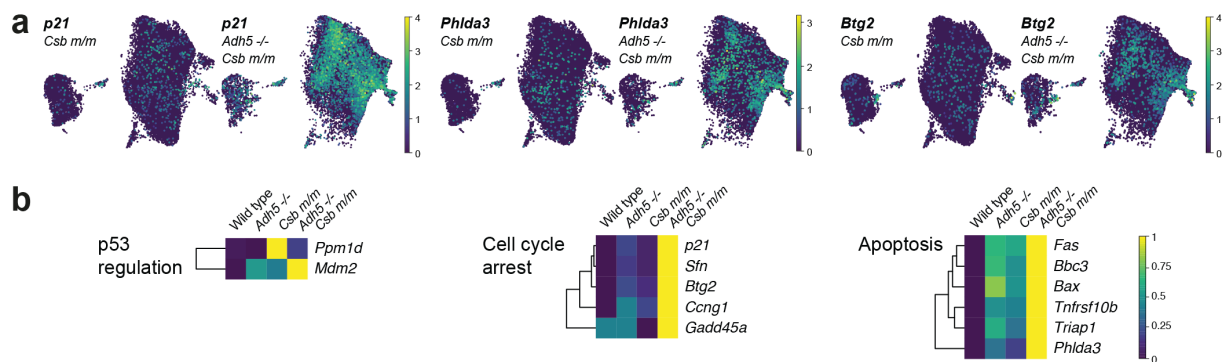


Figure 6.09 –p53 activation in *Adh5*^{-/-}*Csb*^{m/m} PT cells

a) Feature pots of the *p53* targets *p21*, *Phlda3* and *Btg2* from PT sub-clusters of *Csb*^{m/m} and *Adh5*^{-/-}*Csb*^{m/m} cells. **b)** Heatmap of expression of *p53* target genes in PT cells of *Adh5*^{-/-}*Csb*^{m/m} and control mice.

6.3 Discussion

The kidney is a complex organ composed of many different epithelial cell types along with an array of supporting vascular, stromal and immune cells. This complexity makes understanding the pathophysiology of this organ in disease states very difficult. Recently, sc-RNA sequencing has made it possible to generate a comprehensive gene expression atlas of cell types in the mouse kidney and to map the expression of disease associated genes to specific cell types. For example, expression of genes associated with hereditary defects that lead to proteinuria all mapped to the podocytes (J. Park et al., 2018). These epithelial cells are in the glomerulus and help form the filtration barrier and provide selectivity of filtration thereby preventing leakage of protein into the filtrate resulting in proteinuria. Similarly, the distal segment of the nephron that regulated sodium balance in the blood expressed genes that are associated with hereditary monogenic disorders in blood pressure (J. Park et al., 2018).

Kidney failure in CS is complex and many degenerative pathological findings have been observed. These range from defects in the tubules including tubular atrophy, to defects in the glomerulus thickening of the basement membrane and glomerulosclerosis (Stern-Delfils et al., 2020). Some of these defects may be secondary changes that obscure the underlying pathology. *Adh5^{-/-}Csb^{m/m}* mice show progressive loss of kidney function; finally succumbing to kidney failure, with the end-stage state of the kidney revealing many secondary degenerative changes. Histological examination of young *Adh5^{-/-}Csb^{m/m}* mice suggested that the underlying defect may be tubular in origin, but more detailed analysis was needed to understand why the kidney failed.

In this chapter, we have used a scRNA-seq approach to determine the cellular composition and map expression differences between the *Adh5^{-/-}Csb^{m/m}* kidneys and the allelic controls. Sequencing of 106,531 murine kidney cells resulted in a detailed transcriptional profile for each genotype and revealed that the PT cells were strikingly different in *Adh5^{-/-}Csb^{m/m}* kidneys. Further analysis of the PT cells identified a subset of cells that were unique to the *Adh5^{-/-}Csb^{m/m}* kidneys, their gene expression pattern revealed that these cells are damaged, activating an inflammatory response and a p53 response.

Previously we have identified that there are high levels of formaldehyde modified DNA in the *Adh5^{-/-}* and *Adh5^{-/-}Csb^{m/m}* kidneys (Figure 5.01b), however, only in the absence of CSB do we observe kidney failure associated with PT damage, inflammation and activation of p53

targets. CSB is critical in the response to transcription stress caused by formaldehyde; therefore, it is plausible that persistent transcriptional stress in the PT cells can activate p53. In agreement with this, p53 activation has been previously described in the brains of *Csb^{m/m}* mice (Jaarsma et al., 2011). The p53 targets that were most strongly expressed in the *Adh5^{-/-} Csb^{m/m}* PT cells were those associated with cell cycle arrest and to a lesser extent apoptosis (Figure 6.09b). This suggests that while some PT cells may be undergoing apoptosis there is a stronger signal for these cells to cell cycle arrest. Permanently arrested cells enter a state known as cellular senescence which has been previously observed in cells deficient in the CS proteins (Cordisco et al., 2019; Crochemore et al., 2019). Therefore, in response to increased formaldehyde transcriptional stress, perhaps the PT cells adopt this cellular state via a p53 route.

Senescence accumulation has been proposed to be a driver of chronic kidney disease in aged humans and mice (Docherty et al., 2019; Valentijn et al., 2018). Causative evidence comes from a mouse model that, via a p16 clearance mechanism, can remove naturally occurring senescent cells. Here, mice that have senescent cells removed do not suffer from age related kidney decline (Baker et al., 2016). Furthermore, in response to DNA damage, kidney failure has been observed in a mouse model that has PT specific loss of the DNA damage response kinase ATR. Here, PT cells display elevated p53, cell cycle arrest and are driven into a senescent state (Kishi et al., 2019). Therefore, there is precedence for PT cells to become senescent in response to DNA damage. It is noteworthy that in this example, cisplatin was used as a DNA damaging agent that has overlapping features with formaldehyde in terms of the types of DNA damage it can cause.

Finally, we observe high levels of *Gdf15* expression in the PT cells of *Adh5^{-/-} Csb^{m/m}* kidneys. *Gdf15* contains a p53 binding sequence so is likely part of the p53 response in the PT cells (Osada et al., 2007). The *Gdf15* gene codes for an anorexic hormone whose receptor lies in the brain (Mullican et al., 2017). Cisplatin, which is known to cause similar DNA lesions to formaldehyde, has also been shown to cause PT damage and leads to an increase circulating GDF15. In this context, GDF15 leads to cachexia through food aversion (Hsu et al., 2017a). Therefore, it is possible that the GDF15-GFRAL axis plays a role in the *Adh5^{-/-} Csb^{m/m}* cachexia phenotype through food aversion.

Chapter 7

Formaldehyde transcriptional stress triggers an anorexic DNA damage response

A striking yet unexplained feature of CS is severe growth retardation and cachexia (Laugel, 2013). This imparts a 'bird like' facial appearance in CS children due to loss of peri-orbital fat. Many CS patients have poor appetites and it is common for these individuals to require enteral feeding tubes to sustain essential nutrition (Kubota et al., 2015; B. T. Wilson et al., 2016). Our scRNA-seq analysis revealed a marked induction of *Gdf15* mRNA levels in the PT cells of *Adh5^{-/-}Csb^{m/m}* kidneys. GDF15 has recently been shown to be an anorexic hormone, and the GDF15 receptor GFRAL is restricted to a region in the brainstem that is important for feeding behaviour (Hsu et al., 2017a). Therefore, in the following chapter we will determine if GDF15 could play a causative role in the cachexia of CS by triggering an anorexic response.

7.1 CSB suppresses formaldehyde induced GDF15 secretion

Adh5^{-/-}Csb^{m/m} mice display severe growth failure associated with progressive loss of fat (Figure 4.06a-d), the kidneys from these mice express high levels of *Gdf15* (Figure 6.08a-c). However, for GDF15 to exert its effects as an anorexic hormone it must travel to the GFRAL receptor in the brain (Hsu et al., 2017a). Mice deficient in GDF15 or GFRAL do not suffer from the weight loss effects of cisplatin, highlighting the role of this axis in DNA damage driven cachexia. For this axis to play a role in our model, serum levels in the *Adh5^{-/-}Csb^{m/m}* mice would have to be higher than the allelic controls.

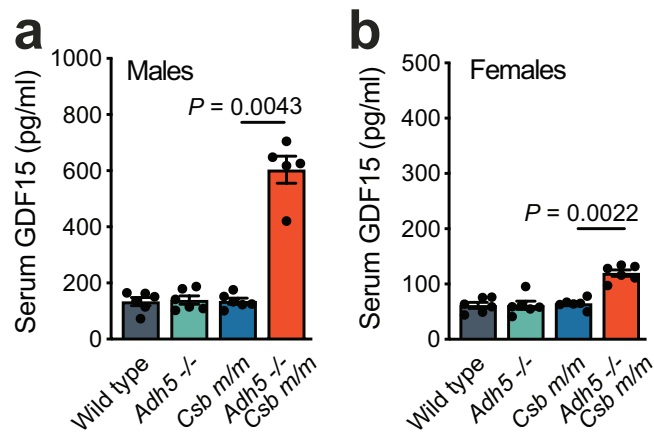


Figure 7.01 – *Adh5*^{-/-} *Csb*^{m/m} mice have elevated serum GDF15

a-b) Serum levels of GDF15 in male (a) and female (b) *Adh5*^{-/-}*Csb*^{m/m} mice with controls measured by ELISA. *P* calculated by two-sided Mann-Whitney test; data shown as mean and s.e.m; *n*= 6, 6, 6, 5 for males and *n*= 6 for females.

A GDF15 ELISA revealed that increased serum levels of GDF15 could be observed in the *Adh5^{-/-}Csb^{m/m}* mice. Strikingly, we found a 4.5-fold and 1.9-fold increase in the serum GDF15 levels in male and female *Adh5^{-/-}Csb^{m/m}* mice, respectively (Figure 7.01a-b). This correlates with our observation that *Adh5^{-/-}Csb^{m/m}* males displayed very marked growth retardation and age-dependent loss of fat compared to females (Figure 4.06a-b).

We next tested if an exogenous source of formaldehyde could induce GDF15 in females and precipitate weight loss. Female *Adh5^{-/-}Csb^{m/m}* mice and controls were challenged with 1.5g/kg dose of weekly I.P. methanol exposure (Figure 7.02a). Indeed, methanol exposure led to a 6.7- fold increase in the levels of serum GDF15 in *Adh5^{-/-}Csb^{m/m}* females, which is 13-fold higher than untreated wild type controls (Figure 7.02b). This was coupled to the induction of GDF15 expression in the PT cells of methanol exposed *Adh5^{-/-}Csb^{m/m}* females by scRNA-seq (Figure 7.02c). Finally, we monitored the weight of these mice over the 10-week duration of the experiment and found that the methanol-treated *Adh5^{-/-}Csb^{m/m}* mice display a marked reduction in weight (Figure 7.02d).

7.2 GDF15 expression is restricted to the kidney in *Adh5^{-/-}Csb^{m/m}* mice

Whilst our scRNA-seq data shows that PT cells express *Gdf15*, we wanted to assess if other organs known to secrete this hormone contributed to the serum levels observed in *Adh5^{-/-}Csb^{m/m}* mice. Recently, this has been done by RNA *in situ* hybridization to assess which tissues express *Gdf15* in response to metformin, a drug used to treat diabetes (Coll et al., 2020). We employed this technique to assess colon, small intestine, skeletal muscle, liver and kidney in 1-year-old *Adh5^{-/-}Csb^{m/m}* male mice alongside controls (Figure 7.03a-b). As expected, *Gdf15* mRNA was elevated in *Adh5^{-/-}Csb^{m/m}* kidney tissue but not in colon, small intestine, skeletal muscle or liver. We did however notice some expression in kidney medullary cells in addition to PT cells (Figure 7.03b). This observation prompted us to assess other kidney cells in the scRNA-seq dataset. Although not significant, *Gdf15* expression was present in more *Adh5^{-/-}Csb^{m/m}* loop of Henle (LOH) cells and collection duct (CD) cells with a higher mean expression level. Methanol exposed *Adh5^{-/-}Csb^{m/m}* females also express *Gdf15* in more LOH cells with a higher mean expression level (Figure 7.03c-f). This suggests that the kidney is a major source of GDF15 in *Adh5^{-/-}Csb^{m/m}* mice, although the PT cells are not the only site of expression.

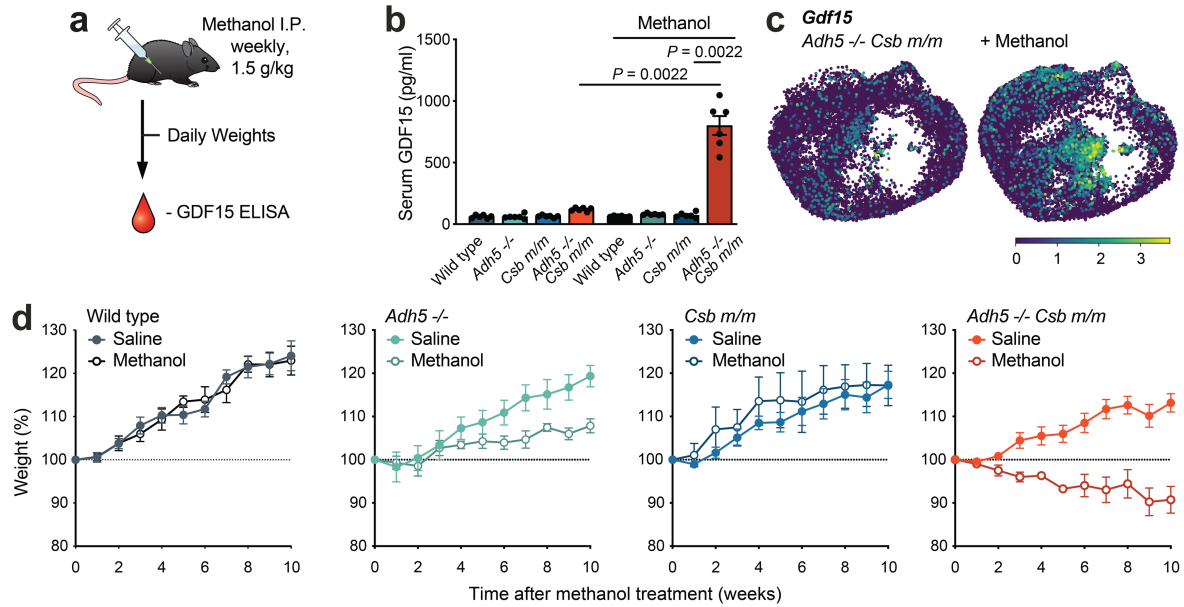


Figure 7.02 – Methanol triggers weight loss and increased secretion of renal GDF15 in *Adh5*^{-/-}*Csb*^{m/m} mice.

a) Scheme outlining methanol challenge and GDF15 measurements **b)** Serum GDF15 levels in female mice following 5 weeks of treatment with methanol or saline (P calculated by two-sided Mann-Whitney test; data shown as mean and s.e.m.; $n = 6$). **c)** Feature plots of *Gdf15* expression from PT cells of *Adh5*^{-/-}*Csb*^{m/m} female mice, exposed to methanol or saline. **d)** Weekly weights of female mice exposed to methanol or saline, data shown as mean and s.e.m.; $n = 4$.

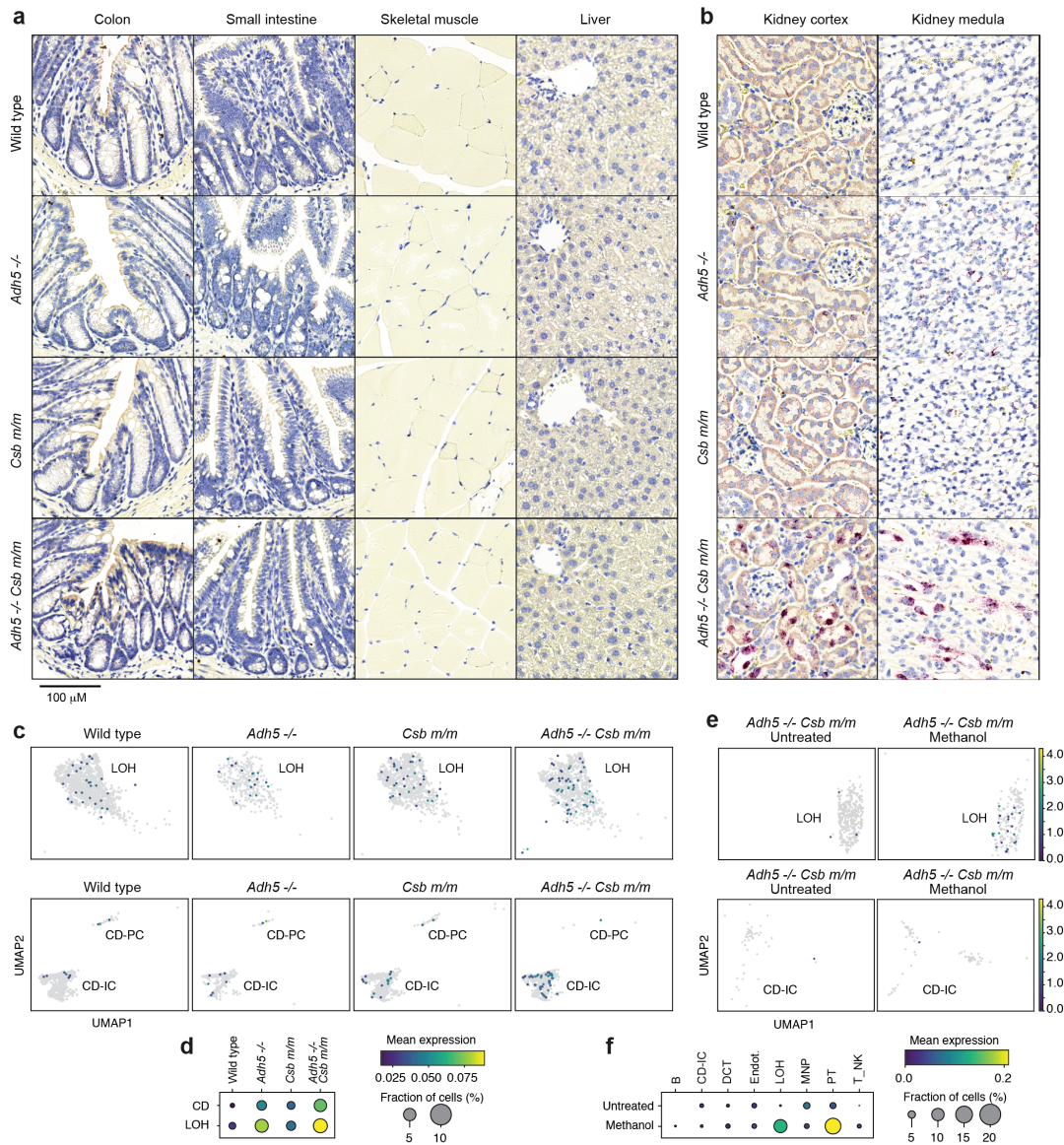


Figure 7.03– *Gdf15* expression in mouse tissues

a-b) Representative images of *in situ* hybridisation for *Gdf15* mRNA (red spots) performed on *Adh5*^{-/-} *Csb*^{*m/m*} and control kidney sections, *n*=3 **c)** Feature plots of *Gdf15* expression from LOH and CD cells for *Adh5*^{-/-} *Csb*^{*m/m*} and control mice. **d)** Dot plot of mean expression and fraction of cells expressing *Gdf15* in the loop of henle (LOH) and collecting duct (CD) for *Adh5*^{-/-} *Csb*^{*m/m*} and control mice. **e)** Feature plots of *Gdf15* expression from LOH and CD cells for *Adh5*^{-/-} *Csb*^{*m/m*} mice treated with methanol or untreated. **f)** Dot plot of mean expression and fraction of cells expressing *Gdf15* in *Adh5*^{-/-} *Csb*^{*m/m*} mice treated with methanol or untreated.

7.3 GDF15 triggers metabolic changes in *Adh5^{-/-}Csb^{m/m}* mice

Although the GDF15-GFRAL axis is a well-established anorexic endocrine circuit that can contribute to weight loss (Hsu et al., 2017a; Mullican et al., 2017), *Adh5^{-/-}Csb^{m/m}* mice may be lean due to GDF15-independent mechanisms. To assess the metabolic profile of *Adh5^{-/-}Csb^{m/m}* mice we performed calorimetry, which measures energy metabolism and open field, as a surrogate for activity levels. Calorimetry revealed a slight increase in respiratory exchange rate (R.E.R), a ratio of oxygen inhalation and carbon dioxide exhalation, which is an estimate of respiratory quotient and reveals the source of energy (carbohydrate or lipid) being used. As a higher R.E.R suggests that carbohydrate is being used as an energy source rather than fat, the elevated R.E.R in *Adh5^{-/-}Csb^{m/m}* mice is likely to result from the reduced fat reserves in these animals (Figure 7.04a). Increased energy expenditure could be a plausible alternative explanation for the extreme cachexia in *Adh5^{-/-}Csb^{m/m}* mice; however, the calorimetry data suggest that the energy expenditure is not elevated in these mice (Figure 7.04b). In agreement with the calorimetry analysis, the open field assessment revealed that there was no increase in the activity levels of *Adh5^{-/-}Csb^{m/m}* mice and that they were in fact indistinguishable from littermate controls (Figure 7.04c).

Increased GDF15 results in reduced food intake and improved glucose tolerance (Coll et al., 2020; Day et al., 2019a). To assess if these changes were present in *Adh5^{-/-}Csb^{m/m}* mice, we monitored food intake for 5 weeks and revealed a lower food intake (Figure 7.04d). Next, we performed a glucose tolerance test to determine if *Adh5^{-/-}Csb^{m/m}* mice have improved glucose tolerance. In agreement with the serum GDF15 levels, male *Adh5^{-/-}Csb^{m/m}* mice displayed marked improvement in their glucose metabolism while *Adh5^{-/-}Csb^{m/m}* females did not. Taken together these data suggest that the cachexia in *Adh5^{-/-}Csb^{m/m}* mice may be mediated by GDF15 and is unlikely to be due to increased metabolism.

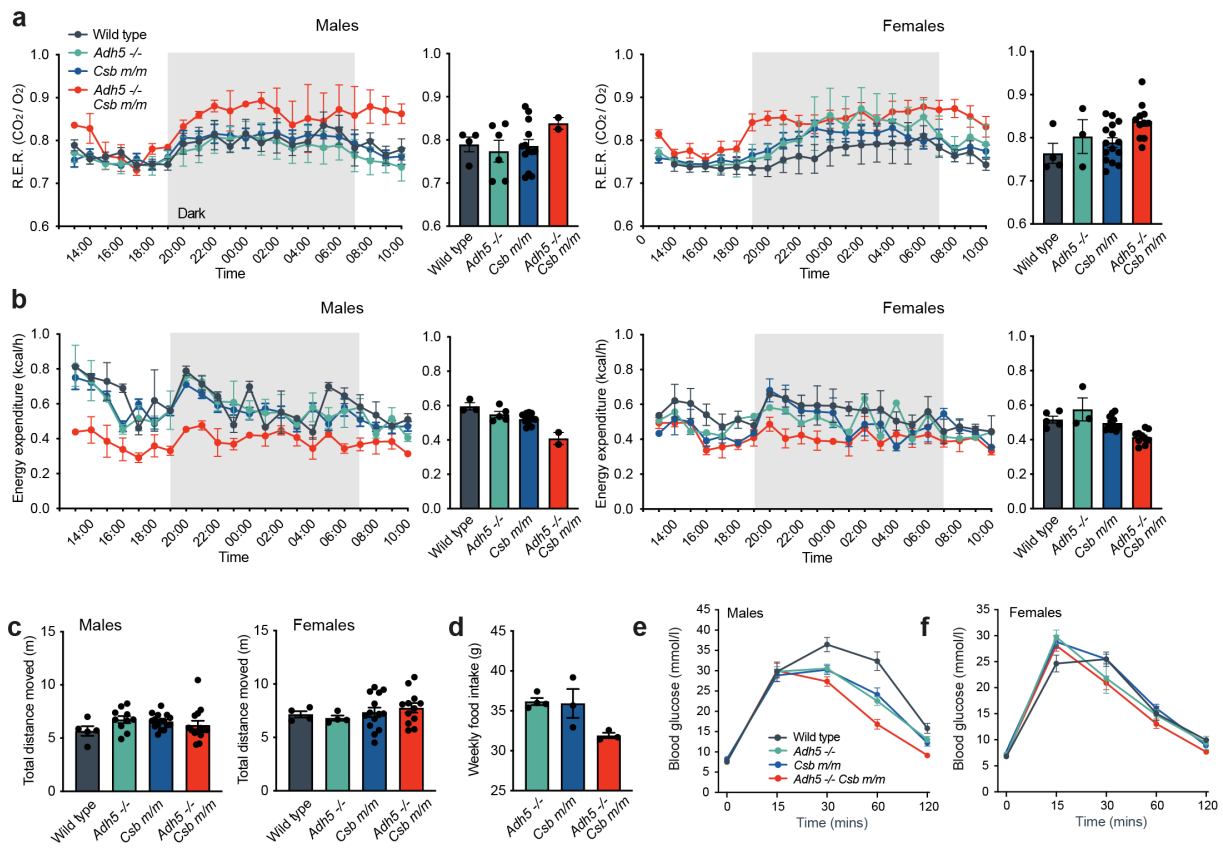


Figure 7.04 Metabolic analysis of *Adh5*^{-/-}*Csb*^{m/m} mice

a-b) Male and female mice were placed in metabolic chambers and respiratory exchange rate (R.E.R) and energy expenditure were measured over a 20-hour period, data shown as mean and s.e.m. $n = 3, 5, 13$ and 2 for males and $n = 7, 4, 11$ and 10 for females. **c)** Male and female mice were placed in open field chambers and activity was measured over 20 minutes, data shown as mean and s.e.m ($n=5, 10, 16$ and 14 for males and $n= 4, 4, 14$ and 12 for females). **d)** Bar chart of weekly food intake from *Adh5*^{-/-}*Csb*^{m/m} and control mice singly housed and averaged out over 5 weeks, data shown as mean and s.e.m, $n=3$. **e)** Glucose tolerance test performed in males and **f)** females ($n=7, 15, 18, 16$ for male wild type, *Adh5*^{-/-}, *Csb*^{m/m}, and *Adh5*^{-/-} *Csb*^{m/m} mice and $n= 6, 4, 16, 13$ for female wild type, *Adh5*^{-/-}, *Csb*^{m/m}, and *Adh5*^{-/-} *Csb*^{m/m} mice.)

7.4 CSB suppresses a p53-dependent anorexic response

GDF15 is also released after exposure to platinum-based chemotherapeutic agents such as cisplatin (Borner et al., 2020a; Breen et al., 2020; Hsu et al., 2017a). However, the molecular mechanism of GDF15 secretion remains unclear. Like formaldehyde, cisplatin induces DNA damage which is repaired by TC-NER (Enoiu et al., 2012a). We exposed wild type and *Csb^{m/m}* mice to cisplatin and monitored the weight and serum GDF15 levels in these animals (Fig. 5e). When wild type mice were exposed to a low dose of cisplatin, we observed no weight loss or induction of serum GDF15. In contrast, *Csb^{m/m}* mice rapidly lost weight and showed a 5-fold induction of serum GDF15, linking serum GDF15 secretion with the repair of cisplatin DNA lesions (Figure 7.05a).

Next, we tested if cisplatin-induced GDF15 release was dependent on the p53 DNA damage response because of the presence of a p53 response element in the 5' UTR of the GDF15 gene (Osada et al., 2007) and the activation of a p53 response in the kidney scRNA-seq data (Figure 6.09a-b). 4mg/kg weekly cisplatin I.P suppresses weight gain in wild type mice and induces a 12-fold induction of serum GDF15. In contrast, *p53^{-/-}* mice continue to gain weight and correspondingly show no induction of serum GDF15 (Figure 7.05b) or *Gdf15* mRNA in PT cells (Figure 7.05c). Taken together these cisplatin experiments show that in response to DNA damage CSB suppresses serum GDF15 levels whereas p53 is essential for increased levels of serum GDF15.

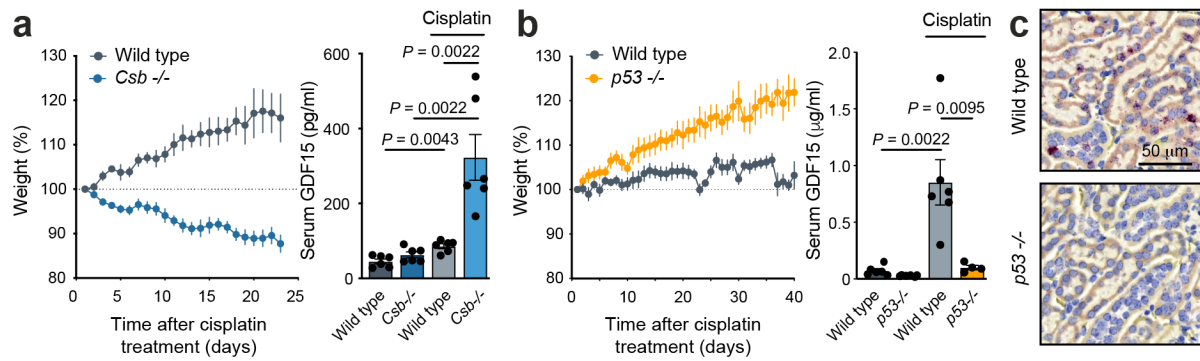


Figure 7.05 CSB suppresses a p53-dependent GDF15 anorexic DNA damage response

a) Daily weights of wild type and *Csb*^{m/m} mice exposed to weekly 0.5 mg/kg cisplatin intra-peritoneal injections alongside serum GDF15 measurements taken before and 4 weeks after weekly injections. *P* calculated using two-sided Mann-Whitney test; data shown as mean and s.e.m.; *n* = 6 mice. **b)** Daily weights of wild type and *p53*^{-/-} mice exposed to weekly 4 mg/kg cisplatin intra-peritoneal injections alongside serum GDF15 measurements taken before and 6 weeks after weekly injections. *P* calculated using two-sided Mann-Whitney test; data shown as mean and s.e.m.; *n* = 6 mice. **c)** *In situ* hybridisation for *Gdf15* mRNA (red spots) performed on wild type and *p53*^{-/-} kidney sections 24 hours after 4 mg/kg cisplatin treatment.

7.5 Blocking GDF15 alleviates cachexia in *Adh5^{-/-}Csb^{m/m}* mice

Finally, to establish if GDF15 contributes to progressive cachexia in *Adh5^{-/-}Csb^{m/m}* mice we tested the consequences of blocking this response with a previously validated GDF15 antibody (Borner et al., 2020). Male *Adh5^{-/-}Csb^{m/m}* mice received a neutralising mouse monoclonal antibody against GDF15 (Mab-1) or an isotype control, weekly, for 1 month (Figure 7.06a). First, we established that both cohorts of mice had similar weights and GDF15 basal levels (Figure 7.06b). Then, *Adh5^{-/-}Csb^{m/m}* mice that were treated with Mab-1 showed a marked and sustained increase in weight that equated to an average of 5% of the original weight. In contrast, the weights of mice treated with control antibody remained unchanged (Figure 7.06c).

Next, we tested if methanol-induced weight loss was also dependent on GDF15. In this experiment, female *Adh5^{-/-}Csb^{m/m}* mice were treated with methanol as done previously (Figure 7.02a), where we have shown that this treatment greatly induces GDF15 secretion (Figure 7.02b). After two weeks of methanol treatment, the two groups were either treated with the GDF15 antibody or sham (Figure 7.06d). First, we established again that the 2 groups had no difference in basal GDF15 levels and weight (Figure 7.06e). Then, after both groups displayed initial weight loss in response to methanol, *Adh5^{-/-}Csb^{m/m}* mice treated with Mab-1 stopped losing weight and began gaining weight. The control antibody cohort continued to lose weight (Figure 7.06f). Therefore, by neutralising the GDF15 response, triggered by formaldehyde, we have attenuated the cachexia phenotype in *Adh5^{-/-}Csb^{m/m}* mice. This data strongly indicates that GDF15 is a casual factor in the cachexia phenotype in *Adh5^{-/-}Csb^{m/m}* mice.

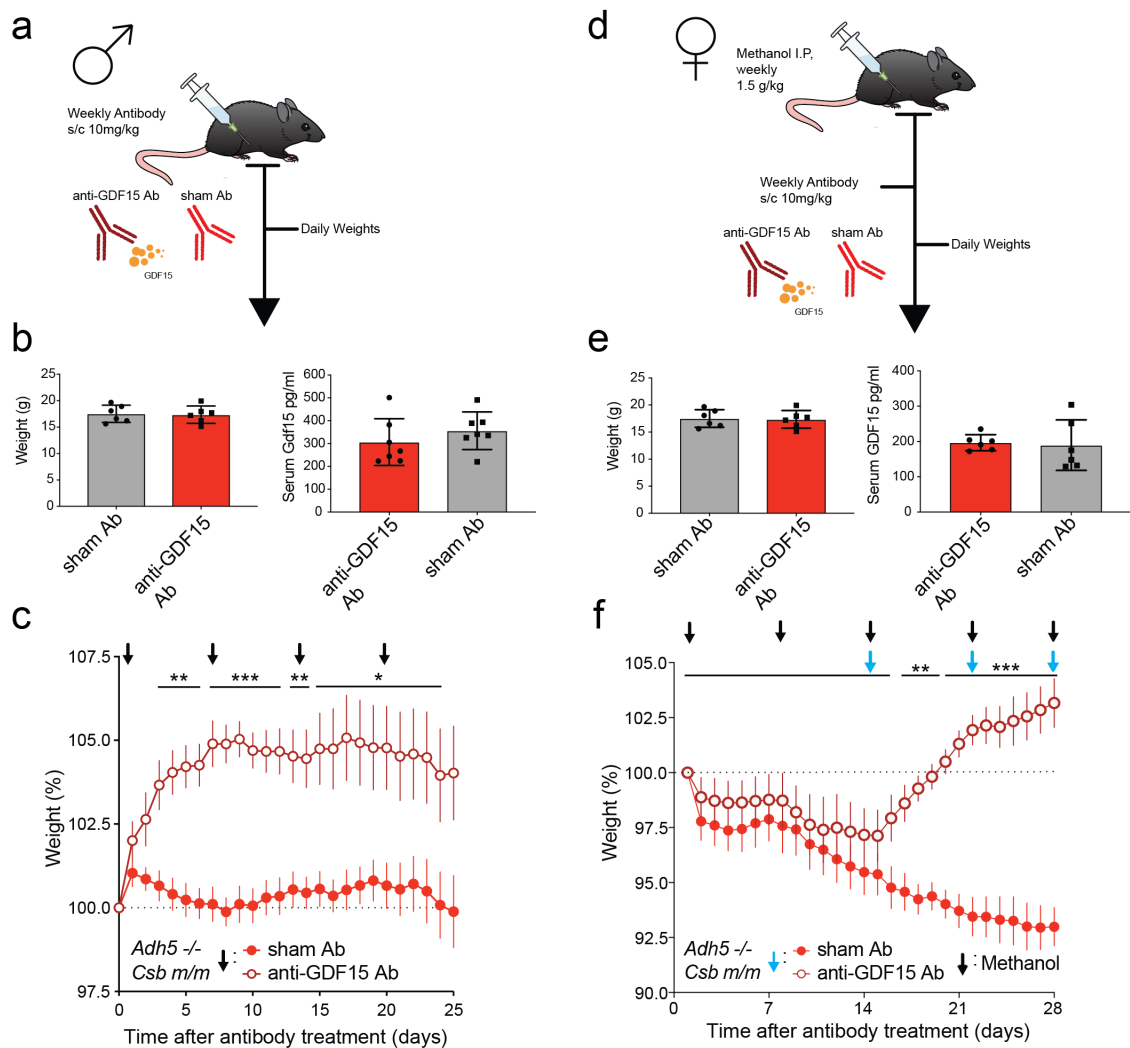


Figure 7.06 GDF15 neutralisation improves weight homeostasis

a) Model of anti-GDF15 antibody or control in $\text{Adh5}^{-/-}\text{Csb}^{m/m}$ males. **b)** Weights and serum GDF15 levels of $\text{Adh5}^{-/-}\text{Csb}^{m/m}$ males prior to antibody exposure P calculated using two-sided Mann-Whitney test; $n=7$ data shown as mean and s.e.m. **c)** 7 day rolling average percentage weight change of $\text{Adh5}^{-/-}\text{Csb}^{m/m}$ mice after treatment with either a neutralising mouse monoclonal antibody to GDF15 (anti-GDF15 Ab) or isotype control (sham Ab), P calculated using two-sided Mann-Whitney test; $n=7$ data shown as mean and s.e.m. arrow denotes day of treatment. **d)** Model of anti-GDF15 antibody or control in $\text{Adh5}^{-/-}\text{Csb}^{m/m}$ females. **e)** Weights and serum GDF15 levels of $\text{Adh5}^{-/-}\text{Csb}^{m/m}$ females prior to antibody exposure P calculated using two-sided Mann-Whitney test; $n=6$ data shown as mean and s.e.m. **f)** 7 day rolling average percentage weight change of $\text{Adh5}^{-/-}\text{Csb}^{m/m}$ mice after treatment with either a neutralising mouse monoclonal antibody to GDF15 (anti-GDF15 Ab) or isotype control (sham Ab), P calculated using two-sided Mann-Whitney test; $n=6$ data shown as mean and s.e.m. arrow denotes day of treatment.

7.6 Discussion

The data presented in this chapter confirm that *Gdf15* is expressed in the kidney in response to formaldehyde, and that GDF15 contributes to the cachexia and weight loss observed in *Adh5^{-/-}Csb^{m/m}* mice. GDF15 acts through its receptor in the brain and is an established endocrine circuit that drives weight loss through appetite suppression. Recent studies have shown that increased circulating GDF15 levels are associated with food aversive behaviour and weight loss (Borner et al., 2020b; Coll et al., 2020; Hsu et al., 2017a; Mullican et al., 2017). This has also been confirmed in animals by genetic inactivation of this endocrine circuit, resulting in the absence of food aversion and subsequent weight loss (Coll et al., 2020; Hsu et al., 2017a; Mullican et al., 2017).

Adh5^{-/-}Csb^{m/m} mice show elevated levels of serum GDF15. In response to methanol, they express *Gdf15* mRNA in the PT cells, elevate their basal serum GDF15 levels and lose weight. Expression of *Gdf15* mRNA in the *Adh5^{-/-}Csb^{m/m}* mice is restricted to the kidney, demonstrating the importance of this organ in mediating cachexia in response to DNA damage. High circulating levels of GDF15 results in food aversive behaviour and improved glucose tolerance (Coll et al., 2020; Day et al., 2019b), importantly we observed both of these in *Adh5^{-/-}Csb^{m/m}* mice and we were also able to rule out increased metabolism as an alternative explanation for the observed cachexia.

The GDF15/GFRAL axis has been best characterised in response to chemotherapy and is thought to mediate food-aversion and weight loss during cancer treatment. Cisplatin, a commonly used chemotherapeutic drug, damages DNA generating mono-adducts and intrastrand crosslinks. As this damage is repaired by TC-NER (Enoiu et al., 2012b), we hypothesised that *Csb^{m/m}* mice may respond to such an insult by losing weight in a GDF15 dependant manner. Strikingly, this occurred at a dose almost 10 times less than wild type mice (Hsu et al., 2017a). Using cisplatin also allowed us to test the requirement for p53 in the GDF15/GFRAL axis triggered by DNA damage. Many targets of p53 were elevated in the PT cells of *Adh5^{-/-}Csb^{m/m}* mice suggesting that GDF15 expression in this context was dependant on its p53 binding domain (Osada et al., 2007). Indeed, in the absence of p53 there was a complete failure of the PT cells to express *Gdf15*, an absence of elevated serum GDF15 and weight loss in response to cisplatin.

Finally, to show causality of GDF15 in the cachexia of *Adh5^{-/-}Csb^{m/m}* male mice and weight loss in response to methanol treatment in *Adh5^{-/-}Csb^{m/m}* female mice we used a GDF15

neutralising antibody. The striking effects observed in the antibody treated mice reveal the potency of the GDF15/GFRAL axis in response to DNA damage. This data therefore suggests that the GDF15/GFRAL axis may be a driver of the extreme failure to thrive observed in human CS. It is imperative that CS patients are measured for serum GDF15 levels, given the successful intervention experiments using the GDF15 mAB.

Chapter 8

Conclusions and future work

8.1 Conclusions

DNA damage can lead to a range of physiological consequences, cancer, loss of tissue homeostasis and ageing. To prevent these outcomes, DNA repair pathways have evolved to fix the many forms of damage that afflict DNA. However, in many circumstances it is still unclear how DNA damage leads to the associated physiological consequences and furthermore it remains unclear what sources of DNA damage necessitate specific types of repair. The work outlined in this thesis sheds light into whether the severe phenotype of XPF-ERCC1 deficiency is due to the loss of both NER and FA repair. It also addresses whether naturally occurring aldehydes are drivers of the NER phenotypes. Finally, after having discovered that formaldehyde can drive the CS phenotype this thesis outlines a mechanism of cachexia in CS.

8.1.1 NER and FA act independently to protect against formaldehyde genotoxicity

XPF-ERCC1 deficiency leads to severe phenotypes in mice and humans. By genetically segregating the functions of XPF-ERCC1 in different repair pathways we sought to understand which functions are required to protect cells from ICLs and preserve liver, kidney and bone marrow function. The results in chapter 3 provide evidence that joint inactivation of NER and FA repair does not explain the XPF-ERCC1 phenotype at the cellular level and in adult mice. These results suggest that XPF-ERCC1 has functions outside of the canonical excision pathways and given the phenotypic overlap between *Csb^{m/m}Xpa^{-/-}* and *Ercc1^{-/-}* mice, and the lack of a synergistic phenotype in *Xpa^{-/-}Fanca^{-/-}* mice, it is likely that a major component of the phenotype of XPF-ERCC1 deficiency results from joint inactivation of NER and CSB functions outside of NER rather than NER and ICL repair (Figure 3.14).

By using the human haploid cell line, we were able to assess the relative contribution of NER and FA in the cellular protection against ICL inducing agents. For MMC, Cisplatin and acetaldehyde, in agreement with our mouse data, we observed that XPF deficiency led to a much greater sensitivity to ICL inducing agents than combined disruption of NER and FA. However, when we exposed the cells to formaldehyde, we revealed a non-epistatic interaction between NER and the FA repair pathway, suggesting independent roles for NER and FA repair in repairing formaldehyde lesions. Given the striking role of formaldehyde in the FA phenotype (Pontel et al., 2015) we next wanted to address whether the same is true for NER phenotypes.

8.1.2 Formaldehyde drives the CS phenotype

In 1968 James Cleaver was able to link the NER genes to the repair of UV induced DNA damage (Cleaver, 1968). This observation provided a link between the phenotype of human XP patients and the source of DNA damage. Despite decades of research, the source of DNA damage that leads to the clinical phenotypes of CS has remained elusive. Here, we have been able to identify an endogenous genotoxin that blocks transcription and leads to the clinical features of CS, formaldehyde. *Adh5^{-/-}Csb^{m/m}* mice display a failure to thrive, neurological deficits and ultimately succumb to kidney failure, furthermore these phenotypes can be exacerbated by exogenous formaldehyde treatment and in tissues most affected by this phenotype we detect high levels of DNA modified by formaldehyde. Endogenous formaldehyde therefore must be considered a potent driver of the CS phenotype. Interestingly, we did not find a genetic interaction between NER and the FA pathway in response to acetaldehyde, nor did we observe any sign of an interaction between *Csb* and *Aldh2*. This suggests that these two closely related aldehydes cause a different spectra of DNA lesions and that the CS phenotype is driven specifically by formaldehyde and not acetaldehyde.

Adh5^{-/-}Csb^{m/m} mice succumb to kidney failure, reflecting an important aspect of the human phenotype and allowing us to probe into the changes that occur in these degenerating cells. We find that the PT cells are prominently affected and show signs of damage, inflammation and activation of p53 target genes. This data along with chronological histological analysis suggests formaldehyde leads to ongoing PT damage that ultimately leads to chronic kidney failure. While these findings are illuminating, the order of events are unknown as is the primary defect that leads to these pathological findings. In our view it is most likely that

formaldehyde DNA damage blocks transcription triggering p53 dependant cell cycle arrest and senescence. Although cellular senescence is cell autonomous it can lead to effects on neighbouring cells and the secretion of the senescence associated secretory phenotype, a pro-inflammatory set of cytokines that triggers immune infiltration.

While there are many negative physiological associations with chronic senescence it is well established that this cellular state prevents cancer (B. Wang et al., 2020). Perhaps then some of the responses we identify in the kidney are also active in the liver and may therefore explain why *Adh5^{-/-}Csb^{m/m}* mice do not develop cancer, unlike *Adh5^{-/-}* single mutant mice. This is akin to CS patients that are not cancer prone in contrast to Xeroderma Pigmentosum (XP) patients (Fassihi et al., 2016; Kubota et al., 2015; Laugel, 2013; B. T. Wilson et al., 2016). Indeed, CSB deficient cells are hypo-mutable following exposure to DNA damage (e.g. UV)(Reid-Bayliss et al., 2016). It is therefore plausible that unresolved transcriptional stress leads to increased resistance to neoplastic transformation via cellular senescence.

8.1.3 An anorexic DNA damage response drives cachexia in CS

The work presented in this thesis outlines a mechanism that contributes to the extreme cachexia observed in CS (Figure 8.01). Endogenous formaldehyde, which induces transcriptional stress, leads to the accumulation of formaldehyde DNA adducts in the kidney. PT cells respond by mounting a p53 response that includes expression of *Gdf15*. Cisplatin, like formaldehyde also causes transcriptional stress and is toxic to kidney PT cells, this drug stimulates GDF15 secretion in a p53 dependent manner providing a molecular mechanism for appetite suppression and weight loss caused by chemotherapeutic drugs. Blocking the GDF15/GFRAL axis has been proposed as a therapeutic option for alleviating the cachexia associated with chemotherapy (Breen et al., 2020) and, given our findings when we block this response in *Adh5^{-/-}Csb^{m/m}* mice, we now propose this could also be employed to prevent cachexia in CS.

The GDF15 response to transcriptional stress in PT cells may have evolved in mammals to detect and then cause aversion to food containing genotoxins. This might be inappropriately engaged in CS because of a failure to relieve transcriptional stress, causing these individuals to reduce food intake. It is also possible that the response is appropriate because food in CS patients might be a potential source of genotoxins such as formaldehyde, thus providing a protective mechanism.

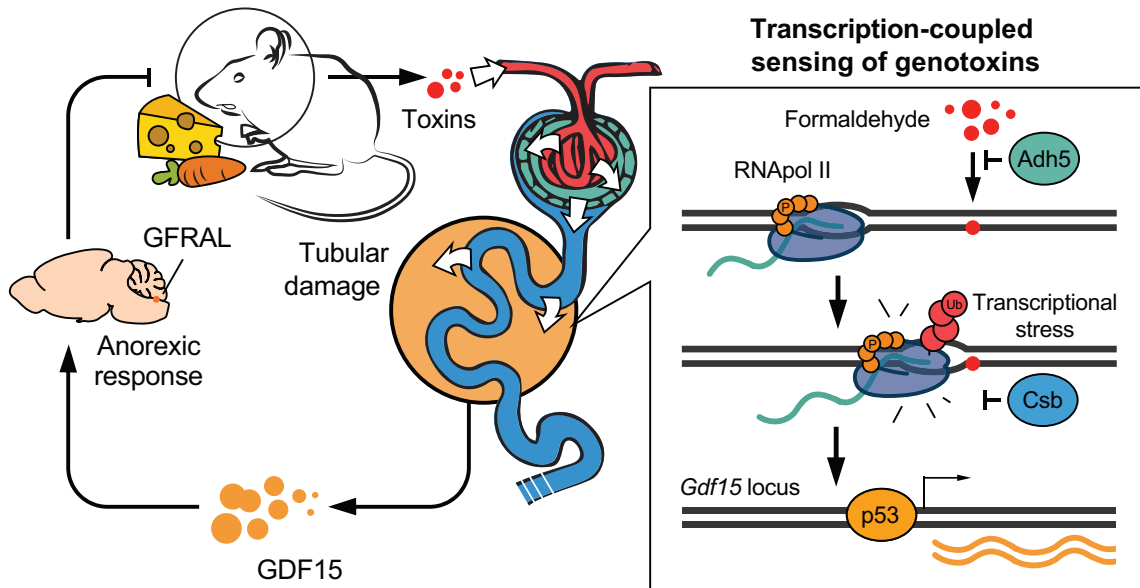


Figure 8.01 – Model of transcriptional stress triggered anorexic response

Model outlining how formaldehyde can damage the PTs and trigger release of the anorexic hormone GDF15 which results in food aversion, presumably to reduce the burden of ingested toxins. Inset, model of the molecular mechanism by which ADH5 and CSB cooperate to protect cells from formaldehyde damage, which is sensed by the stalled transcription machinery and can trigger p53 dependent activation of GDF15.

Support for nutritional genotoxicity comes from the attenuation of neurodegeneration and tubulonephrosis in caloric-restricted mice that lack the TC-NER nuclease XPF-ERCC1 (Vermeij et al., 2016). Finally, in a recent GWAS study on a large cohort of patients with anorexia nervosa, only four *loci* stood out, one of these localised to the gene coding for the DNA repair enzyme MGMT (Watson et al., 2019). Therefore, it is plausible that the induction of GDF15 by DNA damage may have broader implications for human anorectic syndromes.

The GFRAL receptor is located in the brainstem and when activated by GDF15 has been shown to bring about food aversive behaviour (Hsu et al., 2017a; Mullican et al., 2017). Our *Adh5^{-/-}Csb^{m/m}* mice display a lower food intake than allelic controls in agreement with other models of high serum GDF15. However, how activation of GFRAL brings this change in behaviour is unclear. GDF15 is an emetic and has been shown to result in vomiting and nausea, which is possibly what results in food aversion (Borner et al., 2020b; Breen et al., 2020). Therefore, blocking this response may have additional clinical benefits to improving weight homeostasis by also alleviating emesis.

Although high GDF15 is associated with food aversion and weight loss it is not clear that the decreased food intake is the sole reason for GDF15 mediated weight loss. Indeed, GDF15 is responsible for metabolic changes such as increased glucose tolerance and higher energy expenditure (Coll et al., 2020; Day et al., 2019b). One recent study genetically segregated the food aversive phenotype from the metabolic phenotype using *Atgl^{-/-}* mice (Suriben et al., 2020). Here, *Atgl^{-/-}* mice treated with GDF15 AAV displayed food aversion but not the weight loss observed in wild type mice treated with GDF15 AAV. This intriguing study therefore suggests that it is the adipose triglyceride lipase (ATGL) dependent effects on metabolism through which GDF15 triggers weight loss and not just food aversion.

8.1.4 Formaldehyde causes transcription stress

NER consists of 2 sub-pathways that have the same downstream factors but differ in the way they sense lesions, GG-NER detects helix distorting lesions through XPC and TC-NER is triggered after RNAPII stalls at the site of damage (Lans et al., 2019). We find that cells deficient in TC-NER (CSB and XPA) are sensitive to formaldehyde whereas cells deficient in XPC are not. This suggests that the lesions caused by formaldehyde do not result in helix distorting lesions but do result in transcription blocking lesions. This contrasts with UV exposure that leads to both helix distorting lesions and transcription blocking lesions requiring both GG-NER and TC-NER but is like cisplatin. The mechanism of transcriptional stalling by UV and cisplatin lesions have been previously outlined (Brueckner et al., 2007;

Damsma et al., 2007). Here, structural and biochemical work of RNAPII in complex with UV thymine-thymine intra-strand crosslinks (CPDs) and cisplatin 1,2-d(GpG) intra-strand crosslinks reveal that these lesions do indeed form an impediment to the transcribing RNAPII. Chemically, formaldehyde has also been shown to form intra-strand crosslinks (Kawanishi et al., 2014) between GG or GA bases which, given its similarity to the type of lesions caused by UV and cisplatin, may be the reason formaldehyde exposure requires TC-NER.

Despite the requirement for both CSB and XPA in the cellular protection against formaldehyde, the phenotype of *Adh5^{-/-}Csb^{m/m}* mice are much more severe than that of *Adh5^{-/-}Xpa^{-/-}* mice. This is reflected in the human patient phenotype where XPA patients are protected from the severe CS phenotype although they do suffer from additional neurological complications that are absent in XPC, XPE and XPV complementation groups (Fassihi et al., 2016). However, when *Adh5^{-/-}Xpa^{-/-}* mice were challenged with methanol we were able to reveal the CS kidney failure present in *Adh5^{-/-}Csb^{m/m}*. This suggests that there is an *in vivo* contribution of TC-NER in protection against formaldehyde and, given the lack an interaction between formaldehyde and GG-NER, the CS phenotypes in *Adh5^{-/-}Xpa^{-/-}* mice and XPA patients are likely due to loss of TC-NER.

Although XPA deficiency does not lead to the extreme CS phenotypes that are observed in CSB deficiency, mutations in *XPD*, *XPB*, *XPF*, *ERCC1* and *XPG* can give rise to CS (Bogliolo et al., 2013; Kashiwama et al., 2013; Natale & Raquer, 2017). Here, like XPA, the GG-NER pathway is also disabled and therefore, helix-distorting lesions that also block transcription may compound the TC-NER defect. The question then is why do XPA patients not develop the CS phenotype? The explanation may lie in what is left behind at the site of the lesion when different NER factors are absent. In the case of CSB or CSA deficiency the RNAPII remains stalled at the site of the lesion. XPA deficiency would allow CSB to initiate RNAPII backtracking or removal and therefore the lesion would be accessible to other repair factors, but no NER pre-initiation complex would form. Deficiency of the TFIIH factors or nucleases however would trigger persistent repair protein presence (Fan et al., 2008; Sabatella et al., 2018), without the ability to complete the NER process. Therefore, the CS phenotypes in CSA and CSB may be due to persistent RNAPII stalling, whereas deficiency in the TFIIH factors and nucleases result in CS due to NER proteins persisting at the site of the lesion.

Alternatively, the CS phenotype may be due to the combined loss of TC-NER and functions of CSB outside of the canonical TC-NER pathway. As mentioned above, the best evidence for this is that mouse phenotypes of XPC and XPA are made far worse by combined ablation with CSB (Van Der Pluijm et al., 2007). It is therefore possible that formaldehyde interacts with TC-NER and these other functions of CSB. One such function could be CSB's role in preventing RNAPII degradation in response to DNA damage (Tufegdžić Vidaković et al., 2020). Indeed, we show that formaldehyde can trigger the ubiquitination and degradation of RNAPII and that both ADH5 and CSB cooperate to prevent this. At the physiological level, mice with a point mutant in the RNAPII, resulting in no degradation after DNA damage, also display a CS phenotype when crossed with XPA mice, despite having intact CS proteins (Nakazawa et al., 2020). This cross suggests that maintaining RNAPII pools is critical in protecting against CS.

CSB has also been implicated in other transcriptional coupled repair responses outside of TC-NER. The yeast homologue of CSB has been shown to perform lesion bypass over small DNA lesions without triggering the canonical TC-NER route to repair (J. Xu et al., 2017). Therefore, given the ability for formaldehyde to cause many lesions, perhaps the GG or GA intrastrand crosslinks require TC-NER but other formaldehyde adducts can be bypassed by CSB alone, explaining the more severe CSB phenotype in mice crossed with ADH5.

One hypothesis for the CS phenotype is that oxidative damage is the driving force, oxidative damage is preferentially repaired using Base Excision Repair (BER) and there is evidence that this can be coupled to transcription (Guo et al., 2013). Indeed, CSB appears to have a role in this process while XPA is dispensable thereby separating TC-NER and CSB (Menoni et al., 2012). However, oxidative lesions are unlikely to block RNAPII themselves (Charlet-Berguerand et al., 2006), more likely it is the repair process itself that forms the block to transcription. In other words, oxidative damage triggers BER that then forms a temporary transcription block that requires CSB. Indeed, differential CSB responses have been observed when cells are treated with a classical transcription-blocking agent such as UV and oxidative damage (Ranes et al., 2016). However, *in vivo* evidence that oxidative damage causes the CS phenotype is lacking and in the context of formaldehyde, no requirement for BER has been reported. Additionally, we find that the CSB mutant that is proficient in TC-NER but cannot respond to oxidative damage was not sensitive to formaldehyde.

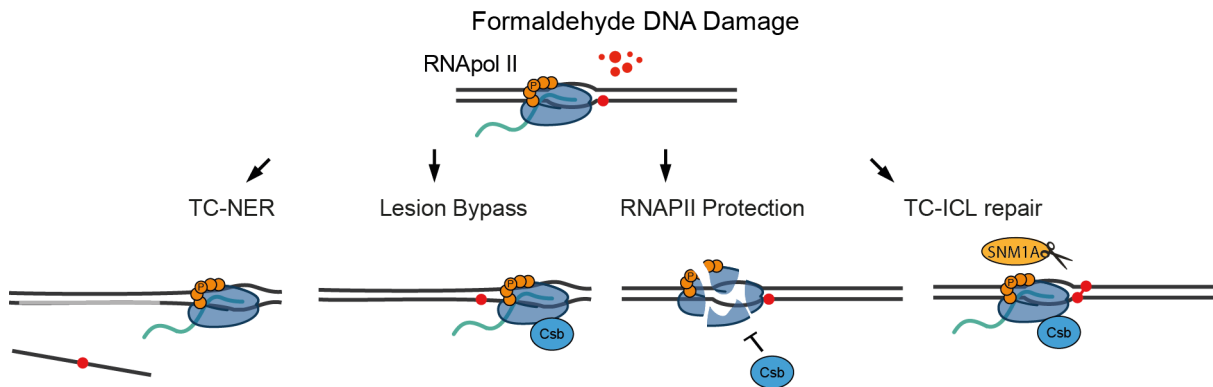


Figure 8.02 – Functions of CSB

Model outlining how formaldehyde DNA damage could lead to many CSB mediated responses such as transcription coupled nucleotide excision repair (TC-NER), lesion bypass, the protection of RNAPII degradation and transcription-coupled interstrand crosslink repair.

It seems unlikely then that formaldehyde results in the CS phenotype via CSB's role in oxidative damage repair. Formaldehyde DNA damage does however require repair via FA repair (Pontel et al., 2015; Rosado et al., 2011); therefore it is possible other DNA repair transactions are present that may interfere with transcription. Or perhaps, given the ability of formaldehyde to form ICL's, CSB repairs these lesions in a transcription coupled manner. Such a pathway has been described which has been reported to repair ICL's in combination with the nuclease SNM1A in cells that divide less frequently (A. T. Wang et al., 2011). Therefore, in *Adh5^{-/-}Csb^{m/m}* mice the severe phenotype could be a consequence of loss of TC-NER in combination with loss of transcription-coupled ICL repair.

In summary, formaldehyde DNA lesions must lead to transcription stress that requires TC-NER. This transcription stress also leads to the ubiquitination and degradation of the RNAPII. At the physiological level, formaldehyde reveals CS in CSB deficient mice but not XPA deficient mice, although there is evidence that some CS phenotypes emerge in *Adh5^{-/-}Xpa^{-/-}* mice. This is unlikely to be due to GG-NER deficiency in *Adh5^{-/-}Xpa^{-/-}* mice, as there appears no requirement for GG-NER to protect against formaldehyde. CSB therefore must protect against formaldehyde genotoxicity in a manner independent from XPA. Attempting to identify which of these processes take place in, for example, the PT cells of *Adh5^{-/-}Xpa^{-/-}* mice but not *Adh5^{-/-}Csb^{m/m}* mice may unravel the function of CSB outside TC-NER that protects against physiological formaldehyde and therefore explain the molecular mechanism underlying CS.

8.2 Future directions

The work contained in this thesis places formaldehyde as an endogenous genotoxin that can lead to the CS phenotype. Furthermore, it has led to insight into the nature of the CS phenotype and reveals a mechanism underlying the cachexia that is a prominent hallmark of this disease. However, key questions remain.

8.2.1 Formaldehyde and the brain

Why the brain degenerates in CS is poorly understood. Patient data has revealed a number of pathological changes in the brain such as hypo myelination, white matter loss, cerebellar atrophy and cortical calcifications but an underlying mechanism remains elusive (Koob et al., 2010; B. T. Wilson et al., 2016). Interestingly, while *Csb^{m/m}* mice lack any behavioural phenotype there is presence of mild neurological features of p53 activation and activated microgliosis (Jaarsma et al., 2011). However, while it has been suggested that demyelination of oligodendrocytes may be the trigger for microgliosis in *Csb^{m/m}* mice (Koob et al., 2010), evidence for this has been lacking. Our data also suggest mild microgliosis in *Csb^{m/m}* mice however there is a striking increase in MAC+ cells in *Adh5^{-/-}Csb^{m/m}* brains. Therefore, if demyelination is the trigger for microgliosis and the underlying neurological defect in CS then *Adh5^{-/-}Csb^{m/m}* mice provide an opportunity to study this.

Another line of evidence has suggested that CS defective cells preferentially reduce expression of neuronal genes leading to an inability to differentiate CS fibroblasts into neurones (Y. Wang et al., 2014). Interestingly this defect can be overcome by driving up expression of genes identified to have reduced in expression by treatment with brain derived neurotrophic factor or pharmacological mimics such as 7,8-dihydroxyflavone and amitriptyline (Y. Wang et al., 2016). With the emergence of the *Adh5^{-/-}Csb^{m/m}* model it is now possible to gain insight into the underlying defect in the brain and trial the interventions in a more suitable model.

One caveat to the *Adh5^{-/-}Csb^{m/m}* model is the length of time for neurological phenotypes to manifest, additionally, the multisystemic phenotype may complicate the study of the brain. The neurological defects of NER mouse models have previously been shown to be cell autonomous through the use of cell type specific models (Barnhoorn et al., 2014a).

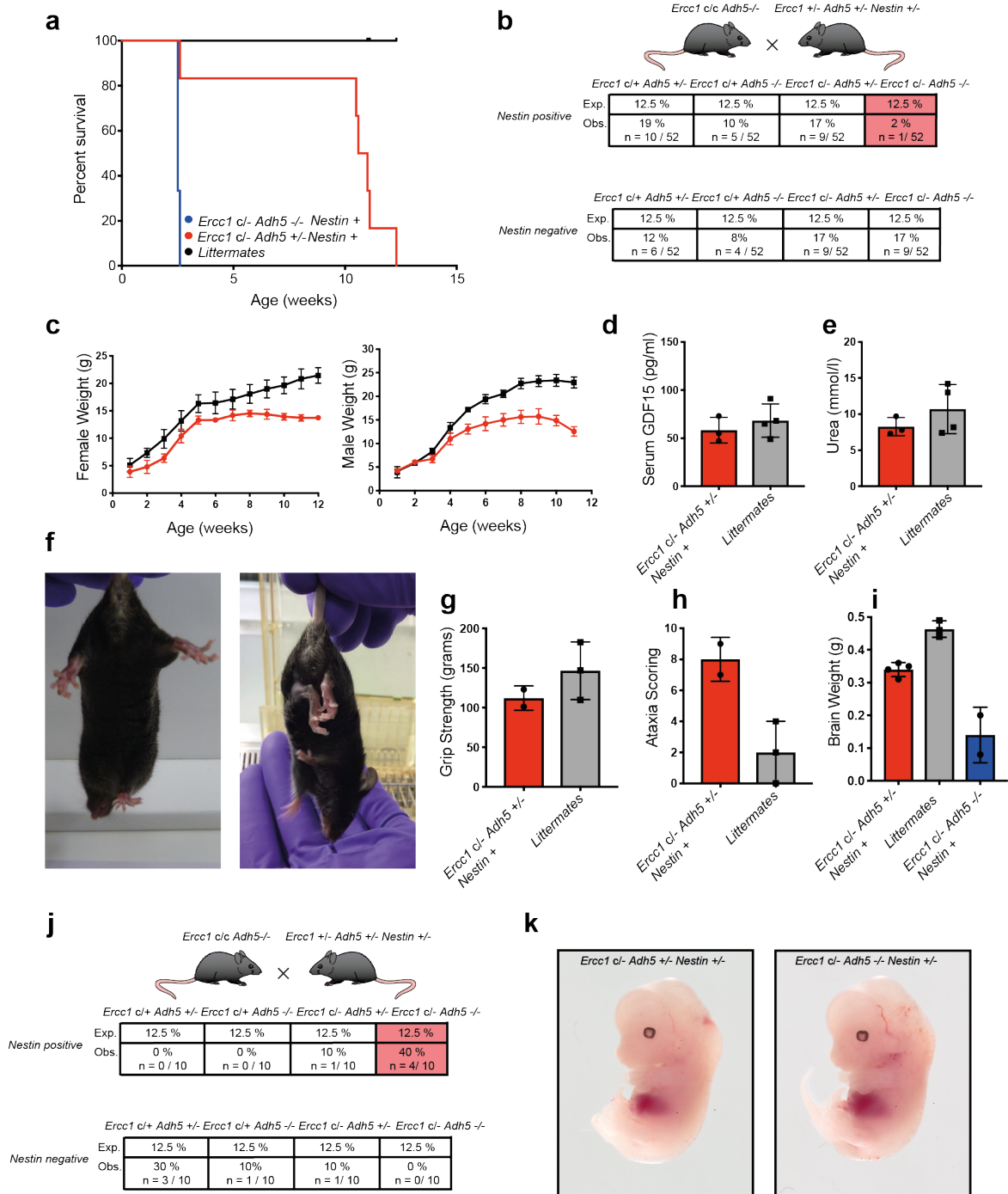


Figure 8.03 - Generating brain specific *Ercc1* mice that accumulate formaldehyde

a) Kaplan-meier curve of *Ercc1*^{cl-Adh5}^{-/-}*Nestin-cre*, *Ercc1*^{cl-Adh5}^{+/-}*Nestin-cre* and littermate controls (*n*=2, 6, 6 respectively) **b**) Mendelian ratios of mice born from *Ercc1*^{cl/c}*Adh5*^{-/-} males *Ercc1*^{+/-}*Adh5*^{+/-}*Nestin-cre* females. **c**) Growth curves of male and female *Ercc1*^{cl-Adh5}^{+/-}*Nestin-cre* mice and littermates (*n*=5 and 9 for females and 3 and 9 for males). **d-e**) Serum levels of GDF15 and Urea (*n*=3, 4 from left to right). **f**) Photos of *Ercc1*^{cl-Adh5}^{+/-}*Nestin-cre* and *Ercc1*^{cl+Adh5}^{+/-}*Nestin-cre* mice undergoing hind limb clasping assessment. **g**) Bar chart of grip strength measurements performed between 8-12 weeks of age (*n*=2, 3 left to right). **h**) Cerebellar ataxia scoring performed between 8-12 weeks of age (*n*=2, 3 left to right). **i**) Brain weights taken from mice in a), littermates were culled alongside *Ercc1*^{cl-Adh5}^{+/-}*Nestin-cre* to provide age matched controls (*n*=4, 3, 2 from left to right). **j**) Mendelian ratios of E13.5 pups from *Ercc1*^{cl/c}*Adh5*^{-/-} males and *Ercc1*^{+/-}*Adh5*^{+/-}*Nestin-cre* females. **k**) Photos of E13.5 pups

Ercc1^{-/-} mice, that lack the TC-NER nuclease, develop spontaneous neurological phenotypes, therefore a brain specific *Ercc1*^{-/-} mouse in the presence and absence of ADH5 may provide a model to study the effects of formaldehyde on the brain in the absence of TC-NER.

To this end, mice that lack ADH5 and carry two copies of a Cre inducible *Ercc1* allele were crossed with mice that were heterozygous for *Adh5*, *Ercc1* and *Nestin-Cre* allele (Figure 8.03b). Nestin is expressed widely in the central nervous tissue and so the presence of this Cre would result in the loss of ERCC1 within the brain (Tronche et al., 1999). This cross yielded very few *Ercc1*^{o/-}*Adh5*^{-/-}*Nestin-Cre* mice (2% rather than 12.5%) and those few that were born died shortly after birth (Figure 8.03a). *Ercc1*^{o/-}*Adh5*^{+/-}*Nestin-Cre* mice however were born at mendelian ratios (Figure 8.03b). These mice displayed a failure to thrive that was independent of GDF15 and kidney dysfunction (Figure 8.03c-e), neurological abnormalities as measured by reduced grip strength, presence of a high cerebellar ataxia score and reduced brain weight (Figure 8.03f-i). Although the brain weight of *Ercc1*^{o/-}*Adh5*^{-/-}*Nestin-Cre* mice appears very low, these mice were not age matched to the controls as these mice died prematurely and therefore could not be assessed for neurological phenotypes. However, *Ercc1*^{o/-}*Adh5*^{-/-}*Nestin-Cre* mice were born at sub-mendelian ratios and had a reduced lifespan suggesting that loss of ADH5 results in a more severe phenotype than brain specific ERCC1 deficient mice alone. We therefore looked at embryonic time points to establish a time when comparisons across all genotypes could be made. Genotyping at E13.5 suggested that the mendelian ratios were rescued at this stage and imaging of E13.5 embryos revealed that *Ercc1*^{o/-}*Adh5*^{-/-}*Nestin-Cre* mice were no different than controls (Figure 8.03j-k). Taken together this suggests that formaldehyde damage to the brain requires protection by the TC-NER nuclease and that the *Ercc1*^{o/-}*Adh5*^{-/-}*Nestin-Cre* E13.5 embryos may provide a model to study the mechanism by which this occurs.

8.2.2 Blood formaldehyde and the CS phenotype

Formaldehyde is an endogenous toxic metabolite capable of causing DNA damage and driving both the FA and CS phenotypes. By removing this threat to the genome, it may therefore be possible to alleviate symptoms of these phenotypes. However, to do this a better understanding of where formaldehyde comes from is first needed. One recent study has suggested that cells release formaldehyde during transcriptional reprogramming that occurs in cellular differentiation (X. Shen et al., 2020). This possibly explains why haematopoietic stem and progenitor cells, which are continuously undergoing rapid differentiation to maintain blood homeostasis, are more susceptible to formaldehyde

damage. Although important, it is difficult to see how this discovery can be exploited to improve physiological consequences of formaldehyde toxicity. Manipulating such a fundamental process may prove difficult and lead to undesirable effects.

Another possibility is that peripheral tissues excrete formaldehyde into the circulation to be removed via the kidney. Evidence for this comes from previous work in *Adh5^{-/-}Fancd2^{-/-}* mice transplanted with wild type bone marrow. As expected in this instance the blood phenotype is rescued, so too however is the kidney dysfunction (Pontel et al., 2015). This suggests that blood formaldehyde may contribute to the decline of peripheral tissues, if true, this would allow for systemic intervention to prevent formaldehyde-associated phenotypes. It would also point to formaldehyde as a circulating factor that can contribute to decline in organ function more generally.

To address whether systemic formaldehyde could indeed contribute to the CS phenotype in the brain and kidney of *Adh5^{-/-}Csb^{m/m}* mice we employed the *Adh5* Switch allele (*Adh5 sw*). For the generation of the *Adh5 sw* allele a targeting vector containing an inverted exon 3 flanked by loxP sites was integrated into the endogenous *Adh5* allele. In the presence of Cre recombinase this allele is then 'switched' so that exon 3 becomes restored and ADH5 expression returns (Figure 8.04a). Therefore, by using the *Adh5 sw* allele in combination with the haematopoietic specific *Vav1-icre* allele (Jasper de Boer et al., 2003) we can switch on expression of *Adh5* solely in the haematopoietic lineage. This allele, when combined with CSB deficiency, would then provide a model for studying the effects of circulating formaldehyde on phenotypes in peripheral tissues (Figure 8.04b). To validate the *Adh5 sw* allele we isolated tMEFS from *Adh5^{sw/sw}* mice, transfected them with a vector containing cre recombinase and studied ADH5 expression by western blot (Figure 8.04c). This revealed that *Adh5^{sw/sw}* tMEFS did not contain any ADH5 expression, but this expression returned in the presence of cre recombinase.

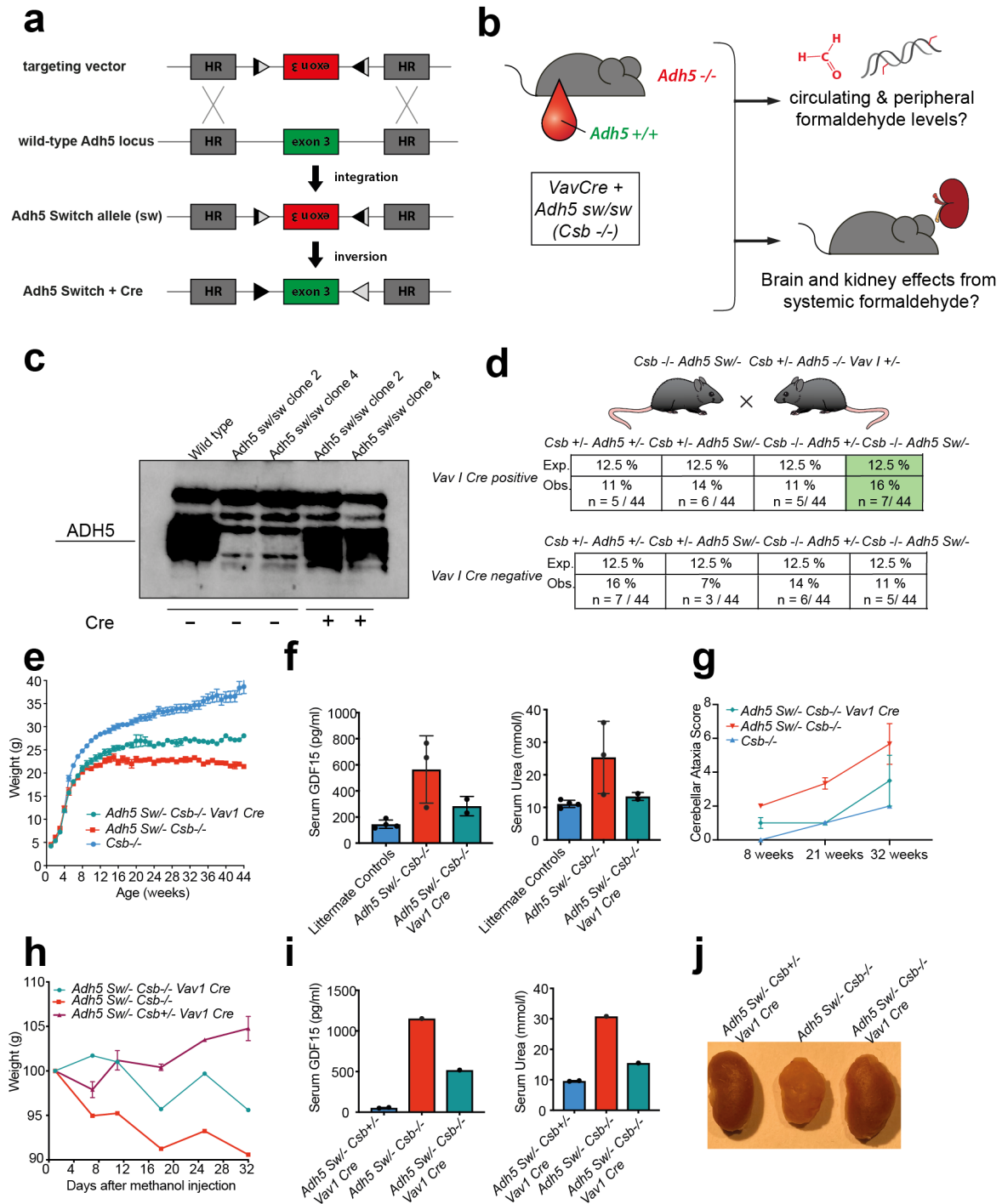


Figure 8.04 – Effects of blood formaldehyde on the CS phenotype

a) Scheme outlining the *Adh5* switch allele **b)** Scheme outlining the generation of a CS model designed to study the effects of systemic formaldehyde on peripheral tissues **c)** ADH5 Western blot of tMEFs derived from wild type or *Adh5*^{sw/sw} mice in the presence or absence of cre. **d)** Mendelian ratios of mice born from *Csb*^{m/m} *Adh5*^{sw/+} females and *Csb*^{m/m} *Adh5*^{-/-} *Vav1-cre* males. **e)** Growth curves of *Csb*^{m/m}, *Csb*^{m/m} *Adh5*^{sw/-} and *Csb*^{m/m} *Adh5*^{sw/-} *Vav1-cre* mice (*n*=12, 5, 6 respectively) **f)** Serum levels of GDF15 and urea taken from 32-week-old males (*n*=4, 3, 2 from left to right) **g)** Cerebellar ataxia scoring performed at 8, 21 and 32 weeks of age (*n*=3). **h)** Weight curves of female *Csb*^{m/m} *Adh5*^{sw/-} *Vav1-cre*, *Csb*^{m/m} *Adh5*^{sw/-} and *Csb*^{m/m} *Adh5*^{sw/-} *Vav1-cre* mice after weekly methanol i.p.s. (*n*=2, 1, 1) **i)** Serum levels of GDF15 and urea taken from females after 5 weeks of methanol treatment (*n*=2, 1, 1) **k)** Photos of female kidneys after 5 weeks of methanol exposure.

Having validated the allele, we next generated *Adh5^{sw/-}Csb^{m/m}Vav1-icre* mice, for this we crossed *Csb^{m/m}Adh5^{+/sw}* females with *Csb^{+/m}Adh5^{-/-}Vav1-icre*. This yielded both *Csb^{m/m}Adh5^{sw/-}* and *Csb^{m/m}Adh5^{sw/-}Vav1-icre* mice at mendelian ratios (12.5%) (Figure 8.04d). *Adh5^{-/-}Csb^{m/m}* mice display a failure to thrive driven by damaged kidney PT cells expressing the anorexic hormone GDF15. To assess whether blood formaldehyde could be contributing to this phenotype we compared *Adh5^{-sw}Csb^{m/m}* mice to *Adh5^{-sw}Csb^{m/m}Vav1-icre* mice. *Adh5^{-sw}Csb^{m/m}Vav1-icre* mice showed improved weight gain, reduced GDF15 serum levels and reduced serum urea levels compared to *Adh5^{-sw}Csb^{m/m}* mice (Figure 8.04e-f). Additionally, *Adh5^{-sw}Csb^{m/m}Vav1-icre* mice displayed a slower progression of neurological phenotypes than *Adh5^{-sw}Csb^{m/m}* mice (Figure 8.04g).

Finally, *Adh5^{-sw}Csb^{m/m}* female CS phenotypes can be exacerbated by exogenous formaldehyde through a methanol challenge. We compared this to *Adh5^{-sw}Csb^{m/m}Vav1-icre* and observed a milder weight loss, GDF15 and Urea serum increase (Figure 8.04h-i) and at necropsy the kidneys from *Adh5^{-sw}Csb^{m/m}Vav1-icre* did not display the extreme shrunken nodular appearance associated with *Adh5^{-/-}Csb^{m/m}* female mice post methanol challenge (Figure 8.04j). Taken together, although preliminary, these data suggest that systemic formaldehyde contributes to the CS phenotypes in *Adh5^{-/-}Csb^{m/m}* mice and by switching on expression of ADH5 in the blood these phenotypes can be alleviated. Further work is needed however to repeat these experiments and to identify whether changes in serum formaldehyde and formaldehyde exposure levels in the affected tissues are responsible for the alleviated phenotype.

8.2.3 Formaldehyde and senescence

CS patients display neurological decline, cachexia, sarcopenia and functional decline in organs (Laugel, 2013; Nance & Berry, 1992; B. T. Wilson et al., 2016). These characteristics are often associated with ageing and indeed CS is commonly referred to as a disease of accelerated ageing (S. Wang et al., 2020). One biological correlate of ageing is an increase in cellular senescence and this burden of senescent cells in aged individuals has been implicated in the many features of ageing (Baker et al., 2016). Perhaps therefore CS individuals undergo accelerated ageing due to accelerated senescence. Support for this idea has been provided in cellular systems where CSB deficient cells display premature senescence (Crochemore et al., 2019; S. Wang et al., 2020), therefore it is important to establish whether this extends to the physiological state. *Adh5^{-/-}Csb^{m/m}* mice have high serum levels of GDF15 and blocking this improves weight homeostasis in these animals. GDF15 has recently been established as a core component of the senescent associated secretory

phenotype (SASP) (Basisty et al., 2020), it is also one of the most significantly increased serum proteins associated with age in humans and mice (Lehallier et al., 2019; Tanaka et al., 2018). For cells to become senescent they must first become permanently cell cycle arrested. This can occur as a result of many stimuli, importantly for the *Adh5^{-/-}Csb^{m/m}* context, DNA damage is well known to trigger this (Campisi & D'Adda Di Fagagna, 2007; B. Wang et al., 2020). DNA damage activates p53 that then leads to increased p21 expression that restricts cell cycle progression and triggers cellular senescence.

Evidence that senescent cells can contribute to the ageing phenotype has been demonstrated using mouse models that can have their senescent cells removed. Removal of senescent cells at regular intervals not only extended lifespan but also improved tissue function in aged mice (Baker et al., 2016). More recently, intervention studies using drugs and CAR T cells that target senescent cells have also been shown to alleviate senescent associated phenotypes (Amor et al., 2020; Fuhrmann-Stroissnigg et al., 2017). Therefore, this approach should be considered for CS, however first more evidence is needed that the CS phenotype is a consequence of an increased burden of senescent cells.

PT cells in *Adh5^{-/-}Csb^{m/m}* mice express high levels of *Gdf15* and *p21*, suggesting that these cells are becoming senescent. Recent reviews have suggested that 4 markers of senescence are required to conclude that cells are indeed becoming senescent, we therefore cross referenced our scRNA-seq data with a recent study (Amor et al., 2020) that examined many surface markers of senescence. Using this approach, we identified a further two markers of senescence in our *Adh5^{-/-}Csb^{m/m}* PT cells, *Phlda3* and *Plaur* (Figure 8.05a). Cellular senescence is not only cell autonomous but can also, through a set of pro-inflammatory factors known as the SASP, lead to effects at the organismal level. Indeed GDF15 is one of these core SASP components (Basisty et al., 2020) and is elevated in serum from *Adh5^{-/-}Csb^{m/m}* mice. We assessed whether other SASP components were elevated in serum from *Adh5^{-/-}Csb^{m/m}* mice and noted that many were in males at 1 year of age (Figure 8.05b). Furthermore, we saw a clear increase in female SASP levels after methanol challenge (Figure 8.05c).

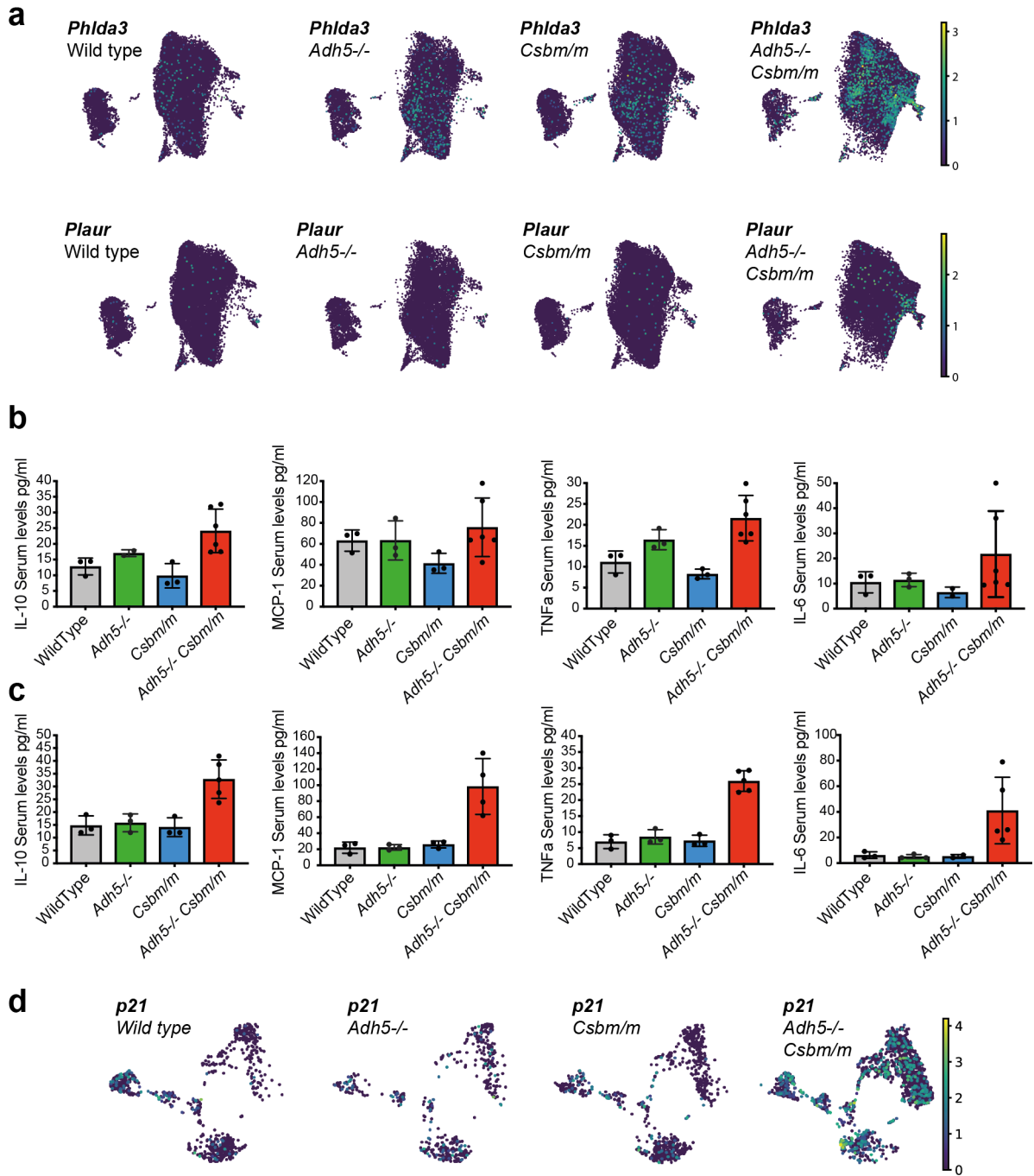


Figure 8.05 – Cellular senescence in *Adh5*^{-/-}*Csbm*^{m/m} mice

a) PT feature plots of expression of the senescent markers *phlda3* and *plaur* **b)** Serum levels of SASP markers taken from male mice aged 12 months ($n=3, 3, 3, 5$ from left to right) **c)** Serum levels of SASP markers taken from female mice 5 weeks after methanol treatment ($n=3, 3, 3, 5$ from left to right). **d)** MNP feature plots of *p21* expression

Finally, it has recently been shown that senescent immune cells in *Ercc1^{fl/fl} Vav1-icre* mice can lead to peripheral senescence in other organs (Yousefzadeh et al., 2021). Therefore, we assessed *p21* expression in mononuclear phagocytes (MNP) from our kidney scRNA-seq data and indeed identified high *p21* expression in *Adh5^{-/-}Csb^{m/m}* MNP cells (Figure 8.05d). Taken together this data suggests that the PT cells in *Adh5^{-/-}Csb^{m/m}* mice are becoming senescent and triggering the secretion of SASP factors that may be contributing to the *Adh5^{-/-}Csb^{m/m}* phenotype. Furthermore, the identification of high expression of *p21* in the MNP cells suggests that there may be a blood defect in *Adh5^{-/-}Csb^{m/m}* mice that may also be contributing to senescence in peripheral tissues. It should be considered therefore that although the rescue observed in *Adh5^{sw/-}Csb^{m/m}Vav1-icre* mice is most likely due to increased systemic detoxification of formaldehyde it may be due to the alleviation of a hematopoietic senescent phenotype.

8.2.4 Dietary manipulation in CS

Adh5^{-/-}Csb^{m/m} display GDF15 mediated cachexia; GDF15 exerts its effects at least in part through food aversion (Hsu et al., 2017b). Therefore, dietary manipulation in order to encourage increased calorie intake may prove useful in preventing cachexia in CS. Indeed such approaches have already been tested in *Csb^{m/m}* mice (Scheibye-knudsen et al., 2015). Here, effects of a high fat diet (HFD), caloric restriction and resveratrol supplementation were examined and a HFD alleviated some of the mild neurological and metabolic defects in *Csb^{m/m}* mice. We therefore tested the effects of a HFD diet on *Adh5^{-/-}Csb^{m/m}* and controls (Figure 8.06a), as expected wild type mice gained 60% body weight after 13 weeks on a HFD, in contrast *Adh5^{-/-}Csb^{m/m}* mice only gained 20% body weight over the 13 weeks. Interestingly, both *Adh5^{-/-}* and *Csb^{m/m}* mice displayed minor increases in weight after HFD compared with wild type mice. GDF15 levels in *Adh5^{-/-}Csb^{m/m}* mice were not significantly different when exposed to a HFD suggesting that there was no effect on the kidney deterioration (Figure 8.06b). As previously reported wild type mice exposed to a HFD developed high levels of serum GDF15 after a few months of treatment (Patel et al., 2019). However, both *Adh5^{-/-}* and *Csb^{m/m}* mice did not match the wild type GDF15 levels and instead appeared protected from weight gain.

In summary, *Adh5^{-/-}Csb^{m/m}* mice did gain some weight through exposure to a HFD, perhaps though the percentage weight gain of these mice is limited due to the high levels of GDF15 resulting in food aversion. Future work that neutralizes the GDF15 response in combination with a HFD may yield maximum weight gain in these mice and prove useful for clinical management of CS. Finally, while the GDF15 levels are slightly elevated in *Adh5^{-/-}* mice they

are not in *Csb^{m/m}* mice and yet these mice are protected from HFD induced obesity. Perhaps then, mild transcription defects bring about protection from HFD induced obesity by GDF15 independent mechanisms.

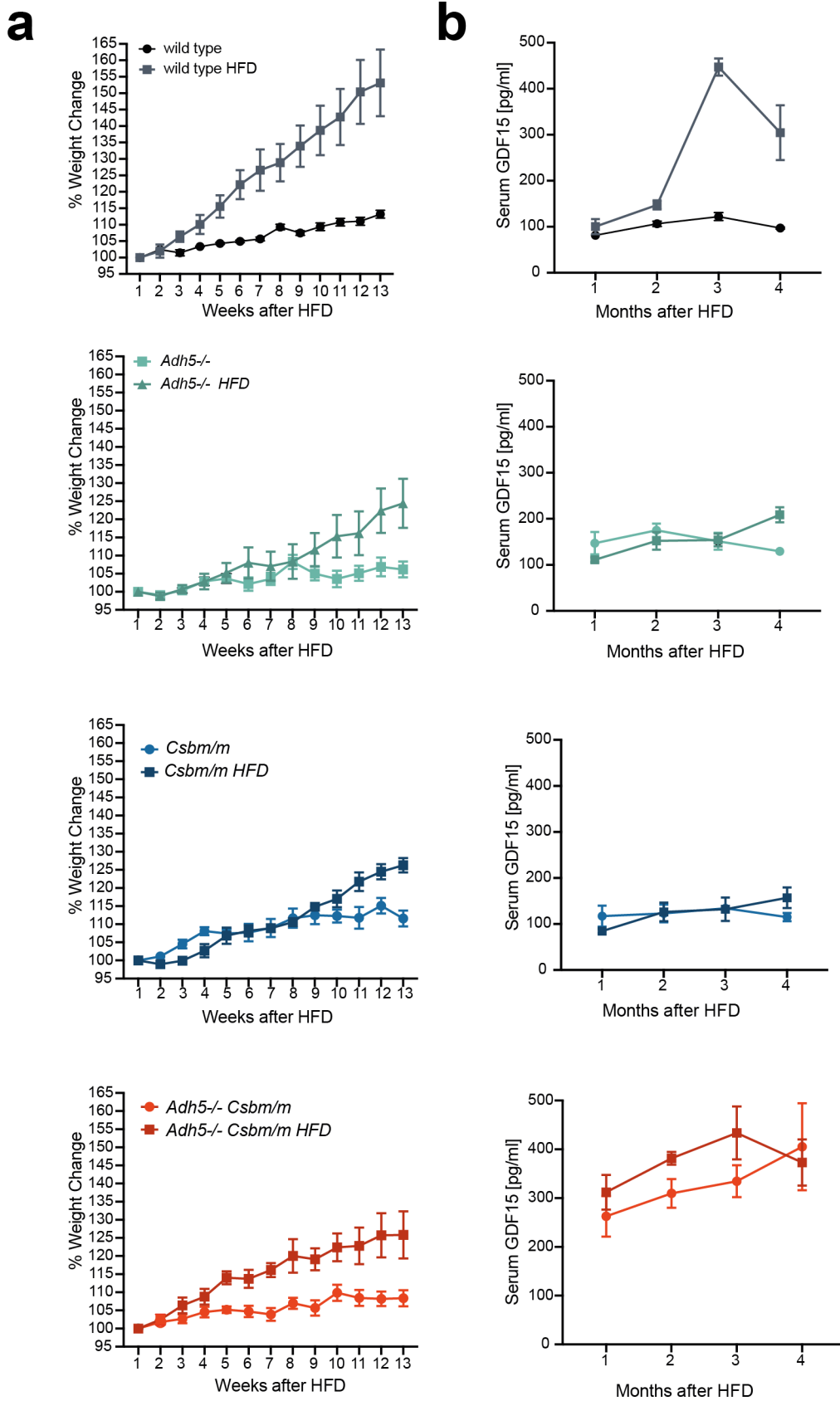


Figure 8.06 – HFD exposure of *Adh5*^{-/-}*Csbm*^{m/m} mice

a) Weekly weights of mice taken after exposure to a HFD compared to control chow (n=3) b) Serum GDF15 levels taken monthly from mice on a HFD compared to normal chow (n=3).

8.2.5 Concluding Remarks

The establishment of the *Adh5^{-/-}Csb^{m/m}* mouse model as a model of CS will shed new light onto this complex disease. Here we have shown that the kidney PT cells are particularly vulnerable to transcription blocking DNA damage, further studies may reveal cell types in the brain that are also vulnerable to these forms of damage. Research on this model has already pointed towards clinical intervention in CS using GDF15 neutralising antibodies and dietary intervention. Furthermore, if formaldehyde exerts its effects in the brain and kidney of *Adh5^{-/-}Csb^{m/m}* mice via the blood then perhaps blood detoxification of formaldehyde offers another potential route of intervention. Metformin has been suggested to act as a formaldehyde sponge and has been used to improve haematopoiesis and delay tumour formation in Fanconi deficient mice (Zhang et al., 2016) therefore it may extend to the CS phenotype.

Here we show that GDF15 has a causal role in the abnormal weight homeostasis in the context of CS and chemotherapy. However, it seems unlikely that this hormone is the sole reason for this. Other mouse models have shown that FGF21 is frequently secreted alongside GDF15 in response to stress (Forsström et al., 2019; Khan et al., 2017). High serum levels of FGF21 can also result in weight loss (Jimenez et al., 2018) and so it is possible that other stress responses contribute to the cachexia and weight loss brought on by formaldehyde. Indeed, the interaction between formaldehyde and weight homeostasis is a complicated one highlighted by the failure of *Adh5^{-/-}* mice to gain weight on a high fat diet. This intriguing finding appears independent of GDF15 and requires further investigation.

Bibliography

- Ahmad, A., Robinson, A. R., Duensing, A., van Drunen, E., Beverloo, H. B., Weisberg, D. B., Hasty, P., Hoeijmakers, J. H. J., & Niedernhofer, L. J. (2008). ERCC1-XPF Endonuclease Facilitates DNA Double-Strand Break Repair. *Molecular and Cellular Biology*, 28(16), 5082–5092. <https://doi.org/10.1128/MCB.00293-08>
- Al-Minawi, A. Z., Saleh-Gohari, N., & Helleday, T. (2008). The ERCC1/XPF endonuclease is required for efficient single-strand annealing and gene conversion in mammalian cells. *Nucleic Acids Research*, 36(1), 1–9. <https://doi.org/10.1093/nar/gkm888>
- Alcón, P., Shakeel, S., Chen, Z. A., Rappsilber, J., Patel, K. J., & Passmore, L. A. (2020). FANCD2–FANCI is a clamp stabilized on DNA by monoubiquitination of FANCD2 during DNA repair. *Nature Structural and Molecular Biology*, 27(3), 240–248. <https://doi.org/10.1038/s41594-020-0380-1>
- Alexandrov, L. B., Nik-Zainal, S., Wedge, D. C., Aparicio, S. A. J. R., Behjati, S., Biankin, A. V., Bignell, G. R., Bolli, N., Borg, A., Børresen-Dale, A. L., Boyault, S., Burkhardt, B., Butler, A. P., Caldas, C., Davies, H. R., Desmedt, C., Eils, R., Eyfjörd, J. E., Foekens, J. A., ... Stratton, M. R. (2013). Signatures of mutational processes in human cancer. *Nature*, 500(7463), 415–421. <https://doi.org/10.1038/nature12477>
- Alpi, A. F., Pace, P. E., Babu, M. M., & Patel, K. J. (2008). Mechanistic Insight into Site-Restricted Monoubiquitination of FANCD2 by Ube2t, FANCL, and FANCI. *Molecular Cell*, 32(6), 767–777. <https://doi.org/10.1016/j.molcel.2008.12.003>
- Alter, B. P., Greene, M. H., Velazquez, I., & Rosenberg, P. S. (2003). Cancer in Fanconi anemia [4]. *Blood*, 101(5), 2072–2073. <https://doi.org/10.1182/blood-2002-11-3597>
- Amor, C., Feucht, J., Leibold, J., Ho, Y. J., Zhu, C., Alonso-Curbelo, D., Mansilla-Soto, J., Boyer, J. A., Li, X., Giavridis, T., Kulick, A., Houlihan, S., Peerschke, E., Friedman, S. L., Ponomarev, V., Piersigilli, A., Sadelain, M., & Lowe, S. W. (2020). Senolytic CAR T cells reverse senescence-associated pathologies. *Nature*, 583(7814), 127–132. <https://doi.org/10.1038/s41586-020-2403-9>
- Anandarajan, V., Noguchi, C., Oleksak, J., Grothusen, G., Terlecky, D., & Noguchi, E. (2020). Genetic investigation of formaldehyde - induced DNA damage response in *Schizosaccharomyces pombe*. *Current Genetics*, 66(3), 593–605. <https://doi.org/10.1007/s00294-020-01057-z>
- Andersen, S. L., Bergstralh, D. T., Kohl, K. P., LaRocque, J. R., Moore, C. B., & Sekelsky, J. (2009). Drosophila MUS312 and the Vertebrate Ortholog BTBD12 Interact with DNA Structure-Specific Endonucleases in DNA Repair and Recombination. *Molecular Cell*, 35(1), 128–135. <https://doi.org/10.1016/j.molcel.2009.06.019>
- Andressoo, J.-O., Weeda, G., de Wit, J., Mitchell, J. R., Beems, R. B., van Steeg, H., van der Horst, G. T. J., & Hoeijmakers, J. H. (2009). An Xpb Mouse Model for Combined Xeroderma Pigmentosum and Cockayne Syndrome Reveals Progeroid Features upon Further Attenuation of DNA Repair. *Molecular Cellular Biology*, 29(5), 1276–1290. <https://doi.org/10.1128/mcb.01229-08>
- Andressoo, J. O., Mitchell, J. R., de Wit, J., Hoogstraten, D., Volker, M., Toussaint, W., Speksnijder, E., Beems, R. B., van Steeg, H., Jans, J., de Zeeuw, C. I., Jaspers, N. G. J., Raams, A., Lehmann, A. R., Vermeulen, W., Hoeijmakers, J. H. J., & van der Horst, G. T. J. (2006). An Xpd mouse model for the combined xeroderma pigmentosum/Cockayne syndrome exhibiting both cancer predisposition and segmental progeria. *Cancer Cell*, 10(2), 121–132. <https://doi.org/10.1016/j.ccr.2006.05.027>
- Andrews, A. D., Barrett, S. F., Yoder, F. W., & Robbins, J. H. (1978). Cockayne's syndrome fibroblasts have increased sensitivity to ultraviolet light but normal rates of unscheduled dna synthesis. *Journal of Investigative Dermatology*, 70(5), 237–239.

- <https://doi.org/10.1111/1523-1747.ep12541383>
- Anindya, R., Mari, P. O., Kristensen, U., Kool, H., Giglia-Mari, G., Mullenders, L. H., Fousteri, M., Vermeulen, W., Egly, J. M., & Svejstrup, J. Q. (2010). A Ubiquitin-Binding Domain in Cockayne Syndrome B Required for Transcription-Coupled Nucleotide Excision Repair. *Molecular Cell*, *38*(5), 637–648. <https://doi.org/10.1016/j.molcel.2010.04.017>
- Antoniou, A., Pharoah, P. D. P., Narod, S., Risch, H. A., Eyfjord, J. E., Hopper, J. L., Loman, N., Olsson, H., Johannsson, O., Borg, Å., Pasini, B., Radice, P., Manoukian, S., Eccles, D. M., Tang, N., Olah, E., Anton-Culver, H., Warner, E., Lubinski, J., ... Easton, D. F. (2003). Average risks of breast and ovarian cancer associated with BRCA1 or BRCA2 mutations detected in case series unselected for family history: A combined analysis of 22 studies. *American Journal of Human Genetics*, *72*(5), 1117–1130. <https://doi.org/10.1086/375033>
- Auerbach, A. D. (2009). Fanconi anemia and its diagnosis. *Mutation Research - Fundamental and Molecular Mechanisms of Mutagenesis*, *668*(1–2), 4–10. <https://doi.org/10.1016/j.mrfmmm.2009.01.013>
- Baer, S., Tuzin, N., Kang, P. B., Mohammed, S., Kubota, M., van Ierland, Y., Busa, T., Rossi, M., Morel, G., Michot, C., Baujat, G., Durand, M., Obringer, C., Le May, N., Calmels, N., & Laugel, V. (2021). Growth charts in Cockayne syndrome type 1 and type 2. *European Journal of Medical Genetics*, *64*(1). <https://doi.org/10.1016/j.ejmg.2020.104105>
- Baker, D. J., Childs, B. G., Durik, M., Wijers, M. E., Sieben, C. J., Zhong, J., A. Saltness, R., Jeganathan, K. B., Verzosa, G. C., Pezeshki, A., Khazaie, K., Miller, J. D., & Van Deursen, J. M. (2016). Naturally occurring p16 Ink4a-positive cells shorten healthy lifespan. *Nature*, *530*(7589), 184–189. <https://doi.org/10.1038/nature16932>
- Barnhoorn, S., Uittenboogaard, L. M., Jaarsma, D., Vermeij, W. P., Tresini, M., Weymaere, M., Menoni, H., Brandt, R. M. C., de Waard, M. C., Botter, S. M., Sarker, A. H., Jaspers, N. G. J., van der Horst, G. T. J., Cooper, P. K., Hoeijmakers, J. H. J., & van der Pluijm, I. (2014a). Cell-Autonomous Progeroid Changes in Conditional Mouse Models for Repair Endonuclease XPG Deficiency. *PLoS Genetics*, *10*(10), 7–9. <https://doi.org/10.1371/journal.pgen.1004686>
- Barroca, V., Mouthon, M. A., Lewandowski, D., Brunet de la grange, P., Gauthier, L. R., Pflumio, F., Boussin, F. D., Arwert, F., Riou, L., Allemand, I., Romeo, P. H., & Fouchet, P. (2012). Impaired functionality and homing of fancg-deficient hematopoietic stem cells. *Human Molecular Genetics*, *21*(1), 121–135. <https://doi.org/10.1093/hmg/ddr447>
- Basisty, N., Kale, A., Jeon, O. H., Kuehnemann, C., Payne, T., Rao, C., Holtz, A., Shah, S., Sharma, V., Ferrucci, L., Campisi, J., & Schilling, B. (2020). A proteomic atlas of senescence-associated secretomes for aging biomarker development. *PLoS Biology*, *18*(1), e3000599. <https://doi.org/10.1371/journal.pbio.3000599>
- Bellelli, R., Borel, V., Logan, C., Svendsen, J., Cox, D. E., Nye, E., Metcalfe, K., O'Connell, S. M., Stamp, G., Flynn, H. R., Snijders, A. P., Lassailly, F., Jackson, A., & Boulton, S. J. (2018). Polε Instability Drives Replication Stress, Abnormal Development, and Tumorigenesis. *Molecular Cell*, *70*(4), 707–721.e7. <https://doi.org/10.1016/j.molcel.2018.04.008>
- Benjamini, Y., & Hochberg, Y. (1995). Controlling the False Discovery Rate: A Practical and Powerful Approach to Multiple Testing. *Journal of the Royal Statistical Society: Series B (Methodological)*, *57*(1), 289–300. <https://doi.org/10.1111/j.2517-6161.1995.tb02031.x>
- Bennardo, N., Cheng, A., Huang, N., & Stark, J. M. (2008). Alternative-NHEJ is a mechanistically distinct pathway of mammalian chromosome break repair. *PLoS Genetics*, *4*(6), e1000110. <https://doi.org/10.1371/journal.pgen.1000110>
- Bergmann, E., & Egly, J. M. (2001). Trichothiodystrophy, a transcription syndrome. *Trends in Genetics*, *17*(5), 279–286. [https://doi.org/10.1016/S0168-9525\(01\)02280-6](https://doi.org/10.1016/S0168-9525(01)02280-6)
- Bogliolo, M., Schuster, B., Stoepker, C., Derkunt, B., Su, Y., Raams, A., Trujillo, J. P., Minguillón, J., Ramírez, M. J., Pujol, R., Casado, J. A., Baños, R., Rio, P., Knies, K., Zúñiga, S., Benítez, J., Bueren, J. A., Jaspers, N. G. J., Schärer, O. D., ... Surrallés, J. (2013). Mutations in ERCC4, encoding the DNA-repair endonuclease XPF, cause Fanconi anemia. *American Journal of Human Genetics*, *92*(5), 800–806.

- <https://doi.org/10.1016/j.ajhg.2013.04.002>
Borner, T., Shaulson, E. D., Ghidewon, M. Y., Barnett, A. B., Horn, C. C., Doyle, R. P., Grill, H. J., Hayes, M. R., & De Jonghe, B. C. (2020a). GDF15 Induces Anorexia through Nausea and Emesis. *Cell Metabolism*, 31(2), 351-362.e5.
<https://doi.org/10.1016/j.cmet.2019.12.004>
- Bradford, P. T., Goldstein, A. M., Tamura, D., Khan, S. G., Ueda, T., Boyle, J., Oh, K. S., Imoto, K., Inui, H., Moriwaki, S. I., Emmert, S., Pike, K. M., Raziuddin, A., Plona, T. M., DiGiovanna, J. J., Tucker, M. A., & Kraemer, K. H. (2011). Cancer and neurologic degeneration in xeroderma pigmentosum: Long term follow-up characterises the role of DNA repair. *Journal of Medical Genetics*, 48(3), 168–176.
<https://doi.org/10.1136/jmg.2010.083022>
- Brash, D. E., Rudolph, J. A., Simon, J. A., Lin, A., Mckenna, G. J., Baden, H. P., Halperin, A. J., & Pontén, J. (1991). A role for sunlight in skin cancer: UV-induced p53 mutations in squamous cell carcinoma. *Proceedings of the National Academy of Sciences of the United States of America*, 88(22), 10124–10128.
<https://doi.org/10.1073/pnas.88.22.10124>
- Breen, D. M., Kim, H., Bennett, D., Calle, R. A., Collins, S., Esquejo, R. M., He, T., Joaquim, S., Joyce, A., Lambert, M., Lin, L., Pettersen, B., Qiao, S., Rossulek, M., Weber, G., Wu, Z., Zhang, B. B., & Birnbaum, M. J. (2020). GDF-15 Neutralization Alleviates Platinum-Based Chemotherapy-Induced Emesis, Anorexia, and Weight Loss in Mice and Nonhuman Primates. *Cell Metabolism*, 32(6), 938-950.e6.
<https://doi.org/10.1016/j.cmet.2020.10.023>
- Brooks, C. R., Yeung, M. Y., Brooks, Y. S., Chen, H., Ichimura, T., Henderson, J. M., & Bonventre, J. V. (2015). KIM-1/ TIM-1-mediated phagocytosis links ATG5/ULK1-dependent clearance of apoptotic cells to antigen presentation. *The EMBO Journal*, 34(19), 2441–2464. <https://doi.org/10.15252/embj.201489838>
- Brooks, P. J., Enoch, M. A., Goldman, D., Li, T. K., & Yokoyama, A. (2009). The alcohol flushing response: An unrecognized risk factor for esophageal cancer from alcohol consumption. *PLoS Medicine*, 6(3), 0258–0263.
<https://doi.org/10.1371/journal.pmed.1000050>
- Brueckner, F., Hennecke, U., Carell, T., & Cramer, P. (2007). CPD Damage Recognition by Transcribing RNA Polymerase II. *Science*, 315(5813), 859–862.
<https://doi.org/10.1126/science.1135400>
- Campisi, J., & D'Adda Di Fagagna, F. (2007). Cellular senescence: When bad things happen to good cells. *Nature Reviews Molecular Cell Biology*, 8(9), 729–740.
<https://doi.org/10.1038/nrm2233>
- Ceccaldi, R., Parmar, K., Mouly, E., Delord, M., Kim, J. M., Regairaz, M., Pla, M., Vasquez, N., Zhang, Q. S., Ponderre, C., Peffault De Latour, R., Gluckman, E., Cavazzana-Calvo, M., Leblanc, T., Larghero, J., Grompe, M., Socié, G., D'Andrea, A. D., & Soulier, J. (2012). Bone marrow failure in fanconi anemia is triggered by an exacerbated p53/p21 DNA damage response that impairs hematopoietic stem and progenitor cells. *Cell Stem Cell*, 11(1), 36–49. <https://doi.org/10.1016/j.stem.2012.05.013>
- Ceccaldi, R., Sarangi, P., & D'Andrea, A. D. (2016). The Fanconi anaemia pathway: New players and new functions. *Nature Reviews Molecular Cell Biology*, 17(6), 337–349.
<https://doi.org/10.1038/nrm.2016.48>
- Charlet-Berguerand, N., Feuerhahn, S., Kong, S. E., Ziserman, H., Conaway, J. W., Conaway, R., & Egly, J. M. (2006). RNA polymerase II bypass of oxidative DNA damage is regulated by transcription elongation factors. *EMBO Journal*, 25(23), 5481–5491. <https://doi.org/10.1038/sj.emboj.7601403>
- Chatzinikolaou, G., Apostolou, Z., Aid-Pavlidis, T., Ioannidou, A., Karakasilioti, I., Papadopoulos, G. L., Aivaliotis, M., Tsekrekou, M., Strouboulis, J., Kosteas, T., & Garinis, G. A. (2017). ERCC1-XPF cooperates with CTCF and cohesin to facilitate the developmental silencing of imprinted genes. *Nature Cell Biology*, 19(5), 421–432.
<https://doi.org/10.1038/ncb3499>
- Cheng, G., Shi, Y., Sturla, S. J., Jalas, J. R., McIntee, E. J., Villalta, P. W., Wang, M., &

- Hecht, S. S. (2003a). Reactions of formaldehyde plus acetaldehyde with deoxyguanosine and DNA: Formation of cyclic deoxyguanosine adducts and formaldehyde cross-links. *Chemical Research in Toxicology*, *16*(2), 145–152. <https://doi.org/10.1021/tx025614r>
- Cheng, G., Shi, Y., Sturla, S. J., Jalas, J. R., McIntee, E. J., Villalta, P. W., Wang, M., & Hecht, S. S. (2003b). Reactions of formaldehyde plus acetaldehyde with deoxyguanosine and DNA: formation of cyclic deoxyguanosine adducts and formaldehyde cross-links. *Chemical Research in Toxicology*, *16*(2), 145–152. <https://doi.org/10.1021/tx025614r>
- Cheo, D. L., Ruven, H. J. T., Meira, L. B., Hammer, R. E., Burns, D. K., Tappe, N. J., van Zeeland, A. A., Mullenders, L. H. F., & Friedberg, E. C. (1997). Characterization of defective nucleotide excision repair in XPC mutant mice. *Mutation Research*, *374*(1), 1–9. [https://doi.org/10.1016/s0027-5107\(97\)00046-8](https://doi.org/10.1016/s0027-5107(97)00046-8)
- Cho. (2016). 乳鼠心肌提取 HHS Public Access. *Physiology & Behavior*, *176*(1), 100–106. <https://doi.org/10.1080/10409238.2017.1304353>.The
- Cho, J. S., Kook, S. H., Robinson, A. R., Niedernhofer, L. J., & Lee, B. C. (2013). Cell autonomous and nonautonomous mechanisms drive hematopoietic stem/progenitor cell loss in the absence of DNA repair. *Stem Cells*, *31*(3), 511–525. <https://doi.org/10.1002/stem.1261>
- Christensen, J. L., Wright, D. E., Wagers, A. J., & Weissman, I. L. (2004). Circulation and chemotaxis of fetal hematopoietic stem cells. *PLoS Biology*, *2*(3), 368–377. <https://doi.org/10.1371/journal.pbio.0020075>
- Cockayne, E. A. (1946). Dwarfism with retinal atrophy and deafness. *Archives of Disease in Childhood*, *21*(105), 52–54. <https://doi.org/10.1136/adc.21.105.52>
- Coin, F., Bergmann, E., Tremeau-Bravard, A., & Egly, J. M. (1999). Mutations in XPB and XPD helicases found in xeroderma pigmentosum patients impair the transcription function of TFIIH. *EMBO Journal*, *18*(5), 1357–1366. <https://doi.org/10.1093/emboj/18.5.1357>
- Coll, A. P., Chen, M., Taskar, P., Rimmington, D., Patel, S., Tadross, J. A., Cimino, I., Yang, M., Welsh, P., Virtue, S., Goldspink, D. A., Miedzybrodzka, E. L., Konopka, A. R., Esponda, R. R., Huang, J. T. J., Tung, Y. C. L., Rodriguez-Cuenca, S., Tomaz, R. A., Harding, H. P., ... O'Rahilly, S. (2020). GDF15 mediates the effects of metformin on body weight and energy balance. *Nature*, *578*(7795), 444–448. <https://doi.org/10.1038/s41586-019-1911-y>
- Cordisco, S., Tinaburri, L., Teson, M., Orioli, D., Cardin, R., Degan, P., Stefanini, M., Zambruno, G., Guerra, L., & Dellambra, E. (2019). Cockayne Syndrome Type A Protein Protects Primary Human Keratinocytes from Senescence. *Journal of Investigative Dermatology*, *139*(1), 38–50. <https://doi.org/10.1016/j.jid.2018.06.181>
- Crochemore, C., Fernández-Molina, C., Montagne, B., Salles, A., & Ricchetti, M. (2019). CSB promoter downregulation via histone H3 hypoacetylation is an early determinant of replicative senescence. *Nature Communications*, *10*(1). <https://doi.org/10.1038/s41467-019-13314-y>
- Crossan, G. P., van der Weyden, L., Rosado, I. V., Langevin, F., Gaillard, P.-H. L., McIntyre, R. E., Gallagher, F., Kettunen, M. I., Lewis, D. Y., Brindle, K., Arends, M. J., Adams, D. J., & Patel, K. J. (2011). Disruption of mouse Slx4, a regulator of structure-specific nucleases, phenocopies Fanconi anemia. *Nature Genetics*. <https://doi.org/10.1038/ng.752>
- Damsma, G. E., Alt, A., Brueckner, F., Carell, T., & Cramer, P. (2007). Mechanism of transcriptional stalling at cisplatin-damaged DNA. *Nature Structural and Molecular Biology*, *14*(12), 1127–1133. <https://doi.org/10.1038/nsmb1314>
- Day, E. A., Ford, R. J., Smith, B. K., Mohammadi-Shemirani, P., Morrow, M. R., Gutgesell, R. M., Lu, R., Raphenya, A. R., Kabiri, M., McArthur, A. G., McInnes, N., Hess, S., Paré, G., Gerstein, H. C., & Steinberg, G. R. (2019a). Metformin-induced increases in GDF15 are important for suppressing appetite and promoting weight loss. *Nature Metabolism*, *1*(12), 1202–1208. <https://doi.org/10.1038/s42255-019-0146-4>

- Day, E. A., Ford, R. J., Smith, B. K., Mohammadi-Shemirani, P., Morrow, M. R., Gutgesell, R. M., Lu, R., Raphenya, A. R., Kabiri, M., McArthur, A. G., McInnes, N., Hess, S., Paré, G., Gerstein, H. C., & Steinberg, G. R. (2019b). Metformin-induced increases in GDF15 are important for suppressing appetite and promoting weight loss. *Nature Metabolism*, 1(12), 1202–1208. <https://doi.org/10.1038/s42255-019-0146-4>
- De Boer, Jan, De Wit, J., Van Steeg, H., Berg, R. J. W., Morreau, H., Visser, P., Lehmann, A. R., Duran, M., Hoeijmakers, J. H. J., & Weeda, G. (1998). A mouse model for the basal transcription/DNA repair syndrome trichothiodystrophy. *Molecular Cell*, 1(7), 981–990. [https://doi.org/10.1016/S1097-2765\(00\)80098-2](https://doi.org/10.1016/S1097-2765(00)80098-2)
- de Boer, Jasper, Williams, A., Skavdis, G., Harker, N., Coles, M., Tolaini, M., Norton, T., Williams, K., Roderick, K., Potocnik, A. J., & Kioussis, D. (2003). Transgenic mice with hematopoietic and lymphoid specific expression of Cre. *European Journal of Immunology*, 33(2), 314–325. <https://doi.org/10.1002/immu.200310005>
- de Vries, A., van Oostrom, C. T., Hofhuis, F. M., Dortant, P. M., Berg, R. J., de Gruijl, F. R., Wester, P. W., van Kreijl, C. F., Capel, P. J., van Steeg, H., & Verbeek, S. J. (1995). Increased susceptibility to ultraviolet-B and carcinogens of mice lacking the DNA excision repair gene XPA. *Nature*, 377(6545), 169–173. <https://doi.org/10.1038/377169a0>
- De Waard, H., De Wit, J., Gorgels, T. G. M. F., Van den Aardweg, G., Andressoo, J. O., Vermeij, M., Van Steeg, H., Hoeijmakers, J. H. J., & Van der Horst, G. T. J. (2003). Cell type-specific hypersensitivity to oxidative damage in CSB and XPA mice. *DNA Repair*, 2(1), 13–25. [https://doi.org/10.1016/S1568-7864\(02\)00188-X](https://doi.org/10.1016/S1568-7864(02)00188-X)
- Dieterle, F., Perentes, E., Cordier, A., Roth, D. R., Verdes, P., Grenet, O., Pantano, S., Moulin, P., Wahl, D., Mahl, A., End, P., Staedtler, F., Legay, F., Carl, K., Laurie, D., Chibout, S. D., Vonderscher, J., & Maurer, G. (2010). Urinary clusterin, cystatin C, B2-microglobulin and total protein as markers to detect drug-induced kidney injury. *Nature Biotechnology*, 28(5), 463–469. <https://doi.org/10.1038/nbt.1622>
- DiGiovanna, J. J., & Kraemer, K. H. (2012). Shining a light on xeroderma pigmentosum. *The Journal of Investigative Dermatology*, 132(3 Pt 2), 785–796. <https://doi.org/10.1038/jid.2011.426>
- Dingler, F. A., Wang, M., Mu, A., Millington, C. L., Oberbeck, N., Watcham, S., Pontel, L. B., Kamimae-Lanning, A. N., Langevin, F., Nadler, C., Cordell, R. L., Monks, P. S., Yu, R., Wilson, N. K., Hira, A., Yoshida, K., Mori, M., Okamoto, Y., Okuno, Y., ... Patel, K. J. (2020). Two Aldehyde Clearance Systems Are Essential to Prevent Lethal Formaldehyde Accumulation in Mice and Humans. *Molecular Cell*, 80(6), 996–1012.e9. <https://doi.org/10.1016/j.molcel.2020.10.012>
- Docherty, M. H., O’Sullivan, E. D., Bonventre, J. V., & Ferenbach, D. A. (2019). Cellular senescence in the kidney. *Journal of the American Society of Nephrology*, 30(5), 726–736. <https://doi.org/10.1681/ASN.2018121251>
- Doig, J., Anderson, C., Lawrence, N. J., Selfridge, J., Brownstein, D. G., & Melton, D. W. (2006). Mice with skin-specific DNA repair gene (Ercc1) inactivation are hypersensitive to ultraviolet irradiation-induced skin cancer and show more rapid actinic progression. *Oncogene*, 25(47), 6229–6238. <https://doi.org/10.1038/sj.onc.1209642>
- Domenech, C., Maillard, L., Rousseau, A., Guidez, F., Petit, L., Pla, M., Clay, D., Guimiot, F., Sanfilippo, S., Jacques, S., de la Grange, P., Robil, N., Soulier, J., & Souyri, M. (2018). Studies in an early development window unveils a severe HSC defect in both murine and human Fanconi Anemia. *Stem Cell Reports*, 11(5), 1075–1091. <https://doi.org/10.1016/j.stemcr.2018.10.001>
- Donehower, L. A., Harvey, M., Slagle, B. L., McArthur, M. J., Montgomery, C. A., Butel, J. S., & Bradley, A. (1992). Mice deficient for p53 are developmentally normal but susceptible to spontaneous tumours. *Nature*, 356(6366), 215–221. <https://doi.org/10.1038/356215a0>
- Dubois, E. L., Guillon-Sert, L., Béliveau, M., Parmar, K., Chagraoui, J., Vignard, J., Pauty, J., Caron, M. C., Coulombe, Y., Buisson, R., Jacquet, K., Gamblin, C., Gao, Y., Laprise, P., Lebel, M., Sauvageau, G., D’Andrea, A., & Masson, J. Y. (2019). A Fanci knockout

- mouse model reveals common and distinct functions for FANCI and FANCD2. *Nucleic Acids Research*, 47(14), 7532–7547. <https://doi.org/10.1093/nar/gkz514>
- Effects, T. H., Gas, M., Pechura, L. C. M., Rall, D. P., Effects, H., Gas, M., Isbn, M., Pdf, T., Press, N. A., Press, N. A., Academy, N., Academy, N., & Press, N. A. (1993). Veterans at risk: the health effects of mustard gas and Lewisite. In *Choice Reviews Online* (Vol. 31, Issue 04). <https://doi.org/10.5860/choice.31-2145>
- Enoiu, M., Jiricny, J., & Schärer, O. D. (2012). Repair of cisplatin-induced DNA interstrand crosslinks by a replication-independent pathway involving transcription-coupled repair and translesion synthesis. *Nucleic Acids Research*, 40(18), 8953–8964. <https://doi.org/10.1093/nar/gks670>
- Espinosa, J. M., Verdun, R. E., & Emerson, B. M. (2003). p53 functions through stress- and promoter-specific recruitment of transcription initiation components before and after DNA damage. *Molecular Cell*, 12(4), 1015–1027. [https://doi.org/10.1016/S1097-2765\(03\)00359-9](https://doi.org/10.1016/S1097-2765(03)00359-9)
- Fagbemi, A. F., Orelli, B., & Schärer, O. D. (2011). Regulation of endonuclease activity in human nucleotide excision repair. *DNA Repair*, 10(7), 722–729. <https://doi.org/10.1016/j.dnarep.2011.04.022>
- Fan, L., Fuss, J. O., Cheng, Q. J., Arvai, A. S., Hammel, M., Roberts, V. A., Cooper, P. K., & Tainer, J. A. (2008). XPD Helicase Structures and Activities: Insights into the Cancer and Aging Phenotypes from XPD Mutations. *Cell*, 133(5), 789–800. <https://doi.org/10.1016/j.cell.2008.04.030>
- Fassihi, H., Sethi, M., Fawcett, H., Wing, J., Chandler, N., Mohammed, S., Craythorne, E., Morley, A. M. S., Lim, R., Turner, S., Henshaw, T., Garrod, I., Giunti, P., Hedderly, T., Abiona, A., Naik, H., Harrop, G., McGibbon, D., Jaspers, N. G. J., ... Lehmann, A. R. (2016). Deep phenotyping of 89 xeroderma pigmentosum patients reveals unexpected heterogeneity dependent on the precise molecular defect. *Proceedings of the National Academy of Sciences of the United States of America*, 113(9), E1236–E1245. <https://doi.org/10.1073/pnas.1519444113>
- Fekairi, S., Scaglione, S., Chahwan, C., Taylor, E. R., Tissier, A., Coulon, S., Dong, M. Q., Ruse, C., Yates, J. R., Russell, P., Fuchs, R. P., McGowan, C. H., & Gaillard, P. H. L. (2009). Human SLX4 Is a Holliday Junction Resolvase Subunit that Binds Multiple DNA Repair/Recombination Endonucleases. *Cell*, 138(1), 78–89. <https://doi.org/10.1016/j.cell.2009.06.029>
- Feng, D., Ngov, C., Henley, N., Boufaied, N., & Gerarduzzi, C. (2019). Characterization of Matricellular Protein Expression Signatures in Mechanistically Diverse Mouse Models of Kidney Injury. *Scientific Reports*, 9(1), 1–14. <https://doi.org/10.1038/s41598-019-52961-5>
- Fiesco-Roa, M. O., Giri, N., McReynolds, L. J., Best, A. F., & Alter, B. P. (2019). Genotype-phenotype associations in Fanconi anemia: A literature review. *Blood Reviews*, 37, 100589. <https://doi.org/10.1016/j.blre.2019.100589>
- Forsström, S., Jackson, C. B., Carroll, C. J., Kuronen, M., Pirinen, E., Pradhan, S., Marmyleva, A., Auranen, M., Kleine, I. M., Khan, N. A., Roivainen, A., Marjamäki, P., Liljenbäck, H., Wang, L., Battersby, B. J., Richter, U., Velagapudi, V., Nikkanen, J., Euro, L., & Suomalainen, A. (2019). Fibroblast Growth Factor 21 Drives Dynamics of Local and Systemic Stress Responses in Mitochondrial Myopathy with mtDNA Deletions. *Cell Metabolism*, 30(6), 1040-1054.e7. <https://doi.org/10.1016/j.cmet.2019.08.019>
- Freitas, M. C. S., Uchida, Y., Lassman, C., Danovitch, G. M., Busuttil, R. W., & Kupiec-Weglinski, J. W. (2011). Type I interferon pathway mediates renal ischemia/reperfusion injury. *Transplantation*, 92(2), 131–138. <https://doi.org/10.1097/TP.0b013e318220586e>
- Fuhrmann-Stroissnigg, H., Ling, Y. Y., Zhao, J., McGowan, S. J., Zhu, Y., Brooks, R. W., Grassi, D., Gregg, S. Q., Stripay, J. L., Dorransoro, A., Corbo, L., Tang, P., Bukata, C., Ring, N., Giacca, M., Li, X., Tchkonja, T., Kirkland, J. L., Niedernhofer, L. J., & Robbins, P. D. (2017). Identification of HSP90 inhibitors as a novel class of senolytics. *Nature Communications*, 8(1). <https://doi.org/10.1038/s41467-017-00314-z>

- Furuta, T., Ueda, T., Aune, G., Sarasin, A., Kraemer, K. H., & Pommier, Y. (2002). Transcription-coupled nucleotide excision repair as a determinant of cisplatin sensitivity of human cells. *Cancer Research*, *62*(17), 4899–4902.
- Garaycochea, J. I., Crossan, G. P., Langevin, F., Daly, M., Arends, M. J., & Patel, K. J. (2012). Genotoxic consequences of endogenous aldehydes on mouse haematopoietic stem cell function. *Nature*, *489*(7417), 571–575. <https://doi.org/10.1038/nature11368>
- Garaycochea, J. I., Crossan, G. P., Langevin, F., Mulderrig, L., Louzada, S., Yang, F., Guilbaud, G., Park, N., Roerink, S., Nik-Zainal, S., Stratton, M. R., & Patel, K. J. (2018). Alcohol and endogenous aldehydes damage chromosomes and mutate stem cells. *Nature*, *553*(7687), 171–177. <https://doi.org/10.1038/nature25154>
- Ghezraoui, H., Oliveira, C., Becker, J. R., Bilham, K., Moralli, D., Anzilotti, C., Fischer, R., Deobagkar-Lele, M., Sanchiz-Calvo, M., Fueyo-Marcos, E., Bonham, S., Kessler, B. M., Rottenberg, S., Cornall, R. J., Green, C. M., & Chapman, J. R. (2018). 53BP1 cooperation with the REV7-shieldin complex underpins DNA structure-specific NHEJ. *Nature*, *560*(7716), 122–127. <https://doi.org/10.1038/s41586-018-0362-1>
- Goto, M., Ishikawa, Y., Sugimoto, M., & Furuichi, Y. (2013). Werner syndrome: A changing pattern of clinical manifestations: In Japan (1917~2008). *BioScience Trends*, *7*(1), 13–22. <https://doi.org/10.5582/bst.2013.v7.1.13>
- Gregersen, L. H., & Svejstrup, J. Q. (2018). The Cellular Response to Transcription-Blocking DNA Damage. *Trends in Biochemical Sciences*, *43*(5), 327–341. <https://doi.org/10.1016/j.tibs.2018.02.010>
- Guainazzi, A., Campbell, A. J., Angelov, T., Simmerling, C., & Schäfer, O. D. (2010). Synthesis and molecular modeling of a nitrogen mustard DNA interstrand crosslink. *Chemistry - A European Journal*, *16*(40), 12100–12103. <https://doi.org/10.1002/chem.201002041>
- Guo, J., Hanawalt, P. C., & Spivak, G. (2013). Comet-FISH with strand-specific probes reveals transcription-coupled repair of 8-oxoGuanine in human cells. *Nucleic Acids Research*, *41*(16), 7700–7712. <https://doi.org/10.1093/nar/gkt524>
- Guyenet, S. J., Furrer, S. A., Damian, V. M., Baughan, T. D., la Spada, A. R., & Garden, G. A. (2010). A simple composite phenotype scoring system for evaluating mouse models of cerebellar ataxia. *Journal of Visualized Experiments*, *39*, 1–3. <https://doi.org/10.3791/1787>
- Hedberg, J. J., Griffiths, W. J., Nilsson, S. J. F., & Höög, J. O. (2003). Reduction of S-nitrosoglutathione by human alcohol dehydrogenase 3 is an irreversible reaction as analysed by electrospray mass spectrometry. *European Journal of Biochemistry*, *270*(6), 1249–1256. <https://doi.org/10.1046/j.1432-1033.2003.03486.x>
- Henrich, V. C., Vogtli, M. E., Antoniewski, C., Spindler-Barth, M., Przibilla, S., Nouredine, M., & Lezzi, M. (2000). Widespread recombinase expression using FLPeR (flipper) mice. *Genesis*, *28*(3–4), 106–110. [https://doi.org/10.1002/1526-968X\(200011/12\)28:3/4<106::AID-GENE30>3.0.CO;2-T](https://doi.org/10.1002/1526-968X(200011/12)28:3/4<106::AID-GENE30>3.0.CO;2-T)
- Hill, R., & Crossan, G. P. (2019). DNA crosslink repair safeguards genomic stability during pre-meiotic germ cell development. *Nature Genetics*.
- Hill, R. J., & Crossan, G. P. (2019). DNA cross-link repair safeguards genomic stability during premeiotic germ cell development. *Nature Genetics*, *51*(8), 1283–1294. <https://doi.org/10.1038/s41588-019-0471-2>
- Hira, A., Yabe, H., Yoshida, K., Okuno, Y., Shiraishi, Y., Chiba, K., Tanaka, H., Miyano, S., Nakamura, J., Kojima, S., Ogawa, S., Matsuo, K., Takata, M., & Yabe, M. (2013). Variant ALDH2 is associated with accelerated progression of bone marrow failure in Japanese Fanconi anemia patients. *Blood*, *122*(18), 3206–3209. <https://doi.org/10.1182/blood-2013-06-507962>
- Hodskinson, M. R. G., Silhan, J., Crossan, G. P., Garaycochea, J. I., Mukherjee, S., Johnson, C. M., Schäfer, O. D., & Patel, K. J. (2014). Mouse SLX4 is a tumor suppressor that stimulates the activity of the nuclease XPF-ERCC1 in DNA crosslink repair. *Molecular Cell*, *54*(3), 472–484. <https://doi.org/10.1016/j.molcel.2014.03.014>
- Houghtaling, S., Timmers, C., Noll, M., Finegold, M. J., Jones, S. N., Stephen Meyn, M., &

- Grompe, M. (2003). Epithelial cancer in Fanconi anemia complementation group D2 (Fancd2) knockout mice. *Genes and Development*, 17(16), 2021–2035. <https://doi.org/10.1101/gad.1103403>
- Hsu, J. Y., Crawley, S., Chen, M., Ayupova, D. A., Lindhout, D. A., Higbee, J., Kutach, A., Joo, W., Gao, Z., Fu, D., To, C., Mondal, K., Li, B., Kekatpure, A., Wang, M., Laird, T., Horner, G., Chan, J., Mcentee, M., ... Allan, B. B. (2017a). Non-homeostatic body weight regulation through a brainstem-restricted receptor for GDF15. *Nature*, 550(7675), 255–259. <https://doi.org/10.1038/nature24042>
- Hsu, J. Y., Crawley, S., Chen, M., Ayupova, D. A., Lindhout, D. A., Higbee, J., Kutach, A., Joo, W., Gao, Z., Fu, D., To, C., Mondal, K., Li, B., Kekatpure, A., Wang, M., Laird, T., Horner, G., Chan, J., Mcentee, M., ... Allan, B. B. (2017b). Non-homeostatic body weight regulation through a brainstem-restricted receptor for GDF15. *Nature*, 550(7675), 255–259. <https://doi.org/10.1038/nature24042>
- Huang, J., Arsenault, M., Kann, M., Lopez-Mendez, C., Saleh, M., Wadowska, D., Taglienti, M., Ho, J., Miao, Y., Sims, D., Spears, J., Lopez, A., Wright, G., & Hartwig, S. (2013). The transcription factor sry-related HMG box-4 (SOX4) is required for normal renal development in vivo. *Developmental Dynamics*, 242(6), 790–799. <https://doi.org/10.1002/dvdy.23971>
- Huang, J. C., Zamble, D. B., Reardon, J. T., Lippard, S. J., & Sancar, A. (1994). HMG-domain proteins specifically inhibit the repair of the major DNA adduct of the anticancer drug cisplatin by human excision nuclease. *Proceedings of the National Academy of Sciences of the United States of America*, 91(22), 10394–10398. <https://doi.org/10.1073/pnas.91.22.10394>
- Ishiai, M., Kimura, M., Namikoshi, K., Yamazoe, M., Yamamoto, K., Arakawa, H., Agematsu, K., Matsushita, N., Takeda, S., Buerstedde, J.-M., & Takata, M. (2004). DNA cross-link repair protein SNM1A interacts with PIAS1 in nuclear focus formation. *Molecular and Cellular Biology*, 24(24), 10733–10741. <https://doi.org/10.1128/MCB.24.24.10733-10741.2004>
- Itoh, T., Cado, D., Kamide, R., & Linn, S. (2004). *DDB2 gene disruption leads to skin tumors and resistance to apoptosis after exposure to ultraviolet light but not a chemical carcinogen*.
- Jaarsma, D., van der Pluijm, I., de Waard, M. C., Haasdijk, E. D., Brandt, R., Vermeij, M., Rijksen, Y., Maas, A., van Steeg, H., Hoeijmakers, J. H. J., & van der Horst, G. T. J. (2011). Age-related neuronal degeneration: Complementary roles of nucleotide excision repair and transcription-coupled repair in preventing neuropathology. *PLoS Genetics*, 7(12), 6–8. <https://doi.org/10.1371/journal.pgen.1002405>
- Jimenez, V., Jambrija, C., Casana, E., Sacristan, V., Muñoz, S., Darriba, S., Rodó, J., Mallol, C., Garcia, M., León, X., Marcó, S., Ribera, A., Elias, I., Casellas, A., Grass, I., Elias, G., Ferré, T., Motas, S., Franckhauser, S., ... Bosch, F. (2018). FGF21 gene therapy as treatment for obesity and insulin resistance. *EMBO Molecular Medicine*, 10(8). <https://doi.org/10.15252/emmm.201708791>
- Kamileri, I., Karakaslioti, I., Sideri, A., Kosteas, T., Tatarakis, A., Talianidis, I., & Garinis, G. A. (2012). Defective transcription initiation causes postnatal growth failure in a mouse model of nucleotide excision repair (NER) progeria. *Proceedings of the National Academy of Sciences of the United States of America*, 109(8), 2995–3000. <https://doi.org/10.1073/pnas.1114941109>
- Kamimae-Lanning, A. N., Goloviznina, N. A., & Kurre, P. (2013). Fetal origins of hematopoietic failure in a murine model of Fanconi anemia. *Blood*, 121(11), 2008–2012. <https://doi.org/10.1182/blood-2012-06-439679>
- Kashiyama, K., Nakazawa, Y., Pilz, D. T., Guo, C., Shimada, M., Sasaki, K., Fawcett, H., Wing, J. F., Lewin, S. O., Carr, L., Li, T.-S., Yoshiura, K., Utani, A., Hirano, A., Yamashita, S., Greenblatt, D., Nardo, T., Stefanini, M., McGibbon, D., ... Ogi, T. (2013). Malfunction of nuclease ERCC1-XPF results in diverse clinical manifestations and causes Cockayne syndrome, xeroderma pigmentosum, and Fanconi anemia. *American Journal of Human Genetics*, 92(5), 807–819. <https://doi.org/10.1016/j.ajhg.2013.04.007>

- Kawanishi, M., Matsuda, T., & Yagi, T. (2014). Genotoxicity of formaldehyde: Molecular basis of DNA damage and mutation. *Frontiers in Environmental Science*, 2(SEP), 1–8. <https://doi.org/10.3389/fenvs.2014.00036>
- Khan, N. A., Nikkanen, J., Yatsuga, S., Jackson, C., Wang, L., Pradhan, S., Kivelä, R., Pessia, A., Velagapudi, V., & Suomalainen, A. (2017). mTORC1 Regulates Mitochondrial Integrated Stress Response and Mitochondrial Myopathy Progression. *Cell Metabolism*, 26(2), 419–428.e5. <https://doi.org/10.1016/j.cmet.2017.07.007>
- Kishi, S., Brooks, C. R., Taguchi, K., Ichimura, T., Mori, Y., Akinfolarin, A., Gupta, N., Galichon, P., Elias, B. C., Suzuki, T., Wang, Q., Gewin, L., Morizane, R., & Bonventre, J. V. (2019). Proximal tubule ATR regulates DNA repair to prevent maladaptive renal injury responses. *Journal of Clinical Investigation*, 129(11), 4797–4816. <https://doi.org/10.1172/JCI122313>
- Klein Douwel, D., Boonen, R. A. C. M., Long, D. T., Szybowska, A. A., Räschele, M., Walter, J. C., & Knipscheer, P. (2014). XPF-ERCC1 acts in Unhooking DNA interstrand crosslinks in cooperation with FANCD2 and FANCP/SLX4. *Molecular Cell*, 54(3), 460–471. <https://doi.org/10.1016/j.molcel.2014.03.015>
- Knipscheer, P., Räschele, M., Smogorzewska, A., Enoiu, M., Ho, T. V., Schäerer, O. D., Elledge, S. J., & Walter, J. C. (2009). The Fanconi anemia pathway promotes replication-dependent DNA interstrand cross-link repair. *Science (New York, N. Y.)*, 326(5960), 1698–1701. <https://doi.org/10.1126/science.1182372>
- Kokic, G., Chernev, A., Tegunov, D., Dienemann, C., Urlaub, H., & Cramer, P. (2019). Structural basis of TFIIH activation for nucleotide excision repair. *Nature Communications*, 10(1), 1–9. <https://doi.org/10.1038/s41467-019-10745-5>
- Kokic, G., Wagner, F. R., Chernev, A., Urlaub, H., & Cramer, P. (2021). Structural basis of human transcription–DNA repair coupling. *Nature*, 26(April). <https://doi.org/10.1038/s41586-021-03906-4>
- Koob, M., Laugel, V., Durand, M., Fothergill, H., Dalloz, C., Sauvanaud, F., Dollfus, H., Namer, I. J., & Dietemann, J. L. (2010). Neuroimaging in Cockayne syndrome. *American Journal of Neuroradiology*, 31(9), 1623–1630. <https://doi.org/10.3174/ajnr.A2135>
- Kubota, M., Ohta, S., Ando, A., Koyama, A., Terashima, H., Kashii, H., Hoshino, H., Sugita, K., & Hayashi, M. (2015). Nationwide survey of Cockayne syndrome in Japan: Incidence, clinical course and prognosis. *Pediatrics International*, 57(3), 339–347. <https://doi.org/10.1111/ped.12635>
- Kutler, D. I., Singh, B., Satagopan, J., Batish, S. D., Berwick, M., Giampietro, P. F., Hanenberg, H., & Auerbach, A. D. (2003). A 20-year perspective on the International Fanconi Anemia Registry (IFAR). *Blood*, 101(4), 1249–1256. <https://doi.org/10.1182/blood-2002-07-2170>
- Kuykendall, J. R., & Bogdanffy, M. S. (1992). Efficiency of DNA-histone crosslinking induced by saturated and unsaturated aldehydes in vitro. *Mutation Research*, 283(2), 131–136. [https://doi.org/10.1016/0165-7992\(92\)90145-8](https://doi.org/10.1016/0165-7992(92)90145-8)
- Langevin, F., Crossan, G. P., Rosado, I. V., Arends, M. J., & Patel, K. J. (2011). Fancd2 counteracts the toxic effects of naturally produced aldehydes in mice. *Nature*, 475(7354), 53–59. <https://doi.org/10.1038/nature10192>
- Lans, H., Hoeijmakers, J. H. J., Vermeulen, W., & Marteijn, J. A. (2019). The DNA damage response to transcription stress. *Nature Reviews Molecular Cell Biology*, 20(December). <https://doi.org/10.1038/s41580-019-0169-4>
- Laugel, V. (2013). Cockayne syndrome: The expanding clinical and mutational spectrum. *Mechanisms of Ageing and Development*, 134(5–6), 161–170. <https://doi.org/10.1016/j.mad.2013.02.006>
- Lavigne, M. D., Konstantopoulos, D., Ntakou-Zamplara, K. Z., Liakos, A., & Fousteri, M. (2017). Global unleashing of transcription elongation waves in response to genotoxic stress restricts somatic mutation rate. *Nature Communications*, 8(1). <https://doi.org/10.1038/s41467-017-02145-4>
- Le May, N., Fradin, D., Iltis, I., Bougnères, P., & Egly, J. M. (2012). XPG and XPF

- Endonucleases Trigger Chromatin Looping and DNA Demethylation for Accurate Expression of Activated Genes. *Molecular Cell*, 47(4), 622–632. <https://doi.org/10.1016/j.molcel.2012.05.050>
- Le May, N., Mota-Fernandes, D., Vélez-Cruz, R., Iltis, I., Biard, D., & Egly, J. M. (2010). NER Factors Are Recruited to Active Promoters and Facilitate Chromatin Modification for Transcription in the Absence of Exogenous Genotoxic Attack. *Molecular Cell*, 38(1), 54–66. <https://doi.org/10.1016/j.molcel.2010.03.004>
- Lehallier, B., Gate, D., Schaum, N., Nanasi, T., Lee, S. E., Yousef, H., Moran Losada, P., Berdnik, D., Keller, A., Verghese, J., Sathyan, S., Franceschi, C., Milman, S., Barzilai, N., & Wyss-Coray, T. (2019). Undulating changes in human plasma proteome profiles across the lifespan. *Nature Medicine*, 25(12), 1843–1850. <https://doi.org/10.1038/s41591-019-0673-2>
- Lindahl, T. (1993). Instability and decay of the primary structure of DNA. *Nature*, 362(6422), 709–715. <https://doi.org/10.1038/362709a0>
- Liu, J., Kumar, S., Dolzhenko, E., Alvarado, G. F., Guo, J., Lu, C., Chen, Y., Li, M., Dessing, M. C., Parvez, R. K., Cippà, P. E., Krautzberger, A. M., Saribekyan, G., Smith, A. D., & McMahon, A. P. (2017). Molecular characterization of the transition from acute to chronic kidney injury following ischemia/reperfusion. *JCI Insight*, 2(18). <https://doi.org/10.1172/jci.insight.94716>
- Liu, L., Yan, Y., Zeng, M., Zhang, J., Hanes, M. A., Ahearn, G., McMahon, T. J., Dickfeld, T., Marshall, H. E., Que, L. G., & Stamler, J. S. (2004). Essential Roles of S-Nitrosothiols in Vascular Homeostasis and Endotoxic Shock. *Cell*, 116(4), 617–628. [https://doi.org/10.1016/S0092-8674\(04\)00131-X](https://doi.org/10.1016/S0092-8674(04)00131-X)
- Long, D. T., Joukov, V., & Walter, J. C. (2011). *Interstrand Cross-Link Repair*. 333(July), 84–88.
- Lu, K., Collins, L. B., Ru, H., Bermudez, E., & Swenberg, J. A. (2010). Distribution of DNA adducts caused by inhaled formaldehyde is consistent with induction of nasal carcinoma but not leukemia. *Toxicological Sciences*, 116(2), 441–451. <https://doi.org/10.1093/toxsci/kfq061>
- Lynch, H. T., & De la Chapelle, A. (1999). Genetic susceptibility to non-polyposis colorectal cancer. *Journal of Medical Genetics*, 36(11), 801–818. <https://doi.org/10.1136/jmg.36.11.801>
- Marteijn, J. A., Lans, H., Vermeulen, W., & Hoeijmakers, J. H. J. (2014). Understanding nucleotide excision repair and its roles in cancer and ageing. *Nature Reviews. Molecular Cell Biology*, 15(7), 465–481. <https://doi.org/10.1038/nrm3822>
- Martín-Pardillos, A., Tsaalbi-Shtylik, A., Chen, S., Lazare, S., Van Os, R. P., Dethmers-Ausema, A., Fakouri, N. B., Bosshard, M., Aprigliano, R., Van Loon, B., Salvatori, D. C. F., Hashimoto, K., Van Der Spek, C. D., Moriya, M., Rasmussen, L. J., De Haan, G., Raaijmakers, M. H. G. P., & De Wind, N. (2017). Genomic and functional integrity of the hematopoietic system requires tolerance of oxidative DNA lesions. *Blood*, 130(13), 1523–1534. <https://doi.org/10.1182/blood-2017-01-764274>
- Masutani, C., Kusumoto, R., & Yamada, A. (1999). *The XPV (xeroderma pigmentosum variant) gene encodes human DNA polymerase η* . 399(June), 700–704.
- Mayne, L., & Lehmann, A. R. (1982). Failure of RNA synthesis to recover after UV irradiation: An early defect in cells from individuals with Cockayne syndrome and xeroderma pigmentosum. *Mutation Research*, 96(1), 140. [https://doi.org/10.1016/0027-5107\(82\)90047-1](https://doi.org/10.1016/0027-5107(82)90047-1)
- McHugh, P. J., Sones, W. R., & Hartley, J. A. (n.d.). Repair of Intermediate Structures Produced at DNA Interstrand Cross-Links in *Saccharomyces cerevisiae*. *Molecular and Cellular Biology*, 20(10), 3425–3433. <https://doi.org/10.1128/mcb.20.10.3425-3433.2000>
- McInnes, L., Healy, J., Saul, N., & Großberger, L. (2018). UMAP: Uniform Manifold Approximation and Projection. *Journal of Open Source Software*, 3(29), 861. <https://doi.org/10.21105/joss.00861>
- McWhir, J., Selfridge, J., Harrison, D. J., Squires, S., & Melton, D. W. (1993). Mice with DNA repair gene (ERCC-1) deficiency have elevated levels of p53, liver nuclear

- abnormalities and die before weaning. *Nature Genetics*, 5(3), 217–224.
<https://doi.org/10.1038/ng1193-217>
- Meetei, A. R., De Winter, J. P., Medhurst, A. L., Wallisch, M., Waisfisz, Q., Van de Vrugt, H. J., Oostra, A. B., Yan, Z., Ling, C., Bishop, C. E., Hoatlin, M. E., Joenje, H., & Wang, W. (2003). A novel ubiquitin ligase is deficient in Fanconi anemia. *Nature Genetics*, 35(2), 165–170. <https://doi.org/10.1038/ng1241>
- Menoni, H., Hoeijmakers, J. H. J., & Vermeulen, W. (2012). Nucleotide excision repair-initiating proteins bind to oxidative DNA lesions in vivo. *Journal of Cell Biology*, 199(7), 1037–1046. <https://doi.org/10.1083/jcb.201205149>
- Moeller, B. C., Lu, K., Doyle-Eisele, M., McDonald, J., Gigliotti, A., & Swenberg, J. A. (2011). Determination of N 2-hydroxymethyl-dG adducts in the nasal epithelium and bone marrow of nonhuman primates following 13CD 2-formaldehyde inhalation exposure. *Chemical Research in Toxicology*, 24(2), 162–164. <https://doi.org/10.1021/tx1004166>
- Moser, J., Kool, H., Giakzidis, I., Caldecott, K., Mullenders, L. H. F., & Foustner, M. I. (2007). Sealing of Chromosomal DNA Nicks during Nucleotide Excision Repair Requires XRCC1 and DNA Ligase III α in a Cell-Cycle-Specific Manner. *Molecular Cell*, 27(2), 311–323. <https://doi.org/10.1016/j.molcel.2007.06.014>
- Motycka, T. A., Bessho, T., Post, S. M., Sung, P., & Tomkinson, A. E. (2004). Physical and functional interaction between the XPF/ERCC1 endonuclease and hRad52. *The Journal of Biological Chemistry*, 279(14), 13634–13639.
<https://doi.org/10.1074/jbc.M313779200>
- Mullican, S. E., Lin-Schmidt, X., Chin, C. N., Chavez, J. A., Furman, J. L., Armstrong, A. A., Beck, S. C., South, V. J., Dinh, T. Q., Cash-Mason, T. D., Cavanaugh, C. R., Nelson, S., Huang, C., Hunter, M. J., & Rangwala, S. M. (2017). GFRAL is the receptor for GDF15 and the ligand promotes weight loss in mice and nonhuman primates. *Nature Medicine*, 23(10), 1150–1157. <https://doi.org/10.1038/nm.4392>
- Muniandy, P. A., Thapa, D., Thazhathveetil, A. K., Liu, S., & Seidman, M. M. (2009a). Repair of laser-localized DNA interstrand cross-links in G1 phase mammalian cells. *The Journal of Biological Chemistry*, 284(41), 27908–27917.
<https://doi.org/10.1074/jbc.M109.029025>
- Muniandy, P. A., Thapa, D., Thazhathveetil, A. K., Liu, S. ting, & Seidman, M. M. (2009b). Repair of laser-localized DNA interstrand cross-links in G1 phase mammalian cells. *Journal of Biological Chemistry*, 284(41), 27908–27917.
<https://doi.org/10.1074/jbc.M109.029025>
- Muñoz, I. M., Hain, K., Déclais, A. C., Gardiner, M., Toh, G. W., Sanchez-Pulido, L., Heuckmann, J. M., Toth, R., Macartney, T., Eppink, B., Kanaar, R., Ponting, C. P., Lilley, D. M. J., & Rouse, J. (2009). Coordination of Structure-Specific Nucleases by Human SLX4/BTBD12 Is Required for DNA Repair. *Molecular Cell*, 35(1), 116–127.
<https://doi.org/10.1016/j.molcel.2009.06.020>
- Muñoz, M. J., Nieto Moreno, N., Giono, L. E., Cambindo Botto, A. E., Dujardin, G., Bastianello, G., Lavore, S., Torres-Méndez, A., Menck, C. F. M., Blencowe, B. J., Irimia, M., Foiani, M., & Kornblihtt, A. R. (2017). Major Roles for Pyrimidine Dimers, Nucleotide Excision Repair, and ATR in the Alternative Splicing Response to UV Irradiation. *Cell* (12), 2868–2879. <https://doi.org/10.1016/j.celrep.2017.02.066>
- Nakane, H., Takeuchi, S., Nakatsu, Y., Murai, H., Nakatsurut, Y., Hirota, S., Kitamura, Y., Katoll, Y., Ii, Y. T., Miyauchi, H., Horio, T., Tokunaga, T., Matsunagap, T., Nikaidop, O., Nishimune, Y., & Okada, Y. (1995). *lacking the xeroderma pigmentosum group A gene*. 377(September), 165–168.
- Nakazawa, Y., Hara, Y., Oka, Y., Komine, O., van den Heuvel, D., Guo, C., Daigaku, Y., Isono, M., He, Y., Shimada, M., Kato, K., Jia, N., Hashimoto, S., Kotani, Y., Miyoshi, Y., Tanaka, M., Sobue, A., Mitsutake, N., Suganami, T., ... Ogi, T. (2020). Ubiquitination of DNA Damage-Stalled RNAPII Promotes Transcription-Coupled Repair. *Cell*, 180(6), 1228-1244.e24. <https://doi.org/10.1016/j.cell.2020.02.010>
- Nance, M. A., & Berry, S. A. (1992). Cockayne Syndrome: Review of 140 cases. *American Journal of Medical Genetics*, 42(1), 68–84. <https://doi.org/10.1002/ajmg.1320420115>

- Natale, V., & Raquer, H. (2017). Xeroderma pigmentosum-Cockayne syndrome complex. *Orphanet Journal of Rare Diseases*, 12(1), 1–11. <https://doi.org/10.1186/s13023-017-0616-2>
- Niedernhofer, L. J., Garinis, G. A., Raams, A., Lalai, A. S., Robinson, A. R., Appeldoorn, E., Odijk, H., Oostendorp, R., Ahmad, A., van Leeuwen, W., Theil, A. F., Vermeulen, W., van der Horst, G. T. J., Meinecke, P., Kleijer, W. J., Vijg, J., Jaspers, N. G. J., & Hoeijmakers, J. H. J. (2006). A new progeroid syndrome reveals that genotoxic stress suppresses the somatotroph axis. *Nature*, 444(7122), 1038–1043. <https://doi.org/10.1038/nature05456>
- Niedernhofer, L. J., Odijk, H., Budzowska, M., van Drunen, E., Maas, A., Theil, A. F., de Wit, J., Jaspers, N. G. J., Beverloo, H. B., Hoeijmakers, J. H. J., & Kanaar, R. (2004). The Structure-Specific Endonuclease Ercc1-Xpf Is Required To Resolve DNA Interstrand Cross-Link-Induced Double-Strand Breaks. *Molecular and Cellular Biology*, 24(13), 5776–5787. <https://doi.org/10.1128/mcb.24.13.5776-5787.2004>
- Nik-Zainal, S., Davies, H., Staaf, J., Ramakrishna, M., Glodzik, D., Zou, X., Martincorena, I., Alexandrov, L. B., Martin, S., Wedge, D. C., Van Loo, P., Ju, Y. S., Smid, M., Brinkman, A. B., Morganella, S., Aure, M. R., Lingjærde, O. C., Langerød, A., Ringnér, M., ... Stratton, M. R. (2016). Landscape of somatic mutations in 560 breast cancer whole-genome sequences. *Nature*, 534(7605), 47–54. <https://doi.org/10.1038/nature17676>
- Oberbeck, N., Langevin, F., King, G., deWind, N., Crossan, G. P., & Patel, K. J. (2014). Maternal Aldehyde Elimination during Pregnancy Preserves the Fetal Genome. *Molecular Cell*, 55(6), 807–817. <https://doi.org/10.1016/j.molcel.2014.07.010>
- Ohkumo, T., Kondo, Y., Yokoi, M., Tsukamoto, T., Yamada, A., Sugimoto, T., Kanao, R., Higashi, Y., Kondoh, H., Tatematsu, M., Masutani, C., & Hanaoka, F. (2006). UV-B Radiation Induces Epithelial Tumors in Mice Lacking DNA Polymerase η and Mesenchymal Tumors in Mice Deficient for DNA Polymerase ι . *Molecular and Cellular Biology*, 26(20), 7696–7706. <https://doi.org/10.1128/mcb.01076-06>
- Oka, Y., Hamada, M., Nakazawa, Y., Muramatsu, H., Okuno, Y., Higasa, K., Shimada, M., Takeshima, H., Hanada, K., Hirano, T., Kawakita, T., Sakaguchi, H., Ichimura, T., Ozono, S., Yuge, K., Watanabe, Y., Kotani, Y., Yamane, M., Kasugai, Y., ... Ogi, T. (2020). Digenic mutations in ALDH2 and ADH5 impair formaldehyde clearance and cause a multisystem disorder, AMeD syndrome. *Science Advances*, 6(51), 1–15. <https://doi.org/10.1126/SCIADV.ABD7197>
- Olbrich, T., Mayor-Ruiz, C., Vega-Sendino, M., Gomez, C., Ortega, S., Ruiz, S., & Fernandez-Capetillo, O. (2017). A p53-dependent response limits the viability of mammalian haploid cells. *Proceedings of the National Academy of Sciences of the United States of America*, 114(35), 9367–9372. <https://doi.org/10.1073/pnas.1705133114>
- Olivieri, M., Cho, T., Álvarez-Quilón, A., Li, K., Schellenberg, M. J., Zimmermann, M., Hustedt, N., Rossi, S. E., Adam, S., Melo, H., Heijink, A. M., Sastre-Moreno, G., Moatti, N., Szilard, R. K., McEwan, A., Ling, A. K., Serrano-Benitez, A., Ubhi, T., Feng, S., ... Durocher, D. (2020). A Genetic Map of the Response to DNA Damage in Human Cells. *Cell*, 182(2), 481–496.e21. <https://doi.org/10.1016/j.cell.2020.05.040>
- Orelli, B., McClendon, T. B., Tsodikov, O. V., Ellenberger, T., Niedernhofer, L. J., & Scha, O. D. (2010). The XPA-binding domain of ERCC1 Is Required for Nucleotide Excision Repair but Not Other DNA Repair Pathways. *Journal of Biological Chemistry*, 285(6), 3705–3712. <https://doi.org/10.1074/jbc.M109.06753>
- Osada, M., Park, H. L., Park, M. J., Liu, J. W., Wu, G., Trink, B., & Sidransky, D. (2007). A p53-type response element in the GDF15 promoter confers high specificity for p53 activation. *Biochemical and Biophysical Research Communications*, 354(4), 913–918. <https://doi.org/10.1016/j.bbrc.2007.01.089>
- Osterod, M., Larsen, E., Le Page, F., Hengstler, J. G., Van der Horst, G. T. J., Boiteux, S., Klungland, A., & Epe, B. (2002). A global DNA repair mechanism involving the Cockayne syndrome B (CSB) gene product can prevent the in vivo accumulation of endogenous oxidative DNA base damage. *Oncogene*, 21(54), 8232–8239.

- <https://doi.org/10.1038/sj.onc.1206027>
- Ogi, T., Limsirichaikul, S., Overmeer, M., Volker, M., Takenaka, K., Cloney, R., Nakazawa, Y., Niimi, A., Miki, Y., Jaspers, N. G., Mullenders, L. H. F., Yamashita, S., Fousteri, M. I., & Lehmann, A. R. (2010). Article Three DNA Polymerases , Recruited by Different Mechanisms , Carry Out NER Repair Synthesis in Human Cells. *Molecular Cell*, *37*(5), 714–727. <https://doi.org/10.1016/j.molcel.2010.02.009>
- Pace, P., Johnson, M., Tan, W. M., Mosedale, G., Sng, C., Hoatlin, M., de Winter, J., Joenje, H., Gergely, F., & Patel, K. J. (2002). FANCE: the link between Fanconi anaemia complex assembly and activity. *The EMBO Journal*, *21*(13), 3414–3423. <https://doi.org/10.1093/emboj/cdf355>
- Park, H., Kim, C. H., Jeong, J. H., Park, M., & Kim, K. S. (2016). GDF15 contributes to radiation-induced senescence through the ros-mediated p16 pathway in human endothelial cells. *Oncotarget*, *7*(9), 9634–9644. <https://doi.org/10.18632/oncotarget.7457>
- Park, J., Shrestha, R., Qiu, C., Kondo, A., Huang, S., Werth, M., Li, M., Barasch, J., & Suszták, K. (2018). Single-cell transcriptomics of the mouse kidney reveals potential cellular targets of kidney disease. *Science*, *360*(6390), 758–763. <https://doi.org/10.1126/science.aar2131>
- Parmar, K., Kim, J., Sykes, S. M., Shimamura, A., Stuckert, P., Zhu, K., Hamilton, A., Deloach, M. K., Kutok, J. L., Akashi, K., Gilliland, D. G., & D'andrea, A. (2010). Hematopoietic stem cell defects in mice with deficiency of Fancd2 or Usp1. *Stem Cells (Dayton, Ohio)*, *28*(7), 1186–1195. <https://doi.org/10.1002/stem.437>
- Patel, S., Alvarez-Guaita, A., Melvin, A., Rimmington, D., Dattilo, A., Miedzybrodzka, E. L., Cimino, I., Maurin, A. C., Roberts, G. P., Meek, C. L., Virtue, S., Sparks, L. M., Parsons, S. A., Redman, L. M., Bray, G. A., Liou, A. P., Woods, R. M., Parry, S. A., Jeppesen, P. B., ... O'Rahilly, S. (2019). GDF15 Provides an Endocrine Signal of Nutritional Stress in Mice and Humans. *Cell Metabolism*, *29*(3), 707-718.e8. <https://doi.org/10.1016/j.cmet.2018.12.016>
- Pontel, L. B., Rosado, I. V., Burgos-Barragan, G., Garaycochea, J. I., Yu, R., Arends, M. J., Chandrasekaran, G., Broecker, V., Wei, W., Liu, L., Swenberg, J. A., Crossan, G. P., & Patel, K. J. (2015). Endogenous formaldehyde is a hematopoietic stem cell genotoxin and metabolic carcinogen. *Molecular Cell*, *60*(1), 177–188. <https://doi.org/10.1016/j.molcel.2015.08.020>
- Popescu, D. M., Botting, R. A., Stephenson, E., Green, K., Webb, S., Jardine, L., Calderbank, E. F., Polanski, K., Goh, I., Efremova, M., Acres, M., Maunder, D., Vegh, P., Gitton, Y., Park, J. E., Vento-Tormo, R., Miao, Z., Dixon, D., Rowell, R., ... Haniffa, M. (2019). Decoding human fetal liver haematopoiesis. *Nature* *574*(7778), 365-371. <https://doi.org/10.1038/s41586-019-1652-y>
- Prasher, J. M., Lalai, A. S., Heijmans-Antonissen, C., Ploemacher, R. E., Hoeijmakers, J. H. J., Touw, I. P., & Niedernhofer, L. J. (2005). Reduced hematopoietic reserves in DNA interstrand crosslink repair-deficient Ercc1^{-/-} mice. *EMBO Journal*, *24*(4), 861–871. <https://doi.org/10.1038/sj.emboj.7600542>
- Rainey, R. N., Ng, S. Y., Llamas, J., van der Horst, G. T. J., & Segil, N. (2016). Mutations in cockayne syndrome-associated genes (Csa and Csb) predispose to cisplatin-induced hearing loss in mice. *Journal of Neuroscience*, *36*(17), 4758–4770. <https://doi.org/10.1523/JNEUROSCI.3890-15.2016>
- Rajendra, E., Oestergaard, V. H., Langevin, F., Wang, M., Dornan, G. L., Patel, K. J., & Passmore, L. A. (2014). The Genetic and Biochemical Basis of FANCD2 Monoubiquitination. *Molecular Cell*, *54*(5), 858–869. <https://doi.org/10.1016/j.molcel.2014.05.001>
- Ranes, M., Boeing, S., Wang, Y., Wienholz, F., Menoni, H., Walker, J., Encheva, V., Chakravarty, P., Mari, P. O., Stewart, A., Giglia-Mari, G., Snijders, A. P., Vermeulen, W., & Svejstrup, J. Q. (2016). A ubiquitylation site in Cockayne syndrome B required for repair of oxidative DNA damage, but not for transcription-coupled nucleotide excision repair. *Nucleic Acids Research*, *44*(11), 5246–5255. <https://doi.org/10.1093/nar/gkw216>

- Reid-Bayliss, K. S., Arron, S. T., Loeb, L. A., Bezrookov, V., & Cleaver, J. E. (2016). Why Cockayne syndrome patients do not get cancer despite their DNA repair deficiency. *Proceedings of the National Academy of Sciences of the United States of America*, *113*(36), 10151–10156. <https://doi.org/10.1073/pnas.1610020113>
- Rockx, D. A. P., Mason, R., Van Hoffen, A., Barton, M. C., Citterio, E., Bregman, D. B., Van Zeeland, A. A., Vrieling, H., & Mullenders, L. H. F. (2000). UV-induced inhibition of transcription involves repression of transcription initiation and phosphorylation of RNA polymerase II. *Proceedings of the National Academy of Sciences of the United States of America*, *97*(19), 10503–10508. <https://doi.org/10.1073/pnas.180169797>
- Rosado, I. V., Langevin, F., Crossan, G. P., Takata, M., & Patel, K. J. (2011). Formaldehyde catabolism is essential in cells deficient for the Fanconi anemia DNA-repair pathway. *Nature Structural and Molecular Biology*, *18*(12), 1432–1434. <https://doi.org/10.1038/nsmb.2173>
- Sabatella, M., Theil, A. F., Ribeiro-Silva, C., Slyskova, J., Thijssen, K., Voskamp, C., Lans, H., & Vermeulen, W. (2018). Repair protein persistence at DNA lesions characterizes XPF defect with Cockayne syndrome features. *Nucleic Acids Research*, *46*(18), 9563–9577. <https://doi.org/10.1093/nar/gky774>
- Sala-Trepat, M., Rouillard, D., Escarceller, M., Laquerbe, A., Moustacchi, E., & Papadopoulou, D. (2000). Arrest of S-phase progression is impaired in Fanconi anemia cells. *Experimental Cell Research*, *260*(2), 208–215. <https://doi.org/10.1006/excr.2000.4994>
- Sands, A. T., Abuin, A., Sanchez, A., Conti, C. J., & Bradley, A. (1995). High susceptibility to ultraviolet-induced carcinogenesis in mice lacking XPC. *Nature*, *377*(6545), 162–165. <https://doi.org/10.1038/377162a0>
- Sanghani, P. C., Bosron, W. F., & Hurley, T. D. (2002). Human glutathione-dependent formaldehyde dehydrogenase. Structural changes associated with ternary complex formation. *Biochemistry*, *41*(51), 15189–15194. <https://doi.org/10.1021/bi026705q>
- Sarkar, S., Davies, A. A., Ulrich, H. D., & McHugh, P. J. (2006). DNA interstrand crosslink repair during G1 involves nucleotide excision repair and DNA polymerase ζ . *EMBO Journal*, *25*(6), 1285–1294. <https://doi.org/10.1038/sj.emboj.7600993>
- Sasaki, M. S., & Tonomura, A. (1973). A High Susceptibility of Fanconi's Anemia to Chromosome Breakage by DNA Cross-linking Agents. *Cancer Research*, *33*(8), 1829–1836.
- Scheibye-knudsen, M., Mitchell, S. J., Fang, E. F., Iyama, T., Ward, T., Wang, J., Dunn, C. A., Singh, N., Veith, S., Hasan, M. M., Mangerich, A., Wilson, M. A., Mattson, M. P., Linda, H., Cogger, V. C., Warren, A., Couteur, D. G. Le, Wilson, D. M., Croteau, D. L., ... Vilhelm, A. (2015). A High Fat Diet and NAD⁺ Rescue Premature Aging in Cockayne Syndrome. *Cell Metabolism*, *20*(5), 840–855. <https://doi.org/10.1016/j.cmet.2014.10.005.A>
- Scheibye-Knudsen, M., Ramamoorthy, M., Sykora, P., Maynard, S., Lin, P. C., Minor, R. K., Wilson, D. M., Cooper, M., Spencer, R., de Cabo, R., Croteau, D. L., & Bohr, V. A. (2012). Cockayne syndrome group B protein prevents the accumulation of damaged mitochondria by promoting mitochondrial autophagy. *Journal of Experimental Medicine*, *209*(4), 855–869. <https://doi.org/10.1084/jem.20111721>
- Schwab, R. A., Nieminuszczy, J., Shah, F., Langton, J., Lopez Martinez, D., Liang, C. C., Cohn, M. A., Gibbons, R. J., Deans, A. J., & Niedzwiedz, W. (2015). The Fanconi Anemia Pathway Maintains Genome Stability by Coordinating Replication and Transcription. *Molecular Cell*, *60*(3), 351–361. <https://doi.org/10.1016/j.molcel.2015.09.012>
- Scrima, A., Koničková, R., Czyzewski, B. K., Kawasaki, Y., Jeffrey, P. D., Groisman, R., Nakatani, Y., Iwai, S., Pavletich, N. P., & Thomä, N. H. (2008). Structural Basis of UV DNA-Damage Recognition by the DDB1-DDB2 Complex. *Cell*, *135*(7), 1213–1223. <https://doi.org/10.1016/j.cell.2008.10.045>
- Selfridge, J., Hsia, K. T., Redhead, N. J., & Melton, D. W. (2001). Correction of liver dysfunction in DNA repair-deficient mice with an ERCC1 transgene. *Nucleic Acids Research*, *29*(22), 4541–4550. <https://doi.org/10.1093/nar/29.22.4541>

- Shakeel, S., Rajendra, E., Alcón, P., O'Reilly, F., Chorev, D. S., Maslen, S., Degliesposti, G., Russo, C. J., He, S., Hill, C. H., Skehel, J. M., Scheres, S. H. W., Patel, K. J., Rappsilber, J., Robinson, C. V., & Passmore, L. A. (2019). Structure of the Fanconi anaemia monoubiquitin ligase complex. *Nature*, *575*(7781), 234–237. <https://doi.org/10.1038/s41586-019-1703-4>
- Shen, J.-L., & Loeb, L. A. (2000). The Werner syndrome gene. *Trends Genet.*, *16*(99), 213–220. [http://dx.doi.org/10.1016/S0168-9525\(99\)01970-8](http://dx.doi.org/10.1016/S0168-9525(99)01970-8)
- Shen, X., Wang, R., Kim, M. J., Hu, Q., Hsu, C. C., Yao, J., Klages-Mundt, N., Tian, Y., Lynn, E., Brewer, T. F., Zhang, Y., Arun, B., Gan, B., Andreeff, M., Takeda, S., Chen, J., Park, J. il, Shi, X., Chang, C. J., ... Li, L. (2020). A Surge of DNA Damage Links Transcriptional Reprogramming and Hematopoietic Deficit in Fanconi Anemia. *Molecular Cell*, *80*(6), 1013-1024.e6. <https://doi.org/10.1016/j.molcel.2020.11.040>
- Shiomi, N., Kito, S., Oyama, M., Matsunaga, T., Harada, Y.-N., Ikawa, M., Okabe, M., & Shiomi, T. (2004). Identification of the XPG Region That Causes the Onset of Cockayne Syndrome by Using Xpg Mutant Mice Generated by the cDNA-Mediated Knock-In Method. *Molecular and Cellular Biology*, *24*(9), 3712–3719. <https://doi.org/10.1128/mcb.24.9.3712-3719.2004>
- Sladek, F. M., Munn, M. M., Rupp, W. D., & Howard-Flanders, P. (1989). In vitro repair of psoralen-DNA cross-links by RecA, UvrABC, and the 5'-exonuclease of DNA polymerase I. *Journal of Biological Chemistry*, *264*(12), 6755–6765. [https://doi.org/10.1016/s0021-9258\(18\)83494-9](https://doi.org/10.1016/s0021-9258(18)83494-9)
- Slyskova, J., Sabatella, M., Ribeiro-Silva, C., Stok, C., Theil, A. F., Vermeulen, W., & Lans, H. (2018). Base and nucleotide excision repair facilitate resolution of platinum drugs-induced transcription blockage. *Nucleic Acids Research*, *46*(18), 9537–9549. <https://doi.org/10.1093/nar/gky764>
- Sonohara, Y., Yamamoto, J., Tohashi, K., Takatsuka, R., Matsuda, T., Iwai, S., & Kuraoka, I. (2019). Acetaldehyde forms covalent GG intrastrand crosslinks in DNA. *Scientific Reports*, *9*(1), 1–8. <https://doi.org/10.1038/s41598-018-37239-6>
- Stern-Delfils, A., Spitz, M. A., Durand, M., Obringer, C., Calmels, N., Olagne, J., Pillay, K., Fieggen, K., Laugel, V., & Zaloszcyc, A. (2020). Renal disease in Cockayne syndrome. *European Journal of Medical Genetics*, *63*(1), 103612. <https://doi.org/10.1016/j.ejmg.2019.01.002>
- Strathdee, C. A., Gavish, H., Shannon, W. R., & Buchwald, M. (1992). Erratum: Cloning of cDNAs for Fanconi's anaemia by functional complementation (Nature (1992) 356 (763-767)). *Nature*, *358*(6385), 434. <https://doi.org/10.1038/358434a0>
- Stuart, T., Butler, A., Hoffman, P., Hafemeister, C., Papalexi, E., Mauck, W. M., Hao, Y., Stoeckius, M., Smibert, P., & Satija, R. (2019). Comprehensive Integration of Single-Cell Data. *Cell*, *177*(7), 1888-1902.e21. <https://doi.org/10.1016/j.cell.2019.05.031>
- Sugasawa, K., Ng, J. M. Y., Masutani, C., Iwai, S., Van Der Spek, P. J., Eker, A. P. M., Hanaoka, F., Bootsma, D., & Hoeijmakers, J. H. J. (1998). Xeroderma pigmentosum group C protein complex is the initiator of global genome nucleotide excision repair. *Molecular Cell*, *2*(2), 223–232. [https://doi.org/10.1016/S1097-2765\(00\)80132-X](https://doi.org/10.1016/S1097-2765(00)80132-X)
- Suriben, R., Chen, M., Higbee, J., Oeffinger, J., Ventura, R., Li, B., Mondal, K., Gao, Z., Ayupova, D., Taskar, P., Li, D., Starck, S. R., Chen, H. I. H., McEntee, M., Katewa, S. D., Phung, V., Wang, M., Kekatpure, A., Lakshminarasimhan, D., ... Allan, B. B. (2020). Antibody-mediated inhibition of GDF15–GFRAL activity reverses cancer cachexia in mice. *Nature Medicine*, *26*(8), 1264–1270. <https://doi.org/10.1038/s41591-020-0945-x>
- Svendsen, J. M., Smogorzewska, A., Sowa, M. E., O'Connell, B. C., Gygi, S. P., Elledge, S. J., & Harper, J. W. (2009). Mammalian BTBD12/SLX4 Assembles A Holliday Junction Resolvase and Is Required for DNA Repair. *Cell*, *138*(1), 63–77. <https://doi.org/10.1016/j.cell.2009.06.030>
- Tanaka, T., Biancotto, A., Moaddel, R., Moore, A. Z., Gonzalez-Freire, M., Aon, M. A., Candia, J., Zhang, P., Cheung, F., Fantoni, G., Semba, R. D., & Ferrucci, L. (2018). Plasma proteomic signature of age in healthy humans. *Aging Cell*, *17*(5), 1–13. <https://doi.org/10.1111/acel.12799>

- Tapias, A., Auriol, J., Forget, D., Enzlin, J. H., Scha, O. D., Coin, F., Coulombe, B., & Egly, J. (2004). *Ordered Conformational Changes in Damaged DNA Induced by Nucleotide Excision Repair Factors* *. 279(18), 19074–19083. <https://doi.org/10.1074/jbc.M312611200>
- Thompson, L. H., Brookman, K. W., Weber, C. A., Salazar, E. P., Reardon, J. T., Sancar, A., Deng, Z., & Siciliano, M. J. (1994). Molecular cloning of the human nucleotide-excision-repair gene ERCC4. *Proceedings of the National Academy of Sciences of the United States of America*, 91(15), 6855–6859. <https://doi.org/10.1073/pnas.91.15.6855>
- Tian, M., Jones, D. A., Smith, M., Shinkura, R., & Alt, F. W. (2004). Deficiency in the Nuclease Activity of Xeroderma Pigmentosum G in Mice Leads to Hypersensitivity to UV Irradiation. *Molecular and Cellular Biology*, 24(6), 2237–2242. <https://doi.org/10.1128/mcb.24.6.2237-2242.2004>
- Tian, Ming, Shinkura, R., Shinkura, N., & Alt, F. W. (2004). Growth retardation, early death, and DNA repair defects in mice deficient for the nucleotide excision repair enzyme XPF. *Molecular and Cellular Biology*, 24(3), 1200–1205. <https://doi.org/10.1128/mcb.24.3.1200-1205.2004>
- Traag, V. A., Waltman, L., & van Eck, N. J. (2019). From Louvain to Leiden: guaranteeing well-connected communities. *Scientific Reports*, 9(1), 5233. <https://doi.org/10.1038/s41598-019-41695-z>
- Tronche, F., Kellendonk, C., Kretz, O., Gass, P., Anlag, K., Orban, P. C., Bock, R., Klein, R., & Schütz, G. (1999). Disruption of the glucocorticoid receptor gene in the nervous system results in reduced anxiety. *Nature Genetics*, 23(1), 99–103. <https://doi.org/10.1038/12703>
- Tufegdžić Vidaković, A., Harreman, M., Dirac-Svejstrup, A. B., Boeing, S., Roy, A., Encheva, V., Neumann, M., Wilson, M., Snijders, A. P., & Svejstrup, J. Q. (2019). Analysis of RNA polymerase II ubiquitylation and proteasomal degradation. *Methods*, 159–160(February), 146–156. <https://doi.org/10.1016/j.ymeth.2019.02.005>
- Tufegdžić Vidaković, A., Mitter, R., Kelly, G. P., Neumann, M., Harreman, M., Rodríguez-Martínez, M., Herlihy, A., Weems, J. C., Boeing, S., Encheva, V., Gaul, L., Milligan, L., Tollervey, D., Conaway, R. C., Conaway, J. W., Snijders, A. P., Stewart, A., & Svejstrup, J. Q. (2020). Regulation of the RNAPII Pool Is Integral to the DNA Damage Response. *Cell*, 180(6), 1245–1261.e21. <https://doi.org/10.1016/j.cell.2020.02.009>
- Vaidya, V. S., Ramirez, V., Ichimura, T., Bobadilla, N. A., & Bonventre, J. V. (2006). Urinary kidney injury molecule-1: A sensitive quantitative biomarker for early detection of kidney tubular injury. *American Journal of Physiology - Renal Physiology*, 290(2), 517–529. <https://doi.org/10.1152/ajprenal.00291.2005>
- Valentijn, F. A., Falke, L. L., Nguyen, T. Q., & Goldschmeding, R. (2018). Cellular senescence in the aging and diseased kidney. *Journal of Cell Communication and Signaling*, 12(1), 69–82. <https://doi.org/10.1007/s12079-017-0434-2>
- van der Horst, G. T. J., Meira, L., Gorgels, T. G. M. F., de Wit, J., Velasco-Miguel, S., Richardson, J. A., Kamp, Y., Vreeswijk, M. P. G., Smit, B., Bootsma, D., Hoeijmakers, J. H. J., & Friedberg, E. C. (2002). UVB radiation-induced cancer predisposition in Cockayne syndrome group A (Csa) mutant mice. *DNA Repair*, 1(2), 143–157. [https://doi.org/10.1016/S1568-7864\(01\)00010-6](https://doi.org/10.1016/S1568-7864(01)00010-6)
- Van Der Horst, G. T. J., Meira, L., Gorgels, T. G. M. F., De Wit, J., Velasco-Miguel, S., Richardson, J. A., Kamp, Y., Vreeswijk, M. P. G., Smit, B., Bootsma, D., Hoeijmakers, J. H. J., & Friedberg, E. C. (2002). UVB radiation-induced cancer predisposition in Cockayne syndrome group A (Csa) mutant mice. *DNA Repair*, 1(2), 143–157. [https://doi.org/10.1016/S1568-7864\(01\)00010-6](https://doi.org/10.1016/S1568-7864(01)00010-6)
- van der Horst, G. T., van Steeg, H., Berg, R. J., van Gool, A. J., de Wit, J., Weeda, G., Morreau, H., Beems, R. B., van Kreijl, C. F., de Gruijl, F. R., Bootsma, D., & Hoeijmakers, J. H. J. (1997). Defective transcription-coupled repair in Cockayne syndrome B mice is associated with skin cancer predisposition. *Cell*, 89(3), 425–435. [https://doi.org/10.1016/s0092-8674\(00\)80223-8](https://doi.org/10.1016/s0092-8674(00)80223-8)
- van der Pluijm, I., Garinis, G. A., Brandt, R. M. C., Gorgels, T. G. M. F., Wijnhoven, S. W.,

- Diderich, K. E. M., de Wit, J., Mitchell, J. R., van Oostrom, C., Beems, R., Niedernhofer, L. J., Velasco, S., Friedberg, E. C., Tanaka, K., van Steeg, H., Hoeijmakers, J. H. J., & van der Horst, G. T. J. (2007). Impaired genome maintenance suppresses the growth hormone-insulin-like growth factor 1 axis in mice with Cockayne syndrome. *PLoS Biology*, *5*(1), e2. <https://doi.org/10.1371/journal.pbio.0050002>
- Van Der Pluijm, I., Garinis, G. A., Brandt, R. M. C., Gorgels, T. G. M. F., Wijnhoven, S. W., Diderich, K. E. M., De Wit, J., Mitchell, J. R., Van Oostrom, C., Beems, R., Niedernhofer, L. J., Velasco, S., Friedberg, E. C., Tanaka, K., Van Steeg, H., Hoeijmakers, J. H. J., & Van Der Horst, G. T. J. (2007). Impaired genome maintenance suppresses the growth hormone-insulin-like growth factor 1 axis in mice with cockayne syndrome. *PLoS Biology*, *5*(1), 0023–0038. <https://doi.org/10.1371/journal.pbio.0050002>
- van der Weegen, Y., Golan-Berman, H., Mevissen, T. E. T., Apelt, K., González-Prieto, R., Goedhart, J., Heilbrun, E. E., Vertegaal, A. C. O., van den Heuvel, D., Walter, J. C., Adar, S., & Luijsterburg, M. S. (2020). The cooperative action of CSB, CSA, and UVSSA target TFIIH to DNA damage-stalled RNA polymerase II. *Nature Communications*, *11*(1), 1–16. <https://doi.org/10.1038/s41467-020-15903-8>
- van Houten, B., Gamper, H., Holbrook, S. R., Hearst, J. E., & Sancar, A. (1986). Action mechanism of ABC excision nuclease on a DNA substrate containing a psoralen crosslink at a defined position. *Proceedings of the National Academy of Sciences of the United States of America*, *83*(21), 8077–8081. <https://doi.org/10.1073/pnas.83.21.8077>
- Verhagen-Oldenampsen, J. H. E., Haanstra, J. R., van Strien, P. M. H., Valkhof, M., Touw, I. P., & von Lindern, M. (2012). Loss of Ercc1 Results in a Time- and Dose-Dependent Reduction of Proliferating Early Hematopoietic Progenitors. *Anemia*, *2012*(Mmc), 1–9. <https://doi.org/10.1155/2012/783068>
- Vermeij, W. P., Dollé, M. E. T., Reiling, E., Jaarsma, D., Payan-Gomez, C., Bombardieri, C. R., Wu, H., Roks, A. J. M., Botter, S. M., Van Der Eerden, B. C., Youssef, S. A., Kuiper, R. V., Nagarajah, B., Van Oostrom, C. T., Brandt, R. M. C., Barnhoorn, S., Imholz, S., Pennings, J. L. A., De Bruin, A., ... Hoeijmakers, J. H. J. (2016). Restricted diet delays accelerated ageing and genomic stress in DNA-repair-deficient mice. *Nature*, *537*(7620), 427–431. <https://doi.org/10.1038/nature19329>
- Wang, A. T., Sengerová, B., Cattell, E., Inagawa, T., Hartley, J. M., Kiakos, K., Burgess-Brown, N. A., Swift, L. P., Enzlin, J. H., Schofield, C. J., Gileadi, O., Hartley, J. A., & McHugh, P. J. (2011). Human SNM1A and XPF-ERCC1 collaborate to initiate DNA interstrand cross-link repair. *Genes & Development*, *25*(17), 1859–1870. <https://doi.org/10.1101/gad.15699211>
- Wang, B., Kohli, J., & Demaria, M. (2020). file:///Users/patellab/Downloads/s41591-020-0945-x.pdf Senescent Cells in Cancer Therapy: Friends or Foes? *Trends in Cancer*, *6*(10), 838–857. <https://doi.org/10.1016/j.trecan.2020.05.004>
- Wang, S., Min, Z., Ji, Q., Geng, L., Su, Y., Liu, Z., Hu, H., Wang, L., Zhang, W., Suzuiki, K., Huang, Y., Zhang, P., Tang, T. S., Qu, J., Yu, Y., Liu, G. H., & Qiao, J. (2020). Rescue of premature aging defects in Cockayne syndrome stem cells by CRISPR/Cas9-mediated gene correction. *Protein and Cell*, *11*(1), 1–22. <https://doi.org/10.1007/s13238-019-0623-2>
- Wang, Y., Chakravarty, P., Ranes, M., Kelly, G., Brooks, P. J., Neilan, E., Stewart, A., Schiavo, G., & Svejstrup, J. Q. (2014). Dysregulation of gene expression as a cause of cockayne syndrome neurological disease. *Proceedings of the National Academy of Sciences of the United States of America*, *111*(40), 14454–14459. <https://doi.org/10.1073/pnas.1412569111>
- Wang, Y., Jones-Tabah, J., Chakravarty, P., Stewart, A., Muotri, A., Laposa, R. R., & Svejstrup, J. Q. (2016). Pharmacological Bypass of Cockayne Syndrome B Function in Neuronal Differentiation. *Cell Reports*, *14*(11), 2554–2561. <https://doi.org/10.1016/j.celrep.2016.02.051>
- Watson, H. J., Yilmaz, Z., Thornton, L. M., Hübel, C., Coleman, J. R. I., Gaspar, H. A., Bryois, J., Hinney, A., Leppä, V. M., Mattheisen, M., Medland, S. E., Ripke, S., Yao, S., Giusti-Rodríguez, P., Hanscombe, K. B., Purves, K. L., Adan, R. A. H., Alfredsson, L.,

- Ando, T., ... Bulik, C. M. (2019). Genome-wide association study identifies eight risk loci and implicates metabo-psychiatric origins for anorexia nervosa. *Nature Genetics*, *51*(8), 1207–1214. <https://doi.org/10.1038/s41588-019-0439-2>
- Weber, C. A., Salazar, E. P., Stewart, S. A., & Thompson, L. H. (1988). Molecular cloning and biological characterization of a human gene, ERCC2, that corrects the nucleotide excision repair defect in CHO UV5 cells. *Molecular and Cellular Biology*, *8*(3), 1137–1146. <https://doi.org/10.1128/mcb.8.3.1137>
- Weeda, G., Donker, I., de Wit, J., Morreau, H., Janssens, R., Vissers, C. J., Nigg, A., van Steeg, H., Bootsma, D., & Hoeijmakers, J. H. (1997). Disruption of mouse ERCC1 results in a novel repair syndrome with growth failure, nuclear abnormalities and senescence. *Current Biology*, *7*(6), 427–439.
- Weeda, G., van Ham, R. C., Masurel, R., Westerveld, A., Odijk, H., de Wit, J., Bootsma, D., van der Eb, A. J., & Hoeijmakers, J. H. (1990). Molecular cloning and biological characterization of the human excision repair gene ERCC-3. *Molecular and Cellular Biology*, *10*(6), 2570–2581. <https://doi.org/10.1128/mcb.10.6.2570>
- Wei, W., Li, B., Hanes, M. A., Kakar, S., Chen, X., & Liu, L. (2010). S-nitrosylation from GSNOR deficiency impairs DNA repair and promotes hepatocarcinogenesis. *Science Translational Medicine*, *2*(19). <https://doi.org/10.1126/scitranslmed.3000328>
- Weissman, L., de Souza-Pinto, N. C., Stevensner, T., & Bohr, V. A. (2007). DNA repair, mitochondria, and neurodegeneration. *Neuroscience*, *145*(4), 1318–1329. <https://doi.org/10.1016/j.neuroscience.2006.08.061>
- Westerveld, A., Hoeijmakers, J. H. J., Van Duin, M., De Wit, J., Odijk, H., Pastink, A., Wood, R. D., & Bootsma, D. (1984). Molecular cloning of a human DNA repair gene. *Nature*, *310*(5976), 425–429. <https://doi.org/10.1038/310425a0>
- Whitney, M. A., Royle, G., Low, M. J., Kelly, M. A., Axthelm, M. K., Reifsteck, C., Olson, S., Braun, R. E., Heinrich, M. C., Rathbun, R. K., Bagby, G. C., & Grompe, M. (1996). Germ cell defects and hematopoietic hypersensitivity to γ -interferon in mice with a targeted disruption of the fanconi anemia C gene. *Blood*, *88*(1), 49–58. <https://doi.org/10.1182/blood.v88.1.49.bloodjournal88149>
- Wilson, B. T., Stark, Z., Sutton, R. E., Danda, S., Ekbote, A. V., Elsayed, S. M., Gibson, L., Goodship, J. A., Jackson, A. P., Keng, W. T., King, M. D., McCann, E., Motojima, T., Murray, J. E., Omata, T., Pilz, D., Pope, K., Sugita, K., White, S. M., & Wilson, I. J. (2016). The Cockayne Syndrome Natural History (CoSyNH) study: Clinical findings in 102 individuals and recommendations for care. *Genetics in Medicine*, *18*(5), 483–493. <https://doi.org/10.1038/gim.2015.110>
- Wilson, M. D., Harreman, M., & Svejstrup, J. Q. (2013). Ubiquitylation and degradation of elongating RNA polymerase II: The last resort. *Biochimica et Biophysica Acta - Gene Regulatory Mechanisms*, *1829*(1), 151–157. <https://doi.org/10.1016/j.bbagr.2012.08.002>
- Wolf, F. A., Angerer, P., & Theis, F. J. (2018). SCANPY: large-scale single-cell gene expression data analysis. *Genome Biology*, *19*(1), 15. <https://doi.org/10.1186/s13059-017-1382-0>
- Wolock, S. L., Lopez, R., & Klein, A. M. (2019). Scrublet: Computational Identification of Cell Doublets in Single-Cell Transcriptomic Data. *Cell Systems*, *8*(4), 281–291.e9. <https://doi.org/10.1016/j.cels.2018.11.005>
- Wong, J. C. Y., Alon, N., Mckerlie, C., Huang, J. R., Meyn, M. S., & Buchwald, M. (2003). Targeted disruption of exons 1 to 6 of the Fanconi Anemia group A gene leads to growth retardation, strain-specific microphthalmia, meiotic defects and primordial germ cell hypoplasia. *Human Molecular Genetics*, *12*(16), 2063–2076. <https://doi.org/10.1093/hmg/ddg219>
- Xu, J., Lahiri, I., Wang, W., Wier, A., Cianfrocco, M. A., Chong, J., Hare, A. A., Dervan, P. B., DiMaio, F., Leschziner, A. E., & Wang, D. (2017). Structural basis for the initiation of eukaryotic transcription-coupled DNA repair. *Nature*, *551*(7682), 653–657. <https://doi.org/10.1038/nature24658>
- Xu, Y., Wu, Z., Liu, L., Liu, J., & Wang, Y. (2019). Rat Model of Cockayne Syndrome

- Neurological Disease. *Cell Reports*, 29(4), 800-809.e5. <https://doi.org/10.1016/j.celrep.2019.09.028>
- Young, M. D., & Behjati, S. (2018). SoupX removes ambient RNA contamination from droplet based single cell RNA sequencing data. *BioRxiv*, 303727. <https://doi.org/10.1101/303727>
- Young, M. D., Mitchell, T. J., Vieira Braga, F. A., Tran, M. G. B., Stewart, B. J., Ferdinand, J. R., Collord, G., Botting, R. A., Popescu, D. M., Loudon, K. W., Vento-Tormo, R., Stephenson, E., Cagan, A., Farndon, S. J., Velasco-Herrera, M. D. C., Guzzo, C., Richoz, N., Mamanova, L., Aho, T., ... Behjati, S. (2018). Single-cell transcriptomes from human kidneys reveal the cellular identity of renal tumors. *Science*, 361(6402), 594–599. <https://doi.org/10.1126/science.aat1699>
- Yousefzadeh, M. J., Flores, R. R., Zhu, Y., Schmiechen, Z. C., Brooks, R. W., Trussoni, C. E., Cui, Y., Angelini, L., Lee, K. A., McGowan, S. J., Burrack, A. L., Wang, D., Dong, Q., Lu, A., Sano, T., O’Kelly, R. D., McGuckian, C. A., Kato, J. I., Bank, M. P., ... Niedernhofer, L. J. (2021). An aged immune system drives senescence and ageing of solid organs. *Nature*, 594(7861), 100-105. <https://doi.org/10.1038/s41586-021-03547-7>
- Yu, R., Lai, Y., Hartwell, H. J., Moeller, B. C., Doyle-Eisele, M., Kracko, D., Bodnar, W. M., Starr, T. B., & Swenberg, J. A. (2015). Formation, accumulation, and hydrolysis of endogenous and exogenous formaldehyde-induced DNA damage. *Toxicological Sciences*, 146(1), 170–182. <https://doi.org/10.1093/toxsci/kfv079>
- Yurchenko, A. A., Padioleau, I., Matkarimov, B. T., Soulier, J., Sarasin, A., & Nikolaev, S. (2020). XPC deficiency increases risk of hematologic malignancies through mutator phenotype and characteristic mutational signature. *Nature Communications*, 11(1), 1–11. <https://doi.org/10.1038/s41467-020-19633-9>
- Zhang, Q. S., Marquez-Loza, L., Eaton, L., Duncan, A. W., Goldman, D. C., Anur, P., Watanabe-Smith, K., Rathbun, R. K., Fleming, W. H., Bagby, G. C., & Grompe, M. (2010). *Fancd2*^{-/-} mice have hematopoietic defects that can be partially corrected by resveratrol. *Blood*, 116(24), 5140–5148. <https://doi.org/10.1182/blood-2010-04-278226>
- Zhang, Q. S., Tang, W., Deater, M., Phan, N., Marcogliese, A. N., Li, H., Al-Dhalimy, M., Major, A., Olson, S., Monnat, R. J., & Grompe, M. (2016). Metformin improves defective hematopoiesis and delays tumor formation in Fanconi anemia mice. *Blood*, 128(24), 2774–2784. <https://doi.org/10.1182/blood-2015-11-683490>

Supplemental tables

Supplementary Table 1. gRNAs

Gene	Left CRISPR	Right CRISPR
<i>XPC</i>	5' GTTTGAGACATATCTTCGGAGGG 3'	5' CAACAAATAGTGAAAAATCTGGG 3'
<i>XPA</i>	5' GAATCCACATCATTACAATGGG 3'	5' TTCACAATAAATTTAAGAGGTGG 3'
<i>CSB (ERCC6)</i>	5' TTCAAATGCTTCCCCAGTACAGG 3'	5' GAGAAGTCTCCATAAACACAGG 3'
<i>XPF (ERCC4)</i>	5' GACAAGACTCGATTATTCTGTGG 3'	5' TTTCGCCAGAAAAACAAACGTGG 3'
<i>FANCL</i>	5' ACAGCACGCAGAATTGCATTAGG 3'	5' TTTTCTGGCTCAAGTACCCAGG 3'

Supplementary Table 2. Screening by PCR

Gene	Forward Primer	Reverse Primer
<i>XPC</i>	5' TTTGAGGCATGTAGGTGAGGTGT 3'	5' CCACGCTGATCTCTTTCAGTGT 3'
<i>XPA</i>	5' CTCCTCACCATCGCTTACTTCAG 3'	5' GGAGATGGAGGTGAAAGAGGGTA 3'
<i>CSB (ERCC6)</i>	5' AGTGTCCCCTTTTCTAAGTTTCTCC 3'	5' CTACATTCGATTGATGCAGGATGAC 3'
<i>XPF (ERCC4)</i>	5' TCCATCCAGCCTTTATTTCAGATACC 3'	5' TCAAAGCAGAAGTGGTAATGTTAGC 3'
<i>FANCL 5' arm</i>	5' TTTTGGCAGGGGAGTTAACCTT 3'	5' GCGATCTCTGGGTTCTACGTTAGTG 3'
<i>FANCL 3' arm</i>	5' CACACCTCCCCTGAACCTGAAAC 3'	5' TAAGCCTTTCACCTAAGGCTGGCA 3'

Supplementary Table 3. Sanger sequencing of PCR products

Gene	Forward Primer	Reverse Primer
<i>XPC</i>	5' TTTGCTGGTGAGAAGGAGC 3'	5' GCAGCAAAGCCAGAAATAAAGC 3'
<i>XPA</i>	5' CCTTTTTGCTGTGTGTGC 3'	5' CACTCTGTAAGCAAAAGCC 3'
<i>CSB (ERCC6)</i>	5' ACCAATTTATGAGCCTGGCC 3'	5' GCAGAGGAGCGTTTTAGGGT 3'
<i>XPF (ERCC4)</i>	5' CTCTGTTCTGTGCGTGGCTA 3'	5' CACATAATGTTCTTTACCTTGCCA 3'

Supplemental Table 4 - Top 100 Marker Genes For each PT Sub-cluster

PT-0	PT-1	PT-2	PT-3	PT-4	PT-5	PT-6	PT-7
Gatm	Kap	Spp2	Gm27200	Kim-1	Serpina1f	Lypd2	Pbk
Gsta2	Gm48281	Apob	Vmn1r18	Gbp2b	Akr1c18	Proser2	Hmnr
Gm10639	Hpd	Slc5a2	Gm47689	Serpina10	Cyp7b1	Upk3b	Ccnb2
Car3	Gm4208	Ugt2b34	Gm11713	Ubd	Ceacam2	Bst1	Prc1
Hbb-bt	Synpr	Slc3a2	Gm15261	Tgtp1	Rhox6	Sptssb	Cdkn3
Gm36372	Ctxn3	F5	Gm26981	ligp1	Serpina1d	Upk1b	Ccnb1
Oat	Slco1a1	Slc34a3	D830024N08Rik	Gbp2	Serpina1b	Slc4a11	Ube2c
Cox6a2	Azgp1	Cyp2d26	AY074887	H2-DMb2	Serpina1a	Fst	Cdca3
D630023F18Rik	Cndp2	Spp1	B430010I23Rik	Cxcl10	Apoa4	Psca	Ckap2l
Gm11837	Acsm3	Apoe	Gm26699	Ifi47	Slco4c1	Ppl	Cdk1
Fabp3	Napsa	Gc	Gm14764	Ifit1	Slc22a19	Sprr1a	Ckap2
Ccdc151	Apoh	Hexa	Gm26632	Gbp3	Slc22a13	Spon1	Mxd3
Hbb-bs	Dpys	Slc6a19	Gm26917	Gm17416	Methig1	Tshz2	Aurka
Car2	Irx3	Mdk	Gm40055	Dpysl3	Bcat1	Apela	Plk1
Id3	Slc7a13	Slc7a8	Egfros	Ifit2	Irx1	Ptpn14	Cdc20
Npl	Mir124-2hg	Slc7a7	4921539H07Rik	Isg15	Aqp4	Ncam1	Lockd
Selenow	Inmt	Endod1	Lncpint	Cbr3	Myo5a	Wnt7b	Top2a
Phgdh	Gm15563	Dpep1	Gm6999	C3	Arg2	Ankrd1	Ccna2
Cotl1	Hsd11b1	Pdzk1ip1	Gm45509	Psmb8	Cldn3	Cdh6	Esco2
Fabp1	Nudt19	Agmo	Shhg11	Ifit3	Mep1b	Rab27b	Birc5
Lyplal1	Cyp2d9	Gpat3	Kcnq1ot1	Ephx1	Mettl7a2	Krt19	Tpx2
Fhit	Bdh1	Lgmn	4930518I15Rik	Psmb9	Tspan13	Cldn4	Racgap1
Slc25a4	Cyp2a4	Steap1	Vmn1r19	Gstp3	Scd1	Runx1	Rrm2
Nap115	Ly6a	Slc4a4	Pde4d	Fgb	Fam107a	Upk3a	Cenpf
Bex4	Hsd17b2	Dhrs7	Cd27	Xaf1	Slc7a12	Akap12	Cenpm
Cdkl1	Lpl	Alpl	Gm26767	Rtp4	Slc22a7	Foxc1	Knstrn
Tceal9	Mogat1	Prss23	Vmn1r20	Cd74	Napsa	4930523C07Rik	Kif20a
Rasl2-9	Ggct	Cfi	Gm26601	Ifit3b	Irx2	Fry	Kif11
Uap111	Chst7	Tmem86b	Gm26724	Cfi	Cryab	Rbms3	Cenpa
Tfpi2	Pzp	Gm11127	Gm26890	Fga	Kcnk1	Thbs1	Mki67
Atp6v1g1	Gm15348	Creg1	Gm26627	Igtp	Ppic	Nupr1	Pclaf
Pde1a	Tmigd1	Lgals3bp	Gm43625	Fgg	Gdgd3	Plet1	Tacc3
Psat1	Ly6e	Cdh2	AC121960.2	H2-Ab1	Agt	Hacd4	Cdca8
Gsta4	Eci3	Tcn2	Gm26798	Hspb1	Mfsd2a	Krt18	Nusap1
Tagln2	Slc5a10	Slc2a2	Gm26518	Bst2	Slc39a8	S100a6	Ect2
Psph	Nat8	Ctsl	D230017M19Rik	H2-DMA	Cp	Dnm3	Trim59
Nepn	Vps8	Tfpi	9430060I03Rik	Cyp4a14	Hmgcr	Plcb4	Gins2
Acaa2	Akr1c14	Gldc	1700109H08Rik	Irf1	C8a	Apobec3	Hells
Cpne4	Rpl3l	H2-DMb1	Nudt8-1	Irf7	Itih5	Basp1	Smc2
Cdc42ep5	Slc27a2	Gpx3	Gm12981	C4b	Serpine2	Lcn2	Mad21l
8430408G22Rik	Cyp2e1	Slc16a1	Gm48855	H2-Aa	Cdo1	Cp	Cenpw
Halr1	Acy3	Igfbp7	Gm26830	Tmsb10	Cyp51	L1cam	Atad2
Mif	Slc22a7	Enpp2	Pou5f2	Cyr61	Gpm6a	Tacstd2	Spdl1
Triqk	Ccl28	Tmem27	2510017J16Rik	Sfn	Mme	Ltbp3	Spc24
Tceal8	Cd36	Sirpa	Igf2bp3	Parp14	Cyp2a4	Emp2	Cenpe
Maoa	0610031O16Rik	Lrp2	2610037D02Rik	Capg	Tmc4	Il17re	Tk1
Gsto1	Ces2c	Elovl2	Ugt1a6a	Aldh1a1	Kif20b	l"#l\$	Stmn1
Fam213b	0610040F04Rik	Slc43a2	Gm46218	Psmb10	Pantr1	Dsp	Cks1b
Fabp7	Car4	Gabrb3	Neat1	Gbp7	Mpv17l	Mpxq1	E2f1
Rbp1	Mpv17l	Cadm4	Gm9925	Phlda3	Aadat	Arl4c	Lig1
Spns3	Arsg	Prom1	Gm16170	p21	Tmigd1	Ehf	Lmnb1
Osr2	Reep5	Slc16a10	Gm42047	Tnfrsf12a	Apobec2	Timp2	Tubb5
Idh1	Mep1b	Slc2a5	Gm48960	H2-Eb1	Mep1a	Ly6d	Serpib8
Rab42	Ggt1	Tmed6	Malat1	Cp	Apoc3	Sh2d4a	Hba-a2
Gng11	Tmem45b	Slc39a5	Gm20696	Fam131c	Slc7a13	Nbl1	Ezh2
Rtl8b	Lipo3	Folh1	9530034E10Rik	Cryab	Slc10a2	Bcam	Prim1
Ass1	Ace	Gpc3	Schip1	Dcdc2a	Acsm3	Anxa1	Smc4
Rtl8a	Ces2b	Ctsb	Col27a1	AW112010	Hsd17b2	Anxa3	Hba-a1
Cela1	Gm27216	Fads1	Gdap10	Serpib9	Akr1c14	Sytl2	H2afx
Serpib6a	Cyp4b1	Psap	Unc13c	Irgm2	Gstm1	Hspa1b	Hmgb2
Akr1a1	Mep1a	Hspa5	Gm19325	Rhob	Kap	Stox2	Tuba1b
Id4	Slc22a6	Lipa	Gm29666	Stat1	Crot	Tbc1d4	Cox6b2
Smap2	Aadat	Cd63	Gm42726	Gdf15	Rnf24	Zfx3	Ccdc34
Hba-a1	Tnfsf10	Tspan7	E130102H24Rik	Ces2e	Pou3f3	Efemp1	Pmf1
Plin3	Pank1	Slc5a12	Gm13830	H2-DMb1	Slc6a18	Jag1	Haus4
1700067K01Rik	Adh1	G6pc	BC005561	Ces1g	Kyat3	Anxa2	Cdkn2d